DOTTORATO DI RICERCA IN CHIMICA

Convenzione tra
UNIVERSITÀ DEGLI STUDI DI TRIESTE

UNIVERSITÀ CA’ FOSCARI DI VENEZIA
Cotutela con

UNIVERSITÀ DI ANVERSA

CICLO XXXIV

PFAS sensing: Concept design of electrochemical and optical, bio- and biomimetic strategies

Settore scientifico-disciplinare: CHIM01 CHIMICA ANALITICA

Dottoranda **GIULIA MORO**

Coordinatore **PROF. ENZO ALESSIO**

Supervisore di tesi **PROF. LIGIA MARIA MORETTO**

Co-supervisore di tesi **PROF. KAROLIEN DE WAEL**

ANNO ACCADEMICO 2020/2021

Ph.D in Chemistry

UNIVERSITY OF TRIESTE

UNIVERSITY CA' FOSCARI OF VENICE

Joint with
UNIVERSITY OF ANTWERP

CYCLE XXXIV

PFAS sensing: Concept design of electrochemical and optical, bio- and biomimetic strategies

Specific subject area: ANALYTICAL CHEMISTRY

Ph.D student
GIULIA MORO

Coordinator
PROF. ENZO ALESSIO

Thesis Supervisors
PROF. LIGIA MARIA MORETTO
PROF. KAROLIEN DE WAEL

ACCADEMIC YEAR 2020/2021

Table of Contents

Università
Ca'Foscari
Venezia

UNIVERSITÀ
DEGLI STUDI
DI TRIESTE

Universiteit
Antwerpen

MIUR

To all L. M. M., M.L.M.,
Or simply M.L.

“Mais alors, que dois-je devenir ?”
“Un Curieux.”
“Ce n’est pas un métier.”
“Ce n’est pas encore un métier. Voyagez, écrivez, traduisez, apprenez à vivre partout. Commencez tout de suite. L’avenir est aux curieux de profession.”

Jules et Jim, François Truffaut,1962

PFASensing

Concept Design of Electrochemical and Optical, Bio- and Biomimetic Strategies

PFASensing focuses on the concept design of electrochemical and optical, bio- and biomimetic strategies for the quantitative or semi-quantitative determination of ubiquitous environmental contaminants, namely per- and polyfluorinated alkyl substances (PFAS). PFAS are a class of more than 3000 manmade chemicals, that constitute a global issue due to their bioaccumulation and toxic behaviour. In the last two decades, improved regulatory plans and phase-out initiatives supported by in-depth environmental and toxicological studies limited the usage of PFAS. However, as Barceló and Ruan pointed out "*this is not the end of the story*" since novel fluorinated compounds continue to enter the market to replace the old ones and answer our industrial needs.

These *forever chemicals* are well-known in Europe, particularly in the regions of two of the partner institutions of this Joint PhD project (Ca' Foscari University of Venice in Veneto region and the University of Antwerp in the Flanders region of Belgium). In the **Veneto region**, PFAS groundwater contamination started early 2000s in the area of Trissino (Veneto) due to the discharges of the local industries, especially Miteni S.p.a. Since 2013, the media, national and local associations involved (i.e., Legambiente, Greenpeace) are promoting sensibilisation campaigns rising the awareness of the citizens and institutions around this issue. In **Flanders region**, especially in Antwerp, the media hurricane started last summer (2021) when the PFAS levels of tap water were declared to be higher than in the rest of Belgium (>30 ng/L). The data reported by local newspapers dated from 2018 to 2021. These two examples underline the urgency of facing PFAS water contamination and develop new analytical tools.

In this frame, the design of portable and cost-affordable sensing platform which can be applied in large-scale, highly frequent monitoring plans is crucial. So far, numerous colorimetric and electrochemical sensors have been reported for the rapid quantification or qualitative screening of PFAS. However, most of these sensing platforms did not reach the market, yet. Apart from **facing the challenges linked to the technological transfer steps**, we believe in the need of identifying new sensing strategies by changing the criteria used in the design of these devices.

We need to **develop tuneable platforms** able to follow the fast and "*never-ending evolution*" of these fluorinated pollutants. We improved the scientific research creating a well-structured network in which **the findings of toxicological studies can be further applied in the design of sensing strategies** or even bioremediation tools.

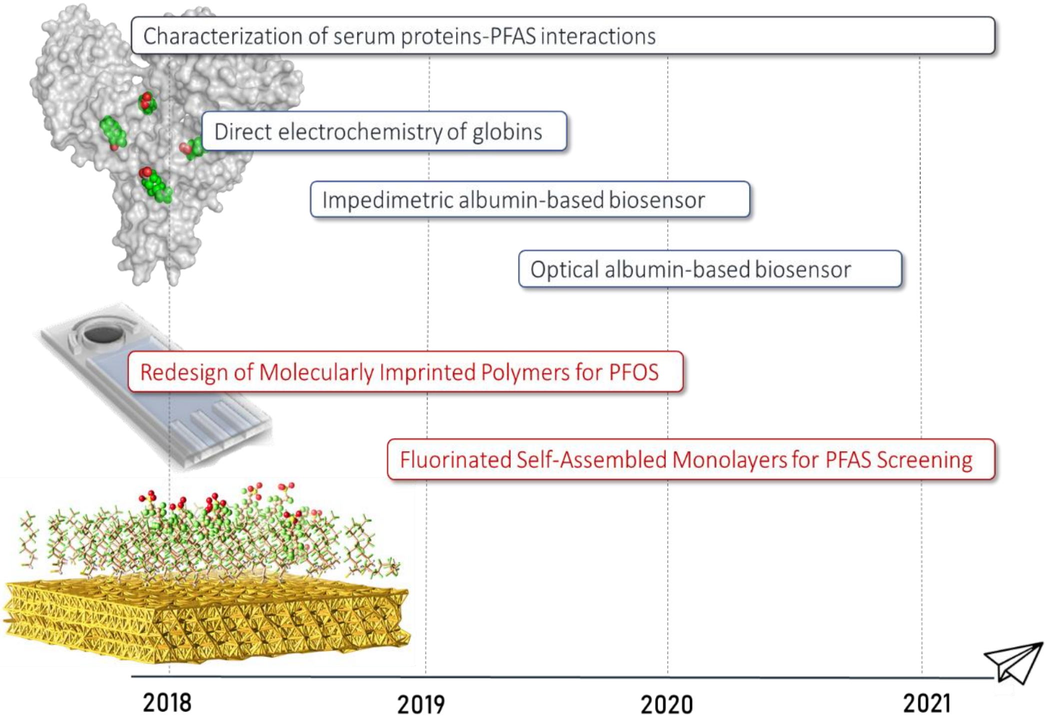

Figure 1. *Flow chart of PFASensing project describing the articulation of our study from 2018 to 2021. From the development of biosensing optical and electrochemical platforms using serum protein as biorecognition layers to the redesign of molecularly imprinted polymer-based voltammetric sensors and the investigation of fluorinated self-assembled monolayers applicability in PFAS screening.*

PFASensing started answering these needs by investigating new biosensing strategies, applying structural biology in bioreceptor design, combining and comparing different sensing platforms, redesigning existing PFAS sensors and testing possible screening method. The different proof-of-concept studies developed within the frame of PFASensing and summarised in **Figure 1** are described in the following chapters:

Chapter 1 - *The Never-ending Story of PFAS: the State of Art*

A brief introduction to the "*endless story*" of PFAS pollution is reported highlighting the global widespread of PFAS, the lack of systematic mapping and monitoring of polluted sites in Europe and the current state of art of the analytical techniques.

Chapter 2 - *Screening Protein Bioreceptor for PFAS: The Globins Family*
Aiming to transpose toxicological studies in PFAS biosensing design, we follow the changes in the electrochemical behaviour of globins upon PFAS exposure, supporting our data interpretation using native mass spectrometry.

Chapter 3 - *Screening Protein Bioreceptors for PFAS: Delipidated Albumin*
Apart from globins, also delipidated human serum albumin was considered for application in PFAS sensing. In this second case-study, a multi-analytical approach was designed aiming to assess the binding kinetics, mechanism and sites as well as the complex stoichiometry and stability.

Chapter 4 - *Applying delipidated hSA in impedimetric sensors: A portable strategy*
An impedimetric label-free biosensor was designed using albumin as biorecognition layer for perfluorooctanoic acid. The protein bioreceptor was immobilized at screen-printed electrodes previously modified via electropolymerisation developing a method which is compatible with EDC/NHS chemistry.

Chapter 5 - *Applying dhSA in electrochemical sensing: A haem-mediated strategy*
The possibility to further combine albumin bioreceptor within a voltammetric sensing strategy was investigated using a natural redox probe, the haem groups, whose interaction with albumin depends on the protein conformation.

Chapter 6 - *Applying dhSA in Optical Biosensors: A Label-free Strategy*
Albumin was immobilized also at D-shaped optical fibers developing a Lossy-Mode-Resonance-based label-free platform. This proof-of-concept study is one of the first examples in which this kind of optical sensors is used for the determination of small-molecules, such as perfluorooctanoic acid.

Chapter 7 - *Molecularly Imprinted Polymers-based Sensor: Practicalities and Pitfalls*
Redesigning existing PFAS sensors to advance in the technological transfer process entails facing several challenges. We observe that when working with electropolymerised molecularly imprinted polymers (MIP), a high control of the electrode surface features is required. A surface characterisation study enabling MIP mapping was carried out in this chapter.

Chapter 8 - *Fluorinated Self-Assembled Monolayers: Different Architectures for PFAS Screening*

Should we take advantage of fluorophilic interactions for the development of PFAS screening sensors? The results presented in this chapter seemed to confirm this possibility. The electrochemical study of different fluorinated self-assembled monolayers has been supported by molecular dynamic simulations.

Chapter 9 - *General Summary and Future Perspectives*

Where should we go now? Towards the design of class-selective sensing platforms for the preliminary screening of the total amount of PFAS in water. Indeed, single-substance detection devices are not able to follow the fast growth of this class of contaminants and do not match the needs of the market. Drawing some general conclusions, we provide a critical discussion of the future perspective of PFASensing: the need to innovate and redesign.

Appendix I - *Analytical Techniques*

The theoretical principles and basic concepts regarding the analytical techniques applied in this PhD work are briefly summarized in this section. Since PFASensing focuses mainly on the development of electrochemical sensing strategies, emphasis is given to voltammetric and impedimetric techniques. All surface characterisation techniques used were mentioned together with the ones used for the study of the protein-ligand complexes.

Appendix II - *List of Publications*

Appendix II summarises the publications of these three-years Joint PhD project. The abstracts of each publication are reported to provide a general understanding of the contents. Indirectly, this section offers an overview of the side-projects and fruitful collaborations cultivated in these years.

|1

The Never-ending Story of PFAS: The State of Art

Abstract

Per- and polyfluoroalkyl substances (PFAS) are synthetic compounds, which have been created in the early 40s to answer the needs of the construction industry as well as electronics, food packaging, household, textile manufacturers. Their groundbreaking capacity to resist extreme physical and chemical conditions like high temperatures and corrosion, and to be simultaneously liphophobic and hydrophobic are of great importance for industrial applications. However, these properties are also responsible for the hazardous effects of PFAS pollution, their toxicity and persistence in the environment. PFAS contamination and its long-term effects need to be carefully monitored to safeguard the overexposed population and our ecosystem. To this aim, the levels of these "forever chemicals" in environmental matrices (mainly water and soil) and biological fluids (plasma) has to be constantly monitored. Mapping PFAS contamination will help studying the long-term effects of these chemicals and reducing the potentially dangerous exposition of living organisms and, therefore, their impact on the ecosystem.

This general introduction will focus on the evolution of PFAS contaminants and their "endless story" providing a detailed state of art of screening and confirmatory analytical methods currently in use for PFAS monitoring. In the editorial of the special issue "Analysis of Perfluoroalkyl Substances in the Environment and Human Health Samples", edited by Damià Barceló and Ting Ruan for Trends in Analytical Chemistry in October 2019, the authors underlined that PFAS determination poses several open challenges. With this overview we aimed to briefly describe these challenges and underline how the development of novel sensing strategies can contribute to face them. Chromatographic and mass spectrometry-based hyphenated techniques play a key role in the quantification of PFAS in environmental matrices. However, their applicability in frequent, large-scale monitoring plans is not affordable and we need to design other analytical tools able to provide a first screening of these compounds.

"These chemicals have large quantities in numbers and complexity in molecular structure, which bring more analytical issues on chromatographic separation, structure elucidation, accurate quantification, and biological effect assessment".

D. Barceló, T. Ruan, TrAC, 2019,[1].

1.1 What to Know about PFAS

1.1.1 Perfluoroalkyl Substances: Widespread Use and Production Routes

Per- and polyfluoroalkyl substances (PFAS) represent a group of manmade chemicals that have been produced since the 1940s to answer several industrial needs [2,3]. Their revolutionary resistance/resilience explains their extensive use and consequent spreading into every environmental compartment: air, soil, and water. Nowadays, PFAS are known for their presence in sources of drinking water and food, and their harmful effects on living organisms' health [4]. Environmental protection agencies (i.e., EAE, EEA) are mobilized to ensure a better consideration of the risks those substances pose to health and environment. This PhD project will be focused on *per*fluoroalkyl substances, as summarised in **Table 1.1**. Chemically speaking, *per*fluoroalkyl substances are aliphatic compounds where all the hydrogen atoms of the aliphatic chain have been substituted by fluorine atoms, while the head group consists of a carboxylic or sulphonic functionality [2]. Most PFAS are characterised by a water-soluble hydrophilic head group and a water insoluble hydrophobic and oleophobic fluorinated tail, as shown in **Figure 1.1.** For simplicity, PFAS can be grouped in two categories depending on the chain length: *long* and *short chain* [5,6]. According to the definition given by the Organisation for Economic Cooperation and Development, *long chain* PFAS are perfluoroalkyl carboxylic acids with eight or more carbon atoms (six or more perfluorinated carbons) and perfluoroalkyl sulfonates with six or more perfluorinated carbons. *Long chain* compounds, such as perfluorooctanoic acid (PFOA) and perfluorooctanesulfonic acid (PFOS) [7,8] are the most ubiquitous and toxic members of this family of water contaminants. It is worth noting that new generations of *short chain* PFAS with chain lengths ranging from six to four carbon atoms continue to enter the market to answer industrial needs [9,10]. The extreme resistance of PFAS to natural degradation processes is due to the remarkable chemico-physical stability of the perfluorinated chain that arises from the unique properties of the elemental fluorine: it has the highest electronegativity among all elements, has high electron affinity, high oxidation potential and oxidation energy. Their stability is mainly due to the carbon-fluorine (C-F) bond, which is one of the strongest of organic chemistry, with a bond energy of about 466 KJ/mol. The oleophobicity is a consequence of the low polarizability of the C-F, which makes fluorocarbons intermolecular attractive interactions (London force) lower compared to hydrocarbons. The small size of covalently bonded fluorine (0.72 Å) allows an efficient shielding of a perfluorinated carbon atom without steric stress, contributing to the perfluoroalkyl chain extreme stability. PFAS are stable to alkali, acids, oxidation and can be heated up to 400°C without decomposition [11,12].

Table 1.1 *Summary of the most common perfluoroalkyl substances name, acronym and structural formula.*

Name	Acronym	Structural formula
Hexafluoropropylene oxide dimer	GenX/HFPO-DA	$C_6F_{11}O_3H$
Perfluorbutanesulfonic acid	PFBS	$C_4F_{11}SO_3H$
Perfluorodecanoic acid	PFDA	$C_{10}F_{19}O_2H$
Perfluorododecanoic acid	PFDoA	$C_{12}F_{23}O_2H$
Perfluoroheptanoic acid	PFHpA	$C7F_{13}O_2H$
Perfluorohexanesulfonic acid	PFHxS	$C_6F_{13}SO_3H$
Perfluorohexanoic acid	PFHxA	$C_6F_{11}O_2H$
Perfluorononanoic acid	PFNA	$C_9F_{16}O_2H$
Perfluorooctanesulfonic acid	PFOS	$C_8F_{17}SO_3H$
Perfluorooctanoic acid	PFOA	$C_8F_{15}O_2H$
Perfluorotetradecanoic acid	PFTeDA	$C_{14}F_{27}O_2H$
Perfluorotridecanoic acid	PFTrDA	$C_{13}F_{25}O_2H$
Perfluorundecanoic acid	PFUnA	$C_{11}F_{21}O_2H$

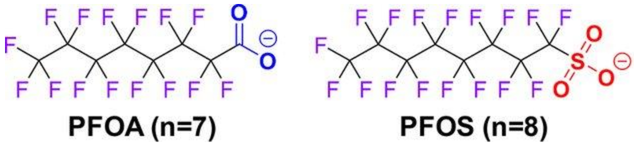

Figure 1.1. Chemical structures of PFOA and PFOS with emphasis on the fluorinated tails and the anionic hydrophilic head groups (in blue and red, respectively).

Perfluorinated surfactants can lower the surface tension of water to half the value attainable with the use of analogous hydrocarbon surfactants, and can be applied in harsh conditions (i.e., high temperature/pressure). PFAS industrial application include military equipment, firefighting foams, erosion inhibitors in aircraft fluids, and consumer products of daily use, such as cookware, pizza boxes, and stain repellents, as depicted in **Figure 1.2**. Despite their versatility, PFAS have soon been discovered to be persistent and accumulate in animal and vegetal tissues with adverse outcomes [13]. As a result, several PFAS have been listed in the *Stockholm Convention on Persistent Organics Pollutants* of 2009, and in the U.S.A. the industry voluntary phased-out PFOS and PFOA, while local and national governments launched restrictions for their use and production worldwide [14]. However, "*this is not the end of the story*" as pointed out by D. Barceló et al.: a more systematic and synergic strategy should be considered from the legal authorities and environmental agencies to face PFAS pollution [1].

Despite the variety of applications, **PFAS synthesis** follows two main routes: **electrochemical fluorination** (**ECF**) and **telomerization**. The primary manufacturers are DuPont and 3M Company [6,15]. ECF is performed by dissolving or dispersing the substrate (linear sulfonyl or acyl halide) in anhydrous hydrogen fluoride in an electrochemical reactor. A voltage below 8 V (typically 5-7 V) is applied, fluorination occurs at the anode and hydrogen evolves at the cathode. The cathode is usually made of iron or nickel and the anode is made of nickel. The passage of direct current in the solution causes the formation of free radicals leading to chain rearrangements and breakage. This results in a mixture of linear and branched perfluorinated isomers and homologues of the raw material. In the synthesis of PFOS and PFOA, a mixture of 70-80% of linear products and 20-30% of branched products is obtained. Cell temperature is kept under the boiling point of hydrogen fluoride (20 °C). Electrochemical methods have been also applied to operate PFAS removal [16]. **Telomerization** consists in a radical polymerization where a perfluoroalkyl iodide (*telogen*), most commonly pentafluoroethyliodide (CF_3CF_2I), reacts with tetrafluoroethylene (*taxogen*), CF_2CF_2, to yield a mixture of longer perfluoroalkyl iodide (*telomer*). The telomer is finally oxidised to give perfluoro alcohols, perfluoro carboxylic acids and perfluoro sulphonic acids. Telomerization produces completely linear PFAS with an elevate number of carbons [17]. A general knowledge of the synthetic paths in use is fundamental if we consider that most PFAS emissions come from production plants. These latter have been identified as the main sources of PFAS environment pollution [18] together with the other emission sources summarised in the infographic of **Figure 1.2**.

1.1.2 PFAS Sources of Exposure and Effects on Living Organisms' Health

How do PFAS reach drinking water, food, air, and soil? PFAS are released in the environment mainly by chemical industries and then **transported** over long distances, far from their source of emission. Following several routes, PFAS penetrate into the soil and then reach the groundwater, therefore easily attaining human beings. **Human beings** are exposed to PFAS from many sources: they can be introduced in the human organism by ***ingestion***, ***inhalation,*** and ***skin penetration*** [18]. Ingestion of PFAS-contaminated tap water has been identified as the primary source of exposure (>90% of total PFAS exposure) for populations living near contaminated sites [19,20]. **Food** can be contaminated with water used in farming, or by the use of treated municipal sludge and biosolids as fertilizers in crops [18]. Fortunately, this happens in a limited number of cases. According to Vestergren *et al.*,*"(…) food intake is the major contemporary exposure pathway for the background population, whereas drinking water exposure is dominant for populations near sources of contaminated drinking water"*[21]. Another common route of contact with perfluoroalkyl carboxylic acids is its presence in **non-stick cookware** and in oil-resistant lining of **food packaging** treated with fluorotelomer (fluoropolymer) as an unwanted by-product of the telomerization process [22]. As a representative example of the presence of these compounds in food, it was reported that microwave popcorn could account for about 20% of the PFOA exposure in adults consuming 10 bags a year if 1% of the fluorotelomers are metabolized to PFOA. **Indoor**

dust has been reported to contain PFAS and to be a source of exposure via inhalation, hand-to-mouth contact and skin penetration, contributing up to 15% to adult PFAS exposure [18]. The reported PFAS in indoor dusts are predominantly PFOA, PFOS and PFNA, and the PFAS total concentration ranges from 100 to 917 ng/g [23].

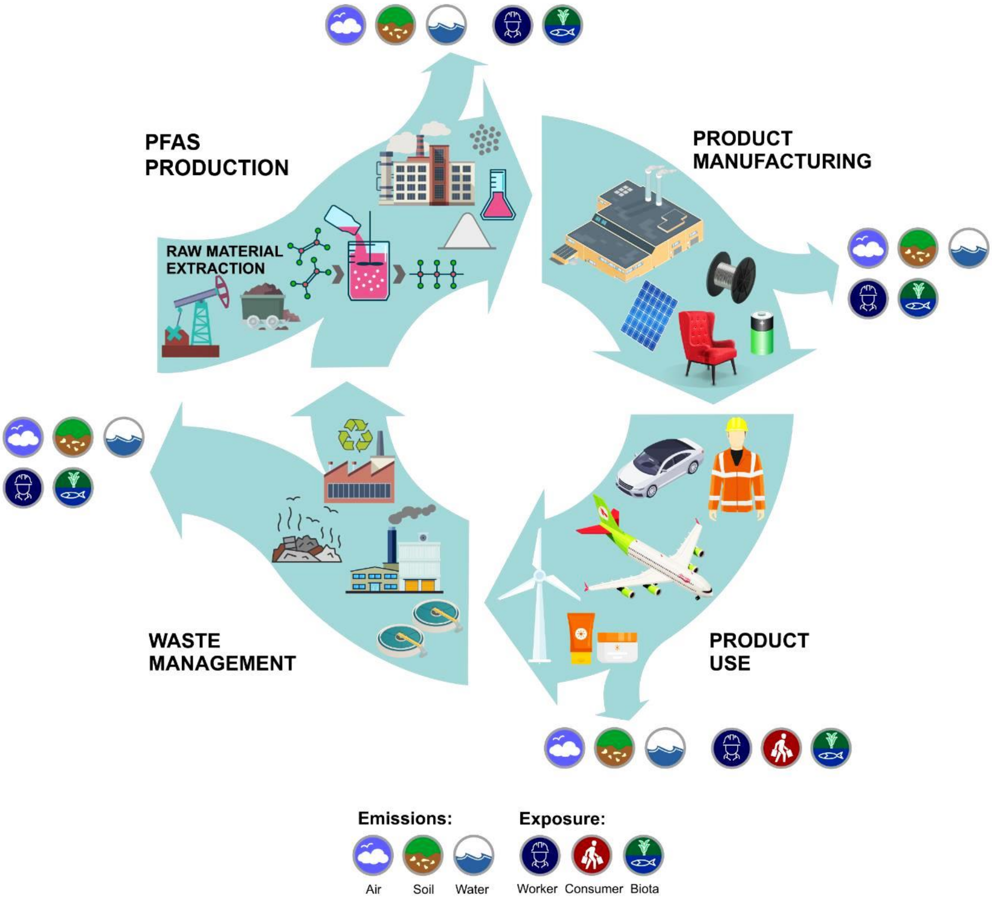

Figure 1.2 *Emission and exposure to PFAS during their lifecycle (source: EEA-ETC report, Systemic view on fluorinated polymers, forthcoming, 2020).*

As summarised in **Figure 1.3**, the exposure to PFAS leads to several **adverse effects in human beings and animals,** including: toxicity on liver, kidney and immune system, mesothelioma, liver, testicular and kidney cancer, infertility, thyroid diseases, endocrine interferent, higher risk of diabetes mellitus, hypercholesterolemia, ulcerative colitis, pregnancy-induced hypertension and pre-eclampsia [13,24].

In a recent study Foresta *et al*. [25] investigated the effects of PFAS on **human fertility**. Recent research has focused mostly on female fecundity, but both *in vitro* and animal studies have shown a detrimental effect of PFOA and PFOS on testicular functions as well, by the alteration of steroidogenic machinery and subsequent defect of spermatogenesis [4,26–28]. In the epidemiologic studies, the data collected indicated that PFAS activity might be linked also to the genetic expression of sex hormones nuclear receptors, suggesting that PFAS might induce the blood-testis barrier dysfunction and infertility [29–32]. When human beings and animals eat or drink food or water contaminated by PFAS, these latter are absorbed and **bioaccumulated** in the body for relatively long periods of time. Therefore, a constant exposure to PFAS from different sources over time results in the accumulation of meaningful levels of these substances in the body (tissues and blood), leading to the above mentioned pathologies [21,33]. To be more specific, we can relate PFAS toxic effects to their long elimination half-life[1] ($t_{1/2}$). The average $t_{1/2}$ depends on the PFAS chain length: *long chain* PFAS are reported to have longer $t_{1/2}$, an average of 2-5 years for PFOA and PFOS, while *short chain* has average $t_{1/2}$ of days, an average of 26 days for PFBS [18].

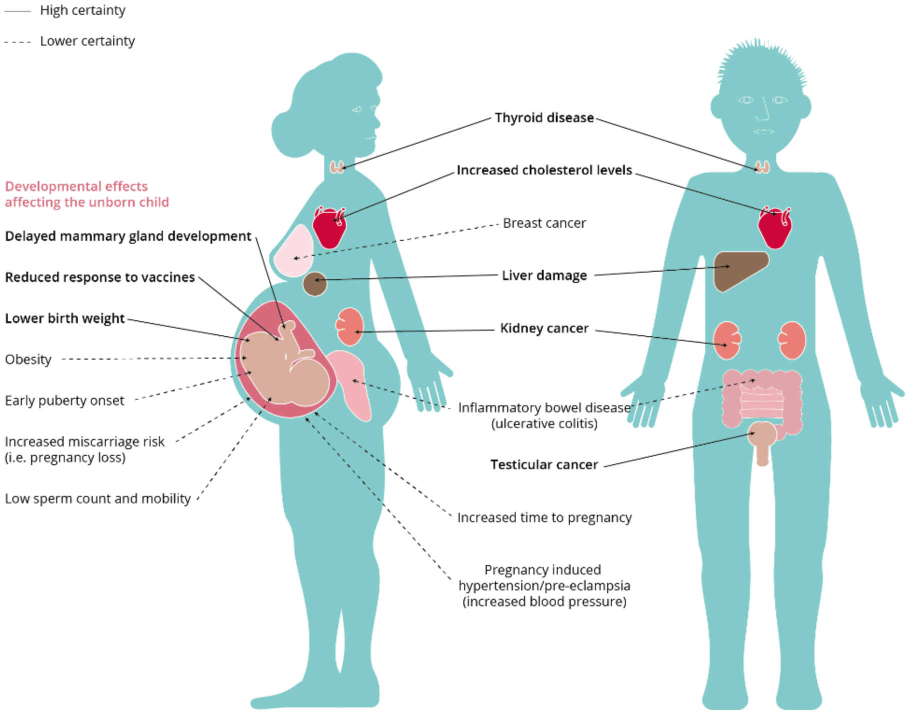

Figure 1.3 *Main adverse effects of PFAS on human body. Image reprinted from EEA official website*[2].

Organic fluorine was firstly detected in human **blood** in 1968 using ^{19}F Nuclear Magnetic Resonance; however only in 1976 its presence was related to PFOA [26,34]. Nowadays, PFOS and PFOA are present in the blood of virtually every American citizen in the low nanomolar range concentration (416 nM for PFOS) [21]. In the period between 1999 and 2014, PFOA and PFOS concentration in American citizens decreased by 70% and 84%, respectively, as a result of phasing out of PFOA and PFOS in the US.

---

[1] *Elimination half-life of a molecule in human body is the time it takes from its maximum concentration to half maximum concentration*.

[2] *https://www.eea.europa.eu/publications/emerging-chemical-risks-in-europe/emerging-chemical-risks-in-europe*

Higher concentrations are detected in the blood of people exposed to PFAS in the workplace, with values ranging from 5 to 24 µM in blood of PFAS production plants workers [27,28]. This can be considered an extreme example of PFAS impact on a confined population, however meaningful levels (nM) of PFOA/PFOS in blood were reported even for European and especially Italian citizens. In Italy, high levels of PFAS contamination were observed in Veneto and Piemonte regions in correspondence to PFAS production plants of Miteni and Solvay, respectively [35]. Blood levels of PFAS **70 times higher** than the national average were found in people, irrespective of age, living in Veneto areas contaminated by Miteni [35–37].

1.1.3 PFAS Open Challenges: from Regulation to Remediation

Globally regulated PFAS. Since 2009, perfluorooctane sulfonic acid (**PFOS**) and its derivatives have been included in the inventory of the International Stockholm Convention as emerging contaminants and, as a consequence, an action plan to limit PFOS use was drafted. Since 2010, PFOS use has been restricted in the EU according to the EU's Persistent Organic Pollutants (POPs) Regulation. In addition, the Stockholm Convention regulates the global elimination of perfluorooctanoic acid (PFOA), its salts and PFOA-related compounds. PFOA has been banned under the POPs Regulation since 4 July 2020. Perfluorohexane sulfonic acid (PFHxS), its salts and related compounds as well as perfluorinated carboxylic acids (C9-14 PFCAs) are being considered for inclusion in the Stockholm Convention and consequent global elimination [38–40].

***REACH** restrictions around the world, values summary in **Table 1.2**.* Perfluorinated carboxylic acids (C9-14 PFCAs), their salts and precursors will be restricted in the **EU/EEA** from February 2023 onwards, following a decision taken by the European Commission. Meanwhile, the government of **Norway** has proposed a restriction on perfluorohexane-1-sulphonic acid (PFHxS), its salts and related substances. In June 2020, the European Chemical Agency's (**ECHA**) scientific committees shared their opinion supporting these restrictions and the proposal is currently with the European Commission for decision, including representative of the EU countries. In **Germany,** the competent authority has also submitted a further restriction proposal for undecafluorohexanoic acid (PFHxA), its salts and related substances. **Netherlands** and **Germany**, with the support from **Norway, Denmark** and **Sweden,** are preparing a restriction proposal to cover a wide range of PFAS uses – in support of the statements made in the Environment Council in December 2019. They are expected to submit the proposal to ECHA by 15 July 2022. Furthermore, ECHA will submit a restriction proposal in January 2022 for PFAS used in firefighting foams. Numerous other PFAS are in the **REACH** Candidate List for **substances of very high concern** (**SVHC**). In June 2019 and January 2020, two PFAS groups were identified as SVHC, based on their persistence, mobility and toxicity, and were considered a threat to human health and wildlife. These groups are: (*i*) 2,3,3,3-tetrafluoro-2-(heptafluoropropoxy) propionic acid, its salts and its acyl halides (HFPO-DA), a short-chain PFAS substitute for PFOA in fluoropolymer production (its ammonium salt is commonly known as **GenX**), (*ii*) perfluorobutane sulfonic acid (PFBS) and its salts, the current alternative to PFOS. This SVHC identification indicated these PFAS as of equivalent concern to carcinogens, mutagens and reprotoxicants (CMRs) and persistent and toxic/very persistent and very bioaccumulative (PBTs/vPvBs) chemicals. Only few PFAS show a common **classification** and **labelling** under the Labelling and Packaging (**CLP**) regulation.

Since 2014, an informal **coordination group** of several EU Member States, ECHA, and the European Commission has screened data on PFAS contained in ECHA's registration database and coordinated group-based regulatory work. Despite operating a more efficient approach compared to single-substance regulation, this work has only been able to cover the PFAS groups of highest urgency due to the very large number of PFAS. ECHA's database contains information on over **2 000 individual PFAS** on the EU market. To face this scenario, ECHA acknowledges a **holistic group approach** to the regulatory assessment and risk management, as requested in the proposal for an EU strategy for PFAS submitted in December 2019. The recast of the **Drinking Water Directive**, which took effect on 12 January 2021, includes a limit of 0.5 μg/L for all PFAS. This is in line with a grouping approach for all PFAS. As anticipated, PFAS are released into the environment through industrial manufacturing not directly linked to **food production,** and through the use and **disposal of PFAS-containing** products. The main contributors to human dietary exposure are certain **vegetables** and **drinking water**, but also fish and seafood, meat and meat products, eggs, milk and dairy products [41]. In September 2020, the **European Food Safety Authority** (EFSA) set a new safety threshold for the main perfluoroalkyl substances that accumulate in the body (tolerable weekly intake (**TWI**) of 4.4 nanograms per kilogram of body weight per week). EFSA's scientific advice will support risk managers in their decisions on how best to protect consumers from exposure to PFAS through food. The rising concern for PFAS pollution, the evidence of toxic effects and the growing interest of public opinion, have led to extensive regulatory policies in the United States and Europe, as showed in **Table 1.2**. The American Environmental Protection Agency (EPA) **Office of Water** indicated a lifetime health advisory limit of 70 ng/L for PFOS and PFOA in drinking water, while in Italy, until 2017, the so-called *performance limit* was 60 ng/L for PFOS and 500 ng/L for PFOA. After the PFAS contamination of surface and groundwater resulting from Miteni plant (Trissino) emissions, **Veneto region imposed a strict regulation for PFAS**, lowering the drinking water limits to 30 ng/L for PFOS and 60 ng/L for PFOA [42,43]. Despite their differences, all regulations presented aim to safeguard water safety, particularly for populations living near contaminated areas.

Table 1.2 *Health advisory/performance limits of PFOA and PFOS for drinking water in USA, Italy, Veneto Region, Germany and United Kingdom [12,42,43].*

State	PFOS (ng L^{-1})	PFOA (ng L^{-1})
USA	70	70
Veneto region (before 2017)	60	500
Veneto region	30	60
Germany	100	100
United Kingdom	300	10 000

When considering drinking water limits, it has to be considered that PFAS are a wide and fast developing class of chemicals, since industries are gradually replacing common long chains with novel short chains, but only the drinking water levels of the most common and studied PFAS are regulated [12]. The industrial practice of **phasing out a PFAS and replacing it** with a structurally similar one is an easier and less expensive strategy than identifying a nonfluorinated alternative and converting the whole manufacturing process. This "**replacement strategy**" increases both the numbers of PFAS on the market and the difficulties in tracking them, without solving the health issues. PFAS manufactures are often reluctant to communicate PFAS structures, residual intermediates, by-products and confidential toxicity studies [44]. In this scenario, tuneable analytical tools are urgently needed.

1.2 Analytical methods for PFAS detection

The analytic techniques for PFAS detection in water can be divided in confirmatory and screening methods [14,45]. **Confirmatory methods** rely mainly on the application of hyphenated techniques, where a separation technique (e.g., liquid chromatography) is coupled with an online spectroscopic detection (e.g., mass spectrometry). Confirmatory techniques are powerful analytical tools which allow the simultaneous identification and quantitative determination of contaminants, even in complex environmental matrices. However, the samples must be collected, then brought to a centralized facility and subjected to a laborious pre-treatment requiring long analysis times. **Screening methods** are mainly based on sensing platforms designed to detect the targeted molecule with or without minimal pre-treatment, providing qualitative or semiquantitative results, and allowing the performance of large-scale monitoring plans. Among screening methods, which include also sensing platforms, optical and electrochemical sensing strategies have been largely investigated for environmental and clinical applications.

A chemical sensor is a compact device that transforms chemical information into an analytically useful signal [46]. The chemical information can originate from a chemical reaction with the participation of the analyte, or from a physical property of the system investigated. Chemical sensors contain two basic functional units: a *receptor* or *recognition layer* and a *transducer* part. In the receptor, specific chemical information is transformed into a form of energy which can be measured by the transducer, that transforms this energy in the analytical signal. The transducer itself does not present selectivity. Chemical sensors are classified according to the operating principle of the transducer: thermal, mass, optical, colorimetric, potentiometric, amperometric or voltametric. Sensing strategies may be classified either as *switch-on* when the analytical signal is enhanced in the presence of increasing concentrations of target molecule or *switch-off* when the signal is quenched. Compared to confirmatory techniques, the main advantages of sensors are the low costs, the rapidity of operation, and their portability.

Let's take a step back. Our current knowledge on PFAS can largely be attributed to Hansen *et al.,* who pioneered their detection with the use of high-performance liquid chromatography coupled to tandem mass spectrometry (HPLC-MS/MS) searching for PFAS in human serum [47]. Since then, an ever-growing variety of instrumental chromatographic configurations were reported in the literature for quantitative or qualitative PFAS analysis. Instrumental variations can result in different sensitivities, analytical time, and costs; therefore, a clear understanding of the possible choices is crucial when selecting the appropriate analytical tool. In all the cases, prior to the chromatographic analysis, several steps of pre-treatment, extraction, and clean-up of aqueous samples are often necessary to remove potentially interfering substances. To this aim, several techniques have been applied, such as solid-phase extraction (SPE) and liquid-liquid extraction (LLE). Recent advancements for the most precise extraction of PFAS involve solid-phase microextraction (SPME) and dispersive liquid-liquid microextraction (DLLME), [48,49]. The applicability of each extraction technique can differ based on the analytes. High-performance liquid chromatography (HPLC) is the most commonly applied analytical method for PFAS in aqueous matrices, generally presenting good sensitivity and limits of detection in the range of a few ng/L, which are satisfying PFAS regulation limits [50,51]. Comparing HPLC-MS/MS to UHPLC-MS/MS and capillary LC-MS for analysis of PFAS in river waters, HPLC scored the lowest for linearity of response, analytical speed, sensitivity, and reproducibility [52]. The higher investment cost of UHPLC systems can be compensated by the reduction in solvent volumes and associated disposal costs, as well as reducing the analytical time, which is around 50% lower. However, transition from HPLC to UHPLC systems requires time and resources, since HPLC methods are already very well established. **Gas chromatography** (GC) is less commonly applied, due to the limitation of the volatility of PFAS, and is applied for mainly determination of airborne PFAS [53].

Chromatography is commonly coupled with MS as **detection method;** typically, MS is carried out by electron impact (EI) or chemical ionisation (CI). Generally, MS/MS systems provide significantly better accuracy than MS systems, due to the increased selectivity of double mass filtering. Simcik and Dorweiler reported quantification limits in the range of 0.28 to 0.58 ng L^{-1} for surface waters with the use of MS, while comparable limits have been reported for detection in serum [54,55]. When MS systems are used for PFAS detection, efficient sample clean-up steps and robust quality assurance information are needed to exclude the possibility of sample contamination. Overestimation of absolute recoveries (>100%) is often being reported. This is indicative of matrix and absorption effects that can cause signal suppression or enhancement. Matrix-matched calibration standards have shown to compensate for this issue [56].

1.3 PFAS Sensing Platforms

Electrochemical sensing methods are successfully applied to nonelectroactive targets using indirect detection strategies. These methods usually record changes in the electrochemical signal of an electroactive probe in the presence/absence of the target, when the latter interacts with a molecular recognition layer (*receptor*) present on the electrode surface (*transducer*) [57]. These electrode modifications include bioreceptors and biomimetic receptors such as antibodies, enzymes, peptides, aptamers and molecularly imprinted polymers (MIP). For instance, indirect detection can exploit the inhibition of an enzymatic receptor and the consequent decrease in the signal of its electroactive products to determine a target able to selectively bind and inactivate the enzyme [57]. In other cases, the target concentration results to be proportional to changes in the charge transfer resistance at a MIP after the recognition event [58]. To enhance the sensitivity of the final devices, these receptors are often immobilized on hierarchical nanomaterials and/or nanocomposites [59]. Moreover, indirect monitoring can be extended to the detection of electroactive targets with a non-characteristic electrochemical fingerprint, especially in complex matrices (such as blood, wastewater, etc.). In general, the signal amplification and adaptability of these **indirect electrochemical sensing strategies** make them particularly attractive for the detection of nonelectroactive contaminants at very low concentrations. In literature, different approaches to the development of sensing strategies for PFAS have been reported so far, including: colorimetric, optical, fluorescence spectrophotometric, and electrochemical-based sensors.

Colorimetric detection strategies are based on the change/development of solution colour in presence of the target molecule, due to the interaction between the analyte and a molecular recognition system (see **Figure 1.4**). The anionic nature of PFAS has been exploited by *Fang et al.*, who proposed a portable smartphone app-based system for colorimetric detection: PFOA and PFOS bind to a cationic dye and a forman ion pair that can be extracted in non-aqueous phase for colorimetric analysis [45]. In this case, other ionic surfactants cause interference, and solid or liquid phase extraction is necessary prior to analysis to remove possible interferences. However, these detection strategies did not achieve detection limits required by health advisory bodies/performance limits and further development is necessary.

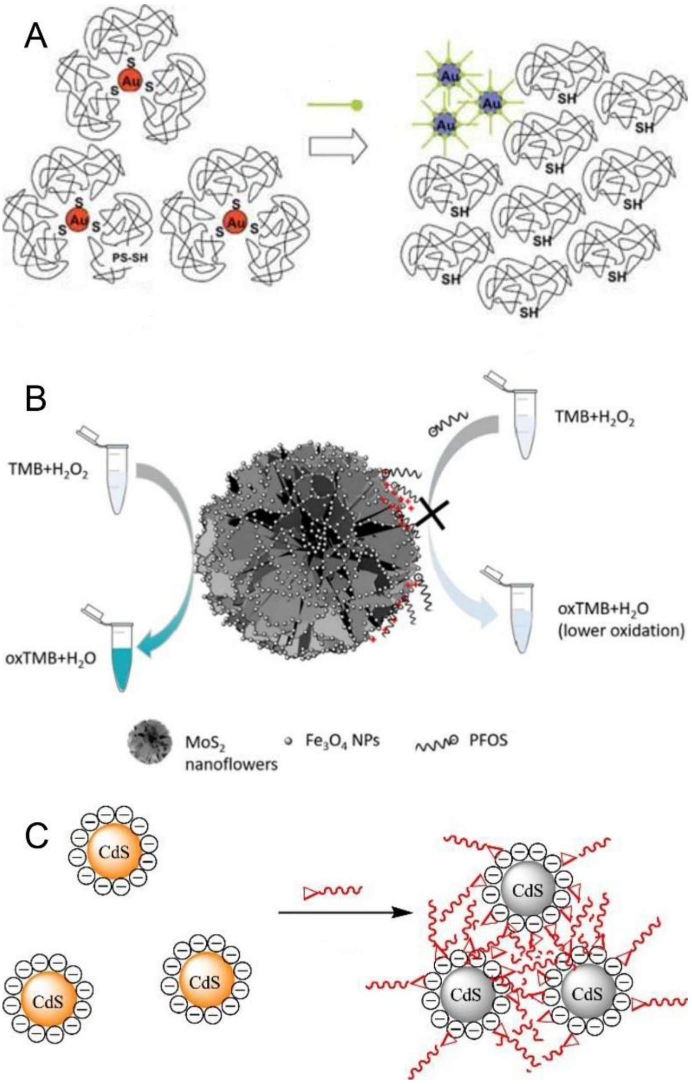

Figure 1.4 *Comparison of recent colorimetric sensing strategies for long-chain PFAS: (**A**)polystyrene-modified gold nanoparticles for the PFOA screening (PFOA in green), (**B**) peroxidase-mimicking 3D magnetic MoS2/Fe3O4 nanocomposites used in PFOS screening and (**C**) fluorescent detection of PFOA by the aggregation of MPA-CdS quantum dots (PFOA in red). This overview is reprinted with permission from [45].*

Niu et al. exploited the **size-dependent colour** of gold nanoparticles for PFAS class detection in water. Gold nanoparticles (Au-NPs) were first modified with perfluorinated thiols [60]. The specific fluorophilic interactions between the fluorinated thiols and PFAS tails led to the absorption of PFAS on the perfluorinated thiols layer, and to the aggregation of Au-NPs. The colour of the sample solution and its absorbance in the UV−Vis range change progressively upon increased PFAS concentrations, therefore the colorimetric test results to be semi-quantitative. This sensor exhibits PFAS-class selectivity, and a detection limit of 100 ng/L was obtained.

PFAS **fluorescence** detection strategies draw researchers' attention in the last ten years [45]. These sensors are based on the enhancement or reduction of fluorescence that arise from the interaction between PFAS and a molecular system bearing a site with affinity for PFAS. Recently, *Cheng et al.* reported a selective *turn-on* fluorescence sensor for PFOA and PFOS based on the fluorescence enhancement in system [61]. *Cheng et al.* also reported a fluorescence sensor where the PFOS molecule enhances the fluorescence of a carbon dots-berberine chloride hydrate system. This sensor exhibits improved selectivity toward PFOS [62]. A fluorescence enhancement (*switch-on*) approach is preferred to a fluorescence quenching (*switch-off*) one, since the former reduces the chance of false positive data by other fluorescent quenchers existing in samples [63]. However, these platforms did not reach the detection limit required by health advisory bodies/performance limits.

Electrochemical sensors based on (bio)mimetic receptors, such as **molecularly imprinted polymers (MIP),** were largely applied as reviewed by *Menger et al.* and further discussed in **Chapter 7** [45]. Also, **self-assembled monolayers** (**SAM**) have been reported for PFAS detection and are believed to receive more attention in the near future. *Fang et al.* reported a detection strategy for PFOA employing SAM modified gold electrodes [64,65]. This strategy provides insightful results about SAM-PFAS interactions, as further described in **Chapter 8.**

Recent advances on new sensing platforms offer an opportunity to develop inexpensive, user-friendly sensors for water safety, large-scale environmental monitoring, and direct *in situ* analysis. Regardless of the detection strategy, sensors need to be robust, stable, reliable, and target-selective for application in environmental matrices.

Acknowledgments

I would like to thank Ettore Martini for his master thesis work. My gratitude to my supervisors and all the "AXES girls". Thank you for sharing the challenge of writing a review together, thousands fruitful discussions, your enthusiasm, the coffee times, the drawings and even the grammar checks. You teach me creative synthesis, competences valorisation and how I want to be as a researcher! Thank you Hanan, Karen, Noelia (x2), Liselotte, Camila, Sara, Elise and (in the backstage) Anca, Vanoushe and Victoria!

References

[1] D. Barceló, T. Ruan, Challenges and perspectives on the analysis of traditional perfluoroalkyl substances and emerging alternatives, TrAC - Trends Anal. Chem. 121 (2019) 2–3. https://doi.org/10.1016/j.trac.2019.07.016.

[2] R.C. Buck, J. Franklin, U. Berger, J.M. Conder, I.T. Cousins, P. De Voogt, A.A. Jensen, K. Kannan, S.A. Mabury, S.P.J. van Leeuwen, Perfluoroalkyl and polyfluoroalkyl substances in the environment: Terminology, classification, and origins, Integr. Environ. Assess. Manag. 7 (2011) 513–541. https://doi.org/10.1002/ieam.258.

[3] C.F. Kwiatkowski, D.Q. Andrews, L.S. Birnbaum, T.A. Bruton, J.C. DeWitt, D.R.U. Knappe, M. V Maffini, M.F. Miller, K.E. Pelch, A. Reade, A. Soehl, X. Trier, M. Venier, C.C. Wagner, Z. Wang, A. Blum, Scientific Basis for Managing PFAS as a Chemical Class, Environ. Sci. Technol. Lett. 7 (2020) 532–543. https://doi.org/10.1021/acs.estlett.0c00255.

[4] L. Giari, C. Guerranti, G. Perra, M. Lanzoni, E.A. Fano, G. Castaldelli, Occurrence of perfluorooctanesulfonate and perfluorooctanoic acid and histopathology in eels from north Italian waters, Chemosphere. 118 (2015) 117–123. https://doi.org/10.1016/j.chemosphere.2014.06.066.

[5] X. Bai, Y. Son, Perfluoroalkyl substances (PFAS) in surface water and sediments from two urban watersheds in Nevada, USA, Sci. Total Environ. 751 (2021) 141622. https://doi.org/https://doi.org/10.1016/j.scitotenv.2020.141622.

[6] R.C. Buck, J. Franklin, U. Berger, J.M. Conder, I.T. Cousins, P. De Voogt, A.A. Jensen, K. Kannan, S.A. Mabury, S.P.J. van Leeuwen, Perfluoroalkyl and polyfluoroalkyl substances in the environment: Terminology, classification, and origins, Integr. Environ. Assess. Manag. 7 (2011) 513–541. https://doi.org/10.1002/ieam.258.

[7] J.N. Meegoda, J.A. Kewalramani, B. Li, R.W. Marsh, A review of the applications, environmental release, and remediation technologies of per-and polyfluoroalkyl substances, Int. J. Environ. Res. Public Health. 17 (2020) 1–26. https://doi.org/10.3390/ijerph17218117.

[8] P. Zhao, X. Xia, J. Dong, N. Xia, X. Jiang, Y. Li, Y. Zhu, Short- and long-chain perfluoroalkyl substances in the water, suspended particulate matter, and surface sediment of a turbid river, Sci. Total Environ. 568 (2016) 57–65. https://doi.org/https://doi.org/10.1016/j.scitotenv.2016.05.221.

[9] P. Minuz, L. De Toni, S. Dall'Acqua, A. Di Nisio, I. Sabovic, M. Castelli, A. Meneguzzi, C. Foresta, Interference of C6O4 on platelet aggregation pathways: Cues on the new-generation of perfluoro-alkyl substance, Environ. Int. 154 (2021) 106584. https://doi.org/https://doi.org/10.1016/j.envint.2021.106584.

[10] Y. Pan, J. Wang, L.W.Y. Yeung, S. Wei, J. Dai, Analysis of emerging per- and polyfluoroalkyl substances: Progress and current issues, TrAC Trends Anal. Chem. (2019) 115481. https://doi.org/https://doi.org/10.1016/j.trac.2019.04.013.

[11] Z. Abunada, M.Y.D. Alazaiza, M.J.K. Bashir, An Overview of Per- and Polyfluoroalkyl Substances (PFAS) in the Environment: Source, Fate, Risk and Regulations, Water . 12 (2020). https://doi.org/10.3390/w12123590.

[12] A. Cordner, V.Y. De La Rosa, L.A. Schaider, R.A. Rudel, L. Richter, P. Brown, Guideline levels for PFOA and PFOS in drinking water: the role of scientific uncertainty, risk assessment decisions, and social factors, J. Expo. Sci. Environ. Epidemiol. 29 (2019) 157–171. https://doi.org/10.1038/s41370-018-0099-9.

[13] M. Houde, J.W. Martin, R.J. Letcher, K.R. Solomon, D.C.G. Muir, Biological monitoring of polyfluoroalkyl substances: A review, Environ. Sci. Technol. 40 (2006) 3463–3473. https://doi.org/10.1021/es052580b.

[14] C. Bosch-Orea, M. Farré, D. Barceló, Chapter Ten - Biosensors and Bioassays for Environmental Monitoring, in: I. Palchetti, P.-D. Hansen, D.B.T.-C.A.C. Barceló (Eds.), Past, Present Futur. Challenges Biosens. Bioanal. Tools Anal. Chem. A Tribut. to Profr. Marco Mascini, Elsevier, 2017: pp. 337–383. https://doi.org/https://doi.org/10.1016/bs.coac.2017.06.004.

[15] N. V Ignat'ev, Electrochemical Fluorination: A Powerful Tool for the Preparation of Organofluorine Compounds, in: H. Groult, F.R. Leroux, A.B.T.-M.S.P. and R. of F.C. Tressaud (Eds.), Elsevier, 2017: pp. 71–123. https://doi.org/https://doi.org/10.1016/B978-0-12-803740-9.00004-4.

[16] J. Radjenovic, N. Duinslaeger, S.S. Avval, B.P. Chaplin, Facing the Challenge of Poly- and Perfluoroalkyl Substances in Water: Is Electrochemical Oxidation the Answer?, Environ. Sci.

Technol. 54 (2020) 14815–14829. https://doi.org/10.1021/acs.est.0c06212.

[17] R. Dhore, G.S. Murthy, Per/polyfluoroalkyl substances production, applications and environmental impacts, Bioresour. Technol. 341 (2021) 125808. https://doi.org/https://doi.org/10.1016/j.biortech.2021.125808.

[18] E.M. Sunderland, X.C. Hu, C. Dassuncao, A.K. Tokranov, C.C. Wagner, J.G. Allen, A review of the pathways of human exposure to poly- and perfluoroalkyl substances (PFASs) and present understanding of health effects, J. Expo. Sci. Environ. Epidemiol. 29 (2019) 131–147. https://doi.org/10.1038/s41370-018-0094-1.

[19] S. Banzhaf, M. Filipovic, J. Lewis, C.J. Sparrenbom, R. Barthel, A review of contamination of surface-, ground-, and drinking water in Sweden by perfluoroalkyl and polyfluoroalkyl substances (PFASs), Ambio. 46 (2017) 335–346. https://doi.org/10.1007/s13280-016-0848-8.

[20] X.C. Hu, D.Q. Andrews, A.B. Lindstrom, T.A. Bruton, L.A. Schaider, P. Grandjean, R. Lohmann, C.C. Carignan, A. Blum, S.A. Balan, C.P. Higgins, E.M. Sunderland, Detection of Poly- and Perfluoroalkyl Substances (PFASs) in U.S. Drinking Water Linked to Industrial Sites, Military Fire Training Areas, and Wastewater Treatment Plants, Environ. Sci. Technol. Lett. 3 (2016) 344–350. https://doi.org/10.1021/acs.estlett.6b00260.

[21] R. Vestergren, I.T. Cousins, Tracking the Pathways of Human Exposure to Perfluorocarboxylates, Environ. Sci. Technol. 43 (2009) 5565–5575. https://doi.org/10.1021/es900228k.

[22] J. Glüge, M. Scheringer, I.T. Cousins, J.C. DeWitt, G. Goldenman, D. Herzke, R. Lohmann, C.A. Ng, X. Trier, Z. Wang, An overview of the uses of per- and polyfluoroalkyl substances (PFAS), Environ. Sci. Process. Impacts. 22 (2020) 2345–2373. https://doi.org/10.1039/D0EM00291G.

[23] L. Knobeloch, P. Imm, H. Anderson, Perfluoroalkyl chemicals in vacuum cleaner dust from 39 Wisconsin homes, Chemosphere. 88 (2012) 779–783. https://doi.org/https://doi.org/10.1016/j.chemosphere.2012.03.082.

[24] C. Lau, K. Anitole, C. Hodes, D. Lai, A. Pfahles-Hutchens, J. Seed, Perfluoroalkyl acids: A review of monitoring and toxicological findings, Toxicol. Sci. 99 (2007) 366–394. https://doi.org/10.1093/toxsci/kfm128.

[25] C. Foresta, S. Tescari, A. Di Nisio, Impact of perfluorochemicals on human health and reproduction: a male's perspective, J. Endocrinol. Invest. 41 (2018) 639–645. https://doi.org/10.1007/s40618-017-0790-z.

[26] C. Lau, J.L. Butenhoff, J.M. Rogers, The developmental toxicity of perfluoroalkyl acids and their derivatives, Toxicol. Appl. Pharmacol. 198 (2004) 231–241. https://doi.org/https://doi.org/10.1016/j.taap.2003.11.031.

[27] O.G. W., H. Han-Yao, H.K. J., H.K. J., B.J. L., M.J. H., Historical Comparison of Perfluorooctanesulfonate, Perfluorooctanoate, and Other Fluorochemicals in Human Blood, Environ. Health Perspect. 113 (2005) 539–545. https://doi.org/10.1289/ehp.7544.

[28] K. Kannan, S. Corsolini, J. Falandysz, G. Fillmann, K.S. Kumar, B.G. Loganathan, M.A. Mohd, J. Olivero, N. Van Wouwe, J.H. Yang, K.M. Aldous, Perfluorooctanesulfonate and Related Fluorochemicals in Human Blood from Several Countries, Environ. Sci. Technol. 38 (2004) 4489–4495. https://doi.org/10.1021/es0493446.

[29] E. Emerce, Ö. Çetin, Genotoxicity assessment of perfluoroalkyl substances on human sperm, Toxicol. Ind. Health. 34 (2018) 884–890. https://doi.org/10.1177/0748233718799191.

[30] B.P. Rickard, I. Rizvi, S.E. Fenton, Per- and poly-fluoroalkyl substances (PFAS) and female reproductive outcomes: PFAS elimination, endocrine-mediated effects, and disease, Toxicology. 465 (2022) 153031. https://doi.org/https://doi.org/10.1016/j.tox.2021.153031.

[31] Y.R. Kim, N. White, J. Bräunig, S. Vijayasarathy, J.F. Mueller, C.L. Knox, F.A. Harden, R. Pacella, L.-M.L. Toms, Per- and poly-fluoroalkyl substances (PFASs) in follicular fluid from women experiencing infertility in Australia, Environ. Res. 190 (2020) 109963. https://doi.org/https://doi.org/10.1016/j.envres.2020.109963.

[32] W. Wang, W. Zhou, S. Wu, F. Liang, Y. Li, J. Zhang, L. Cui, Y. Feng, Y. Wang, Perfluoroalkyl substances exposure and risk of polycystic ovarian syndrome related infertility in Chinese women, Environ. Pollut. 247 (2019) 824–831. https://doi.org/https://doi.org/10.1016/j.envpol.2019.01.039.

[33] W.S. Guy, D.R. Taves, W.S. Brey, Organic Fluorocompounds in Human Plasma: Prevalence and Characterization, in: Biochem. Involv. Carbon-Fluorine Bond., AMERICAN CHEMICAL SOCIETY, 1976: pp. 117-134 SE–7. https://doi.org/doi:10.1021/bk-1976-0028.ch007.

[34] D.R. Taves, Evidence that there are Two Forms of Fluoride in Human Serum, Nature. 217 (1968) 1050–1051. https://doi.org/10.1038/2171050b0.

[35] G. Bertanza, G.U. Capoferri, M. Carmagnani, F. Icarelli, S. Sorlini, R. Pedrazzani, Long-term investigation on the removal of perfluoroalkyl substances in a full-scale drinking water treatment plant in the Veneto Region, Italy, Sci. Total Environ. 734 (2020) 139154. https://doi.org/https://doi.org/10.1016/j.scitotenv.2020.139154.

[36] P. Gisella, D.R. Filippo, C. Cristina, B. Giulia, Z.J. Maryam, D. Francesca, M. Flavio, Z. Rinaldo, B.A. Maria, S. Giampaolo, V. Silvia, Z. Lorena, M. Marco, M. Domenico, R. Francesca, Serum Levels of Perfluoroalkyl Substances (PFAS) in Adolescents and Young Adults Exposed to Contaminated Drinking Water in the Veneto Region, Italy: A Cross-Sectional Study Based on a Health Surveillance Program, Environ. Health Perspect. 128 (2021) 27007. https://doi.org/10.1289/EHP5337.

[37] A.M. Ingelido, A. Abballe, S. Gemma, E. Dellatte, N. Iacovella, G. De Angelis, F. Zampaglioni, V. Marra, R. Miniero, S. Valentini, F. Russo, M. Vazzoler, E. Testai, E. De Felip, Biomonitoring of perfluorinated compounds in adults exposed to contaminated drinking water in the Veneto Region, Italy, Environ. Int. 110 (2018) 149–159. https://doi.org/https://doi.org/10.1016/j.envint.2017.10.026.

[38] H. Fiedler, I. van der Veen, J. de Boer, Global interlaboratory assessments of perfluoroalkyl substances under the Stockholm Convention on persistent organic pollutants, TrAC - Trends Anal. Chem. 124 (2020). https://doi.org/10.1016/j.trac.2019.03.023.

[39] H. Fiedler, T. Kennedy, B.J. Henry, A Critical Review of a Recommended Analytical and Classification Approach for Organic Fluorinated Compounds with an Emphasis on Per- and Polyfluoroalkyl Substances, Integr. Environ. Assess. Manag. (2020). https://doi.org/10.1002/ieam.4352.

[40] H. Fiedler, I. van der Veen, J. de Boer, Global interlaboratory assessments of perfluoroalkyl substances under the Stockholm Convention on persistent organic pollutants, TrAC - Trends Anal. Chem. 124 (2020). https://doi.org/10.1016/j.trac.2019.03.023.

[41] G.W. Curtzwiler, P. Silva, A. Hall, A. Ivey, K. Vorst, Significance of Perfluoroalkyl Substances (PFAS) in Food Packaging, Integr. Environ. Assess. Manag. 17 (2021) 7–12. https://doi.org/https://doi.org/10.1002/ieam.4346.

[42] www.gazzettaufficiale.it/eli/gu/2016/07/16/165/sg/pdf, Italian Ministry of the Environmental Legislative Decree, Roma, 2016.

[43] Https://bur.regione.veneto.it/BurvServices/pubblica/DettaglioDgr.aspx?id=284035, Deliberazione della Giunta Regionale del Vento n. 1874 del 14 ottobre 2014, (2014) 2–7.

[44] Z. Wang, I.T. Cousins, U. Berger, K. Hungerbühler, M. Scheringer, Comparative assessment of the environmental hazards of and exposure to perfluoroalkyl phosphonic and phosphinic acids (PFPAs and PFPiAs): Current knowledge, gaps, challenges and research needs, Environ. Int. 89–90 (2016) 235–247. https://doi.org/10.1016/j.envint.2016.01.023.

[45] R.F. Menger, E. Funk, C.S. Henry, T. Borch, Sensors for detecting per- and polyfluoroalkyl substances (PFAS): A critical review of development challenges, current sensors, and commercialization obstacles, Chem. Eng. J. 417 (2021) 129133. https://doi.org/https://doi.org/10.1016/j.cej.2021.129133.

[46] A. Hulanicki, S. Glab, F. Ingman, Chemical sensors definitions and classification, Pure Appl. Chem. 63 (1991) 1247–1250. https://doi.org/10.1351/pac199163091247.

[47] K.J. Hansen, L.A. Clemen, M.E. Ellefson, H.O. Johnson, Compound-Specific, Quantitative Characterization of Organic Fluorochemicals in Biological Matrices, Environ. Sci. Technol. 35 (2001) 766–770. https://doi.org/10.1021/es001489z.

[48] M. Monteleone, A. Naccarato, G. Sindona, A. Tagarelli, A rapid and sensitive assay of perfluorocarboxylic acids in aqueous matrices by headspace solid phase microextraction–gas chromatography–triple quadrupole mass spectrometry, J. Chromatogr. A. 1251 (2012) 160–168. https://doi.org/https://doi.org/10.1016/j.chroma.2012.06.033.

[49] J. Wang, Y. Shi, Y. Cai, A highly selective dispersive liquid–liquid microextraction approach based on the unique fluorous affinity for the extraction and detection of per- and polyfluoroalkyl substances coupled with high performance liquid chromatography tandem–mass spectrometry, J. Chromatogr. A. 1544 (2018) 1–7. https://doi.org/https://doi.org/10.1016/j.chroma.2018.02.047.

[50] S.F. Nakayama, M. Yoshikane, Y. Onoda, Y. Nishihama, M. Iwai-Shimada, M. Takagi, Y. Kobayashi, T. Isobe, Worldwide trends in tracing poly- and perfluoroalkyl substances (PFAS) in the environment,

TrAC - Trends Anal. Chem. 121 (2019). https://doi.org/10.1016/j.trac.2019.02.011.

[51] M. Trojanowicz, M. Koc, Recent developments in methods for analysis of perfluorinated persistent pollutants, Microchim. Acta. 180 (2013) 957–971. https://doi.org/10.1007/s00604-013-1046-z.

[52] M. Onghena, Y. Moliner-Martinez, Y. Picó, P. Campíns-Falcó, D. Barceló, Analysis of 18 perfluorinated compounds in river waters: Comparison of high performance liquid chromatography–tandem mass spectrometry, ultra-high-performance liquid chromatography–tandem mass spectrometry and capillary liquid chromatography–mass spectrom, J. Chromatogr. A. 1244 (2012) 88–97. https://doi.org/https://doi.org/10.1016/j.chroma.2012.04.056.

[53] B.F. Scott, C.A. Moody, C. Spencer, J.M. Small, D.C.G. Muir, S.A. Mabury, Analysis for Perfluorocarboxylic Acids/Anions in Surface Waters and Precipitation Using GC−MS and Analysis of PFOA from Large-Volume Samples, Environ. Sci. Technol. 40 (2006) 6405–6410. https://doi.org/10.1021/es061131o.

[54] A. Kärrman, B. van Bavel, U. Järnberg, L. Hardell, G. Lindström, Development of a Solid-Phase Extraction-HPLC/Single Quadrupole MS Method for Quantification of Perfluorochemicals in Whole Blood, Anal. Chem. 77 (2005) 864–870. https://doi.org/10.1021/ac049023c.

[55] M.F. Simcik, K.J. Dorweiler, Ratio of Perfluorochemical Concentrations as a Tracer of Atmospheric Deposition to Surface Waters., Environ. Sci. Technol. 40 (2006) 410. https://doi.org/10.1021/es052244v.

[56] S. Ullah, T. Alsberg, U. Berger, Simultaneous determination of perfluoroalkyl phosphonates, carboxylates, and sulfonates in drinking water, J. Chromatogr. A. 1218 (2011) 6388–6395. https://doi.org/https://doi.org/10.1016/j.chroma.2011.07.005.

[57] G. Moro, K. De Wael, L.M. Moretto, Challenges in the electrochemical (bio)sensing of nonelectroactive food and environmental contaminants, Curr. Opin. Electrochem. 16 (2019) 57–65. https://doi.org/10.1016/j.coelec.2019.04.019.

[58] C. Malitesta, E. Mazzotta, R.A. Picca, A. Poma, I. Chianella, S.A. Piletsky, MIP sensors - The electrochemical approach, Anal. Bioanal. Chem. 402 (2012) 1827–1846. https://doi.org/10.1007/s00216-011-5405-5.

[59] G. Maduraiveeran, M. Sasidharan, V. Ganesan, Electrochemical sensor and biosensor platforms based on advanced nanomaterials for biological and biomedical applications, Biosens. Bioelectron. 103 (2018) 113–129. https://doi.org/10.1016/j.bios.2017.12.031.

[60] H. Niu, S. Wang, Z. Zhou, Y. Ma, X. Ma, Y. Cai, Sensitive Colorimetric Visualization of Perfluorinated Compounds Using Poly(ethylene glycol) and Perfluorinated Thiols Modified Gold Nanoparticles, Anal. Chem. 86 (2014) 4170–4177. https://doi.org/10.1021/ac403406d.

[61] Z. Cheng, L. Du, P. Zhu, Q. Chen, K. Tan, An erythrosin B-based “turn on” fluorescent sensor for detecting perfluorooctane sulfonate and perfluorooctanoic acid in environmental water samples, Spectrochim. Acta Part A Mol. Biomol. Spectrosc. 201 (2018) 281–287. https://doi.org/https://doi.org/10.1016/j.saa.2018.05.013.

[62] C. Fang, M. Megharaj, R. Naidu, Electrochemical switch on-off response of a self-assembled monolayer (SAM) upon exposure to per fl uorooctanoic acid (PFOA), J. Electroanal. Chem. 785 (2017) 249–254. https://doi.org/10.1016/j.jelechem.2016.12.040.

[63] F. Du, F. Zeng, Y. Ming, S. Wu, Carbon dots-based fluorescent probes for sensitive and selective detection of iodide, Microchim. Acta. 180 (2013) 453–460. https://doi.org/10.1007/s00604-013-0954-2.

[64] C. Fang, Z. Sobhani, M. Megharaj, R. Naidu, Electrochemical Proof of Fluorophilic Interaction among Fluoro-Carbon Chains, Electroanalysis. 30 (2018) 2349–2355. https://doi.org/10.1002/elan.201800190.

[65] C. Fang, M. Megharaj, R. Naidu, Electrochemical Studies on Self-assembled Monolayer (SAM) Upon Exposure to Anionic Surfactants: PFOA, PFOS, SDS and SDBS, Electroanalysis. 29 (2017) 2155–2160. https://doi.org/10.1002/elan.201700108.

|2

Screening Protein Bioreceptor for PFAS: The Globins Family

Adapted from:

E. Daems, G. Moro, H. Berghmans, L. M. Moretto, S. Dewilde, A. Angelini, F. Sobott and K. De Wael, "Native mass spectrometry for the design and selection of protein bioreceptors for perfluorinated compounds"
Analyst, 2021, 146, 2065

Abstract

Shall we transfer toxicological findings in bioreceptor design to develop innovative pathways for PFAS biosensing? Toxicological studies provide crucial information about PFAS-biomolecules complexes that can help evaluate their applicability even in biosensing. Characterising PFAS-protein binding is instrumental to the understanding of cellular toxicities, biotransformation pathways, as well as the fate of PFAS.

*Since PFAS were traced in human plasma and recognised globally as hazards for our health, numerous toxicological studies focused on PFAS-serum protein interactions. Haemoglobin and albumin (***Chapter 3***) were specifically considered in these studies. Haemoglobin is part of the superfamily of globins including other haem-proteins, such as neuroglobin (NGB).*

In this chapter, we try to answer our first question by considering the outcomes of previously reported haemoglobin-PFAS studies. These studies underlined that PFAS binding leads to a conformational change in haemoglobin quaternary structure. Such conformation change might result in the redox electrochemical signal of the protein, which depends on the presence of haem groups. Following these changes, we can possibly trace back the presence of PFAS. However, haemoglobin is a tetramer, and its haem group are buried in the amino acid chains, leading its direct electrochemistry to be often difficult to record. Other globins, such as NGB, present a monomeric structure with a more exposed haem, resulting more suitable for the development of electrochemical sensing strategies. Here, a preliminary study of NGB electrochemistry was carried out, evaluating the effect of oxygen. The possible variations of NGB electrochemical behaviour after exposure to PFAS was investigated via voltammetric techniques. This study has a double scope: i) screening PFAS toxicity on NGB, ii) evaluating the protein applicability as PFAS bioreceptor.

*Apart from voltammetric techniques, also native mass spectrometry (MS) was applied. The rich toolbox of native MS enables supporting the electrochemical data interpretation. For this preliminary study, NGB interactions with well-known PFAS, such as perfluorooctanoic acid and perfluorooctanesulfonic acid, were considered to verify the potential of native MS screening approach. This first multi-analytical study, followed by a more complex one (***Chapter 3***), provides an example of how an in-depth understanding of serum proteins-PFAS interactions can contribute to toxicological studies and probe the applicability of these proteins as bioreceptors.*

2.1. Introduction

2.1.1 From Toxicological Studies to Biosensors Design

Biosensing platforms are answering the increasing demand of analytical tools for environmental monitoring [1–3]. A key step in the development of biosensors is the selection of the *bioreceptor* or *biorecognition element*: a biomolecule (i.e., protein, peptide or aptamer) which enables the specific recognition of the analyte and undergoes biochemical changes that can be further translated into a detectable signal, as anticipated in **Chapter 1** [4]. In general, the possibility to combine a (protein) bioreceptor within a biosensing platform depends mainly on the affinity and specificity of the recognition, the compatibility with the matrix of interest (i.e., waste water, biological fluids), the production costs and the physicochemical stability in the required working conditions [5]. These criteria should be carefully evaluated while screening new bioreceptors for small organic molecules, such as PFAS. Although the monitoring of *long-chain* and *short-chain* PFAS through fluorescence-based, optical and electrochemical sensors showed promising results [6–9], the examples of **biosensing platforms** for PFAS are still limited because: *i)* certain types of bioreceptors, such as aptamers, are not compatible with PFAS due to their chemico-physical properties and *ii)* the selection of peptides or nanobodies toward such small highly fluorinated compounds is still an open challenge. In this scenario, proteins, especially serum proteins of toxicological interest, appear to be a suitable alternative, together with more complex strategies, such as the one reported by Cennamo *et al.* The authors developed an immunosensor selecting antibodies which is able to recognise PFOA-bovine serum albumin (BSA) conjugates [10]. Even in this sensing strategy, PFOA is captured by a protein bioreceptor (BSA) and then, detected using an antibody. The analysis of the PFAS sensing literature proved once again the need for investigating new sensing architecture, starting from the recognition, or better, biorecognition layers.

Transposing toxicological studies, particularly the ones focusing on PFAS-protein interactions, **to bioreceptor design** might allow to develop new biosensing platforms and conceptualisation strategies. Toxicological studies provide fundamental information about PFAS-protein complexes by clarifying binding site distributions, affinity constants, stoichiometries, etc. A complete overview of the analytical techniques in use for the characterisation of PFAS-protein complexes, giving emphasis to their limits and potential, was recently reported by Liu *et al.* [11]. For instance, PFAS affinity toward serum proteins such as haemoglobin (Hb) and albumin was extensively characterised by multi-analytical approaches based on fluorescence spectroscopy, mass spectrometry (MS), circular dichroism (CD), isothermal titration calorimetry (ITC), X-ray crystallography, and molecular docking [12–15], as further discussed in **Chapter 3**. A study carried out by Wang *et al*. [16] shows that the **perfluorooctane sulfonate** (PFOS) **has interactions with Hb**. This study was based on CD, UV-VIS spectroscopy, fluorescence spectroscopy and molecular docking analyses. CD data showed that PFOS leads to a significant change in the secondary structure of the protein. UV-VIS and fluorescence results underlined that PFOS binding affects also the tertiary structure of Hb. Also, the symmetry of the haem group was found to be altered, affecting Hb functions (in particular its ability to bind to oxygen). The experimental analyses were supported by a molecular modelling screening which showed that PFOS could enter the main cavity of Hb by several non-covalent interactions. Overall, the Hb-PFOS complex formation causes a conformation change in the protein structure, resulting in a major exposure of the haem group, as showed in **Figure 2.1**.

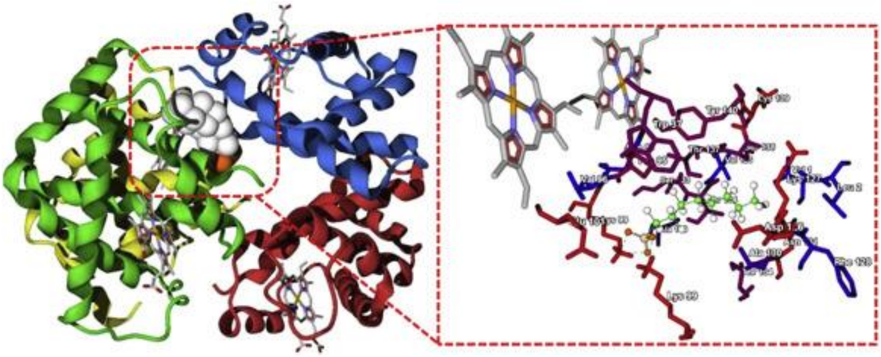

Figure 2.1 *Haemoglobin-PFOS binding mode predicted via molecular docking; zoom in the binding site in proximity of the haem group. Image reprinted from Wang et al. [16]; the original image is in low resolution.*

These findings play a crucial role in the understanding of PFOS toxicity: they explain the relatively long half-life of these contaminants in our blood and also *how* they alter serum protein functions. However, these results show also that the **conformational changes** caused by PFOS binding are highly specific, meaningful, reproducible and do not lead to a sudden denaturation/unfolding phenomenon (PFOS-Hb complex can be considered stable in physiological working conditions). All these characteristics are often required for a bioreceptor, as previously stated. Therefore, Hb or other proteins of the globin superfamily, such as neuroglobin (NGB), should be further considered in the development of biosensing strategies. As described by Wajcman *et al.,* all globins are structurally related and characterised by a common prosthetic group, the *haem group,* [17]. Among globins, Hb is surely the most known, but not the easiest to study via direct electrochemistry, considering that it presents four haem groups buried in the amino acid chains of its tetrameric structure, as shown in **Figure 2.2A-C** [18]. In **Figure 2.2 D-E**, other monomeric globins that are possibly more suitable to test for application as bioreceptors in PFAS electrochemical biosensors are pictured. Globin's electroactive behaviour, especially the one of Hb, was largely applied in fundamental studies, catalysis and design of biosensing strategies, as described by Scheller *et al*. [18], confirming the applicability of this protein superfamily in electrochemical sensors.

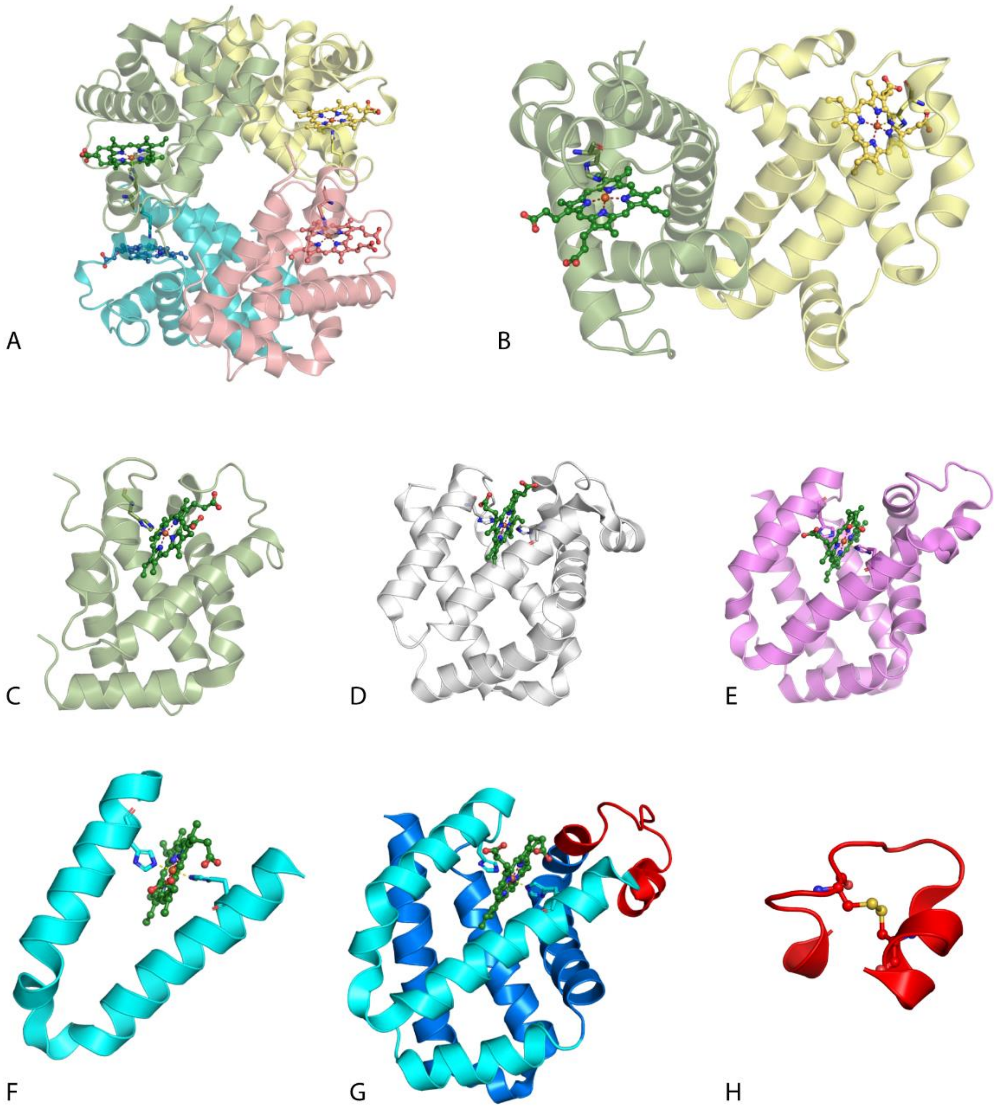

Figure 2.2. *Structure of Hb: tetramer (**A**), dimer (**B**) and monomer (**C**); structure of myoglobin (**D**) and neuroglobin (**E**). Details of neuroglobin structure (**F-H**), particularly the CD region (**H**). Image created with PyMOL* [19], *PDB ID: 1NQP; 3RGK; 1OJ6.*

2.1.2 The Globin Superfamily and Neuroglobin

The *haem group* is responsible for the affinity of globins for oxygen and other diatomic molecules, on which the two possible oxidation states (+2 and +3) of the protein also depend, based on the iron atom at the centre of the *haem group*. The configuration of the iron atom determines the hexacoordinate or pentacoordinate nature of the globins. Most globins are hexacoordinate, while pentacoordination often represents a transition state, since when the metallic centre is in this state of coordination, there is a high affinity for oxygen. In the absence of ligands, the structure will be predominantly hexacoordinate [20]. Furthermore, these coordination changes alter the conformation of the protein, which will therefore have a different behaviour in interactions with other proteins or in redox reactions. By following the electrochemical behaviour of **globins in the absence/presence of ligands**, indirect information can be obtained with respect to the conformational changes induced by the formation of the globin-ligand complex. This is valid for diatomic molecules, such as oxygen or carbon monoxide, as well as for other small molecules (potentially toxic to the protein), such as acrylamide [21]. The interactions with ligands that modify the conformation and behaviour of globins can be fundamental in toxicological studies, since they are capable of altering the functionality of globins. By evaluating the presence or absence of variations in the electrochemical behaviour of the protein, one could confirm or not the presence of a certain ligand/analyte.

Among globins, neuroglobin was selected in this study because of *i)* its monomeric structure, *ii)* its known electrochemical behaviour and *iii)* its conformational changes upon PFAS exposure have not been studied yet. Therefore, our study might also provide useful toxicological information. **NGB protein** was first identified in 2000 by Burmester *et al.* at the University of Mainz, Germany [22]. With a MW of 17 kDa, NGB is expressed in the central and peripheral nervous system, cerebrospinal fluid, retina and endocrine tissues [22,23]. The total concentration of NGB is in any case lower than that of other globins, such as Hb. Although NGB belongs to the class of globins and has similarities with Hb, they appear to have less than 25% of the amino acid sequence (primary structure) in common. The so-called globin fold, on the other hand, generally remains conserved, even if with some modifications. In particular, NGB is a monomeric protein like myoglobin, while the α and β helices are similar to the structure of Hb. NGB rearranges into eight α helices (see **Figure 2.2G**), and is part of the globins with the classic 3/3 α-helical folding and the various helices also give a hydrophobic character to the structure [23].

The **electroactive behaviour of NGB**, as well as Hb, is linked to the presence of the *haem group* consisting of a porphyrin ring, which is coordinated with an iron atom. The presence of this transition metal characterizes the ability of the group, and therefore of the protein, to bind to other substances. The iron atom possesses an octahedral geometry: it can hence up to six bonds, four of which are between iron and the porphyrin ring, therefore remaining on the same plane, and two are in coordination with the histidine of the protein, in particular His-F8 proximal and distal His-E7, out of plane. Thus, NGB is a *hexacoordinate haemo-protein*. When the interaction with distal histidine fails, NGB will be defined as a *pentacoordinate haemoprotein*. In this case, the iron atom will be slightly exposed with respect to the plane, towards the distal histidine. This occurs at the moment of transition, when the ligand comes into contact with the group to bind. As reported by P. Ascenzi *et al*. [24], globins have a high flexibility in the α-helices C, D, E and F, whose spatial configuration can influence the pseudo-enzymatic properties and reactivity with the protein ligands. For example, the interaction and folding of the C and D chains gives rise to the formation of the region called: **CD-loop**/α-helix D region, presented in the previous **Figure 2.2F-H**. The conformational changes of this region, due to the disulphide bridge of the two Cys (CD5) 46-Cys (D5) 55 cysteines, affect the reactivity of the haem group, weakening the coordination bonds of iron and facilitating the entry of the ligands. All this structural information suggests that the interpretation of the changes in NGB electrochemical behaviour might be related to different structural features and conformational changes in the protein structure. Therefore, data interpretation needs to be extremely careful and a multi-analytical approach is preferable to avoid misinterpretations.

NGB electrochemistry was first described by Trashin *et al.* [25] considering different variants of this globin. Under nitrogen atmosphere, NGB shows highly reversible electrochemical behaviour either in solution or immobilized on the electrodes surface. The redox process has a formal potential E^0 of about 0.136 V vs SCE corresponding to $Fe^{3+/2+}$ transition in the haem unit of NGB. Because of hexacoordination of the iron, the haem unit undergoes little structural reorganisation during the reduction/oxidation transition, enhancing electron transfer kinetics. Its redox behaviour is easy to follow since its haem group is less hindered than in Hb.

To support the electrochemical study, we draw upon the **rich toolbox of native mass spectrometry** (MS). This technique is widely applied in the study of noncovalent interactions of small molecules with biomolecules, such as proteins. Its soft ionisation enables to maintain protein-ligand complexes in the gas phase, preserving even relatively weak noncovalent interactions. The complex formation can be followed by monitoring the shifts in the m/z value of the biomolecule. In presence of multiple binding events, these shifts are proportional to the number of ligands bounds. So far, native MS has never been applied in the **screening of possible protein-based bioreceptors** for sensing applications in support of electrochemical data.

In this chapter, NGB electrochemical behaviour in presence/absence of PFAS was studied, while haemoglobin and cytochrome c were used as a reference system. Cytochrome c (cyt c) is a 12 kDa, water-soluble protein and can be considered as a model protein[26,27]. Then, PFAS bioreceptor library was screened by native MS. Through these case studies, we aim to evaluate the applicability of native MS as a complementary method for the design and characterisation of bioreceptors.

2.2. Materials and Methods

2.2.1. Materials

Perfluorooctanoic acid (PFOA, ≥ 96 %), perfluorooctane sulfonic acid potassium salt (PFOS, ≥ 98 %), human haemoglobin (Hb) and cytochrome c from the human heart were purchased from Sigma-Aldrich (Belgium). Recombinant human neuroglobin was expressed and purified as reported previously [24]. The 100 mM ammonium acetate solution pH 6.8 was prepared using ammonium acetate (> 98 %) purchased from Sigma-Aldrich (Belgium). All other reagents were of analytical grade, and solutions were prepared using double distilled deionised water. Human neuroglobin (NGB) was prepared by Prof. S. Dewilde's group (University of Antwerp, Belgium), following the protocol reported in the literature [28]. Stock solutions 1-2 mg mL^{-1} ($2.41*10^{-3}$ M for PFOA and $2.00*10^{-1}$M per PFOS) were prepared with deionized water, 10% MeOH was added to PFOS solution.

2.2.2. Sample Preparation

Prior to use, Hb was dialysed overnight in 100 mM ammonium acetate pH 6.8 using Slide-a-Lyzer Mini dialysis units with a molecular weight cut-off of 3.5 kDa (Thermo Fisher Scientific, Belgium). The denatured samples were directly prepared in 50/50 acetonitrile/MilliQ water with 0.1 % formic acid. The concentrations of the protein solutions were verified using a Nanodrop2000 (Thermo Fisher Scientific) using the parameters in **Table 2.1**. The average of three triplicate measurements was considered. NGB and cyt c were buffer exchanged to 100 mM ammonium acetate pH 6.8 using Micro Bio-spin columns (Bio-gelP6, Bio-rad). Samples of 10 µM protein with the desired concentration of PFOA/PFOS were prepared in 100 mM ammonium acetate pH 6.8. Once the protein prepared, PFOA/PFOS solutions were kept for a maximum of 5 hours in the fridge at 4 ^{0}C. No incubation time with the target was needed before running the measurements.

Table 2.1. Parameters used for Nanodrop2000 measurements.

Protein	Wavelength (nm)	Molecular weight (Da)	E ($mol^{-1}cm^{-1}L$)	PDB
Hb (oxyhaemoglobin)	414	64458	524280	1NQP
NGB	410	17501	12200	1OJ6

2.2.3 Electrochemical Measurements

Electrochemical measurements were carried out using a three-electrode cell setup equipped with: a gold disk electrode (Au-DE) as working electrode (1 mm diameter), a Pt coil counter electrode, and an Ag/AgCl (KCl sat.) reference electrode. CV and Square Wave Voltammetry (SWV) were carried out using the potentiostat PGSTAT101 (Metrohm-autolab) controlled by NOVA 2.0 software. In the standard cell configuration, the three electrodes were immersed in a 10 mL cell with phosphate buffer. In the case of NGB study, a particular configuration with a cellulose dialysis membrane with MWCO4 of 14 kDa (D9777-100FT, Sigma Aldrich) fixed to the working electrode surface was used. This modification of the working electrode allows the protein to be confined on the electrode surface operating with a standard configuration electrochemical cell, without the need to use specific micro-volume cells, such as the Hagen cell [29]. The membrane must allow the protein to remain close to the electrode surface, while ensuring the exchange of ions and the diffusion of other chemical species from the solution to the electrode, and vice versa. Therefore, a membrane with MWCO of 14 kDa will be able to retain proteins with molecular weight greater than 14 kDa such as neuroglobin (17 kDa).

Despite the numerous advantages in terms of versatility, the use of dialysis membranes can present some limitations and problems. In particular, proteins can adsorb to the membrane through hydrophobic interactions, modifying its porosity and making mass transport heterogeneous. These adsorption phenomena are controlled by various factors including the concentration of the protein, the ionic strength of the buffer solution, the pH, the temperature, etc. In the development of the experimental part these factors were carefully considered.

2.2.4. Native MS

A sample volume of approximately 2-4 µL protein solution was required for each measurement, and introduced into the mass spectrometer using nESI with in-house made gold-coated borosilicate capillaries. Two different instruments were used in this process. The hSA measurements were performed on a Q-TOF2 instrument (MSVision) that is modified for the transmission of high-mass macromolecular assemblies. The spray capillary voltage ranged between 1.2 and 1.8 kV, the source temperature was set to 30 °C and the sample and extractor cone were set to 25 V and 10 V, respectively. The collision energy was fixed to 50 V. Gas pressures were 10 mbar and $1{\cdot}10^{-2}$ mbar for the backing and collision gas, respectively. The measurements of the other proteins were performed on a Synapt G2 HDMS instrument (Waters) with N_2 gas (purity 99.9999 %, Messer) in the IM cell and the following instrument settings were used: spray capillary voltage 1.2-1.9 kV, source temperature 30 °C, sampling cone 25 V, extraction cone 1 V, trap collision energy 5 V (for the CIU experiments this was varied from 10 to 150 V), transfer collision energy 0 V, trap DC bias 45 V, IMS wave height 35 V and IMS wave velocity 700 m/s. The backing pressure was set to 3.9 mbar, the source pressure to $2.8{\cdot}10^{-3}$ mbar, the trap pressure to $2.4{\cdot}10^{-2}$ mbar, the IMS pressure to 3.0 mbar, and the transfer pressure to $2.5{\cdot}10^{-2}$ mbar.

All data were analysed using MassLynx v4.2 (Waters) and Driftscope v2.3 (Waters). The Gaussian peak deconvolution algorithm within OriginPro 2018 was used to separate main and shoulder peaks and bound and unbound states. Afterwards, the intensity of these peaks was used to estimate the abundance of each species.

2.3. Results and Discussion

Before starting, preliminary tests were carried out confirming the ability of Hb to bind PFOS and perfluorooctanoic acid (PFOA) using native MS and the eventual possibility to follow this phenomenon via electrochemical mediated strategies, using hydrogen peroxide. From the previous structural considerations and these additional data, we could expect that even NGB is capable of binding PFOS/PFOA. To our knowledge, NGB-PFOS/PFOA interactions were not investigated so far. Possible NGB-PFOS/PFOA interactions were investigated following the changes in NGB electrochemical signal.

2.3.1. Electrochemistry of Neuroglobin

The expected electrochemical behaviour of neuroglobin is a single reversible and monoelectronic redox process. In the analysis of this process, the structural features of NGB must be taken into account. As described in the introduction (**Figure 2.2G,H**), the presence of the CD region can lead to the formation of disulphide bridges between the cysteines of the NGB and, therefore, affect the binding capacity of the protein also with oxygen. However, in the potential range chosen for the NGB analyses, the cysteines will be in the reduced state and hence unable to form the bridge, which therefore does not affect the binding capacity. As reported by Trashin *et al.* [25], the reduction potential of this bridge is -0.194 V and it does not affect the progress of the reaction, as it remains in reduced form. The voltammogram of 20 µM NGB in phosphate buffer solution at pH 7.4, recorded with membrane configuration at a scanning rate of 20 mV s^{-1}, is presented in **Figure 2.3A** (the working conditions had been previously optimized).

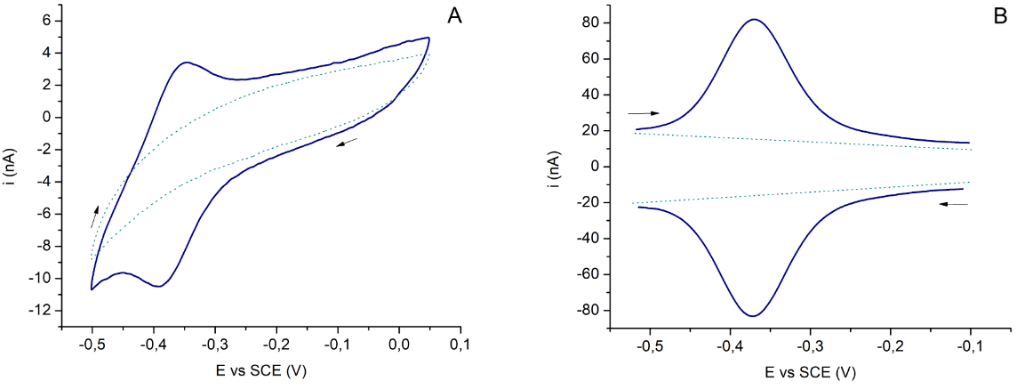

Figure 2.3 *(**A**) Cyclic voltammograms recorded in 20 µM NGB (blue full line) in phosphate buffer pH 7.4 (dotted line) at 20 mV s^{-1} in deaerated solution. (**B**) Anodic and cathodic SWV recorded in 20 µM NGB (blue full line) in phosphate buffer pH 7.4 (dotted line).*

The voltammogram is characterised by a single reversible redox process, with a cathodic peak at approximately -0.387 V vs SCE, followed by an anodic peak at approximately -0.350 V vs SCE ascribed to the haem group, in agreement with data from [25]. The measured peak to peak separation (ΔEp) is 0.037 V, is lower than the expected value for a monoelectronic process in standard conditions (0.059 V). This difference can be ascribed to the experimental conditions used (membrane configuration, see **Section 2.2.3**), in which the analyte is confined close to the electrode surface, and the mass transport is characterized by an apparent diffusion coefficient and thickness of the diffusion layer which are very different from the solution conditions. Such experimental conditions (the presence of the membrane and the orientation of the electrodes) are responsible for the drifting observed in the baseline in the potential window exploited.

The same redox process was investigated with SWV, in order to implement the signal-to-noise ratio. As shown in **Figure 2.3B,** both anodic and cathodic peaks are well defined and present the gaussian shape characteristic of a reversible system.

2.3.2 The Role of Oxygen

NGB is able to coordinate oxygen to the metal centre of the haem group, changing the oxidation state of iron. Therefore, the presence of different concentrations of oxygen might affect the NGB electrochemical signal. These variations need to be carefully evaluated prior to study how PFAS will possibly affect NGB electrochemistry because we will not be able to fully control the presence of oxygen in the PFAS solution added to NGB one using the setup described. It is worth noting that oxygen control is a recurrent issue in globin electrochemical studies.

These preliminary experiments were aimed to understand which parameters of NGB voltammetric response are affected (*Ep, Ip,* etc.) by oxygen presence, how meaningful these variations are and if after oxygen removal (deaeration), the changes result to be completely reversible or not. The voltammetric response of 25 µM NGB after complete deaeration was recorded via CV and SWV in the absence/presence of increasing oxygen concentrations (10-200 µM). The measurements were carried out by successive additions of aerated buffer solution (estimated oxygen concentration of about 260 µM) in deaerated cell solution under argon atmosphere. **Figure 2.4** presents the results obtained in completely deaerated solution in 25 µM NGB after addition of 200 µM of oxygen to exemplify the changes observed. The comparison of these voltammograms clearly shows that the presence of oxygen hinders NGB signal (**Figure 2.4A**). However, keeping the solution under argon atmosphere for >30 min, it is possible to recover NGB original signal (**Figure 2.4B**). The changes upon oxygen addition and removal are even more evident if we consider the current drop/recover recorded by SWV (**Figure 2.4C,D**). Oxygen effect was confirmed to be fully reversible and proportional to oxygen concentration in the range tested (*data not shown*). The decrease in the anodic peak current, Ip_a, values after addition of oxygen concentration < 50 µM were lower than 35%. For the cathode peak current, Ip_c, this decrement reaches the 20% at 50 µM of oxygen. Oxygen concentrations > 150 µM lead to higher currents drops > 50% and the signal recovery even after 2h deaereation treatment was not complete (with a loss of about 10%).

Oxygen contribution should be always taken into account when studying the direct electrochemistry of globins [18,25]. Here, oxygen effect can be limited by including deaeration steps in the analytical protocol used, as done in the next sections. These preliminary data suggest also the possibility to develop a branched project using NGB for the determination of the oxygen concentration of an unknown aqueous solution (*ongoing*).

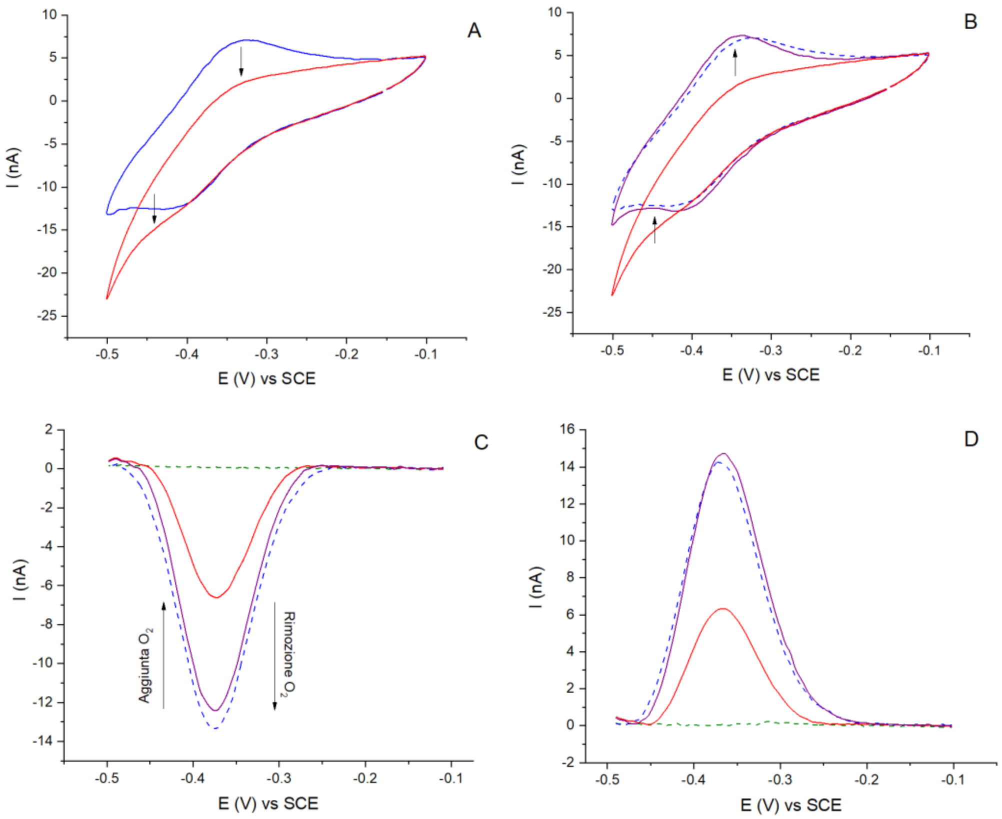

Figure 2.4 *Voltammograms recorded at maximum oxygen concentration 200 µM. (**A**) CV of NGB 25 µM (blue line) followed by the addition of aerated buffer solution (red line). (**B**) CV recorded in the same working conditions after a deaeration of the solution (violet line). (**C-D**) SWV showing cathodic and anodic peaks after addition of oxygen and deaeration (dotted green line-blank; dotted blue line-NGB signal before aeration/ deaeration; solid red line-NGB signal after aeration; solid violet line-NGB signal after deaeration).*

2.3.3. Effect of PFOS and PFOA on the Voltammetric Behaviour of NGB

Solution of PFOS/PFOA were added to NGB solution following the changes in the protein voltammetric response. The three-electrode configuration with dialysis membrane allows to operate PFOS/PFOA additions in the deaerated cell using a syringe. The analytes solutions were previously deaerated; however, we cannot assume to have a complete control of oxygen concentration. The additions operated with a syringe will always introduce oxygen in our system and its concentration is difficult to control and quantify. As observed in **Section 2.3.2**, oxygen can affect NGB cathodic/anodic peak currents when its concentration is greater than 50 µM. But even at lower concentrations, oxygen contribute to alter the current intensities. The changes in the redox behaviour of NGB were recorded after addition of PFOS/PFOA in the presence of increasing concentration of oxygen. By keeping the analyte:protein ratio fixed at 1:10 with 20 µM NGB solution in the membrane, different solutions with an oxygen concentration ranging from 10 to 50 µM were tested. The results are summarised in **Figure 2.5**.

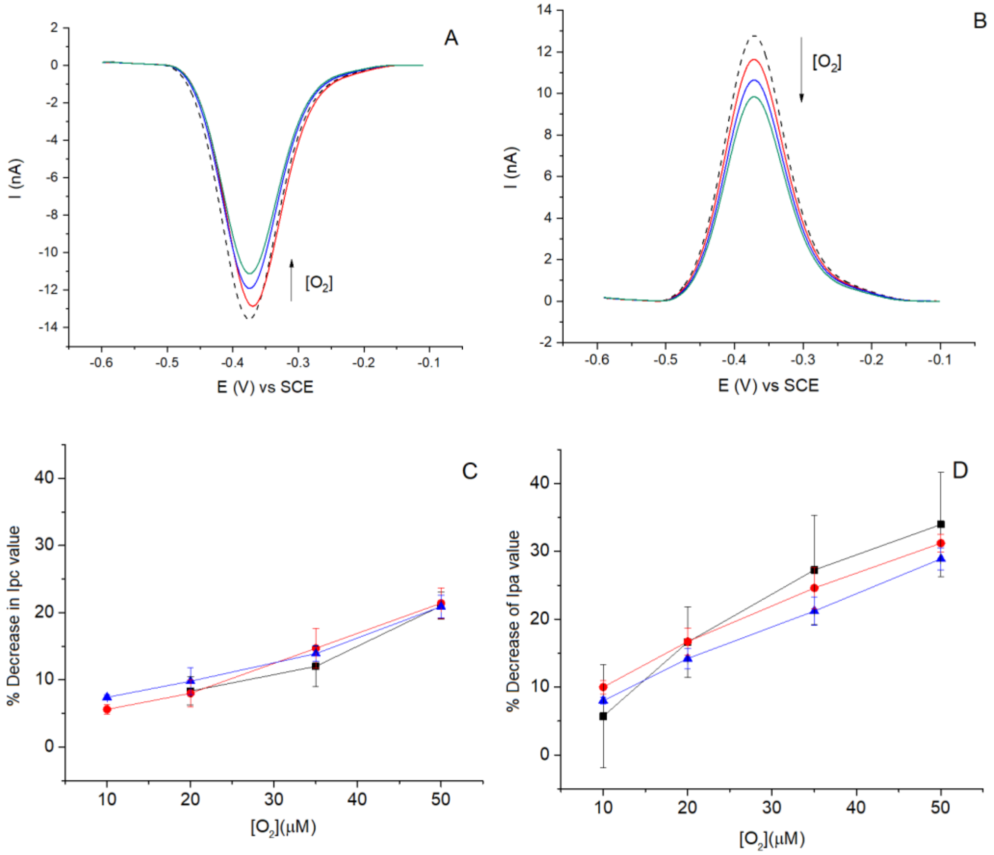

*Figure 2.5 Voltammograms obtained in the presence of PFOS and PFOA contaminants at increasing oxygen concentrations. SWV records of cathodic peaks (**A**) and anodic peaks (**B**) changes upon increasing oxygen concentrations ([O$_2$] increases in the direction of the arrow). Trend of the variation of the cathodic (**C**) and anodic (**D**) peak currents as a function of the increasing oxygen concentration. Tests with oxygen only (black points), with PFOS and oxygen (red line) and with PFOA and oxygen (blue line) are reported.*

From the plots in **Figure 2.5**, we observed a trend which is consistent with the one previously described in the presence of increasing oxygen concentrations. Both cathodic and anodic peak currents decrease linearly at increasing oxygen concentrations, and the presence of PFOS/PFOA did lead to further decreases in the signal. On the contrary, in the presence of PFOS/PFOA, the effect of oxygen is slightly lower: for example, at 50 µM of oxygen there is a decrease of the anodic peak of about 30% in the presence of PFOA or PFOS, compared to the 35% recorded in the absence of contaminants. In **Figure 2.5A**, we can observe that in the presence of PFOS there are also variations in the peak potential (*potential shift*) of ± 5 mV. These shifts were not observed in the anodic process, in **Figure 2.5B**. Considering that these preliminary experiments did not show any unexpected changes in NGB electrochemistry, it was possible to proceed with the study.

For the next experiments, PFOS/PFOA addition was followed by supplementary steps. The system was deaereated (>30 min) and kept under gentile stirring to favour the analytes diffusion and, as a consequence, their interaction with NGB, prior to proceed with the voltammetric study. Once again, we expect the addition of PFOS/PFOA to alter NGB current intensities due to: *i)* oxygen effect limited by the deaereation step and *ii)* the possible contribution of the fluorinated compounds, which can vary the protein conformation leading to a major or minor exposure of the haem group. **Figure 2.6** offers a brief summary of the results obtained at increasing NGB:PFOS/PFOA ratios.

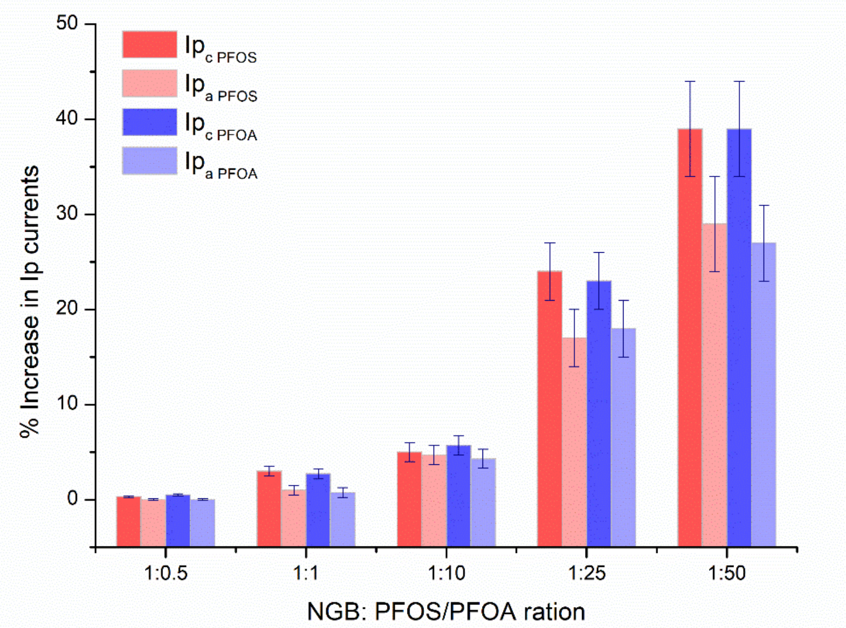

Figure 2.6 *Summary of the changes in current intensities after incubation of increasing ratios of PFOS/PFOA. The changes are expressed as percentages of the increase in the Ip currents (both cathodic, Ipc, and anodic, Ipa, ones) in respect to the intensities recorded with NGB only.*

Upon addition of meaningful PFOS/PFOA ratios, and after reducing the oxygen effect with deaereation, an increase in the peak currents was recorded, which can be ascribed to a major exposure of the haem or a partial unfolding of the protein. However, these data were affected by a scarce reproducibility, as underlined by the error bars in **Figure 2.6.** Consequent voltammetric measurements show a progressive decrease in the currents intensities and meaningful potential shifts suggesting the occurrence of adsorption processes. The potential shifts were considered as well, showing no linear correlation with the increasing PFOS/PFOA ratios added even after 12h or 24h of incubation, as showed in **Figure 2.7**. The same data collection was performed for PFOA at different incubation times (<1h, 12h and 24h) recording similar trends (*data not shown*).

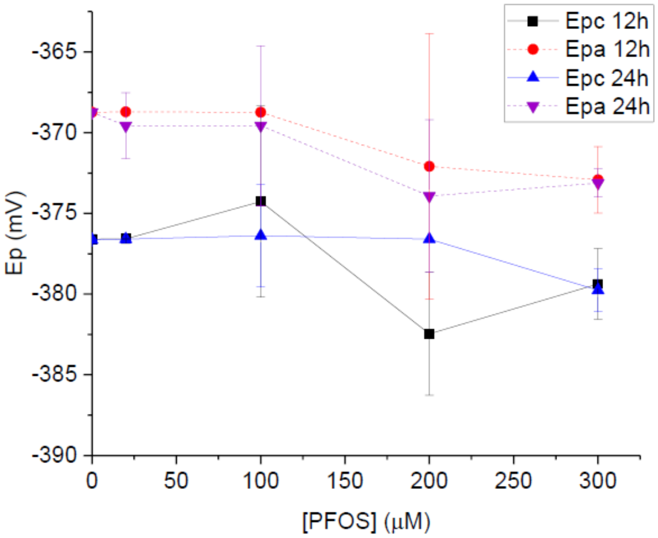

Figure 2.7 *Example of the changes in NGB peak potentials (Ep) after a 12h or 24h exposure to increasing concentration of PFOS.*

Overall, these preliminary results suggest that PFOS/PFOA interactions with NGB are not leading to stable conformation changes recordable via electrochemical methods. The first part of this study allows to develop a methodology to study NGB interaction with small molecules minimizing oxygen contributions. The interpretation of this dataset needs to be further supported by additional analyses for a better understanding of PFOS/PFOA-NGB interaction mechanism. To this aim, native MS was selected. As anticipated in **Section 2.1**, haemoglobin was first screened as a control system to develop a protocol for the study of globin-PFAS interactions.

2.3.4 Native Mass Spectrometry of NGB-PFOA/PFOS Complexes

2.3.4.1 Haemoglobin

Once again, the study of Wang *et al.* and the idea that Hb bind PFOS molecules were considered as a starting point [16]. The native mass spectrum of Hb (**Figure 2.8A**) shows that the protein is mainly present in its native tetrameric form (charge states 17+ to 14+).

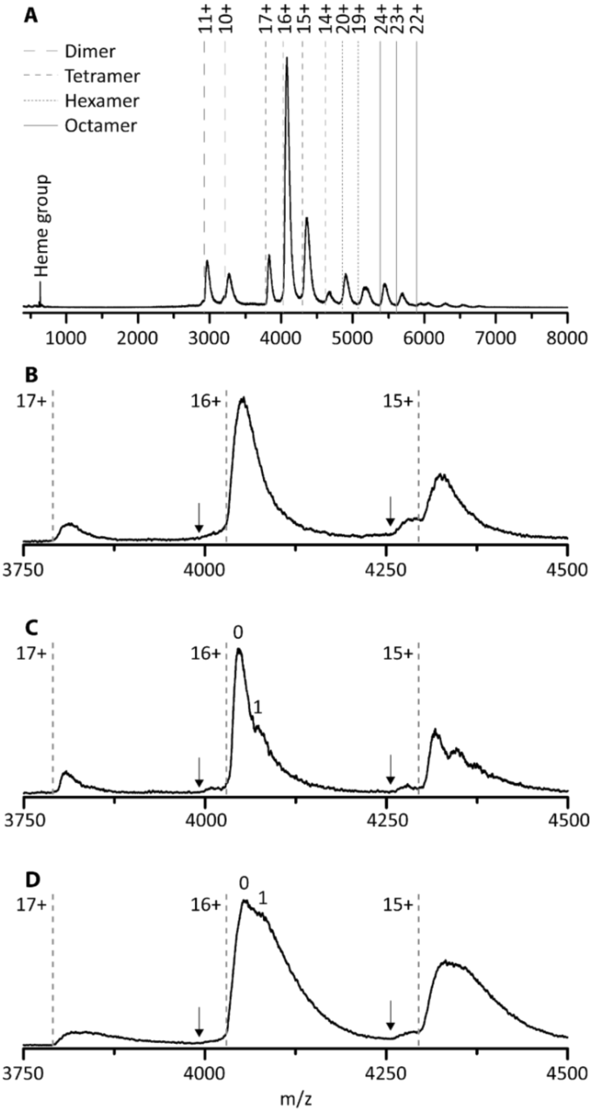

***Figure 2.8**. Native MS spectrum of Hb (**A**) together with a zoom of the tetramer region (**B**). Native MS spectrum of Hb complex with PFOS (**C**) and PFOA (**D**) in a 1:10 protein:target ratio. The dashed lines indicate the theoretical m/z-values of Hb. The arrows indicate the theoretical m/z-value of Hb minus one haem group.*

Upon adding a 10-fold excess of PFOS, a complex with a 1:1 stoichiometry was observed (**Figure 2.8C**), proving the coherence of the native MS data with the literature [16]. After verifying the formation of the Hb-PFOS complex, we studied the interaction of PFOA with Hb. Again, a 1:1 Hb-PFOA complex was observed after addition of a 10-fold excess of the target. The intensity of the peak corresponding to this complex (93%) is higher than the Hb-PFOS complex (51%) (**Figure 2.8D**). In both cases, the haem groups are not removed from the Hb upon binding of PFOA/PFOS, indicating there is no competition between the haem groups and PFOS or PFOA.

These findings are in agreement with the Hb-PFOS complex structure suggested by molecular modelling by Wang *et al*. [16] in which the target molecule was suggested to bind the domain proximal to the haem without any direct interactions with the prosthetic group. Therefore, Hb-PFOA/PFOS screening confirmed the formation of complexes and their stability (i.e., no loss of the haem group), as well as the consistency of MS data with the literature. Once we confirmed the capability of Hb to bind PFAS, it was possible to proceed with the screening of other haemoproteins, such as cytochrome c (cyt c) and NGB. These analyses confirmed the data previously reported and were instrumental to the development of a suitable analytical protocol for the study of globin-PFAS interactions.

2.3.4.2 Cytochrome c and Neuroglobin

Prior to study neuroglobin, cyt c has to be considered as an additional control system in the native MS study. Cyt c was chosen because it is known to bind to lipid bilayers. To check whether cyt c can bind PFOA, native MS experiments were performed (**Figure 2.9**). Cyt c shows two charge states (7+ and 6+) which are heavily adducted with sodium ions (a common contamination in native MS). Upon adding a 10-fold excess of PFOA, no new peaks appeared indicating the lack of a cyt c-PFOA complex (**Figure 2.9A-B**). To verify this observation, the negatively charged PFOS was used as well, but again no complex was observed (**Figure 2.9D**). This was unexpected, since cyt c is known to interact with anionic phospholipids, such as cardiolipin [30]. Over the years, multiple binding sites for these anionic lipids were discovered and it was found that electrostatic forces play a key role in the cyt c-lipid interaction [31,32]. Since PFOA and PFOS mimic fatty acids and are negatively charged at neutral pH, it was plausible that cyt c could interact with these PFAS and could work as a bioreceptor [33]. One possible explanation for the absence of the complex is that cyt c specifically binds cardiolipins and that the PFAS used here are structurally too different to interact with cyt c. The mass spectrum of NGB shown in **Figure 2.9C** is characterised by two prominent charge states (8+ and 7+). Upon adding a 10-fold excess of PFOA, only low-intensity peaks corresponding to the 1:1 complex were observed (**Figure 2.9D**).

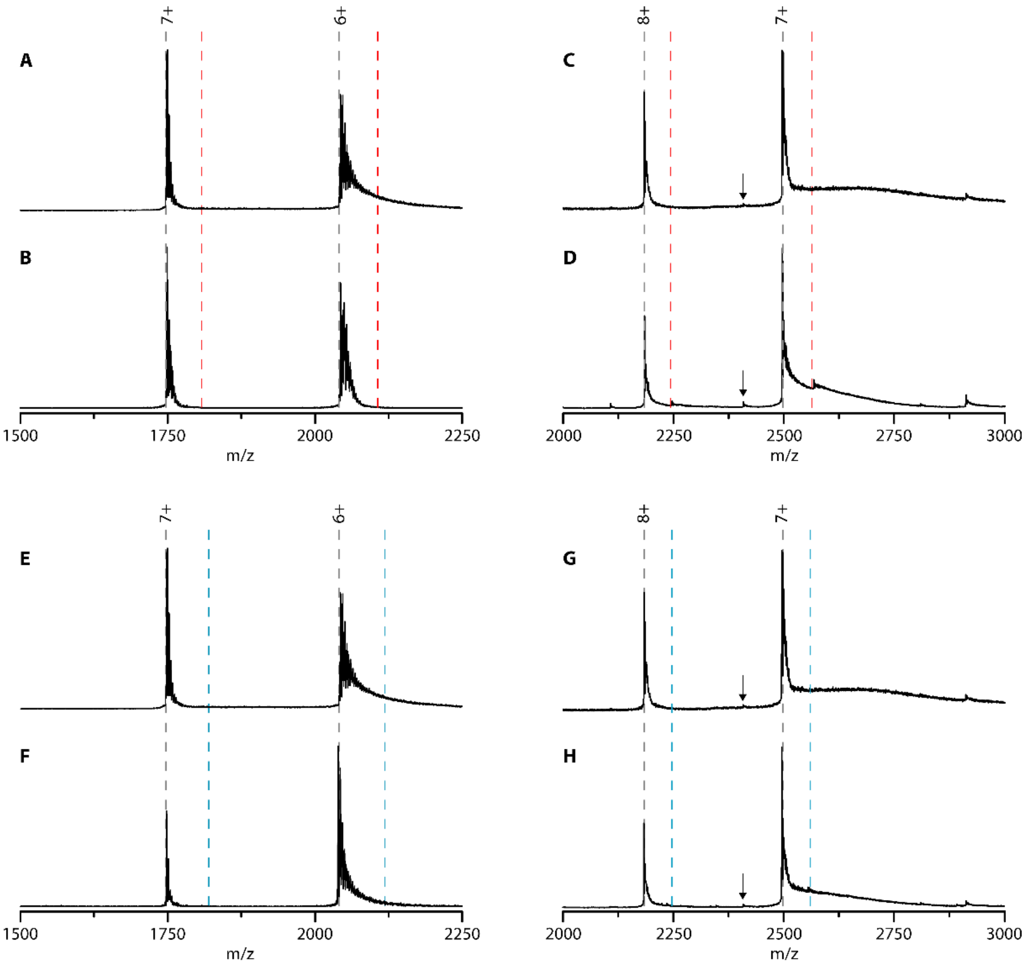

Figure 2.9. Native MS spectra of cyt c (A and B) and NGB (C and D) without (A and C) and in the presence of PFOA in a 1:10 protein:target ratio (B and D, respectively); native MS spectra of cyt c (E and F) and NGB (G and H) without (E and G) and in the presence of PFOS in a 1:10 protein:target ratio (F and H, respectively). The dashed lines indicate the theoretical m/z-values of the protein and 1:1 protein-target complex in grey and red/blue, respectively. The arrows indicate the theoretical m/z-value of NGB without the haem group.

Overall, 87% of the NGB is present in its unbound state and only 13% has one PFOA bound. This indicates NGB is only able to bind PFOA weakly and with a lower affinity than Hb. The most intense peaks correspond to NGB with haem group, and the very low intensity peaks around 2110 and 2410 m/z that are present after addition of PFOA can be assigned to NGB without the haem group. This could suggest that PFOA is affecting the stability of NGB. Furthermore, there is no evidence of NGB without a haem group binding to PFOA. Finally, the NGB-PFOS complex formation was investigated (**Figure 2.9G-H**). The spectra showed that the amount of NGB-PFOS complex formed (7%) is even lower than for NGB-PFOA. From this screening, NGB is found to be a less suitable bioreceptor for PFAS compared to Hb. Very small amount of NGB:PFOS/PFOA were found to be formed, and this can be ascribed to the progressive unfolding of the complex itself. Moreover, the formation of the complex is not favourited: NGB spectra is not deeply affected by PFOS/PFOA presence. These data can partially support the electrochemical study, confirming that the formation NGB: PFOS/PFOA complex is not favoured and compared to Hb:PFAS complexes, NGB ones seems to be less stable.

2.4. Conclusions

Starting from Hb:PFOS complexes, this chapter offers an overview of Hb:PFOS/PFOA interaction, NGB:PFOS/PFOA, and even cyt c: PFOS/PFOA interactions. The results of the electrochemical study showed that NGB redox functionalities are affected by PFAS, but this globin did not show the characteristics required to be applied as a bioreceptor for these contaminants (low reproducibility, no stable complex, etc.).

The second part of the study underlines the potential of applying native MS in the screening of biorecognition elements and implementation of bioreceptor libraries for environmental contaminants such as PFAS. This example illustrate how native MS can contribute to the screening and characterisation of possible bioreceptors. Although many challenges still remain open, our approach has the potential to play an important role in the transfer of toxicological findings to the design of bioreceptors for innovative biosensing strategies. One of the major challenges will be the screening of short-chain PFAS, as discussed in **Chapter 3**. Future research efforts should be oriented toward testing novel proteins and assessing binding affinity and stoichiometry using different molar ratios.

In conclusion, this preliminary study emphasises the importance of multi-analytical approaches in characterising PFAS protein binding. For these reasons, **Chapter 3** will be dedicated to an extensive study of PFOA-albumin interaction with a more structured approach, involving three different analytical methods.

Acknowledgments and Collaborations

Thanks to S. Trashin who taught me all I need to know about neuroglobin. It was a pleasure (and an honour) to work with you Stass! I am grateful to Shahid that was always ready for a "weekend in the lab". Thanks to Giulia Da Pian for dedicating her bachelor thesis to this topic, Elise for sharing also this project, Zainab&Herald for making the project possible and all our supervisors for having suggested new ways to follow. Special thanks to Prof. Frank Sobott for supporting our work, it was nice to see you here in Venice!

References

[1] C. Bosch-Orea, M. Farré, D. Barceló, Chapter Ten - Biosensors and Bioassays for Environmental Monitoring, in: I. Palchetti, P.-D. Hansen, D.B.T.-C.A.C. Barceló (Eds.), Past, Present Futur. Challenges Biosens. Bioanal. Tools Anal. Chem. A Tribut. to Profr. Marco Mascini, Elsevier, 2017: pp. 337–383. https://doi.org/https://doi.org/10.1016/bs.coac.2017.06.004.

[2] B. Liu, J. Zhuang, G. Wei, Recent advances in the design of colorimetric sensors for environmental monitoring, Environ. Sci. Nano. 7 (2020) 2195–2213. https://doi.org/10.1039/D0EN00449A.

[3] G. Moro, K. De Wael, L.M. Moretto, Challenges in the electrochemical (bio)sensing of nonelectroactive food and environmental contaminants, Curr. Opin. Electrochem. 16 (2019) 57–65. https://doi.org/10.1016/j.coelec.2019.04.019.

[4] H. Liu, J. Ge, E. Ma, L. Yang, Advanced biomaterials for biosensor and theranostics, in: L. Yang, S.B. Bhaduri, T.J.B.T.-B. in T.M. Webster (Eds.), Woodhead Publ. Ser. Biomater., Academic Press, 2019: pp. 213–255. https://doi.org/https://doi.org/10.1016/B978-0-12-813477-1.00010-4.

[5] S.B. Patil, V.F. Annese, D.R.S. Cumming, Chapter 8 - Commercial Aspects of Biosensors for Diagnostics and Environmental Monitoring, in: A. Deep, S.B.T.-A. in N. for B. and E.A. Kumar (Eds.), Elsevier, 2019: pp. 133–142. https://doi.org/https://doi.org/10.1016/B978-0-12-817456-2.00008-5.

[6] P.U.A.I. Fernando, M.W. Glasscott, G.K. Kosgei, J.S. Cobb, E.M. Alberts, C.G. Bresnahan, T.C. Schutt, G.W. George, L.C. Moores, Toward Rational Design of Electrogenerated Molecularly Imprinted Polymers (eMIPs): Maximizing Monomer/Template Affinity, ACS Appl. Polym. Mater. 3 (2021) 4523–4533. https://doi.org/10.1021/acsapm.1c00575.

[7] M.W. Glasscott, K.J. Vannoy, R. Kazemi, M.D. Verber, J.E. Dick, μ-MIP: Molecularly Imprinted Polymer-Modified Microelectrodes for the Ultrasensitive Quantification of GenX (HFPO-DA) in River Water, Environ. Sci. Technol. Lett. 7 (2020) 489–495. https://doi.org/10.1021/acs.estlett.0c00341.

[8] N. Karimian, A.M. Stortini, L.M. Moretto, C. Costantino, S. Bogialli, P. Ugo, Electrochemosensor for Trace Analysis of Perfluorooctanesulfonate in Water Based on a Molecularly Imprinted Poly(o-phenylenediamine) Polymer, ACS Sensors. 3 (2018) 1291–1298. https://doi.org/10.1021/acssensors.8b00154.

[9] X. Li, X. Wang, T. Fang, L. Zhang, J. Gong, Disposable photoelectrochemical sensing strip for highly sensitive determination of perfluorooctane sulfonyl fluoride on functionalized screen-printed carbon electrode, Talanta. 181 (2018) 147–153. https://doi.org/https://doi.org/10.1016/j.talanta.2018.01.005.

[10] N. Cennamo, L. Zeni, P. Tortora, M.E. Regonesi, A. Giusti, M. Staiano, S. D'Auria, A. Varriale, A high sensitivity biosensor to detect the presence of perfluorinated compounds in environment, Talanta. 178 (2018) 955–961. https://doi.org/https://doi.org/10.1016/j.talanta.2017.10.034.

[11] X. Liu, M. Fang, F. Xu, D. Chen, Characterization of the binding of per- and poly-fluorinated substances to proteins: A methodological review, TrAC - Trends Anal. Chem. 116 (2019) 177–185. https://doi.org/10.1016/j.trac.2019.05.017.

[12] Y. Wang, H. Zhang, Y. Kang, Z. Fei, J. Cao, The interaction of perfluorooctane sulfonate with hemoglobin: Influence on protein stability, Chem. Biol. Interact. 254 (2016) 1–10. https://doi.org/10.1016/j.cbi.2016.05.019.

[13] Y. Liu, Z. Cao, W. Zong, R. Liu, Interaction rule and mechanism of perfluoroalkyl sulfonates containing different carbon chains with human serum albumin, RSC Adv. 7 (2017) 24781–24788.

https://doi.org/10.1039/c7ra02963b.

[14] Q. Chi, Z. Li, J. Huang, J. Ma, X. Wang, Interactions of perfluorooctanoic acid and perfluorooctanesulfonic acid with serum albumins by native mass spectrometry, fluorescence and molecular docking, Chemosphere. 198 (2018) 442–449. https://doi.org/10.1016/j.chemosphere.2018.01.152.

[15] M. Forsthuber, A.M. Kaiser, S. Granitzer, I. Hassl, M. Hengstschläger, H. Stangl, C. Gundacker, Albumin is the major carrier protein for PFOS, PFOA, PFHxS, PFNA and PFDA in human plasma, Environ. Int. 137 (2020) 105324. https://doi.org/https://doi.org/10.1016/j.envint.2019.105324.

[16] Y. Wang, H. Zhang, Y. Kang, Z. Fei, J. Cao, The interaction of perfluorooctane sulfonate with hemoglobin: Influence on protein stability, Chem. Biol. Interact. 254 (2016) 1–10. https://doi.org/10.1016/j.cbi.2016.05.019.

[17] H. Wajcman, L. Kiger, M.C. Marden, Structure and function evolution in the superfamily of globins, Comptes Rendus - Biol. 332 (2009) 273–282. https://doi.org/10.1016/j.crvi.2008.07.026.

[18] F.W. Scheller, N. Bistolas, S. Liu, M. Jänchen, M. Katterle, U. Wollenberger, Thirty years of haemoglobin electrochemistry, Adv. Colloid Interface Sci. 116 (2005) 111–120. https://doi.org/https://doi.org/10.1016/j.cis.2005.05.006.

[19] G. Janson, C. Zhang, M.G. Prado, A. Paiardini, PyMod 2.0: improvements in protein sequence-structure analysis and homology modeling within PyMOL, Bioinformatics. 33 (2017) 444–446. https://doi.org/10.1093/bioinformatics/btw638.

[20] L. Capece, M.A. Marti, A. Bidon-Chanal, A. Nadra, F.J. Luque, D.A. Estrin, High pressure reveals structural determinants for globin hexacoordination: Neuroglobin and myoglobin cases, Proteins Struct. Funct. Bioinforma. 75 (2009) 885–894. https://doi.org/https://doi.org/10.1002/prot.22297.

[21] B. Batra, S. Lata, M. Sharma, C.S. Pundir, An acrylamide biosensor based on immobilization of hemoglobin onto multiwalled carbon nanotube/copper nanoparticles/polyaniline hybrid film, Anal. Biochem. 433 (2013) 210–217. https://doi.org/https://doi.org/10.1016/j.ab.2012.10.026.

[22] P. Ascenzi, A. di Masi, L. Leboffe, M. Fiocchetti, M.T. Nuzzo, M. Brunori, M. Marino, Neuroglobin: From structure to function in health and disease, Mol. Aspects Med. 52 (2016) 1–48. https://doi.org/https://doi.org/10.1016/j.mam.2016.10.004.

[23] A. Pesce, S. Dewilde, M. Nardini, L. Moens, P. Ascenzi, T. Hankeln, T. Burmester, M. Bolognesi, V.G. Marconi, I.- Roma, Human Brain Neuroglobin Structure Reveals a Distinct Mode of Controlling Oxygen Affinity, 11 (2003) 1087–1095. https://doi.org/10.1016/S0969-2126(03)00166-7.

[24] P. Ascenzi, A. di Masi, G. Fanali, M. Fasano, Heme-based catalytic properties of human serum albumin, Cell Death Discov. 1 (2015) 1–7. https://doi.org/10.1038/cddiscovery.2015.25.

[25] S. Trashin, M. de Jong, E. Luyckx, S. Dewilde, K. De Wael, Electrochemical Evidence for Neuroglobin Activity on NO at Physiological Concentrations., J. Biol. Chem. 291 (2016) 18959–18966. https://doi.org/10.1074/jbc.M116.730176.

[26] M. Murphy, K. Theyagarajan, P. Ganesan, S. Senthilkumar, K. Thenmozhi, Electrochemical biosensor for the detection of hydrogen peroxide using cytochrome c covalently immobilized on carboxyl functionalized ionic liquid/multiwalled carbon nanotube hybrid, Appl. Surf. Sci. 492 (2019) 718–725. https://doi.org/https://doi.org/10.1016/j.apsusc.2019.06.283.

[27] W. WEI, S.-G. WU, Study of Electrooxidation Behavior of Nitrite on Gold Nanoparticles/Graphitizing Carbon Felt Electrode and Its Analytical Application, Chinese J. Anal. Chem. 47 (2019) e19014–e19020. https://doi.org/https://doi.org/10.1016/S1872-2040(19)61142-4.

[28] A. Fago, A.J. Mathews, L. Moens, S. Dewilde, T. Brittain, The reaction of neuroglobin with potential redox protein partners cytochrome b 5 and cytochrome c, FEBS Lett. 580 (2006) 4884–4888. https://doi.org/https://doi.org/10.1016/j.febslet.2006.08.003.

[29] W.R. Hagen, Direct electron transfer of redox proteins at the bare glassy carbon electrode, Eur. J. Biochem. 182 (1989) 523–530. https://doi.org/https://doi.org/10.1111/j.1432-1033.1989.tb14859.x.

[30] V.E. Kagan, H.A. Bayır, N.A. Belikova, O. Kapralov, Y.Y. Tyurina, V.A. Tyurin, J. Jiang, D.A. Stoyanovsky, P. Wipf, P.M. Kochanek, J.S. Greenberger, B. Pitt, A.A. Shvedova, G. Borisenko, Cytochrome c/cardiolipin relations in mitochondria: a kiss of death, Free Radic. Biol. Med. 46 (2009) 1439–1453. https://doi.org/https://doi.org/10.1016/j.freeradbiomed.2009.03.004.

[31] M. Rytömaa, P.K. Kinnunen, Evidence for two distinct acidic phospholipid-binding sites in cytochrome c., J. Biol. Chem. 269 (1994) 1770–1774.

[32] M. Rytömaa, P.K.J. Kinnunen, Reversibility of the Binding of Cytochrome c to Liposomes, J. Biol. Chem. 270 (1995) 3197–3202. https://doi.org/10.1074/jbc.270.7.3197.

[33] T.J.T. Pinheiro, G.A. Elöve, A. Watts, H. Roder, Structural and Kinetic Description of Cytochrome c Unfolding Induced by the Interaction with Lipid Vesicles, Biochemistry. 36 (1997) 13122–13132. https://doi.org/10.1021/bi971235z.

|3

Screening Protein Bioreceptors for PFAS: Delipidated Albumin

Adapted from:

E. Daems, G. Moro, H. Berghmans, L. M. Moretto, S. Dewilde, A. Angelini, F. Sobott and K. De Wael, "Native mass spectrometry for the design and selection of protein bioreceptors for perfluorinated compounds"
Analyst, 2021, 146, 2065

And

L. Maso, M. Trande, S. Liberi, G. Moro, S. Linciano, F. Sobott, S. Covaceuszach, A. Cassetta, S. Fasolato, L. M. Moretto, K. De Wael, L. Cendron and A. Angelini, "Unveiling the binding mode of perfluorooctanoic acid to human serum albumin",
Protein Science, 2021, 4, 30, 830

Abstract

Characterising PFAS-protein binding is instrumental to the understanding of cellular toxicities, biotransformation pathways, as well as the fate of selected PFAS. Since PFAS were traced in human plasma and recognised as global hazards for our health, numerous toxicological studies focused on PFAS-serum protein interactions were carried out, as described in ***Chapter 2****. Globins, especially haemoglobin, and albumin were first considered. Albumin resulted to be affected by PFAS losing its functions. These findings were easily explained considering that PFAS structures mimic the ones of lipids, which are transported by albumin (the main carrier protein we have). An in-depth understanding of PFAS - albumin interactions will allow to evaluate albumin applicability in PFAS biosensing. This possible bioreceptor can be further engineered to improve its performances in terms of selectivity towards the analyte/s.*

In this chapter, perfluorooctanoic acid (PFOA) interactions with delipidated human serum albumin (dhSA) were characterized aiming to transpose toxicological findings in biosensing applications. In this case-study, PFOA was selected as representative of long chain PFAS. The performances of dhSA in presence of excess of PFOA were studied using a multi-analytical approach, untreated albumin was considered as control system. This latter combined: i) the characterisation of the PFOA-dhSA in solution via isothermal titration calorimetry (ITC), ii) a description of the binding site distribution based on X-ray crystallography and iii) an assessment of the complex stability referred to as collision induced unfolding (CIU) study carried out with native mass spectrometry (native MS). The dhSA shows a 4:1 binding stoichiometry and two affinity constants in the low µM-range (0.36 µM and 27.1 µM). ITC was applied to study the changes in the binding affinity at different temperatures and the binding site distribution was screened with competition assays. These findings were confirmed by the X-ray structure of the complex: PFOA binds at four fatty acids (FA) sites acting as a lipid. PFOA mimicking behaviour stabilises the albumin conformation leading to a stable complex, as seen in CIU plots.

This multi-analytical study provides an example of how an in-depth understanding of serum proteins-PFAS interactions can help evaluating the applicability of these proteins as bioreceptors and contribute to toxicological studies at the same time.

3.1. Introduction

The characterisation of PFAS interactions with human serum proteins, such as human serum albumin, is fundamental to evaluate PFAS toxicity, as anticipated in **Chapter 2**. These findings can contribute to the advancement in toxicological studies and be applied in the design of protein-based bioreceptors and, even, in medical treatments for PFAS removal, such as hemoperfusion, plasma-adsorption or plasmapheresis [1,2]. Early studies of PFAS-protein interactions were firstly carried out in the 1950s, aiming to prevent bovine serum albumin denaturation and precipitation after interaction with perfluorooctanoate acid (PFOA) [3–5]. Only in the late 70s, the presence of organofluorine chemicals in human plasma was reported [6] showing the urgent need of understanding **PFAS bioaccumulation paths** in humans. Since then, numerous qualitative/quantitative methods were reported for the characterisation of PFAS-**protein binding** (studying the binding mechanism, kinetics and adverse effects on the activity of proteins) [7]. Among the most common methods we have: separative methods, such as equilibrium dialysis (ED) or size-exclusive chromatography (SEC), calorimetric ones, such as differential scanning calorimetry (DSC) or isothermal titrations (ITC) and spectroscopic methods (i.e., UV-VIS, IR, nuclear magnetic resonance (NMR), circular dichroism (CD), fluorescence). Lately also mass spectrometry (MS), surfactant methods, molecular docking and surface plasmon resonance were reported in protein binding studies. By combining these different methods, we can acquire a better **characterisation of PFAS-protein binding**, overcoming the limits intrinsic to each analytical technique. According to Liu *et al.,* we should focus more **on multi-analytical approaches** integrating emerging analytical techniques to unveil the differences in protein binding of different PFAS, from long to short chain ones, and face PFAS contamination with a more targeted-strategies [7].

In the last decade, the affinity of PFAS, especially PFOA, for human, rat and bovine serum albumins was extensively characterized by multi-analytical approaches [8–11]. The strong affinity of PFOA for human serum albumin can be explain considering that its carboxylic head and fluorinated C_8 tail mimic long-chain fatty acids (FAs) structure enabling PFOA to bind albumin **FAs pockets** and, thus, altering the protein functionalities. Albumin-PFOA interactions are noncovalent, mainly hydrophobic, and influenced by the protein conformation, working and environmental conditions (pH, etc.), as for FAs. However, the binding mechanism of PFOA to albumin is still unclear. To study the binding site distribution, check the affinity constant previously reported and assess the stability of PFOA-albumin complex a multi-analytical study based on ITC, X-ray crystallography and native MS was designed. PFOA was selected as representative of long chain PFAS aiming to use the previous literature to validate the results collected with the proposed approach.

Mature human serum albumin is a not glycosylated globular protein of 585 amino acids with a m. w. of 66.5 kDa [12]. It is the most abundant circulating protein in the plasma with a concentration of about 35-50 gL^{-1} [13]. Mostly synthesised in the liver where the hepatocytes store limited amount, 13-14 g of albumin reaches the intravascular space daily [14]. Compared to other **carrier proteins**, human serum albumin has many low and high affinity binding pockets and is able to reversibly bind a wide range of endogenous (i.e., FAs, lipophilic hormone, hemin, bilirubin, tryptophan) and exogenous ligands (i.e., metal ions, pharmaceutical drugs, anti-tumoral drugs) [12]. The low immunological response and long half-life of albumin has been applied as stabilizing agent to enhance drug potential and delivery system of new designed molecules for specific targets [15]. The secondary structure is composed of 67% α-helix elements arranged in three homologous domains (I-III), whose reciprocal interactions create an asymmetric module with up to nine distinct FAs binding sites, as shown in **Figure 3.1**. The location, nature and conformational organisation of these binding sites in the presence of different FAs has been extensively investigated using multiple yet complementary biophysical tools [16–18]. The **structural studies** of Curry *et al.* allowed describing seven FAs sites with asymmetrical distribution (see FA1-FA7 in **Figure 3.1**).

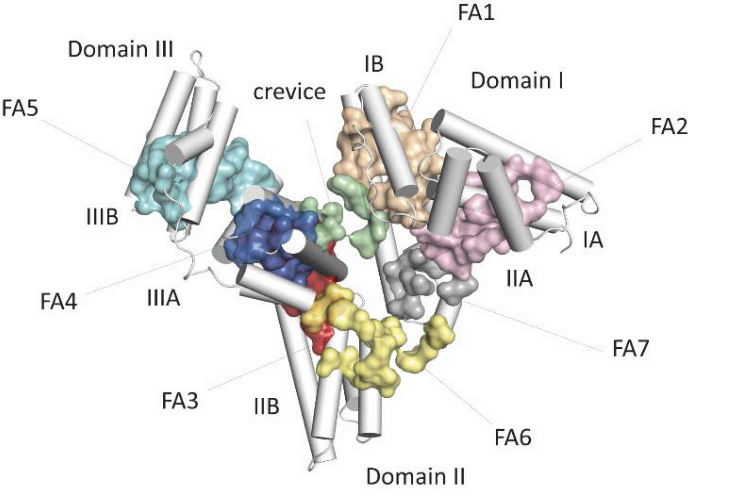

Figure 3.1. *Crystal structure of human serum albumin (PDB identification code: 1E7E) showing the distribution of the domains (**A**) and the fatty acids sites (**B**): FA1 (light orange), FA2 (pink), FA3 (dark red), FA4 (dark blue), FA5 (light blue), FA6 (yellow), FA7 (grey) and crevice (green). The three-dimensional structure model was generated and rendered using PyMOL.*

These sites are located in sub-domain IB (*FA1*), at the interface between sub-domains IA and IIA (*FA2*), in sub-domain IIIA in correspondence of Sudlow's drug-binding site II (*FA3-FA4*), in sub-domain IIIB (*FA5*), at the interface between sub-domains IIA and IIB (*FA6*), in the sub-domain IIA in correspondence of Sudlow's drug-binding site I (*FA7*) and in the crevice between sub-domains IB and IIIA [16,19,20]. Short to medium length FAs (6 to 12 carbons) bind albumin using these pockets with affinities between 0.5 and 60 µM, while the longest ones (14 to 18 carbons) have 10-fold higher affinities (below 50 nM) [21–23]. The lipid affinity for FAs pockets is crucial if we consider that PFOA can possibly compete to access these sites. By studying the PFOA-albumin complex we aimed to elucidate if PFOA is hosted by FAs cavities and, eventually, which ones.

Albumin would represent an abundant, accessible and flexible potential bioreceptor for PFAS biosensing, therefore its applicability as a biorecognition layer needs to be verified. To improve the reproducibility of this possible bioreceptor, a delipidation treatment was introduced. The removal of FAs is expected to improve the selectivity (PFOA will not have to compete with the FAs present in albumin pockets) even though this treatment might also lower the protein stability (FAs were found to stabilise albumin structure, so if absent the albumin unfolding rate might be higher). Delipidated human serum albumin (dhSA) is commonly used in physiological, medical and pharmacokinetics studies to assess the interaction mechanism of this carrier protein with fatty acids, hormones, drugs, etc. PFOA binding to dhSA was not studied, so far. Apart from the binding mechanism, an estimation of the affinity constants in solution and an assessment of the stability of the complex formed is required to evaluate its applicability as bioreceptor. In **Chapter 2**, we saw the importance of probing the protein-analyte with complementary techniques, here a more structured approach is reported. In this chapter, PFOA-dhSA binding in solution was investigated in solution by ITC suggesting the presence of multiple binding sites with different affinity constants for PFOA. A 4:1 PFOA-dhSA stoichiometry was observed with one high and three low affinity binding sites. Competition experiments with well-known albumin-binding drugs allowed locating the high affinity binding site in subdomain IIIA (**Figure 3.1**). Once the formation of the complex was confirmed, the location of the sites was elucidated. We report here the crystal structure of dhSA in complex with PFOA and a medium-chain saturated FA, the myristic acid. A total of eight distinct binding sites, four occupied by PFOAs and four by FAs, have been identified. Then, the stability of the dhSA in comparison to the untreated albumin was probed by collision induced unfolding (CIU) in the native MS study. By activating the albumin ions at increasing collision energies, this ion mobility-mass spectrometry (IM-MS) method enables to discriminate protein isoforms based on their unfolding patterns and stabilities. Overall, the proposed multi-analytical approach allowed to have a better understanding of the interaction between PFOA and dhSA, which can provide not only a better assessment of the absorption and elimination mechanisms of these compounds *in vivo* but also have implications in the development of novel molecular receptors for diagnostic and biotechnological applications.

3.2. Materials and Methods

3.2.1. Materials and Sample Preparation

Recombinant human serum albumin (hSA, Albagen XL) was purchased from Albumin Bioscience (Alabama, US), cytochrome C and sodium myristate from Sigma Aldrich (France). Perfluorooctanoic acid (PFOA, ≥96%) and perfluorooctanesulfonic acid potassium salt (PFOS, ≥98%), perfluorhexanesulfonic acid (PFHxS) and perfluoropentanoic acid (PFPA) were purchased from Sigma Aldrich (Belgium). The 2,3,3,3-tetrafluoro-2-(heptafluoropropoxy)-propanoate ammonium salt (HFPO-DA) was purchased from Carbosynth (UK) and (difluoro{[2,2,4,5-tetrafluoro-5-(trifluoromethoxy)-1,3-dioxolan-4-yl]oxy}acetic acid (C6O4) from Solvay (Italy). A 0.1 M sodium phosphate buffer (NaPi) (>99.0%) 0.1 M of NaCl and 7.5 M ammonium acetate ($NH_4CH_3CO_2$) solutions (>99.0%) were freshly prepared and purchased from Sigma-Aldrich (Belgium). The charcoal was purchased from Caesar & Loretz GmbH (Germany). All the reagents were of analytical grade and solutions were prepared using double distilled deionized water.

Two different types of recombinant human serum albumin (hSA) have been prepared: an untreated and a delipidated form (dhSA). The dhSA was obtained by adsorption onto activated charcoal as described previously [24]. Briefly, the water-washed charcoal (0.4 mg per mg of hSA) was suspended in PBS pH 7.4, the pH was lowered to 3 with a solution 1 M of HCl. The resulting suspension was incubated at least 3 h under gentle shaking at 4 °C. Then, the pH of the supernatant was adjusted to 7.4 using 2 M of NaOH before filtering the supernatant. The polymers/aggregates and the disulphide-bridged dimer formed during protein treatment were removed by size exclusion chromatography (SEC) using a HiLoad 16/600 Superdex 200 pg column (GE Healthcare, Germany) connected to an ÄKTA pure 25 M system (GE Healthcare, Germany) equilibrated with 50 mM NaPi, 100 mM NaCl, pH 7.4. The fractions containing monomeric dhSA protein were pooled and further concentrated by using 10000 NMWL Amicon Ultra-15 ultrafiltration devices (Merck Life Science, Germany) at 4000 g and 4 °C on a Heraeus Multifuge X1R centrifuge (Thermo Fisher Scientific, U.S.A.) to a final protein concentration of 25 mg mL^{-1} (375 µM). Protein concentrations were determined by mySPEC spectrophotometry (VWR, U.K.). The procedure employed for the purification of untreated hSA was identical. Purified hSA proteins were flash frozen in liquid nitrogen and stored at −80 °C. The monodisperse state of concentrated hSA proteins was confirmed by SEC using a Superdex 200 10/300 GL column (GE Healthcare, Germany) connected to an ÄKTA pure 25 M system and equilibrated with 50 mM NaPi, 100 mM NaCl, pH 7.4. Purified hSA proteins were eluted as a single peak at elution volumes (Ve) that corresponds to apparent molecular mass of about 66.5 kDa (monomer).

3.2.2 Isothermal Titration Calorimetry

ITC experiments were performed using a Microcal PEAQ-ITC instrument (Malvern Panalytical). Recombinant dhSA (120 µM), PFOA (4 mM), ibuprofen (4 mM) and 3-carboxy-4-methyl-5-propyl-2-furanpropionic acid (CMPF, 4 mM) were dissolved in 50 mM NaPi, 100 mM NaCl, pH 7.4, while warfarin (8 mM) and iodipamide (4 mM) were dissolved in the same buffer including 2.5% vol/vol DMSO to improve solubility. All working solutions were properly degassed. Titrations were carried out at different temperature values ranging from 12 to 37°C and 750 rpm stirring rate to ensure rapid mixing. A volume of 280 µL of dhSA in the cell was titrated with 40 µL of PFOA, ibuprofen, CMPF, warfarin or iodipamide. The injection volume was 1.5 µL and a 120 s interval between injections was applied to guarantee the equilibrium at each titration point. Each titration involved a total of 25 independent stepwise additions. Initial injection volume (0.4 µL) was excluded from the analysis. The heats of ligands dilutions were subtracted in all experiments. Competition experiments were conducted by adding in the cell saturating concentrations of each single molecule (ibuprofen = 250 µM; CMPF = 250 µM; warfarin = 200 µM; iodipamide = 600 µM) and titrating PFOA (4 mM). Data were analysed using the MicroCal PEAQITC Evaluation software (Malvern). Integrated heat signals were fitted to a "*one set of sites*" or a "*two set of sites*" binding models. Values for the affinity constant ($K_A = K_D^{-1}$) and enthalpy change (ΔH) together with the stoichiometry of the PFOA-dhSA reaction were obtained from the curve fitting. Free energy and the entropy change (ΔS) were calculated from the Gibbs free energy (ΔG) relationships: $-RT\ln K_A = \Delta G = \Delta H - T\Delta S$.

3.2.3 X-ray Crystallography

Crystallisation trials of the defatted recombinant dhSA in complex with PFOA and/or sodium myristate (MYR) were carried out at 285 K in a MRC maxi 48-well crystallisation plate (Hampton Research, CA, USA) using the sitting-drop vapor-diffusion method and the Morpheus MD1-46 protein crystallisation screen kit (Molecular Dimensions Ltd, Suffolk, UK). Droplets of 1.6 µL volume (0.8 µL of protein complex and 0.8 µL of reservoir solution) were set up using an Oryx 8 crystallisation robot (Douglas Instruments Ltd, Berkshire, UK) and equilibrated against 120 µL reservoir solution. In all the cases, the largest crystals were obtained by streak- or micro-seeding into drops that had been allowed to equilibrate for 5–7 days. Best crystals of dhSA incubated with a 10-fold molar excess of PFOA and a 5-fold molar excess of MYR were obtained using: 50 mM HEPES, 50 mM MOPS, 30 mM diethylene glycol, 30 mM triethylene glycol (PGE), 30 mM tetraethylene glycol (PG4), 30 mM pentaethylene glycol, 12.5% v/v MPD, 12.5% w/v PEG 1000, 12.5% w/v PEG 3350 pH 7.5, as precipitant agent. Best crystals of dhSA incubated with a 5-fold molar excess of PFOA and a 10-fold molar excess of MYR were obtained using: 50 mM HEPES, 50 mM MOPS, 20 mM 1,6-hexanediol (HEZ), 20 mM 1-butanol, 20 mM 1,2-propanediol, 20 mM 2-propanol, 20 mM 1,4-butanediol (BUD), 20 mM 1,3-propanediol (PRD), 12.5% v/v MPD, 12.5% w/v PEG 1000 and 12.5% w/v PEG 3350 pH 7.5, as precipitant agent. Best crystals of dhSA incubated with a 10-fold molar excess of MYR were obtained using: 50 mM HEPES, 50 mM MOPS, 30 mM sodium fluoride, 30 mM sodium bromide, 30 mM sodium iodide, 12.5% v/v MPD, 12.5% w/v PEG 1000, 12.5% w/v PEG 3350 pH 7.5, as precipitant agent. For X-ray data collection, crystals were mounted on LithoLoops (Molecular Dimensions Ltd, Suffolk, UK), soaked in cryoprotectant solution (crystallisation buffer added with 20% v/v ethylene glycol (EDO)) and flash-frozen in liquid nitrogen.

X-ray diffraction data of the complexes were collected at the ID30 beamline of the European Synchrotron Radiation Facility (ESRF, Grenoble, France) and at the I04 beamline of Diamond Light Source Ltd (DLS, Oxfordshire, UK). The best crystals of the ternary complex dhSA-PFOA-Myr (1:10:5) obtained using an excess of PFOA over Myr diffracted to 2.10 Å maximum resolution. Crystals belong to the C2 space group, with unit cell parameters: a =184.79 Å, b = 38.51 Å, c = 95.59 Å, α = 90°, β = 104.95° and γ = 90°. The asymmetric unit contains 1 molecule, corresponding to a Matthews coefficient of 2.45 Å^3/Da and a solvent content of about 49.84% of the crystal volume. The best crystals of the ternary complex dhSA-PFOA-Myr (1:5:10) obtained using an excess of Myr over PFOA diffracted to 1.80 Å maximum resolution. Crystals belong to the C2 space group, with unit cell parameters: a =185.06 Å, b = 38.64 Å, c = 96.06 Å, α = 90°, β = 104.88° and γ = 90°. The asymmetric unit contains 1 molecule, corresponding to a Matthews coefficient of 2.48 Å^3/Da and a solvent content of about 50.34% of the crystal volume. The best crystals of the binary complex dhSA-Myr (1:10) diffracted to 1.80 Å maximum resolution. Crystals belong to the I2 space group, with unit cell parameters: a =95.31 Å, b = 38.54 Å, c = 184.28 Å, α = 90°, β = 104.45° and γ = 90°. The asymmetric unit contains 1 molecule, corresponding to a Matthews coefficient of 2.45 Å^3/Da and a solvent content of about 49.71% of the crystal volume. Frames were indexed and integrated with software XIA2, merged and scaled with AIMLESS (CCP4i2 crystallographic package) [25].

The structures were solved by molecular replacement with software PHASER using as a template the model 1BJ5 [26]. Refinement was carried on using REFMAC and PHENIX. Rebuilding and fitting of the PFOAs, MYRs and precipitant/buffer molecules (BUD, EDO, HEZ, MPD, MOPS, PG4, PGE, PRD) was performed manually with graphic software COOT [27]. Since the first cycles of refinement, the electron density corresponding to the bound PFOA and/or Myr molecules were clearly visible in the electron density map. The final model of the ternary complex dhSA-PFOA-Myr (1:10:5) contains 4664 protein atoms, 100 PFOA ligand atoms, 64 MYR ligand atoms, 88 water molecules and 88 atoms of other molecules. The final crystallographic R factor is 0.21 (R_{free} 0.28). The final model of the ternary complex dhSA-PFOA-Myr (1:5:10) contains 4677 protein atoms, 75 PFOA ligand atoms, 96 MYR ligand atoms, 191 water molecules and 80 atoms of other molecules. The final crystallographic R factor is 0.212 (R_{free} 0.245). The final model of the binary complex dhSA-Myr (1:10) contains 4636 protein atoms, 96 MYR ligand atoms, 23 water molecules and 53 atoms of other molecules. The final crystallographic R factor is 0.21 (R_{free} 0.29). Geometrical parameters of the three models are as expected or better for this resolution. The solvent excluded volumes and the corresponding buried surfaces were calculated using PISA software [28] and a spherical probe of 1.5 Å radius. Intra-molecular and inter-molecular hydrogen bond interactions were analysed by PROFUNC [29], LIGPLOT+ [30] and PYMOL [31] software. The interactions established by PFOA atoms were calculated using CLICK server[32].

3.2.4 Native IM-MS and CIU

Prior to use, both untreated and dhSA were defrosted at +4°C in the centrifuge (15 000 g for 5 min) and dialyzed overnight in 100 mM ammonium acetate using Slide-a-Lyzer Mini dialysis units (3,5 kDa MWCO). After dialysis, the concentrations of the protein solutions were checked at λ=280 nm with Nanodrop2000-ThermoScientific using the following parameters for both albumins: MW = 66531 Da and ε=34445 $M^{-1}cm^{-1}$. The average of three consecutive measurements was considered. Then, the protein samples were diluted to a final concentration of 10 µM in ammonium acetate pH 6.8 and aliquot of PFOA solutions were added to prepare the samples. The stock PFOA solution of 5 mM ($C_8HF_{15}O_2$, MW= 414.07 g/mol) was prepared in 0.1 M phosphate buffer saline with 0.1 M of NaCl and sonicated for 10 min. Once prepared the hSA/dhSA and PFOA solutions were kept for max 5 h in the fridge at +4 °C. No incubation time was needed before running the measurements. A volume of approximately 2-4 µL was required for each measurement. The instrument was set using the conditions previously described in **Section 2.2.3**.

The measurements of the other proteins and the CIU experiments of albumin were performed on a Synapt G2 HDMS instrument (Waters) with liquid nitrogen (purity 99 %, Messer) in the IM cell and the following instrument settings were used: spray capillary voltage 1.2-1.9 kV, source temperature 30 °C, sampling cone 25 V, extraction cone 1 V, trap collision energy 5 V (for the CIU experiments this was varied from 10 to 150 V), transfer collision energy 0 V, trap DC bias 45 V, IMS wave height 35 V and IMS wave velocity 700 m/s. The backing pressure was set to 3.9 mbar, the source pressure to $2.8 \cdot 10^{-3}$ mbar, the trap pressure to $2.4 \cdot 10^{-2}$ mbar, the IMS pressure to 3.0 mbar, and the transfer pressure to $2.5 \cdot 10^{-2}$ mbar.

All data were analysed using MassLynx v4.2 (Waters) and Driftscope v2.3 (Waters). The Gaussian peak deconvolution algorithm within OriginPro 2018 was used to separate main and shoulder peaks and bound and unbound states. Afterwards, the intensity of these peaks was used to estimate the abundance of each species. The K_D of untreated hSA-PFOA complex was estimated from a single point measurement, as described by Göth *et al.,* for all charge states and the mean K_D was reported [33]. Arrival times were extracted from the 15+ charge state (no mass selection) from the full width at half maximum of the whole peak, including salt adducts and complexes (where appropriate). This corresponds to an m/z-window from 4435 to 4455 m/z and 4435 to 4520 m/z for the unbound and bound hSA, respectively. Experimental $^{TW}CCS_{N2}$ [34][1] values were calculated using a previously reported method relying on a calibration with other native proteins under the same experimental conditions [35]. During the calibration procedure, a linear fitting was applied according to Thalassinos *et al*. [36]. The CIUSuite 2 software (v2.2) developed by Polasky *et al.* was used to generate the CIU plots and analyse these data [37].

3.3. Results and Discussion

In recent years, the binding of PFOA to albumin has been characterised using multiple analytical techniques and considerable insights have been accumulated, however our understanding of the PFOA-albumin interactions is far from complete [38]. Though human serum albumin has been reported to bind between 1 to more than 10 PFOA molecules with binding affinities ranging from 10^{-2} to 10^{-6} M. The difference in the analytical techniques, sample preparation protocols (i.e., protein purification) and instrumentation used make the results reported in the previous studies often inconsistent and hard to compare. Moreover, a high-resolution structural analysis of the interaction between PFOA and albumin is still **lacking**. For these reasons, the multi-analytical approach reported in this chapter aims to characterise the PFOA-dhSA binding complex in solution by ITC, to elucidate its crystallographic structure, to confirm its stability by native MS and the CIU methods and provide a **consistent** set of data. Prior to describing the results in details, it is worth noting that a total of four PFOA binding sites with different affinities have been determined. The changes in binding stoichiometry and affinity were investigated at different temperatures (from 12 to 37°C). Competition experiments with known dhSA-binding drugs allowed locating the high affinity binding site in sub-domain IIIA. The elucidation of the molecular basis of PFOA -dhSA complex confirmed the FA-like behaviour of this ligand. This information is crucial for the design of **engineered albumin-bioreceptors** for PFAS sensing. In this context, native MS analysis

---

[1] Type of IM, where TW stands for "travelling wave"

completed the dataset with additional information: *i)* delipidated albumin formed more reproducible complexes with PFOA and *ii)* the complex is stable as well as the protein itself (PFOA binding do not lead to albumin partial unfolding).

3.3.1. Characterisation in Solution: ITC

The molecular interaction between PFOA and dhSA was first characterised in solution at 25°C by isothermal titration calorimetry. The raw data reported in **Figure 3.2A** (25°C) were fitted using a *"two sets of sites"* binding model, as explained in **Section 3.2.2**, and the fitting values are summarised in **Table A3.1**, **Annex A**. The results suggest that each dhSA can bind up to four PFOA molecules (4:1 stoichiometry). The PFOA binding sites are grouped into **two pairs** with different dissociation constants (K_D): a high-affinity site (K_D = 0.357 µM) and three low-affinity ones (K_D = 27.1 µM). For all the four sites, the energetic of PFOA binding followed an exothermic reaction. The high affinity site shows a favourable energetic contribution of both enthalpy (ΔH) and entropy (ΔS), suggesting that the interaction is achieved through electrostatic and hydrophobic contribution, as shown in **Figure 3.2B**. Inversely, binding of the PFOA to the three low-affinity sites is mainly characterized by a positive entropic contribution, which can be ascribed to hydrophobic interactions.

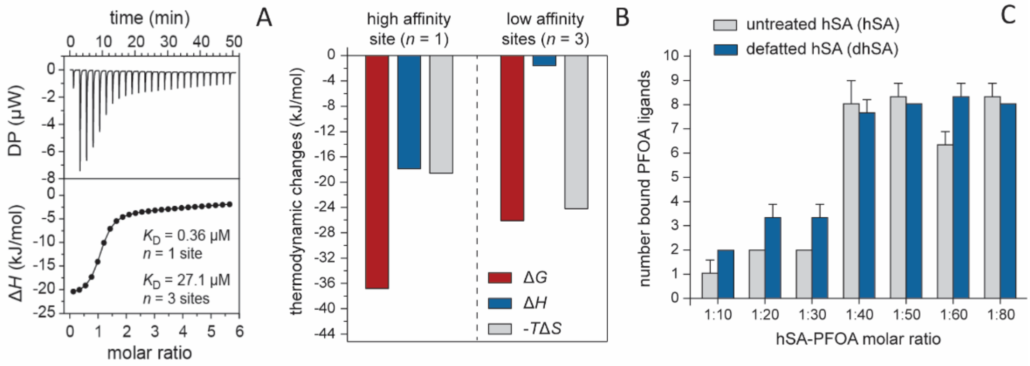

Figure 3.2 *Isothermal titration calorimetry analysis of PFOA binding to dhSA. (**A**) Representative raw trace (top) of the calorimetric titration of PFOA into dhSA and integrated binding isotherm (bottom); (**B**) Summary of thermodynamic parameters. Bar diagram presenting the thermodynamic parameters for the high affinity (left) and low affinity (right) binding site. Gibbs free energy changes (ΔG), enthalpy changes (ΔH) and entropy changes (ΔS) are shown in red, blue and grey, respectively. n indicates the stoichiometry of the binding; (**C**) Column graph reporting the number of PFOA ligands bound to dhSA (gray) and dhSA (blue) human serum albumin. The molecular mass of untreated hSA and dhSA in complex with increasing amount of PFOA was determined using native MS. Values (y-axis) represent the means ± s.e.m. (bars) of at least three independent experiments.*

The effect of the temperature on the binding of PFOA was studied considering a range going from 12-37 °C, as shown in **Figure 3.3**. No significant variations were observed in the stoichiometry nor in the binding affinities when ITC studies were performed at temperatures ranging from 12 to 30°C (**Table A3.1**). On the contrary, a

change in the stoichiometry of the low-affinity binding sites was instead observed at physiological temperature (37°C) with one or two low-affinity sites showing a minor their binding affinity. Though, these sites appear to recur when longer titrations are performed (**Figure 3.3B**). These multiple bindings were observed also via native MS analysis, using increasing molar ratio of PFOA to dhSA. The results revealed the presence of up to eight PFOA binding sites (**Figure 3.2C**). This data is in good agreement with previous studies [39] and confirmed the ability of PFOA to occupy additional dhSA pockets at higher concentrations. A consistent trend in the binding stoichiometry was observed when the analysis was performed using dhSA or untreated hSA, as further discussed in **Section 3.3.3**.

To assign the high affinity binding site, we performed competitive ITC studies using a range of commercially available drugs with known binding affinity and site-selectivity [40]. Drugs binding in the sites FA4, FA6 and FA7 were selected because the structural analysis revealed that these are the preferential pockets for PFOA binding, as described in following **Section 3.3.2**. These drugs include ibuprofen (binding FA4 and FA6), 3-carboxy-4-methyl-5-propyl-2-furanpropionic acid (CMPF; binding FA4 and FA7), warfarin (binding FA7) and iodipamide (binding FA7 and crevice). The superimposition of all albumin-drugs structures presented in **Figure 3.4A** shows the complementary distribution of these sites. By considering presence/absence of a competition equilibria between PFOA and each of these drugs, we will be able to identify the high affinity sites among the four FAs considered. First, titration profiles of the four compounds to dhSA were recorded confirming the binding to the protein and allowing us to assess the optimal saturating conditions for each drug (**Figure 3.4C**, **Table A3.3**). The experimental binding parameters were in good agreement with those reported in the literature [41–43]. The presence of small amounts of DMSO, needed to solubilize some drugs, did not alter the binding parameters of PFOA to dhSA (**Figure 3.4E**, **Table A3.2**). The overlay of the individual titration profiles of PFOA to dhSA saturated with single drug enabled the identification of the highest binding affinity site for PFOA. While the titration profiles obtained in the presence of warfarin- and iodipamide-saturated dhSA are comparable to that of dhSA, those obtained in the presence of ibuprofen- and CMPF-saturated dhSA revealed a nearly saturated flat curve, suggesting a direct competition and preservation of the only lower affinity sites. In addition, the thermodynamic parameters of binding of PFOA to dhSA in the presence of ibuprofen or CMPF show little or null enthalpic contribution, which is instead present when the protein is saturated with iodipamide or warfarin and comparable to that of dhSA (**Figure 3.5**).

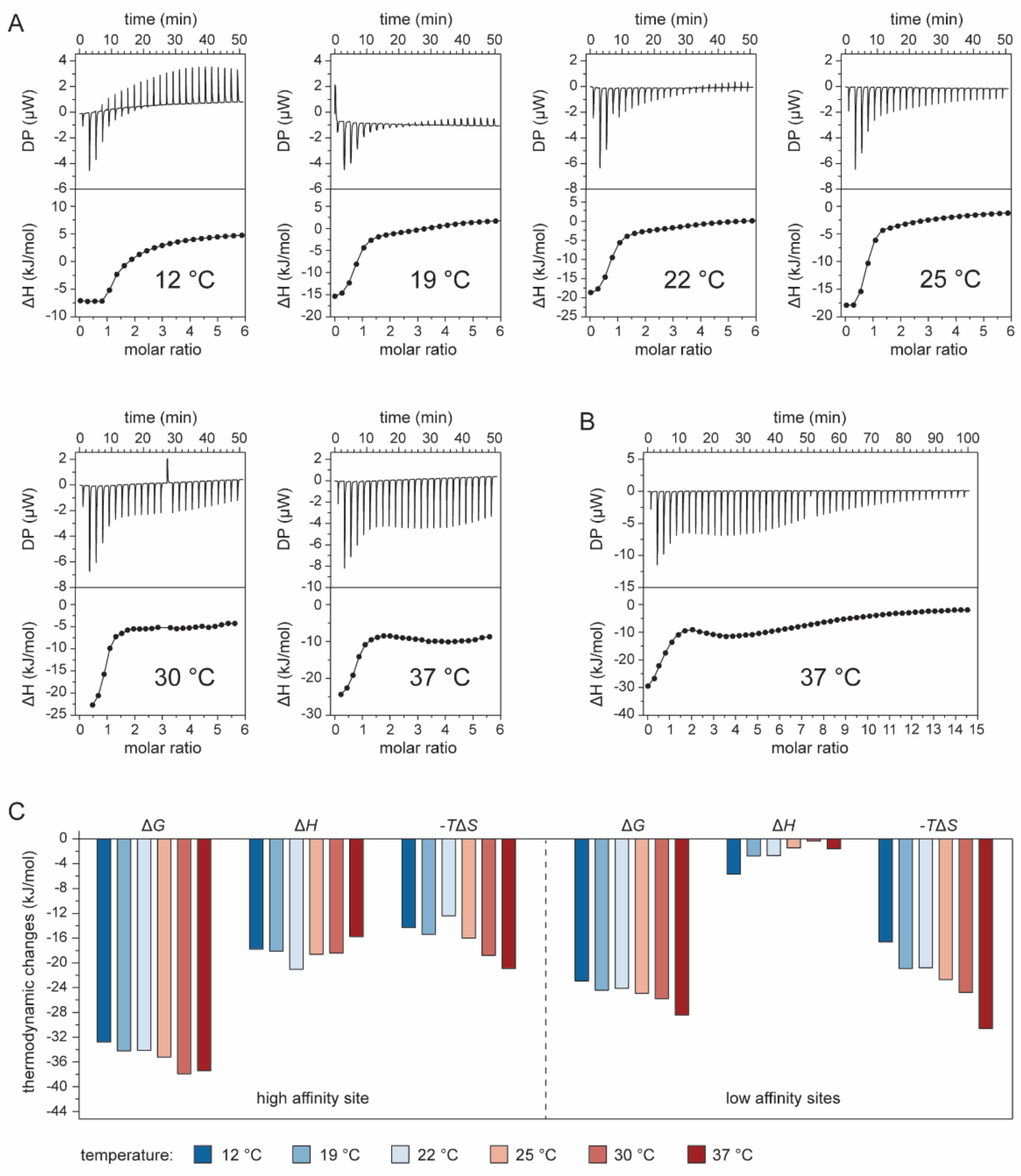

*Figure 3.3 Isothermal titration calorimetry analysis of dhSA binding to PFOA at different temperatures. (**A**) Representative raw trace (top) and integrated binding isotherm (bottom) of the calorimetric titration of PFOA binding to dhSA at 12 °C, 19 °C, 22 °C, 25 °C, 30 °C and 37 °C; (**B**) Representative raw trace (top) and integrated binding isotherm (bottom) of the calorimetric titration of PFOA binding to dhSA for 100 min at 37 °C; (**C**) Summary of thermodynamic parameters. Bar diagram presenting the thermodynamic parameters for the high affinity (left) and low affinity (right) binding sites. Gibbs free energy changes (ΔG), enthalpy changes (ΔH) and entropy changes.*

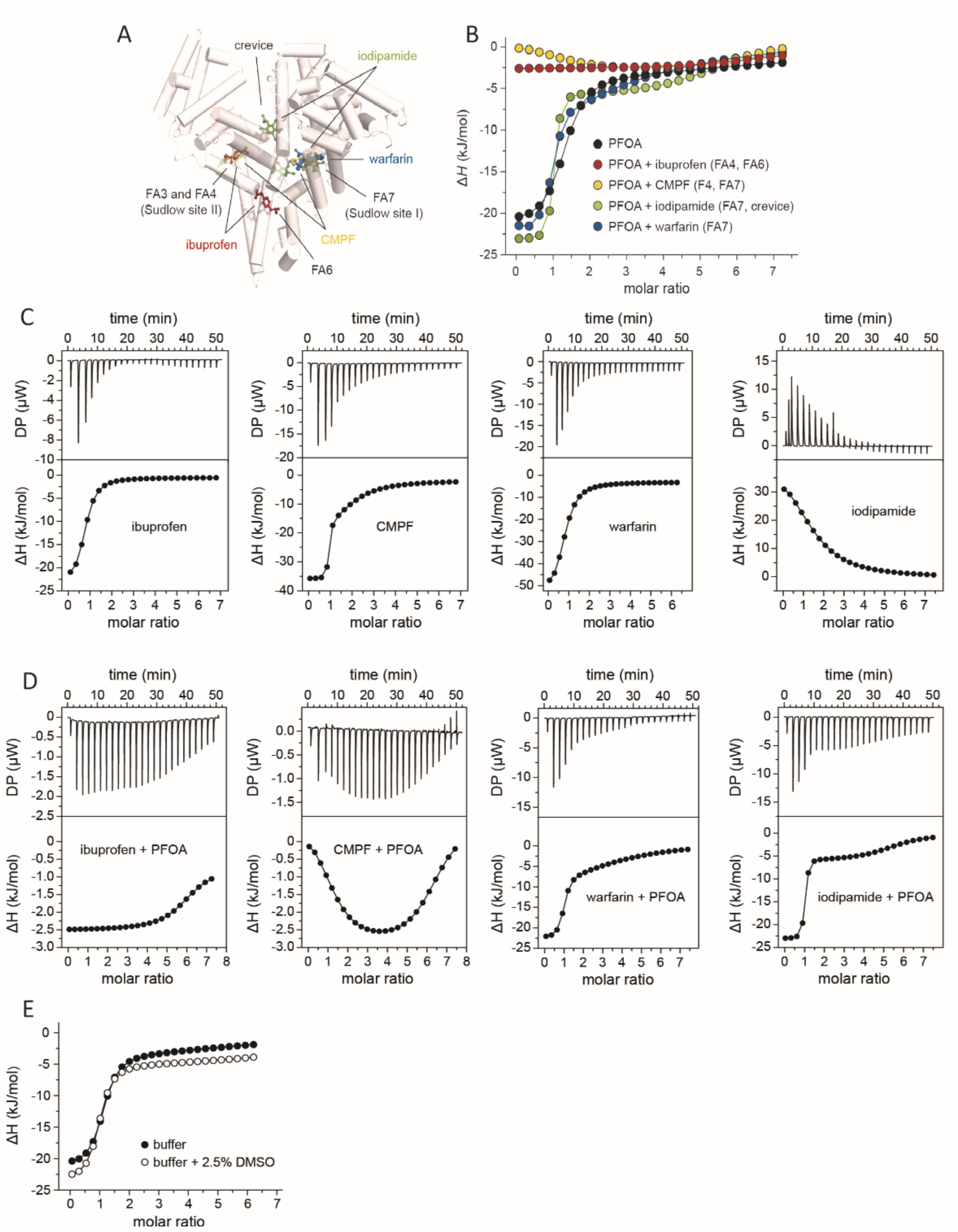

Figure 3.4 *Isothermal titration calorimetry analysis of dhSA binding to four commercially available drugs in the absence and in the presence of PFOA. (**A**) Superimposition of dhSA structure (white) with aligned dhSA-ibuprofen [PDB identification code: 2BXG], dhSA-CMPF [PDB identification code: 2BXA], dhSA-iodipamide [PDB identification code: 2BXN] and dhSA-warfarin [PDB identification code: 2BXD] complexes. Bound molecules are shown in a ball-and-stick representation and coloured as follow: ibuprofen = red, CMPF = yellow, iodipamide = green and warfarin = blue; (**B**) Overlay of the individual titration profiles of PFOA to dhSA saturated with ibuprofen (red), CMPF (yellow), iodipamide (green) and warfarin (blue). Titration profile of PFOA to dhSA alone is shown in black.(**C**) Representative raw trace (top) and integrated binding isotherm (bottom) of the calorimetric titration of ibuprofen, CMPF, warfarin and iodipamide into dhSA; (**D**) Representative raw trace (top) and integrated binding isotherm (bottom) of the calorimetric titration of PFOA*

*binding to ibuprofen-, CMPF-, warfarin- and iodipamide-saturated dhSA; (**E**) Titration profiles of PFOA binding to dhSA in the presence or in the absence of 2.5% v/v DMSO.*

Given that ibuprofen and CMPF share the same FA4 binding site and that among all the compound tested ibuprofen is the only one that does not bind FA7, we can conclude that FA4 is a high affinity site for PFOA, whereas FA6, FA7 and the crevice are the low affinity ones. The results are consistent with the comparative analysis of the interactions of each single molecule of PFOA to the residues of dhSA which shows that the PFOA molecule bound to the FA4 site establishes a higher number of intermolecular contacts if compared to other sites, as described in the next section.

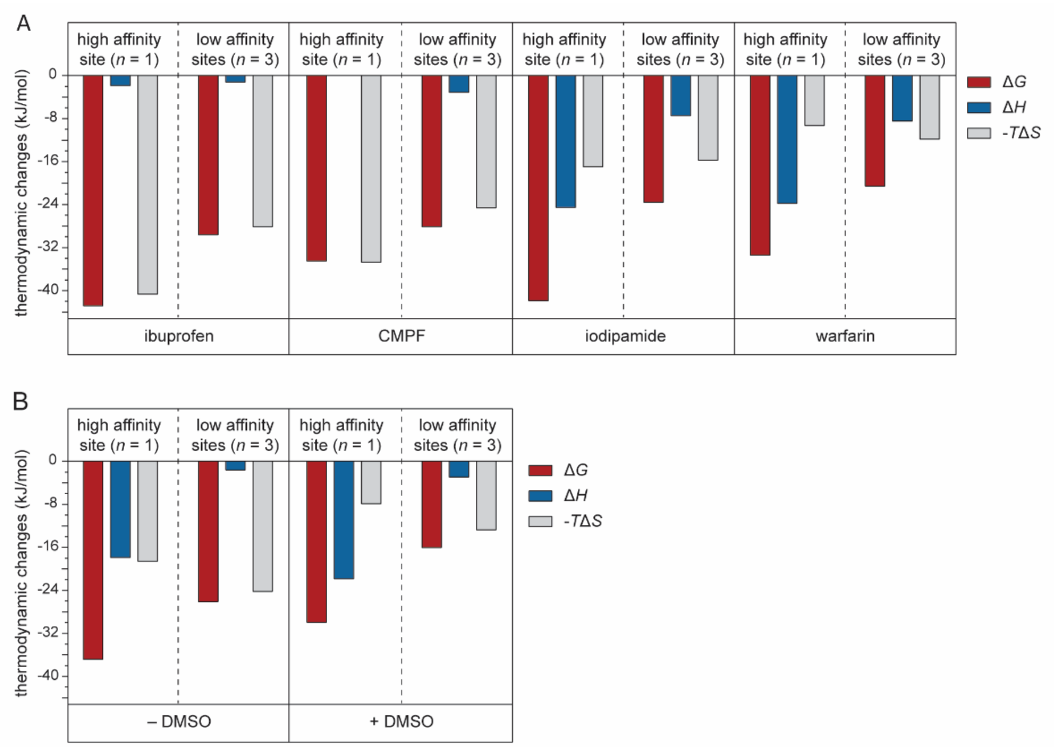

Figure 3.5. *Summary of thermodynamic parameters for the binding of PFOA to hSA in the presence of four commercially available drugs. (**A**) Bar diagram presenting the thermodynamic parameters for the high affinity (left) and low affinity (right) binding site of PFOA to ibuprofen-, CMPF-, warfarin- and iodipamide-saturated dhSA; (**B**) Bar diagram presenting the thermodynamic parameters for the high affinity (left) and low affinity (right) binding site of PFOA to dhSA in absence (left) and presence (right) of 2.5% v/v DMSO. Gibbs free energy changes (ΔG), enthalpy changes (ΔH) and entropy changes (ΔS) are shown in red, blue and grey, respectively. n indicates the stoichiometry of the binding.*

3.3.2 Molecular Binding Mode: X-ray Crystallography

X-ray crystallography was applied to determine the structure of the complex. To resemble the physiological conditions, we co-crystallized dhSA in the presence of both PFOA and the representative long FA myristic acid (Myr). The dhSA-PFOA-Myr complex was prepared by incubating the dhSA protein with a two-fold molar excess of PFOA over Myr, different ratios were tested (**Section 3.2.3**). The best crystals diffracted to 2.10 Å maximum resolution and the structure solved by molecular replacement (**Figure 3.6**, **Table A3.4**, PDB identification code: 7AAE). The polypeptide chain of dhSA could be traced unambiguously from His3 to Leu585. The electron density was clearly visible for all the ligands allowing a definite assignment of the positions and orientations of both PFOA and Myr bound molecules. A total of eight distinct binding sites, four occupied by PFOA and four by Myr, have been identified (**Figure 3.6C**). The binding sites occupied by PFOA are located at the Sudlow's drug-binding site I (subdomain IIA) and II (subdomain IIIA). Here, we refer to these two ligands as **PFOA3** and **PFOA1**. A third molecule, named **PFOA2**, is positioned at the interface of subdomains IIA and IIB (FA6) whereas a fourth binding site (**PFOA4**) laid in the crevice at the interface between sub-domains IB and IIIA. The remaining binding sites FA1, FA2, FA3, and FA5 were all occupied by Myr molecules.

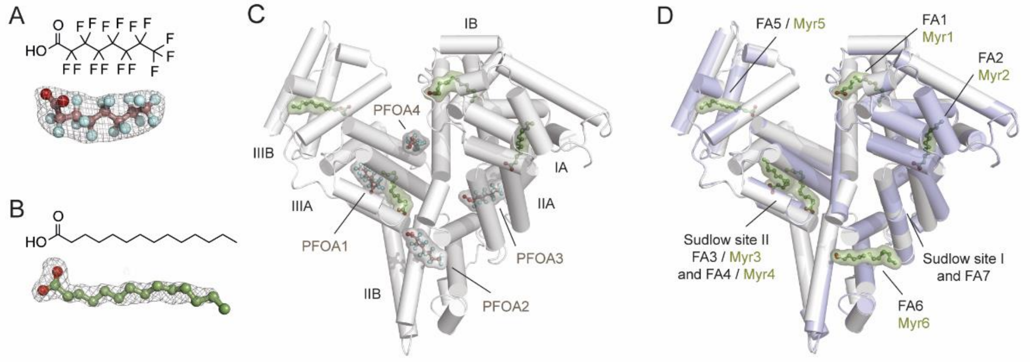

Figure 3.6. *Structure of dhSA in complex with PFOA and Myr. Chemical structure (top) and composite omit maps depicting the* $(F_o – F_c)$ *electron density (bottom) of PFOA (**A**) and Myr (**B**) contoured at* 4σ*; (**C**) Crystal structure of dhSA-PFOA-Myr complex (white) obtained using a twofold molar excess of PFOA over Myr [PDB identification code: 7AAE]; (**D**) Superimposition of dhSA-PFOA-Myr ternary complex (white) with aligned dhSA-Myr binary complex (blue white) [PDB identification code: 7AAI]. The structure of dhSA is organized in homologues domains (I, II and III), subdomains (A and B), fatty acids (FA) and Sudlow's binding sites. The* α*-helices of dhSA are represented by cylinders. Bound PFOA and Myr are shown in a ball-and-stick representation with a semi-transparent van der Waals and coloured by atom type (PFOA: carbon = dark salmon, oxygen = firebrick, fluorine = pale cyan; Myr: carbon = smudge green, oxygen = firebrick). The electron density PFOA and Myr is shown as grey mesh.*

To better compare the binding mode of PFOA with that of Myr, we determined the crystal structure of dhSA-Myr binary complex (**Figure 3.6D**, PDB identification code: 7AAI). Superposition of our two crystal structure complexes with those of other dhSA-FA complexes previously described does not show any striking rearrangements of the main backbone with root mean square deviations of the Cα-atoms that never exceed 0.85 Å [20,44]. Importantly, the pattern of binding of all PFOAs is similar to those of medium-chain FAs. Moreover, no major differences are observed for the side chains of amino acids involved in the binding when compared to other dhSA-FA complexes (**Figure 3.7**).

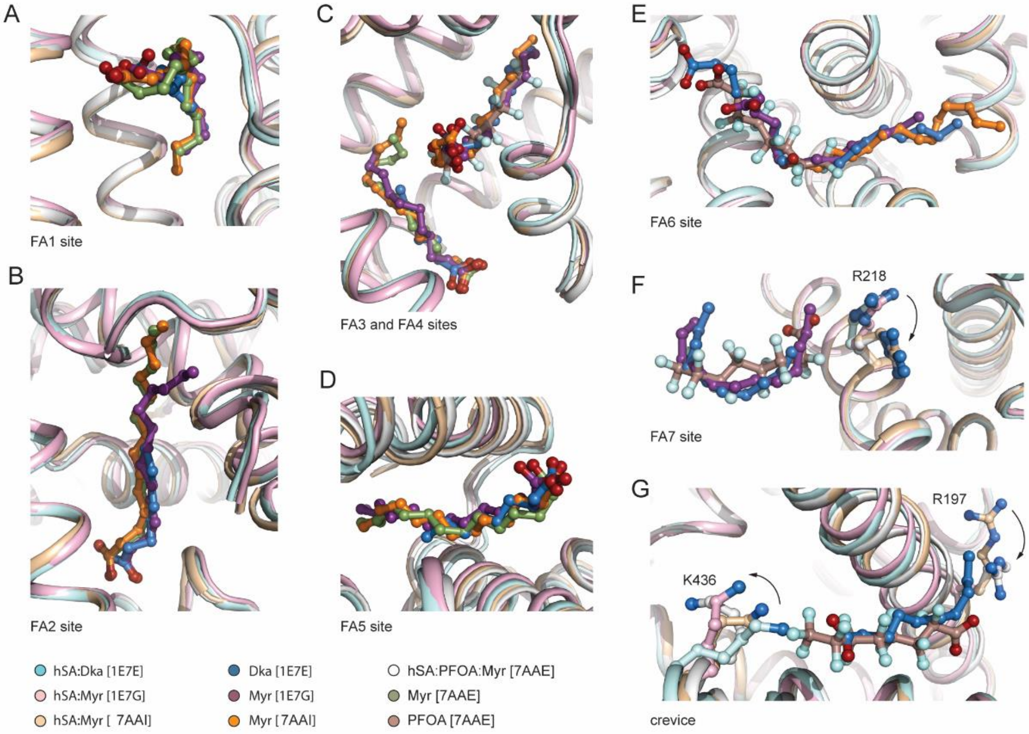

Figure 3.7. Superimposition of the ligand-bind sites of dhSA in complex with PFOA and two saturated FAs: Dka (C10:0), and Myr (C14:0) [46]. *(**A**) Superimposition of Dka and Myr bound to FA1 in sub-domain IB; (**B**) Superimposition of Dka and Myr bound to FA2 in sub-domain IA and IIA; (**C**) Superimposition of Dka, Myr and PFOA bound to FA3 and FA4 in sub-domain IIIA (Sudlow's drug-binding site II); (**D**) Superimposition of Dka and Myr bound to FA5 in sub-domain IIIB; (**E**) Superimposition of Dka, Myr and PFOA bound to FA6 at the interface of subdomains IIA and IIB; (**F**) Superimposition of Dka, Myr and PFOA bound to FA7 in sub-domain IIA (Sudlow's drug-binding site I); (**G**) Superimposition of Dka and PFOA bound to the crevice between sub-domains IB and IIIA. The side chains of amino acids presenting a notable difference are shown (ball-and-stick model). The α-helices of dhSA in complex with Dka (PDB code ID: 1E7E) and Myr (PDB code ID: 1E7G) are coloured in pale cyan and light pink, respectively. The α-helices of dhSA-PFOA-Myr (PDB code ID: 7AAE) and dhSA-Myr (PDB code ID: 7AAI) complexes are coloured in white and wheat, respectively. The selected amino acid side-chains are represented as ball-and-stick and colored by atom type (carbon = white for hSA/PFOA/Myr complex, wheat for hSA-Myr complex, pale cyan for hSA-Dka complex and light pink for hSA-Myr complex; oxygen = firebrick, nitrogen = sky blue). Bound PFOA, Dka and Myr ligands are shown in a ball-and-stick representation and colored by atom type (PFOA: carbon = dark salmon, oxygen = firebrick, fluorine = pale cyan; Myr – 7AAE: carbon = smudge green, oxygen = firebrick; Myr – 7AAI: carbon = orange, oxygen = firebrick; Dka – 1E7E: carbon = purple, oxygen = firebrick and Myr – 1E7G: carbon = purple, oxygen = firebrick).*

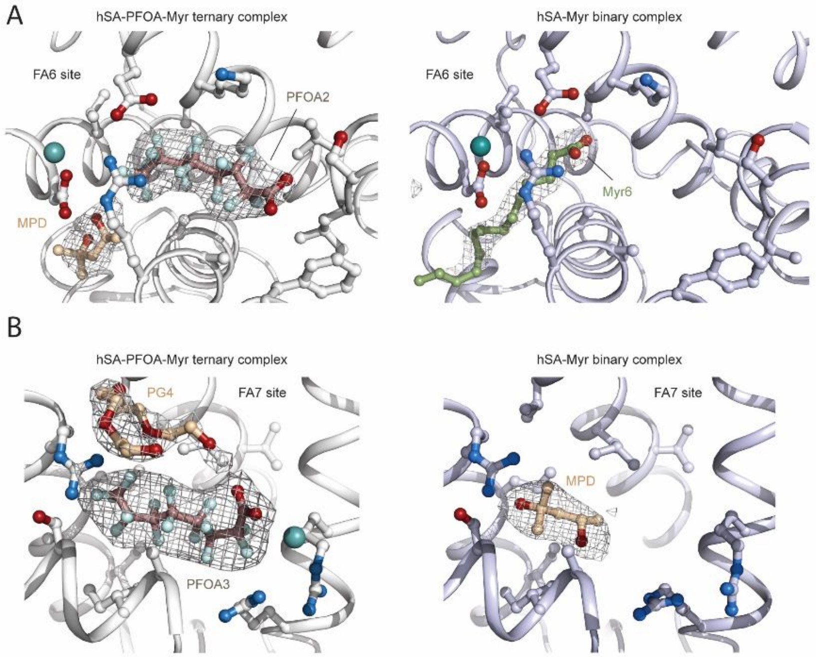

Figure 3.8. *Comparison of FA6 and FA7 ligand occupancy in hSA-PFOA-Myr and hSA-Myr complexes. (**A**) Detailed view of ligands bound to FA6 in hSA-PFOA-Myr (left) and hSA-Myr (right) complexes; (**B**) Detailed view of ligands bound to FA7 in hSA-PFOA-Myr (left) and hSA-Myr (right) complexes. The* α*-helices of hSA in the ternary and binary complex are shown in white and white blue, respectively. The selected amino acid side chains are represented as ball-and-stick and colored by atom type (carbon = white or blue white, oxygen = firebrick, nitrogen = sky blue). Bound molecules are depicted as ball-and-stick models (PFOA: carbon = dark salmon, oxygen = firebrick, fluorine = pale cyan; Myr: carbon = smudge green, oxygen = firebrick; PG4 and MPD: carbon = wheat, oxygen = firebrick). Composite omit maps, representing the (*F_o *-* F_c*) electron density contoured at 4*σ*, are shown as grey mesh. Bound water molecule is shown in light teal.*

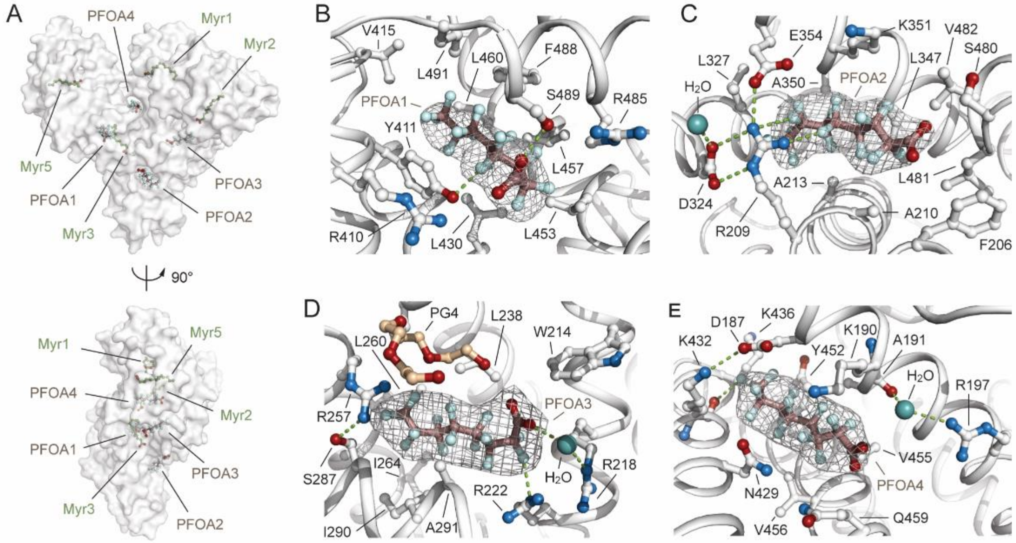

***Figure 3.9**. Details on the binding mode of PFOA to dhSA. (**A**) Molecular surface representation of the overall dhSA-PFOA-Myr complex shown in two orientations (90° rotation); (**B**) PFOA1 bound to FA4 in sub-domain IIIA; (**C**) PFOA2 bound to FA6 at the interface of subdomains IIA and IIB; (**D**) PFOA3 bound to FA7 in sub-*

*domain IIA; (**E**) PFOA4 bound to the crevice between sub-domains IB and IIIA. The α-helices of dhSA are shown in white and the selected amino acid side chains are represented as ball-and-stick and colored by atom type (carbon= white, oxygen= firebrick, nitrogen= sky blue). Bound PFOA molecules are depicted as ball-and-stick models (PFOA: carbon= dark salmon, oxygen= firebrick, fluorine= pale cyan) and the composite omit maps are shown as grey mesh. Bound tetraethylene glycol (PG4) molecule is shown as ball-and-stick model and colored by atom type (carbon = wheat, oxygen = firebrick). Hydrogen bonds, salt bridges and polar interactions are shown as split pea dashed lines. For visualisation, only inter-molecular polar interactions below 3.0 Å are shown.*

Despite several structural analyses reported the presence of different FAs in FA7 site, our binary dhSA-Myr complex shows a 2-methyl-2,4-pentanediol (MPD) molecule bound to it (**Figure 3.8**) [20]. This evidence is consistent with earlier studies reporting a poor and truncated electron density lacking the characteristic expansion at one end necessary to locate the carboxylate head-group of the Myr, thus corroborating the relatively low biding affinity of FAs for this site [45]. Overall, the structure of dhSA in complex with PFOA and Myr revealed the presence of four distinct PFOA binding sites and no conformational differences with those of other dhSA-FA complexes. The electronic density of all PFOA and Myr ligands is well defined allowing an unambiguous assignment of the positions of both hydrophilic carboxylate head-groups and n-tetradecane (C14) methylene or fluorinated n-octyl (C8) lipophilic tails. The **PFOA1** molecule lies in the long and narrow **Sudlow's drug-binding site II** (named FA4), located in sub-domain IIIA, and is positioned approximately at right angles to the Myr molecule (Myr3), located in the nearby FA3 site (**Figure 3.9 A**). Alike FAs, the carboxylate head-group of PFOA1 forms a hydrogen bond with the side chain of Ser489 and polar interactions with side chains of adjacent Asn391, Arg410, and Tyr411 (**Figure 3.9B**). Furthermore, numerous polar interactions are established between fluorine atoms (F3, F11, F12, F14, F17, and F20) and the oxygen and nitrogen atoms of both main and side chains of nearby Tyr411, Phe488, and Ser489 (**Table A3.4**). The rest of the fluorinated n-octyl tail accommodates in the hydrophobic tunnel and establishes non-polar contacts with surrounding Leu387, Tyr411, Val415, Leu430, Leu453, Leu457, Leu460, Arg485, Phe488, Ser489, and Leu491 residues. Notably, the positions of the side chains of the amino acids engaged in contacts with PFOA1 are consistent with those of FAs presented in **Figure 3.7**.

The **PFOA2** occupies **FA6 binding site** at the interface of subdomains IIA and IIB (**Figure 3.9C**). The hydrophilic carboxylate head-group of PFOA2 is involved in polar interactions with adjacent main-chain nitrogen atoms of amino acids Lys351, Leu481, and Val482, while the fluorinated n-octyl tail extends linearly within the narrow hydrophobic tunnel making additional stabilizing contacts with the main and side chains of surrounding Phe206, Arg209, Ala210, Ala213, Leu327, Leu347, Ala350, Lys351, Glu354, Ser480, Leu481, and Val482 residues (**Table A3.4**). The remaining space present at the tip of the fluorinated tail appears to be occupied by a small organic molecule. The detected additional electron density can most likely be attributed to a MPD molecule present in the crystallisation solution as shown in **Figure 3.8**. Again, no difference is observed for the side chains of amino acids involved in the binding to PFOA2 when compared to other albumin-FA complexes. Interestingly, the extended network of hydrogen bonds and polar contacts, made by the side chains of Arg209, Asp324, and Glu354 residues and an interacting water molecule, forms a molecular "net" that holds and further stabilizes the binding of PFOA2 to FA6 site.

The **PFOA3** molecule occupies the **Sudlow's drug-binding site I**, also named FA7, located in sub-domain IIA (**Figure 3.9D**). The carboxylate head-group of PFOA3 establishes hydrogen bonds with adjacent Arg218 and Arg222 residues via a bridging water molecule. One oxygen of the carboxylate head-group of PFOA3 is further involved in a polar contact with an oxygen of the close tetraethylene glycol (PG4) molecule present in the crystallisation solution (**Figure 3.8B**). Notably, the same precipitant molecule appears to play an important role in the formation of polar interactions with the side chains of Arg257 and Ser287, forming a "cap" that helps to grip PFOA3 in the pocket. Again, the fluorinated n-octyl tail accommodates well within the pocket making additional polar and non-polar contacts with the main and side chains of surrounding Trp214, Arg218, Leu219, Arg222, Leu238, Arg257, Leu260, Ala261, Ile264, Ser287, Ile290, and Ala291 residues (**Table A3.4**). The majority of the amino acid side chains, involved in the binding to PFOA3 superimposed well with those of other albumin-FA complexes, except for Arg218 that reorients in between the following Gln221 and Arg222 residues (**Figure 3.7**) [20,47].

Finally, **PFOA4** molecule lays in a large **crevice** located at the interface between sub-domains IB and IIIA (**Figure 3.9E**). This site has been reported to bind exclusively short and medium-chain FAs such as decanoic acid (Dka) and it is therefore not surprising to see a PFOA molecule bound to it instead of a Myr (**Figure 3.7**) [20,44]. Interestingly, the PFOA4 molecule runs in opposite direction than Dka. While the carboxylate head-group of Dka forms a salt bridge with the side chain of Lys436, located at the top of the crevice, the carboxylate head-group of PFOA4 points at the opposite site, towards the solvent, and engages polar contacts with atoms of nearby Lys190, Arg197, and Val455 residues. Again, a water molecule plays a key role in mediating some of these interactions. In addition, a salt-bridge between Asp187 (domain IB) and Lys432 (domain IIIA) forms a side chain strap across the top of the crevice that appears to hold PFOA4 in place. Binding of PFOA4 to this crevice is further stabilized by polar and non-polar contacts of the fluorinated n-octyl tail with the main and side chains of surrounding Asp187, Lys190, Ala191, Asn429, Lys432, Lys436, Tyr452, Val455, Val456, and Gln459 residues (**Table A3.4**). Most of the dhSA side chains that are engaged in PFOA4 binding displayed similar conformations, except for Arg197 (domain IB) and Lys436 (domain IIIA). In the presence of PFOA4, the Arg197 side chain rotates through about 180° to form polar contacts with the carboxylate head-group of PFOA4 (**Figure 3.7**). Similarly, the presence of the fluorinated tail of PFOA4 appears to push away the side chain of Lys436 which undergoes a 180° rotation toward the solvent.

Overall, these data indicate that the binding mode of PFOAs is similar to those of medium-chain FAs and involves both the carboxylate head-group and the fluorinated tail that establish polar and non-polar contacts with surrounding dhSA residues. Data also suggest that PFOA1, located in the FA4 pocket, forms a larger number of inter-molecular interactions, if compared to other bound PFOA molecules. Considering these findings and the previous ITC study, we can anticipate that FA4 is the high affinity site of PFOA. For completeness, PFOA-dhSA complex was compared with PFOS one [38]. The comparison of the dhSA-PFOA-Myr and **hSA-PFOS** (PDB identification code: 4E99) structures revealed differences in the respective binding modes, as shown in **Figure 3.10**. Primarily, the general conformations of the two protein complexes diverge from each other. These major differences were ascribed to either presence or absence of Myr in the complex. The binary hSA-PFOS complex identified solely two PFOS binding sites, one located at Sudlow's drug-binding site II (FA4) and the other at the FA6 binding site (**Figure 3.10**). Interestingly, despite being very similar molecules and occupying the same sites, the binding mode of PFOA and PFOS ligands into FA4 and FA6 pockets varies significantly.

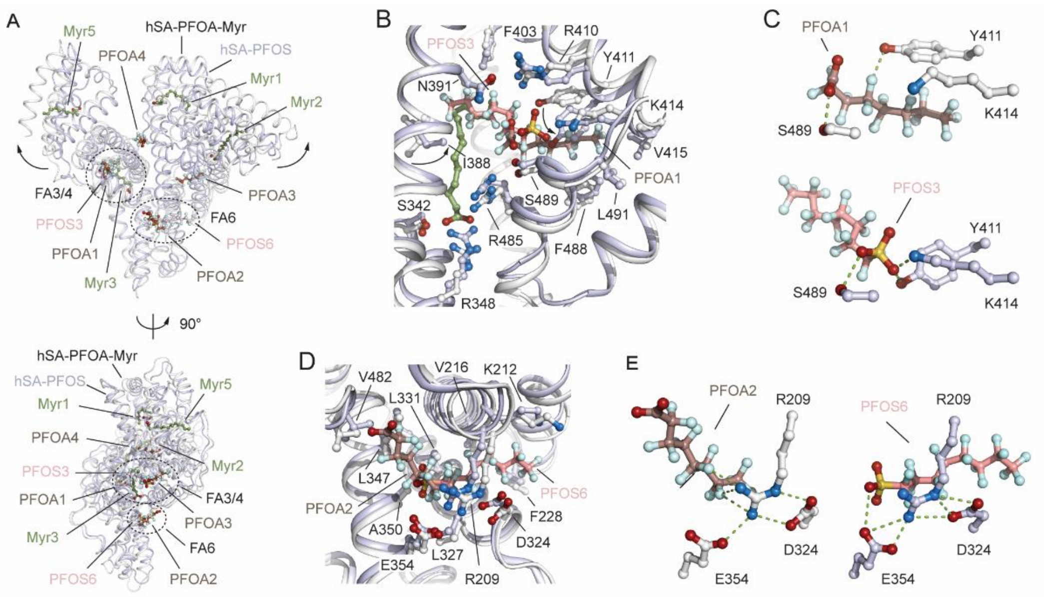

*Figure 3.10. Structural comparison of the ligand binding modes of PFOA and PFOS to dhSA. (**A**) The superimposed dhSA-PFOA-Myr (white/dark salmon/smudge green) and dhSA-PFOS (blue white/salmon; PDB identification code 4E99) complexes are shown in two orientations (90° rotation); (**B**) Detailed view of the superimposed PFOA1 and PFOS3 molecules bound to FA4 in sub-domain IIIA of dhSA; (**C**) Comparison of polar interaction network formed by PFOA1 (top) and PFOS3 (bottom) molecules bound to FA4; (**D**) Detailed view of the superimposed PFOA2 and PFOS6 molecules bound to FA6 in domain II dhSA; (**E**) Comparison of polar interaction network formed by PFOA2 (left) and PFOS6 (right) molecules bound to FA6. For visualisation, only inter-molecular polar interactions below 3.0 Å are shown.*

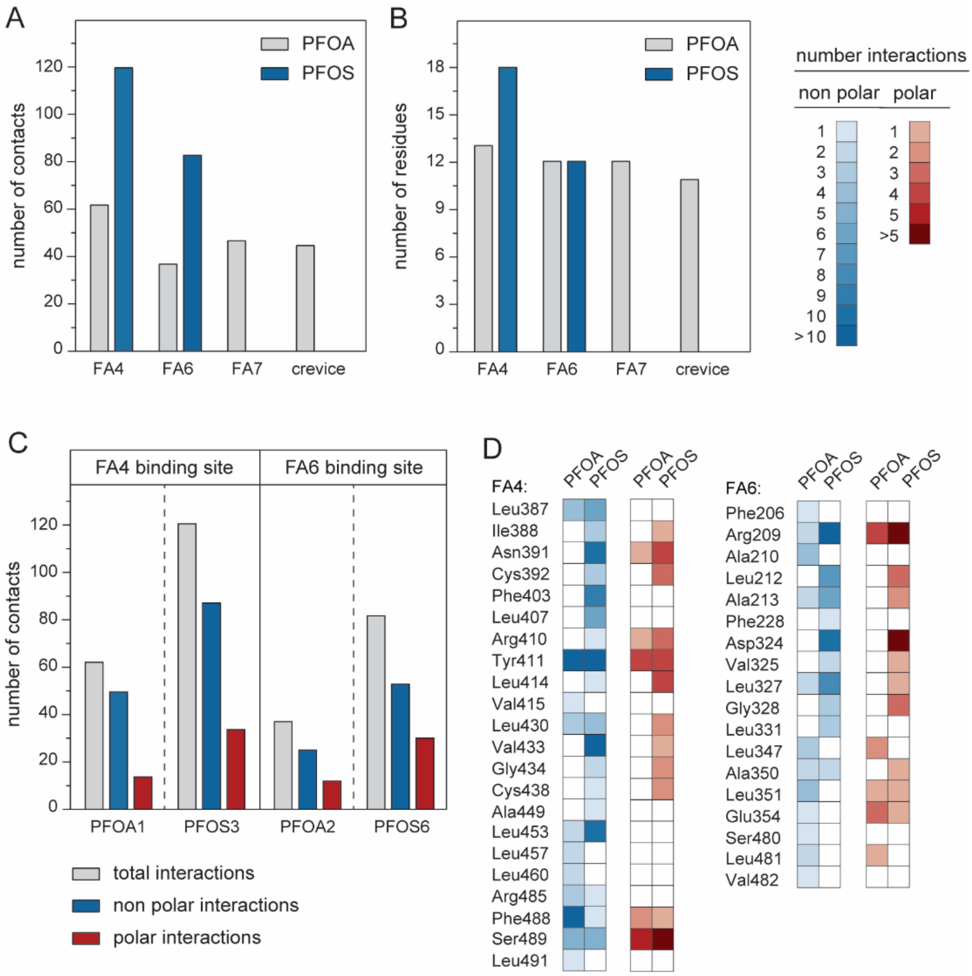

Figure 3.11. *Comparative analysis of the interactions of dhSA residues with PFOA and PFOS ligands. (**A**) Columns graph reporting the total number of interactions of dhSA with PFOA (grey) and PFOS (blue) for binding sites FA4, FA6, FA7 and crevice; (**B**) Columns graph reporting the total number of residues of dhSA interacting with PFOA (grey) and PFOS (blue) on sites FA4, FA6, FA7 and crevice; (**C**) Columns graph reporting the non-polar (blue), polar (red) and total (grey) number of interactions of dhSA with PFOA and PFOS for binding sites FA4 and FA6; (**D**) Heat map visualisation of the number of interactions of dhSA residues involved in binding to PFOA and PFOS ligands* [46]. *The residues of dhSA are indicated as a three numbered letter code. Non-polar and polar interactions are shown in blue and red, respectively. The colour intensity correlates with the number of the interactions, with numerous and few interactions shown as light and dark colours, respectively.*

While the PFOS3 molecule stretches across both FA3 and FA4 binding sites, the PFOA1 ligand occupies solely the FA4 site, with the FA3 pocket being filled by a Myr molecule (Myr3, **Figure 3.10B**). Though the two fluorinated *n*-octyl tails run in opposite directions, the hydrophilic head-groups converges toward the Ser489 residue that establishes a polar interaction with both PFOA and PFOS ligands (**Figure 3.10B**, **Figure 3.11**). The sulfonate head-group of PFOS3 forms a salt bridge with Lys414 and a hydrogen bond with Tyr411, whereas in the case of PFOA1 the Tyr411 is shifted upward and the rotated Lys414 is situated too far to form contacts with the carboxylate head-group (**Figure 3.10C**). Importantly, PFOS3 forms a larger number of inter-molecular interactions with the FA4 pocket residues, if compared to PFOA1. Alike the PFOA2 molecule, PFOS6 occupies FA6 binding site at the interface of subdomains IIA and IIB (**Figure 3.10D**). The hydrophilic head-groups of both PFOA2 and PFOS6 point toward the same direction of the carboxylate head-group of Myr6. While the sulfonate head-group of PFOS3 halts at the centre of the tunnel forming hydrogen bonds with nearby Arg209 and Glu354, the carboxylate head-group of PFOA1 slides toward subdomains IIIA by roughly 7 Å (head-to-head spacing) letting the fluorine atoms of the tail to establish polar interactions with Arg209 and Glu354 (**Figure 3.10E**). Overall, we conclude that while being similar molecules, PFOA and PFOS occupy FA4 and FA6 sites by exploiting different directions and albumin residues. Though albumin appears to bind more PFOA molecules than PFOSs, the latter establish a larger number of inter-molecular contacts and cover larger surfaces of interaction (**Figure 3.11**, **Table A3.3**).

In conclusion, the crystal structure revealed four PFOA binding sites, namely FA4 (Sudlow binding site I), FA6, FA7 (Sudlow binding site II) and crevice. The protein complex overlaps well that of other albumin-FAs. The **binding mode of the PFOA** is similar to those of medium-chain FAs and involves direct or water-mediated interactions of the carboxylate head-groups to nearby basic or polar residues. The lipophilic tails accommodate within the hydrophobic cavities. Though shorter than Myr, PFOA molecules appear to establish a larger number of both polar and non-polar contacts with dhSA residues. Such property could be attributed to the ability of the carbon–fluorine (C-F) bond to participate in multiple non-covalent intermolecular interactions (i.e., C-H···F-C, C-F···F-C, C-F···π, C-F···X where X=N, O, S, halogen). Further in-solution binding studies confirmed the 4:1 PFOA-dhSA stoichiometry and revealed the presence of one high and three low affinity binding sites. Similarly to FAs, the binding of PFOA to dhSA appears to be characterized by a favourable exothermic process and by a gain in entropy most probably due to desolvation of the fluoroalkyl tail [48]. The exothermic process is mainly driven by van der Waals interactions, hydrogen bonds and electrostatic interactions, the gain in entropy is the result of hydrophobic interactions that are stronger than ones with their hydrocarbon analogues. This latter reflects the size of the structured water cage required to solvate the fluorocarbon groups and the entropy gained from desolvation upon protein binding [49]. Though numerous studies indicate the presence of additional PFOA binding sites, our structural and in-solution characterisation revealed that these are unlikely to be physiologically relevant. Additional sites were probably observed to be occupied only because of the lack of FAs or the relatively high concentrations of PFOA were used in previous studies. This is in agreement with the fact that most dhSA sites have greater affinity for long-chain FAs than for PFOA and that the former is normally most prevalent in the circulation. Competition experiments with known dhSA-binding drugs identified the FA4 pocket in sub-domain IIIA as the high affinity binding site for PFOA. Consistent with these evidences, structural analysis of the different PFOA-binding sites revealed that PFOA1 located in FA4 pocket forms a larger number of inter-molecular interactions, if compared to other sites. It is worth noting that the carboxylate head-group of PFOA1 is the only one establishing a hydrogen bond with adjacent dhSA residues. The ability of PFOA1 to outcompete Myr for the FA4 binding, a primary site for medium and long-chain FAs, is remarkable and further supports the key role of dhSA in enhancing the half-life of PFOA in plasma. The low binding of affinities of PFOA to FA6, FA7 and crevice site is anticipated as all these pockets lack positive and polar amino acid side chains necessary for the anchoring of the carboxylic group of PFOA. Our observations are consistent with previous studies. These three binding sites may be the primary site for shorter-chain FAs and are occupied only at high molar ratio of FAs [20]. Finally, comparison of the crystal structures of dhSA in complex with PFOA and PFOS enables to appreciate analogies and differences in the binding mode of two, yet similar, fluoroalkyl substances. While the structure of dhSA in complex with PFOA is wider and displays four bound molecules, the structure of dhSA in complex with PFOS is more compact and includes only two bound ligands. Similarly to PFOA, PFOS occupy FA4 and FA6 pockets and their binding to dhSA appear to be exothermic and driven by both polar and non-polar interactions [50,51]. Yet, the orientations and positions exploited by PFOA and PFOS in FA4 and FA6 pockets differs significantly.

With this first part of the study, we analysed in details the molecular interaction of PFOA with dhSA, the main protein carrier of these widely found toxic compounds in vivo, and we estimate the affinities constants in solution. The results obtained confirmed the possible applicability of dhSA as bioreceptor for PFOA because of: i) the specificity of their interaction (with a binding mechanism different even from PFOS one) and ii) the stability of the complex formed (PFOA as well as FA contributes in the making albumin structure more compact). The stability will be further investigated in the following section. In light of the urgent need to implement better strategies to detect and reduce exposure to PFOA, these findings are expected to have implications not only for the development of novel molecular receptors for biosensor, but also for bioremediation and biomedical applications.

3.3.3 Assessing the Complex Stability: Native MS

IM and CIU: Key-Concepts for the Experimental Design

As mentioned in the introduction, native MS combined with **ion mobility** (IM) offers a rich toolbox for the characterisation of protein-ligand interaction which can be further applied in bioreceptor design. Here, the study of dhSA:PFOA complex with IM is reported as a proof-of-concept study to show how native MS can contribute in the elucidation of PFAS protein binding mechanism and, at the same time, help characterising potential bioreceptors. The important details about native MS, IM and CIU mentioned in Section 3.1 are further described here, for sake of simplicity, aiming to emphasise the potential of these methods in consideration of our *analytical questions* and the experiments.

IM spectrometry enables studying the global size and shape of the ions (i.e., the conformation) in more details and it can even highlight coexisting conformational states within one charge state. IM experiments are carried out in an inert gas (He or N_2) and under the influence of an electric field, the ions are separated based on their mobility and we follow them considering their different *arrival times* [52]. Then, the measured arrival time can be converted to collision cross sections (CCS). The values of these latter can be considered as the average 'shadow' of the ion through all possible orientations. All orientations are equally occurring since the ion tumbles freely in the IM cell. The CCS distribution of a particle represents its diversity in size and shape. It is worth noting that in conventional IM devices (i.e. with a linear drift tube) the arrival time can directly be converted to CCS values [53], but a calibration with ions with a known CCS is often required to have comparable CCS dataset [35,36,54]. During a **collision-induced unfolding** (CIU) experiments, the arrival time, or CCS, of an ion is monitored when raising the collision energy [55]. Typically, stepwise changes of the arrival time are observed: once a critical energy is reached, the analyte unfolds, but in between these critical energies the analyte is stable [56]. Indeed, the collisions with a gas do not only induce the dissociation of complexes in the gas-phase, but usually this is preceded by the unfolding of ions or complexes. This approach allows to examine the conformational stability of biomolecules and their complexes. Here, CIU was applied in the comparison of delipidated and untreated albumin alone and in complex with PFOA. According to Dixit *et al.* [57], CIU is an ion mobility-mass spectrometry method that enables the rapid differentiation of subtly-different protein isoforms based on their unfolding patterns and stabilities. The CIU method required to perform a series of measurements, in which the isolated albumin ions are activated at increasing collision energies. The energetic collisions occurring in the gas-phase increase the internal energy of the biomolecule ions. This event causes a consequent conformational change (namely, *unfold*) without leading to the dissociation of covalent bonds (*primary structure* of the protein is maintained). In this section the results related to the progressive unfolding of the albumin ions followed by IM-MS by considering the changes in the ion collision cross section (CCS) are reported. In this first case study, the possibility of improving hSA-PFOA binding affinity and stoichiometry was tested by comparing untreated and delipidated hSA. The removal of endogenous fatty acids is expected to lead to a better reproducibility of the interaction and a higher sensitivity. To characterise the differences between delipidated and untreated albumin, we first determined the number of binding sites and compared the affinity of both albumin towards PFOA.

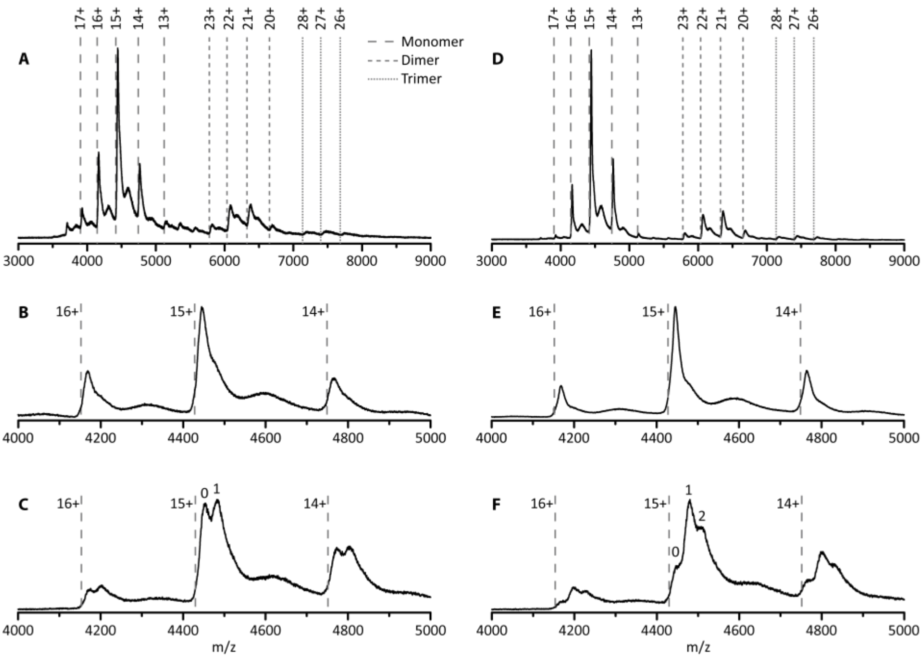

Figure 3.12. Native MS spectra of untreated (A, B, C) and delipidated (D, E, F) dhSA. The full MS spectra of dhSA are given (A and D), together with a zoom of the monomer region (B and E) and spectra of dhSA in complex with PFOA at a 1:10 protein:ligand ratio (C and F). The dashed lines indicate the theoretical m/z-values of the monomer, dimer and trimer of dhSA.

In **Figure 3.12**, the mass spectrum of untreated hSA shows the presence of the protein monomer (charge states 17+ to 13+), nonspecific dimer (charge states 23+ to 20+) and nonspecific trimer (charge states 28+ to 26+). The experimentally determined mass of albumin was found to be 66.7 ± 0.3 kDa, which corresponds well with the mass of mature albumin after the cleavage of the signal peptide and the propeptide resulting in 585 amino acids (66.5 kDa) [58]. Moreover, a small amount of the complete hSA consisting of 609 amino acids (including propeptide and signal peptide) can be observed as the minor charge state distribution in between the main peaks, with an experimentally determined mass of 68.9 ± 0.9 kDa. Analysis of the monomer revealed the presence of a shoulder to the main peak with an intensity of 52% compared to the main peak (**Figure 3.12 B**). This is not observed upon denaturing of the protein (**Figure 3.13 A-B**) and the intensity of the shoulder decreases to 31% upon applying higher collision energies (**Figure 3.13 C-D**). Therefore, this feature is noncovalent in nature and can possibly be ascribed to the presence of long- or short-chain fatty acids [45,59].

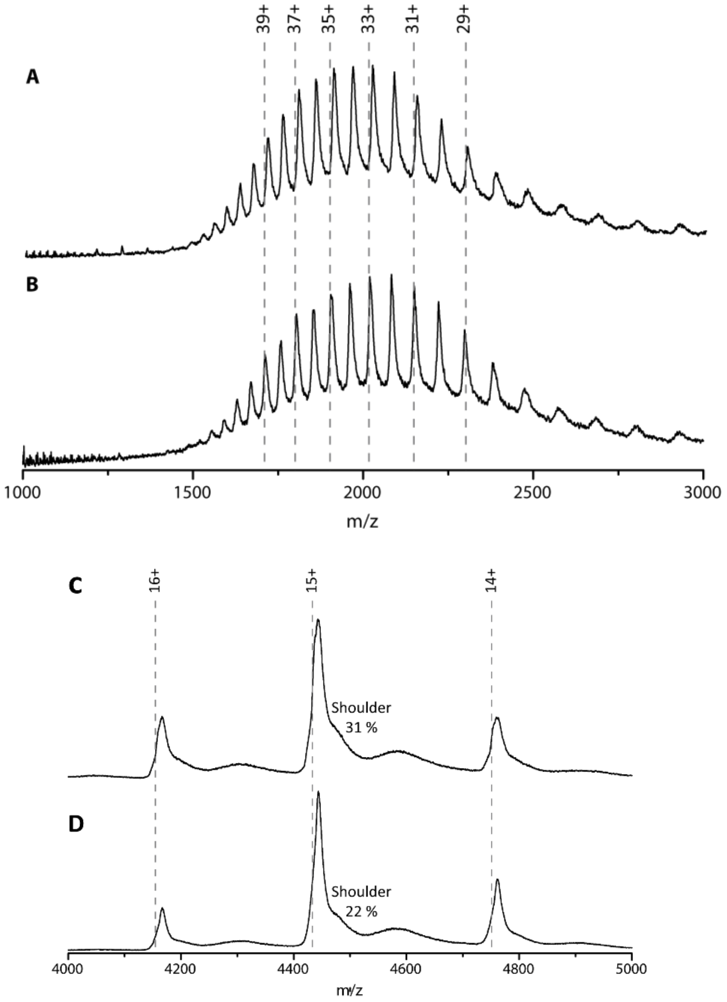

*Figure 3.13. Denatured MS spectra of untreated (**A**) and delipidated (**B**) hSA recorded in 50/50 acetonitrile/MilliQ with 0.1 % formic acid. The dashed lines indicate the theoretical m/z-values of hSA calculated from the theoretical mass of 66531 Da.MS spectra of untreated (**C**) and delipidated (**D**) hSA recorded at 100 V trap collision energy. The dashed lines indicate the theoretical m/z-values of hSA.*

Upon addition of PFOA (10-fold excess), a 1:1 stoichiometry complex was formed as indicated by the appearance of the second peak in **Figure 3.12 C**. Over all charge states present, about 49% of the untreated hSA is present in its unbound state and 51% has one PFOA bound. The K_d was estimated to be 90 ± 5 µM. This value is in agreement with the previously reported K_d of 100 ± 90 µM by Beesoon *et al.* for the albumin-PFOA complex [60]. The observed stoichiometry is lower compared to other values reported in the literature in which bovine serum albumin and rat serum albumin were used

[61,62]. The exact concentration, type and state of the protein used can influence the stoichiometry and results obtained with different instrumentation and working conditions are often not consistent. For this reason, this comparative study to investigate dhSA and untreated albumin differences in PFOA complexes was carried out using the same conditions.

The same experiments were performed with the dhSA and an experimental mass of 66.6 ± 0.2 kDa was obtained. Again, a shoulder is observed on the main peak, but with a lower intensity of only 31% compared to 52% for the untreated hSA, suggesting the delipidation process removed the noncovalent feature (most likely fatty acids) at least partially (**Figure E**). Addition of 10-fold excess of PFOA to dhSA yielded a complex with different stoichiometry (1:2, **Figure 3.12F**). Moreover, the intensity of the hSA peak without any PFOA bound is significantly lower for the dhSA (20%) than for the untreated hSA (49%), suggesting a shift towards more complex formation. The increase of the binding stoichiometry can be attributed to the delipidation step. As such, native MS confirmed that hSA delipidation is important to attain higher binding stoichiometries of the proposed bioreceptor.

Inspecting hSA/dhSA its conformational stability

A protein bioreceptor is expected to selectively recognize the target ligand, this recognition event is followed by an observable physicochemical change resulting in a variation of a measurable dimension in the sensing platform, such current, refractive index, etc. In this frame, the stability of the protein-target complex formed after the recognition event plays a crucial role. Herein, the CIU study of both dhSA and untreated albumin is presented. From the plots in

Figure 3.14A and **C**, it is possible to observe that both proteins showed a similar $^{TW}CCS_{N2}$ (4469 ± 22 Å² and 4458 ± 22 Å² for the native untreated hSA and dhSA, respectively) up to a collision energy of 825 eV, which corresponds with an applied potential difference of 55 V. At higher energies a **multi-step unfolding process started** [63,64]. The first transition occurs between 60 and 70 V and results in a state with a $^{TW}CCS_{N2}$ of 5284 ± 22 Å² and 5262 ± 22 Å² for hSA and dhSA, respectively. Eschweiler *et al.* assigned this second conformation to the unfolding of domain II [63]. The second transition takes place just above 100 V and generates a state with a $^{TW}CCS_{N2}$ of 5563 ± 22 Å² and 5551 ± 22 Å² for hSA and dhSA, respectively, which corresponds to the partial unfolding of domain III. A final unfolding step occurs between 120 and 130 V, which results in a state with a $^{TW}CCS_{N2}$ of 5686 ± 22 Å² and 5641 ± 22 Å² for hSA and dhSA, respectively. This final transition can be ascribed to the unfolding of domain I and the remainder of domain III [63]. The consistency of the unfolding patterns, with a relatively low root-mean-square deviation (RMSD) of 9.26 (**Figure 3.15** and **3.16**), suggested that the delipidation process did not affect the stability of hSA. No significant differences in the unfolding products nor changes in the threshold collision energies were observed. These preliminary results proved that the **delipidation treatment did not affect the protein stability**.

The CIU experiments were also extended to albumin-PFOA complexes, to test whether the presence of ligands influenced the stability of the proteins, particularly the delipidated form. A 10-fold excess of PFOA to albumin was tested and the unfolding pathways of hSA and dhSA are shown in **Figure 3.14 B** and **D**.

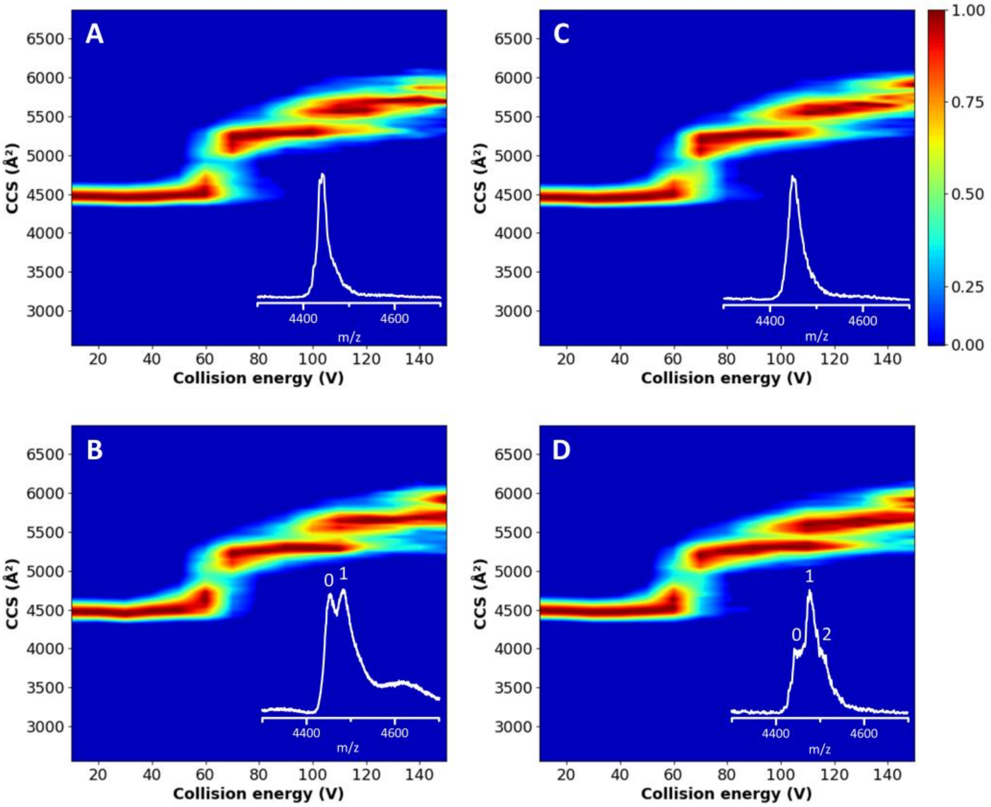

***Figure 3.14**. CIU plots of untreated (**A**) and delipidated (**C**) hSA and of the untreated (**B**) and delipidated (**D**) hSA in complex with PFOA (1:10 protein:PFOA ratio). The $^{TW}CCS_{N2}$ is plotted as function of the trap collision energy and the intensity is shown using a color scale (red is 100 % and blue 0 %). The insets show the peaks selected (15+ charge state) for extraction of the $^{TW}CCS_{N2}$ at a trap collision energy of 60 V. Arrival times were extracted from the whole peak, including salt adducts and complexes (where appropriate).*

To extract the CCS, the full width at half maximum of the complete peak, which contains both the bound and the unbound state, was used since there is no complete separation of both states. The initial conformation presents a $^{TW}CCS_{N2}$ of 4480 ± 22 Å² and unfolds between 60 and 70 V (**Figure 3.15**) to generate a state with a $^{TW}CCS_{N2}$ of 5284 ± 22 Å² and 5306 ± 22 Å² for untreated and delipidated, respectively. The final state has a $^{TW}CCS_{N2}$ of 5641 ± 22 Å². This compares well with the fourth and final state of both proteins without PFOA, indicating that the third feature, corresponding to the partial unfolding of domain III, disappears in the unfolding process of the complex. In general, the unfolding pathways of the complexes were found to be comparable between the two proteins (RMSD of 7.90) as shown in **Figure 3.15**.

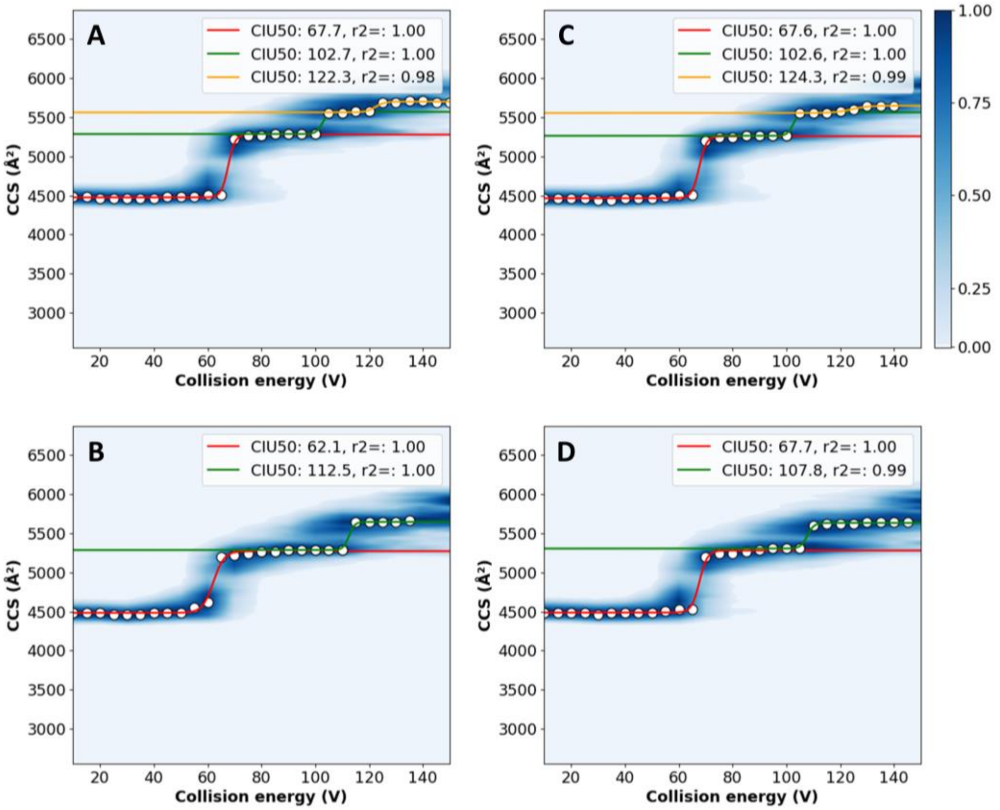

Figure 3.15. *CIU50 analysis performed using CIUSuite 2 on the CIU plots of untreated (**A**) and delipidated (**B**) hSA and of the untreated (**C**) and delipidated (**D**) hSA in complex with PFOA (10-fold excess) shown in **Figure 3.14**.*

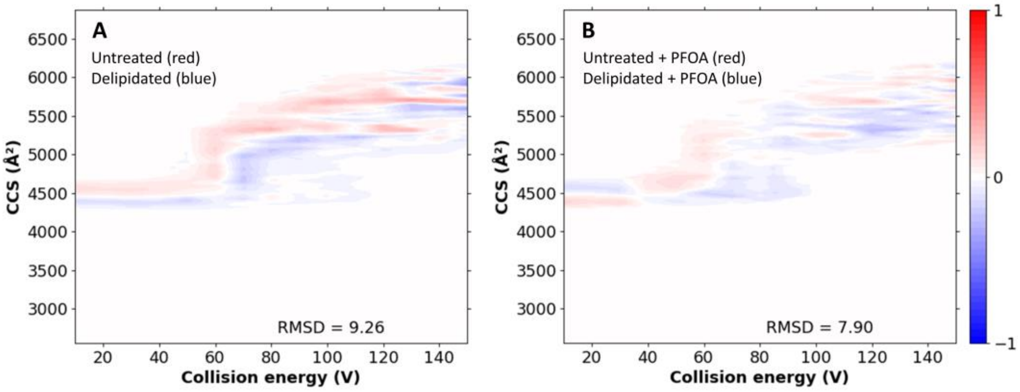

Figure 3.16. *RMSD values and CIU difference plots, generated with CIUSuite, for comparison of the CIU data shown in **Figure 3.14**. The red/blue color code indicates the intensity differences between the CIU plots.*

*Comparisons are made between untreated and dhSA (**A**) untreated hSA in complex with PFOA and delipidated hSA in complex with PFOA (**B**).*

Throughout all conformational transitions and up to the highest energy applied (**Figure 3.17**), PFOA remains bound to hSA (both untreated and delipidated) which illustrates that the strength of ligand binding is comparable to the protein's intramolecular interactions (i.e., conformational stability). This indicates that the binding site for PFOA is not meaningfully affected by the initial unfolding, and implies that the PFOA is most likely buried in the structure of domain I or III[63], rather than binding peripherally to the surface. Since our experimental data shows that the transition corresponding to the partial unfolding of domain III is absent for the hSA-PFOA complexes (**Figure 3.14 B** and **D**), it is clear that the binding of PFOA influences the stability of domain III. This further implies that PFOA is most likely bound in domain III rather than in domain I for both the untreated and delipidated hSA.

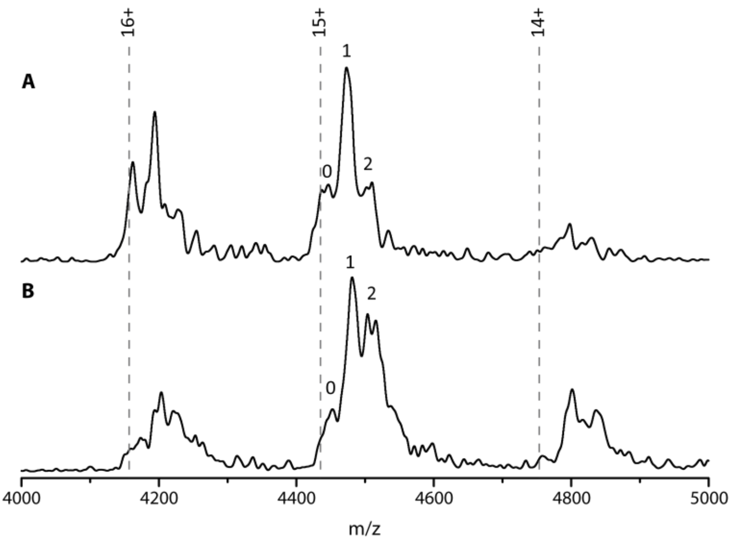

Figure 3.17. *MS spectra of untreated (**A**) and delipidated (**B**) hSA in complex with PFOA at a 1:10 protein:ligand ratio recorded at 150 V trap collision energy on the Synapt G2 instrument. The dashed lines indicate the theoretical m/z-values of hSA.*

This method provides a useful preliminary control to assess the applicability of a protein as bioreceptor under different working conditions. Since no differences in the unfolding paths and stabilities have been observed, our study supports the possibility to use dhSA as a bioreceptor in different sensing platforms.

3.3.4 Extending the study to short-chain PFAS

We are currently applying our multi-analytical approach to the screening of short-chain PFAS of interest for toxicological and environmental studies, such as HFPO-DA and

C6O4 [65–67]. The preliminary results of the ITC analyses showed lower affinity constants for both compounds (in the µM or even mM range) with a stoichiometry of 1:2 dhSA:HFPO-DA/C6O4. The titration curves of HFPO-DA were fitted with a "*sequential binding*" model suggesting that the binding of these fluorinated compounds strongly contributes to compact and stabilise dhSA. So far, the structural characterisation was possible only for dhSA:HFPO-DA complex in presence of mystic acid, while with C6O4 no crystals were obtained. Once again, the results of the crystallographic study were in good agreement with the ones gathered with the ITC study (characterisation in solution): only two HFPO-DA molecules were identified in the contiguous pockets FA3-FA4 (see **Figure 3.1**). The preliminary data show that HFPO-DA binds in FA4, as PFOA, but with a different orientation. Being these results preliminary, no finalise data elaboration will be shown in this chapter. However, the considerations reported so far can help us understanding how the changes in PFAS structure can influence the protein binding mechanism.

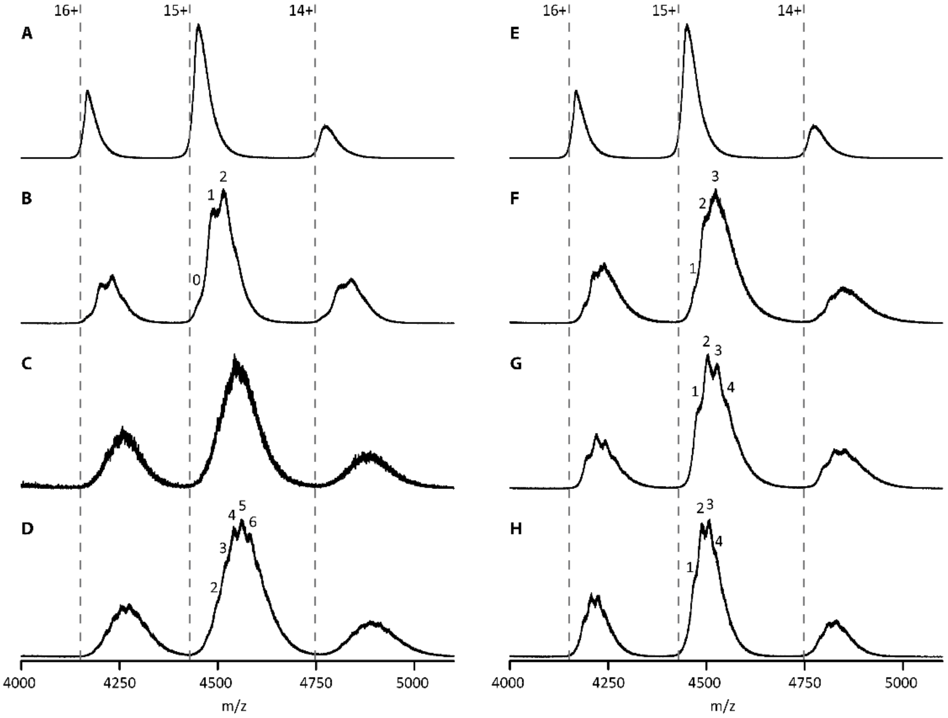

Figure 3.18. *Native MS spectra of dhSA (**A** and **E**). Multiple short chain PFAS were added at a 1:10 protein:target ratio (unless specified otherwise): PFOA (**B**), HFPO-DA in a 1:10 (**C**) and 1:20 (**D**) ratio, C6O4 (**F**), PFHXS (**G**) and PFPA (**H**). The dashed lines indicate the theoretical m/z-values of dhSA.*

In the study of short-chain PFAS binding, also native MS was involved aiming to understand the limit of this technique in this field of studies.

Figure 3.18 report a complete overview of the preliminary MS data obtained for different short-chain PFAS: from HFPO-DA and C6O4 down to PFPA (more details in

Section 3.2.1). With all compounds tested it was possible to observe the formation of complexes differing in stoichiometries proving the potential of native MS even for studying short-PFAS albumin interactions. For comparison dhSA and dhSA:PFOA spectra were reported (**Figure 3.18 A**,**B**,**E**). Interestingly, with a 1:10 dhSA:HFPO-DA ratio it was not possible to observe the complex formation. By adding a doubled ratio, a 1:20, it was possible to observe a complex with a stoichiometry of 1:6 (**Figure 3.18 C-D**). This data might suggest that to dhSA:HFPO-DA complexes are formed when HFPO-DA is in large excess. We can justify this observation by considering the higher water solubility of HFPO-DA compared to PFOA. Further analyses will be required to fully understand the correlation of these data with the binding mechanism of these PFAS. For instance, C6O4 did not show the same behaviour of HFPO-DA, complexes with a 1:3 stoichiometry were observed with a dhSA:C6O4 ratio of 1:10 (**Figure 3.18 F**). In this screening, also PFHxS and PFPA, which will further studied in Chapter 8, were included aiming to probe the potential of native MS (**Figure 3.18 G**,**H**). Surprisingly, even dhSA complexes with PFPA (a C_4 PFAS) were observed.

3.4. Conclusion

Untreated and delipidated hSA in complex with PFOA were characterised using a multi-analytical approach based on: ITC, X-rays crystallography and native MS. The *in solution* binding studies showed a 4:1 PFOA-dhSA stoichiometry and revealed the presence of one high and three low affinity binding sites. The binding was observed to be an exothermic process mainly driven by van der Waals interactions, hydrogen bonds and electrostatic interactions, the gain in entropy is the result of hydrophobic interactions that are stronger than ones with their hydrocarbon analogues. Competition experiments with known dhSA-binding drugs identified the FA4 pocket in sub-domain IIIA as the high affinity binding site for PFOA. Consistent with these evidences, structural analysis of the different PFOA-binding sites revealed that PFOA1 located in FA4 pocket forms a larger number of inter-molecular interactions, if compared to other sites. Indeed, the crystal structure revealed four PFOA binding sites, namely FA4 (Sudlow binding site I), FA6, FA7 (Sudlow binding site II) and crevice.

The protein complex overlaps well with that of other albumin-FAs ones proving that the binding mode of the PFOA is similar to those of medium-chain FAs. It involves direct or water-mediated interactions of the carboxylate head-groups to nearby basic or polar residues, while the lipophilic tails are accommodated within the hydrophobic cavities.

FA4 was found to be the high affinity binding site, while low binding affinities PFOA were observed in FA6, FA7 and crevice site. This behaviour was explained considering that all these pockets lack positive and polar amino acid side chains necessary for the anchoring of the carboxylic group of PFOA. The structural analysis was further extended to the comparison of PFOA and PFOS-albumin complexes, showing the importance and the interest of confronting.

Native MS revealed the higher PFOA binding capacity of dhSA in respect to the untreated hSA. Removal of fatty acids from the hydrophobic pockets facilitates binding of PFOA to the cavities. CIU experiments showed that fatty acid removal did not affect the conformational stability of the protein or the complex itself. PFOA appears to bind tightly to hSA-PFOA as the complex is retained even at high collision energies. This evidence correlates well with protein stability and implies that PFOA is buried in the protein structure. The examples of this chapter and **Chapter 2** illustrate how native MS can contribute to the screening and characterisation of possible bioreceptors. Although many challenges still remain, our approach can play an important role in the transposing toxicological findings in bioreceptor design. One of the major challenges will be the screening of short-chain PFAS which will possibly require a more extensive sample preparation and multiple desalting steps to enhance the peak separation in native MS. Future research efforts should be oriented toward testing novel proteins and assessing binding affinity and stoichiometry using different molar ratios. To address these challenges in the last part of these study we summarised the preliminary results obtained from short-chain PFAS-albumin complexes analysis. These latter suggest the importance of performing extensive screening studies to fully understand the correlation between PFAS structure and the PFAS:albumin complex formed. These findings will further contribute to study PFAS toxicity in humans.

In conclusion, the results described in this chapter confirmed that dhSA has all the characteristics required for being applied as bioreceptor for PFOA sensing. In case of need the selectivity of this protein-based bioreceptor can be enhanced by protein engineering: selecting only the domain hosting the high-affinity binding site (FA4) or improving the affinity of binding sites for the ligand introducing specific amino acids. In the following **Chapters 3-5**, dhSA will be applied as biorecognition layer for PFOA within different sensing strategies.

Acknowledgments and Collaborations

Thanks to all the colleagues directly or indirectly involved in this work that took almost two years to be finalised in all its parts! I am grateful to Prof. Alessandro Angelini who first suggested focusing on albumin and followed all the steps of this path (its challenges, changes and discussions) and to Prof. Laura Cendron for the crystallographic and ITC study. This work would not have been possible without the "magic touch" of Stefano Liberi. Thank you, Stefano, for all we shared (delipidation protocol included!). My gratitude also to Elise Daems, promising researcher and great friend, that taught me all I know about native MS and accepted this challenge (thanks Elise also for the beautiful figures you made of the CIU plots!), and to Prof. Frank Sobott who even "passed by" here in Venice, to discuss our results! In this multi-analytical study taught we faced all the challenges of combining different methods, developing new analytical protocols and confront with the previous literature but, most importantly, I learn the importance of trust in teamworking. Our findings were shared also through a divulgation project ***Inside Biomolecules with XRmol***, *in collaboration with Prof. Marta Simeoni and Sara Corrazza; [https://www.youtube.com/watch?v=yMnZBPS_lfM&t=15s].*

Extract from ***cfNEWS*** *(28/04/2021): What would happen if we could see how PFAS interact with our blood proteins on the screen of our smartphone? What if we could easily understand how PFAS accumulate in our bodies? These are the questions which sparked the idea of using a web application,* ***XRmol***, *to divulge the results of the studies (…) regarding the* ***interaction between PFAS and albumin***, *an important plasma protein which is involved in the transportation of hormones and medication and that has been shown to be the means by which these* ***pollutants enter the human body and accumulate in it***. *"We believe that science awareness should not amount to simplification – we want to create tools that enable the visualisation of the biomolecules we study, so that others can understand their complexity. This video is just the first example of what can be achieved", say* ***Sara Corazza*** *and* ***Giulia Moro***, *who created the YouTube channel* ***Inside Biomolecules with XRmol*** *and the video that shows the interaction between PFOA and albumin.*

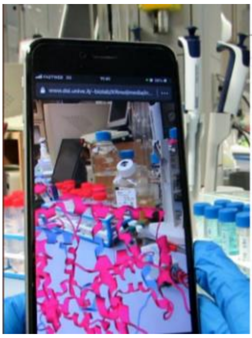

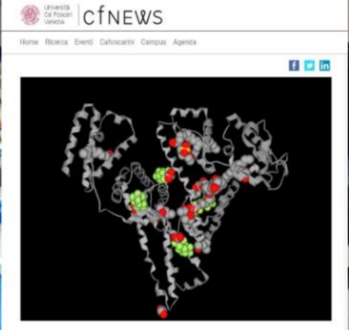

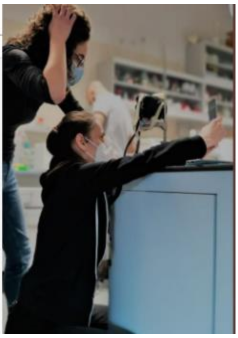

References

[1] P.-I.D. Lin, A. Cardenas, R. Hauser, D.R. Gold, K.P. Kleinman, M.-F. Hivert, A.F. Fleisch, A.M. Calafat, T.F. Webster, E.S. Horton, E. Oken, Per- and polyfluoroalkyl substances and blood lipid levels in pre-diabetic adults—longitudinal analysis of the diabetes prevention program outcomes study, Environ. Int. 129 (2019) 343–353. https://doi.org/https://doi.org/10.1016/j.envint.2019.05.027.

[2] F. Ferrari, M. Manera, S. Mongodi, P. Esposito, C. Ronco, The Role of Perfluorinated Compound Pollution in the Development of Acute and Chronic Kidney Disease, in: Contrib. Nephrol., 2021: pp. 285–296. https://doi.org/10.1159/000517711.

[3] H.B. Klevens, E. Ellenbogens, Protein-fluoroacid interaction. Bovine serum albumin perfluoro-octanoic acid, Discuss. Faraday Soc. 18 (1954) 277–288.

[4] E. Eric, M.P. H., Heat Denaturation of Serum Albumin in Presence of Perfluorooctanoic Acid, Science (80-.). 124 (1956) 266–267. https://doi.org/10.1126/science.124.3215.266.

[5] G.L. Nordby, M.L. Luck, Perfluorooctanoic acid interactions with Human Serum Albumin, J. Biol. Chem. 399 (1956).

[6] W.S. Guy, D.R. Taves, W.S. Brey, Organic Fluorocompounds in Human Plasma: Prevalence and Characterization, in: Biochem. Involv. Carbon-Fluorine Bond., AMERICAN CHEMICAL SOCIETY, 1976: pp. 117-134 SE–7. https://doi.org/doi:10.1021/bk-1976-0028.ch007.

[7] X. Liu, M. Fang, F. Xu, D. Chen, Characterization of the binding of per- and poly-fluorinated substances to proteins: A methodological review, TrAC - Trends Anal. Chem. 116 (2019) 177–185. https://doi.org/10.1016/j.trac.2019.05.017.

[8] Q. Chi, Z. Li, J. Huang, J. Ma, X. Wang, Interactions of perfluorooctanoic acid and perfluorooctanesulfonic acid with serum albumins by native mass spectrometry, fluorescence and molecular docking, Chemosphere. 198 (2018) 442–449. https://doi.org/10.1016/j.chemosphere.2018.01.152.

[9] M. Salvalaglio, I. Muscionico, C. Cavallotti, Determination of energies and sites of binding of PFOA and PFOS to human serum albumin, J. Phys. Chem. B. 114 (2010) 14860–14874. https://doi.org/10.1021/jp106584b.

[10] L.L. Wu, H.W. Gao, N.Y. Gao, F.F. Chen, L. Chen, Interaction of perfluorooctanoic acid with human serum albumin, BMC Struct. Biol. 9 (2009) 5–11. https://doi.org/10.1186/1472-6807-9-31.

[11] X. Han, T.A. Snow, R.A. Kemper, G.W. Jepson, Binding of perfluorooctanoic acid to rat and human plasma proteins, Chem. Res. Toxicol. 16 (2003) 775–781. https://doi.org/10.1021/tx034005w.

[12] M.A. El Hassan, E.A. Azzazy, R. Christenson, All About Albumin: Biochemistry, Genetics, and Medical Applications. Theodore Peters, Jr. San Diego, CA: Academic Press, 1996, 432 pp, \$85.00. ISBN 0-12-552110-3, Clin. Chem. 43 (1997).

[13] S. Choi, E.Y. Choi, D.J. Kim, J.H. Kim, T.S. Kim, S.W. Oh, A rapid, simple measurement of human albumin in whole blood using a fluorescence immunoassay (I), Clin. Chim. Acta. 339 (2004) 147–156. https://doi.org/https://doi.org/10.1016/j.cccn.2003.10.002.

[14] D. Sleep, J. Cameron, L.R. Evans, Albumin as a versatile platform for drug half-life extension, Biochim. Biophys. Acta - Gen. Subj. 1830 (2013) 5526–5534. https://doi.org/https://doi.org/10.1016/j.bbagen.2013.04.023.

[15] G. Rabbani, S.N. Ahn, Structure, enzymatic activities, glycation and therapeutic potential of human serum albumin: A natural cargo, Int. J. Biol. Macromol. 123 (2019) 979–990. https://doi.org/https://doi.org/10.1016/j.ijbiomac.2018.11.053.

[16] I. Petitpas, T. Grüne, A.A. Bhattacharya, S. Curry, Crystal structures of human serum albumin complexed with monounsaturated and polyunsaturated fatty acids, J. Mol. Biol. 314 (2001) 955–960. https://doi.org/10.1006/jmbi.2000.5208.

[17] S. Curry, P. Brick, N.P. Franks, Fatty acid binding to human serum albumin: new insights from crystallographic studies, Biochim. Biophys. Acta. 1441 (1999) 131–140. https://doi.org/10.1016/S1388-1981(99)00148-1.

[18] S. Curry, Beyond expansion: structural studies on the transport roles of human serum albumin., Vox Sang. 83 Suppl 1 (2002) 315–319. https://doi.org/10.1111/j.1423-0410.2002.tb05326.x.

[19] S. Curry, H. Mandelkow, P. Brick, N. Franks, Crystal structure of human serum albumin complexed with fatty acid reveals an asymmetric distribution of binding sites, Nat. Struct. Biol. 5 (1998) 827–835.

[20] A.A. Bhattacharya, T. Grüne, S. Curry, Crystallographic analysis reveals common modes of binding of medium and long-chain fatty acids to human serum albumin, J. Mol. Biol. 303 (2000) 721–732. https://doi.org/10.1006/jmbi.2000.4158.

[21] J.D. Ashbrook, A.A. Spector, E.C. Santos, J.E. Fletcher, Long chain fatty acid binding to human plasma albumin, J. Biol. Chem. 250 (1975) 2333–2338. https://doi.org/10.1016/s0021-9258(19)41721-3.

[22] J.D. Ashbrook, A.A. Spectro, J.E. Fletcher, Medium chain fatty acid binding to human plasma albumin., J. Biol. Chem. 247 (1972) 7038–7042. https://doi.org/10.1016/s0021-9258(19)44690-5.

[23] G. V Richieri, A. Anel, A.M. Kleinfeld, Interactions of long-chain fatty acids and albumin: Determination of free fatty acid levels using the fluorescent probe ADIFAB, Biochemistry. 32 (1993) 7574–7580. https://doi.org/10.1021/bi00080a032.

[24] R.F. Chen, Removal of fatty acids from serum albumin by charcoal treatment., J. Biol. Chem. 242 (1967) 173–181.

[25] L. Potterton, J. Agirre, C. Ballard, K. Cowtan, E. Dodson, P.R. Evans, H.T. Jenkins, R. Keegan, E. Krissinel, K. Stevenson, A. Lebedev, S.J. McNicholas, R.A. Nicholls, M. Noble, N.S. Pannu, C. Roth, G. Sheldrick, P. Skubak, J. Turkenburg, V. Uski, F. von Delft, D. Waterman, K. Wilson, M. Winn, M. Wojdyr, CCP4i2: the new graphical user interface to the CCP4 program suite, Acta Crystallogr. Sect. D. 74 (2018) 68–84. https://doi.org/10.1107/S2059798317016035.

[26] A.J. McCoy, R.W. Grosse-Kunstleve, P.D. Adams, M.D. Winn, L.C. Storoni, R.J. Read, Phaser crystallographic software, J. Appl. Crystallogr. 40 (2007) 658–674. https://doi.org/10.1107/S0021889807021206.

[27] P. Emsley, K. Cowtan, COOT: model-building tools for molecular graphics, Acta Crystallogr. Sect. D. 60 (2004) 2126–2132. https://doi.org/10.1107/S0907444904019158.

[28] E. Krissinel, K. Henrick, Inference of Macromolecular Assemblies from Crystalline State, J. Mol. Biol. 372 (2007) 774–797. https://doi.org/https://doi.org/10.1016/j.jmb.2007.05.022.

[29] R.A. Laskowski, J.D. Watson, J.M. Thornton, ProFunc: a server for predicting protein function from 3D structure, Nucleic Acids Res. 33 (2005) W89–W93. https://doi.org/10.1093/nar/gki414.

[30] A.C. Wallace, R.A. Laskowski, J.M. Thornton, LIGPLOT: a program to generate schematic diagrams of protein-ligand interactions, Protein Eng. Des. Sel. 8 (1995) 127–134. https://doi.org/10.1093/protein/8.2.127.

[31] G. Janson, C. Zhang, M.G. Prado, A. Paiardini, PyMod 2.0: improvements in protein sequence-structure analysis and homology modeling within PyMOL, Bioinformatics. 33 (2017) 444–446. https://doi.org/10.1093/bioinformatics/btw638.

[32] M.N. Nguyen, K.P. Tan, M.S. Madhusudhan, CLICK—topology-independent comparison of biomolecular 3D structures, Nucleic Acids Res. 39 (2011) W24–W28. https://doi.org/10.1093/nar/gkr393.

[33] M. Göth, V. Badock, J. Weiske, K. Pagel, B. Kuropka, Critical evaluation of native electrospray ionization mass spectrometry for fragment-based screening, ChemMedChem. 12 (2017) 1201–1211. https://doi.org/10.1002/cmdc.201700177.

[34] V. Gabelica, A.A. Shvartsburg, C. Afonso, P. Barran, J.L.P. Benesch, C. Bleiholder, M.T. Bowers, A. Bilbao, M.F. Bush, J.L. Campbell, I.D.G. Campuzano, T. Causon, B.H. Clowers, C.S. Creaser, E. De Pauw, J. Far, F. Fernandez-Lima, J.C. Fjeldsted, K. Giles, M. Groessl, C.J. Hogan, S. Hann, H.I. Kim, R.T. Kurulugama, J.C. May, J.A. McLean, K. Pagel, K. Richardson, M.E. Ridgeway, F. Rosu, F. Sobott, K. Thalassinos, S.J. Valentine, T. Wyttenbach, Recommendations for reporting ion mobility mass spectrometry measurements, Mass Spectrom. Rev. 38 (2019) 291–320. https://doi.org/10.1002/mas.21585.

[35] M.F. Bush, Z. Hall, K. Giles, J. Hoyes, C. V. Robinson, B.T. Ruotolo, Collision cross sections of proteins and their complexes: A calibration framework and database for gas-phase structural biology, Anal. Chem. 82 (2010) 9557–9565. https://doi.org/10.1021/ac1022953.

[36] K. Thalassinos, M. Grabenauer, S.E. Slade, G.R. Hilton, M.T. Bowers, J.H. Scrivens, Characterization of phosphorylated peptides using traveling wave-based and drift cell ion mobility mass spectrometry, Anal. Chem. 81 (2009) 248–254. https://doi.org/10.1021/ac801916h.

[37] D.A. Polasky, S.M. Dixit, S.M. Fantin, B.T. Ruotolo, CIUSuite 2: Next-generation software for the analysis of gas-phase protein unfolding data, Anal. Chem. 91 (2019) 3147–3155. https://doi.org/10.1021/acs.analchem.8b05762.

[38] Z. Luo, X. Shi, Q. Hu, B. Zhao, M. Huang, Structural evidence of perfluorooctane sulfonate transport by human serum albumin, Chem. Res. Toxicol. 25 (2012) 990–992. https://doi.org/10.1021/tx300112p.

[39] Q. Chi, Z. Li, J. Huang, J. Ma, X. Wang, Interactions of perfluorooctanoic acid and perfluorooctanesulfonic acid with serum albumins by native mass spectrometry, fluorescence and molecular docking, Chemosphere. 198 (2018) 442–449. https://doi.org/10.1016/j.chemosphere.2018.01.152.

[40] J. Ghuman, P.A. Zunszain, I. Petitpas, A.A. Bhattacharya, M. Otagiri, S. Curry, Structural basis of the drug-binding specificity of human serum albumin, J. Mol. Biol. 353 (2005) 38–52. https://doi.org/10.1016/j.jmb.2005.07.075.

[41] C. Ràfols, S. Amézqueta, E. Fuguet, E. Bosch, Molecular interactions between warfarin and human (HSA) or bovine (BSA) serum albumin evaluated by isothermal titration calorimetry (ITC), fluorescence spectrometry (FS) and frontal analysis capillary electrophoresis (FA/CE), J. Pharm. Biomed. Anal. 150 (2018) 452–459. https://doi.org/https://doi.org/10.1016/j.jpba.2017.12.008.

[42] C. Ràfols, S. Zarza, E. Bosch, Molecular interactions between some non-steroidal anti-inflammatory drugs (NSAID's) and bovine (BSA) or human (HSA) serum albumin estimated by means of isothermal titration calorimetry (ITC) and frontal analysis capillary electrophoresis (FA/CE), Talanta. 130 (2014) 241–250. https://doi.org/https://doi.org/10.1016/j.talanta.2014.06.060.

[43] N. Zaidi, R.H. Khan, A biophysical insight into structural and functional state of human serum albumin in uremia mimic milieu, Int. J. Biol. Macromol. 131 (2019) 697–705. https://doi.org/https://doi.org/10.1016/j.ijbiomac.2019.03.123.

[44] S. Curry, Lessons from the crystallographic analysis of small molecule binding to human serum albumin, Drug Metab. Pharmacokinet. 24 (2009) 342–357. https://doi.org/10.2133/dmpk.24.342.

[45] S. Curry, H. Mandelkow, P. Brick, N. Franks, Crystal structure of human serum albumin complexed with fatty acid reveals an asymmetric distribution of binding sites, Nat. Struct. Biol. 5 (1998) 827–835. https://doi.org/10.1038/1869.

[46] A.A. Bhattacharya, T. Grüne, S. Curry, Crystallographic analysis reveals common modes of binding of medium and long-chain fatty acids to human serum albumin, J. Mol. Biol. 303 (2000) 721–732. https://doi.org/10.1006/jmbi.2000.4158.

[47] I. Petitpas, A.A. Bhattacharya, S. Twine, M. East, S. Curry, Crystal structure analysis of warfarin binding to human serum albumin. Anatomy of drug site I, J. Biol. Chem. 276 (2001) 22804–22809. https://doi.org/10.1074/jbc.M100575200.

[48] I.N. Bojesen, Direct determination of unbound lipophilic ligands in aqueous solutions, Biol. Proced. Online. 6 (2004) 226–234. https://doi.org/10.1251/bpo93.

[49] V.H. Dalvi, P.J. Rossky, Molecular origins of fluorocarbon hydrophobicity, Proc. Natl. Acad. Sci. 107 (2010) 13603 LP – 13607. https://doi.org/10.1073/pnas.0915169107.

[50] Y. Liu, Z. Cao, W. Zong, R. Liu, Interaction rule and mechanism of perfluoroalkyl sulfonates containing different carbon chains with human serum albumin, RSC Adv. 7 (2017) 24781–24788. https://doi.org/10.1039/c7ra02963b.

[51] X. Zhang, L. Chen, X.-C. Fei, Y.-S. Ma, H.-W. Gao, Binding of PFOS to serum albumin and DNA: insight into the molecular toxicity of perfluorochemicals, BMC Mol. Biol. 10 (2009) 16. https://doi.org/10.1186/1471-2199-10-16.

[52] B.C. Bohrer, S.I. Merenbloom, S.L. Koeniger, A.E. Hilderbrand, D.E. Clemmer, Biomolecule analysis by Ion mobility spectrometry, Annu. Rev. Anal. Chem. 1 (2008) 293–327. https://doi.org/10.1146/annurev.anchem.1.031207.113001.

[53] A. Marchand, S. Livet, F. Rosu, V. Gabelica, Drift tube ion mobility: How to reconstruct collision cross section distributions from arrival time distributions?, Anal. Chem. 89 (2017) 12674–12681. https://doi.org/10.1021/acs.analchem.7b01736.

[54] B.T. Ruotolo, J.L.P. Benesch, A.M. Sandercock, S.J. Hyung, C. V. Robinson, Ion mobility-mass spectrometry analysis of large protein complexes, Nat. Protoc. 3 (2008) 1139–1152. https://doi.org/10.1038/nprot.2008.78.

[55] S.J. Hyung, C. V. Robinson, B.T. Ruotolo, Gas-phase unfolding and disassembly reveals stability differences in ligand-bound multiprotein complexes, Chem. Biol. 16 (2009) 382–390. https://doi.org/10.1016/j.chembiol.2009.02.008.

[56] S.M. Dixit, D.A. Polasky, B.T. Ruotolo, Collision induced unfolding of isolated proteins in the gas

phase: past, present, and future, Curr. Opin. Chem. Biol. 42 (2018) 93–100. https://doi.org/10.1016/j.cbpa.2017.11.010.

[57] S.M. Dixit, D.A. Polasky, B.T. Ruotolo, Collision induced unfolding of isolated proteins in the gas phase: past, present, and future, Curr. Opin. Chem. Biol. 42 (2018) 93–100. https://doi.org/10.1016/j.cbpa.2017.11.010.

[58] A. Dugaiczyk, S.W. Law, H.B. Brewer, Nucleotide sequence and the encoded amino acids of human serum albumin mRNA, Proc. Natl. Acad. Sci. U. S. A. 79 (1982) 71–75. https://doi.org/10.1073/pnas.81.1.66.

[59] S. Curry, P. Brick, N.P. Franks, Fatty acid binding to human serum albumin: new insights from crystallographic studies, Biochim. Biophys. Acta - Mol. Cell Biol. Lipids. 1441 (1999) 131–140. https://doi.org/10.1016/S1388-1981(99)00148-1.

[60] S. Beesoon, J.W. Martin, Isomer-specific binding affinity of perfluorooctanesulfonate (PFOS) and perfluorooctanoate (PFOA) to serum proteins, Environ. Sci. Technol. 49 (2015) 5722–5731. https://doi.org/10.1021/es505399w.

[61] H.N. Bischel, L.A. MacManus-Spencer, R.G. Luthy, Noncovalent interactions of long-chain perfluoroalkyl acids with serum albumin, Environ. Sci. Technol. 44 (2010) 5263–5269. https://doi.org/10.1021/es101334s.

[62] X. Han, T.A. Snow, R.A. Kemper, G.W. Jepson, Binding of perfluorooctanoic acid to rat and human plasma proteins, Chem. Res. Toxicol. 16 (2003) 775–781. https://doi.org/10.1021/tx034005w.

[63] J.D. Eschweiler, R.M. Martini, B.T. Ruotolo, Chemical probes and engineered constructs reveal a detailed unfolding mechanism for a solvent-free multidomain protein, J. Am. Chem. Soc. 139 (2017) 534–540. https://doi.org/10.1021/jacs.6b11678.

[64] G. Li, K. DeLaney, L. Li, Molecular basis for chirality-regulated Aβ self-assembly and receptor recognition revealed by ion mobility-mass spectrometry, Nat. Commun. 10 (2019) 5038. https://doi.org/10.1038/s41467-019-12346-8.

[65] X. Bai, Y. Son, Perfluoroalkyl substances (PFAS) in surface water and sediments from two urban watersheds in Nevada, USA, Sci. Total Environ. 751 (2021) 141622. https://doi.org/https://doi.org/10.1016/j.scitotenv.2020.141622.

[66] M.W. Glasscott, K.J. Vannoy, R. Kazemi, M.D. Verber, J.E. Dick, μ-MIP: Molecularly Imprinted Polymer-Modified Microelectrodes for the Ultrasensitive Quantification of GenX (HFPO-DA) in River Water, Environ. Sci. Technol. Lett. 7 (2020) 489–495. https://doi.org/10.1021/acs.estlett.0c00341.

[67] P. Minuz, L. De Toni, S. Dall'Acqua, A. Di Nisio, I. Sabovic, M. Castelli, A. Meneguzzi, C. Foresta, Interference of C6O4 on platelet aggregation pathways: Cues on the new-generation of perfluoro-alkyl substance, Environ. Int. 154 (2021) 106584. https://doi.org/https://doi.org/10.1016/j.envint.2021.106584.

[68] R.A. Laskowski, M.B. Swindells, LigPlot+: Multiple ligand-protein interaction diagrams for drug discovery, J. Chem. Inf. Model. 51 (2011) 2778–2786. https://doi.org/10.1021/ci200227u.

3.1 Annex A

Table A3.1. *Thermodynamic and stoichiometric data for the binding of hSA to PFOA at different temperatures. K_D, equilibrium dissociation constant; ΔH, enthalpy change; ΔG, Gibbs free energy; ΔS, entropy change; T, temperature; n, stoichiometry. Mean values and standard errors have been obtained from the fit of a single titration curve.*

	Temperature					
	12 °C	**19 °C**	**22 °C**	**25 °C**	**30 °C**	**37 °C**
high-affinity sites						
K_{D1} (M)x10^{-7}	7.35 ± 1.18	5.74 ± 0.51	6.96 ± 0.37	5.13 ± 1.17	2.30 ± 1.60	3.94 ± 1.73
ΔH_1 (kJ/mol)	-18.5 ± 0.5	-18.8 ± 0.9	-21.7 ± 2.4	-19.3 ± 0.6	-19.1 ± 0.4	-16.5 ± 1.9
ΔG_1 (kJ/mol)	-33.5	-34.9	-34.8	-35.9	-38.6	-38.1
$-T\Delta S_1$ (kJ/mol)	-15.0	-16.1	-13.1	-16.7	-19.5	-21.6
n_1 (sites)	0.72 ± 0.02	0.71 ± 0.02	0.67 ± 0.06	0.70 ± 0.01	0.63 ± 0.02	0.72 ± 0.03
low-affinity sites						
K_{D2}(M)x 10^{-5}	4.78 ± 0.20	3.33 ± 1.13	4.13 ± 1.80	3.33 ± 1.30	2.70 ± 1.50	1.28 ± 0.30
ΔH_2 (kJ/mol)	-6.35 ± 0.22	-3.44 ± 0.42	-3.34 ± 0.49	-2.15 ± 0.30	-1.01 ± 0.27	-2.26 ± 0.75
ΔG_2 (kJ/mol)	-23.6	-25.1	-24.8	-25.6	-26.5	-29.1
$-T\Delta S_2$ (kJ/mol)	-17.3	-21.6	-21.5	-23.4	-25.5	-31.3
n_2 (sites)	3.29 ± 0.09	3.38 ± 0.09	3.54 ± 0.11	3.58 ± 0.12	3.03 ± 0.59	1.64 ± 0.30
fit model	two set of sites					

Table A3.2. *Thermodynamic and stoichiometric data for the binding of hSA to PFOA and four known hSA-binding drugs: ibuprofen, 3-carboxy-4-methyl-5-propyl-2-furanpropionic acid (CMPF), warfarin and iodipamide. K_D, equilibrium dissociation constant; ΔH, enthalpy change; ΔG, Gibbs free energy; ΔS, entropy change; T, temperature; n, stoichiometry. * Measures were performed in buffer including 2.5% v/v DMSO. Mean values and standard errors of PFOA are the results of the fits of at least three independent experiments. Mean values and standard errors of other ligands have been obtained from the fit of a single titration curve.*

	Ligand dhSA					
	PFOA	**PFOA***	**ibuprofen**	**CMPF**	**warfarin***	**iodipamide***
high-affinity sites						
K_{D1} (M)	(3.57±1.46) 10^{-7}	(5.17±3.90) 10^{-6}	(1.22±0.25) 10^{-5}	(1.21±0.56) 10^{-4}	(1.78 ±0.09) 10^{-5}	(6.66 ± 1.1) 10^{-5}
ΔH_1 (kJ/mol)	-18.2 ± 1.1	-22.1 ± 1.3	-24.0 ± 1.6	-21.1 ± 3.7	-53.7 ± 1.0	-45.7 ± 3.9
ΔG_1 (kJ/mol)	-37.1 ± 1.1	-30.2	-28.1	-22.4	-27.1	-23.9
$-T\Delta S_1$ (kJ/mol)	-18.9 ± 0.7	-8.12	-4.12	-1.28	26.6	-69.5
n_1 (sites)	0.74 ± 0.07	0.87 ± 0.02	0.69 ±0.03	1.37 ± 0.14	0.76 ± 0.01	1.51 ± 0.07
low-affinity sites						
K_{D2} (M)	(2.71±1.40) 10^{-5}	(1.53±0.39) 10^{-3}	–	(1.70±0.80) 10^{-7}	–	–
ΔH_2 (kJ/mol)	-1.90 ± 0.37	-3.14 ± 1.30	–	-33.2 ± 0.8	–	–

ΔG_2 (kJ/mol)	-26.4 ± 1.3	-16.1	–	-38.7	–	–
$-T\Delta S_2$ (kJ/mol)	-24.5 ± 1.6	-13.0	–	-5.49	–	–
n_2 (sites)	2.88 ± 0.36	5.24 ± 1.76	–	0.75 ± 0.12	–	–
fit model	one set of sites	two set of sites	one set of sites	two set of sites	one set of sites	one set of sites

Table A3.3. *Thermodynamic and stoichiometric data for the competitive binding of hSA to PFOA in the presence of ibuprofen, CMPF, warfarin and iodipamide.* K_D*, equilibrium dissociation constant; ΔH, enthalpy change; ΔG, Gibbs free energy; ΔS, and entropy change; T, temperature; n, stoichiometry. * Measures were performed in buffer including 2.5% v/v DMSO. Mean values and standard errors have been obtained from the fit of a single titration curve.*

	Ligand dhSA-PFOA			
	ibuprofen	**CMPF**	**warfarin***	**iodipamide***
	high-affinity sites			
K_{D1} (M)	$(2.87 \pm 5.78)\ 10^{-8}$	$(8.37 \pm 1.57)\ 10^{-7}$	$(1.33 \pm 1.42)\ 10^{-6}$	$(4.19 \pm 6.96)\ 10^{-8}$
ΔH_1 (kJ/mol)	-1.95 ± 0.13	0.27 ± 0.65	-24.0 ± 1.4	-24.9 ± 3.2
ΔG_1 (kJ/mol)	-43.1	-34.8	-33.6	-42.2
$-T\Delta S_1$ (kJ/mol)	-41.1	-35.0	-9.59	-17.3
n_1 (sites)	0.79 ± 0.07	1.16 ± 0.13	0.87 ± 0.02	0.93 ± 0.07
	low-affinity sites			
K_{D2} (M)	$(5.80 \pm 1.13)\ 10^{-6}$	$(1.10 \pm 0.10)\ 10^{-5}$	$(2.27 \pm 1.60)\ 10^{-4}$	$(6.45 \pm 1.96)\ 10^{-5}$
ΔH_2 (kJ/mol)	-1.48 ± 0.08	-3.44 ± 0.18	-8.76 ± 0.42	-7.82 ± 0.55
ΔG_2 (kJ/mol)	-29.9	-28.4	-20.8	-23.9
$-T\Delta S_2$ (kJ/mol)	-28.4	-24.9	-12.1	-16.1
n_2 (sites)	5.04 ± 0.16	5.14 ± 0.17	5.31 ± 0.70	6.18 ± 0.42
fit model	two set of sites	two set of sites	two set of sites	two set of sites

Table A3.4. *Inter-molecular non-polar interactions in the complexes between hSA and PFOA, Myr and Dka. Interactions distances are shorter than 4.0 Å and were defined using the web server PROFUNC[29] or LigPlot*[68].

Binding site	hSA atom / residue	atom, distance (Å)		
		PFOA	Myr	Dka
FA4 (PFOA1)	CG / Leu387	O8 (3.59)		
	CD1 / Leu387	C7 (3.26)	C3 (3.71)	
	CD1 / Leu387	O8 (3.23)		
	CD1 / Leu387	O9 (3.06)		
	CD2 / Leu387		O1 (3.63)	
	NH1 / Arg410		C2 (3.82)	
	CB / Tyr411	F25 (3.46)		C8 (3.62)
	CG / Tyr411	F20 (3.32)	C11 (3.66)	C8 (3.59)
	CG / Tyr411	F25 (3.50)		
	CD1 / Tyr411	F18 (3.19)	C10 (3.81)	C6 (3.74)
	CD1 / Tyr411	F20 (3.41)	C11 (3.43)	
	CD1 / Tyr411	F25 (3.40)		
	CD2 / Tyr411	F20 (3.32)		
	CE1 / Tyr411	F12 (3.26)	O2 (3.52)	C6 (3.63)
	CE1 / Tyr411	F18 (2.85)	C9 (3.75)	O2 (3.58)
	CE1 / Tyr411	F20 (3.50)	C10 (3.82)	
	CE2 / Tyr411	F20 (3.37)		
	CZ / Tyr411	F12 (3.17)	O2 (3.82)	C6 (3.77)
	CZ / Tyr411	F18 (3.57)	C8 (3.71)	O2 (3.53)
	CZ / Tyr411	F20 (3.48)		
	OH / Tyr411	C10 (3.71)	C1 (3.74)	C1 (3.49)
	OH / Tyr411		C2 (3.39)	C2 (3.71)
	OH / Tyr411		C5 (3.78)	C4 (3.88)
	OH / Tyr411		C8 (3.53)	
	CG2 / Val415	F25 (3.84)	C14 (3.34)	C10 (3.51)
	CG2 / Val418		C14 (3.69)	
	CD2 / Leu423		C14 (3.79)	C10 (3.77)
	CG1 / Val426			C9 (3.80)
	CD1 / Leu430	F14 (3.17)		
	CD1 / Leu430	F20 (3.48)		
	CD2 / Leu430	F14 (3.88)		
	CD1 / Leu453	F6 (3.78)		
	CD2 / Leu453	F1 (3.27)		
	CD1 / Leu457		C7 (3.87)	C5 (3.84)
	CD2 / Leu457	F15 (3.28)		
	CD2 / Leu457	F21 (3.71)		
	CD2 / Leu460	F21 (3.14)	C12 (3.74)	C9 (3.70)
	CD2 / Leu460	F23 (3.44)		
	CG / Arg485	F3 (3.55)		
	CD / Arg485	F3 (3.46)		
	CD / Arg485	F6 (3.65)		
	CA / Phe488	F17 (3.59)		
	C / Phe488	F11 (3.47)		
	C / Phe488	F17 (3.72)		

	CB / Phe488	F11 (3.84)	C7 (3.75)	C5 (3.59)
	CB / Phe488	F15 (3.13)		
	CB / Phe488	F17 (2.91)		
	CG / Phe488	F15 (3.66)		C5 (3.90)
	CG / Phe488	F17 (3.24)		
	CD1 / Phe488	F17 (2.94)		
	CD1 / Phe488	F24 (3.43)		
	CE1 / Phe488	F24 (3.73)		
	CA / Ser489	O8 (3.54)		O1 (3.28)
	CA / Ser489	F11 (3.44)	O1 (3.70)	
	CB / Ser489	O8 (2.89)	O1 (3.61)	O1 (3.12)
	CB / Ser489	F11 (3.89)		
	OG / Ser489	C7 (3.55)	C3 (3.36)	C1 (3.85)
	OG / Ser489		C6 (3.84)	C3 (3.84)
	CD1 / Leu491	F24 (3.76)		
FA6 (PFOA2)	CD1 / Phe206	O8 (3.84)		O1 (3.49)
	CE1 / Phe206			O1 (3.01)
	CZ / Phe206			O1 (3.66)
	CZ / Arg209	F15 (3.75)	O1 (3.74)	
	CZ / Arg209	F21 (3.24)		
	CA / Ala210	F11 (3.69)		
	CB / Ala210	F5 (3.89)		C3 (3.87)
	CB / Ala210	F6 (3.22)		C5 (3.57)
	CB / Ala210	F11 (3.77)		
	CB / Ala213	F17 (2.85)	C3 (3.54)	C7 (3.85)
	CB / Ala213	F24 (3.13)		
	OG / Ser232		C10 (3.47)	
	OG / Ser232		C12 (3.46)	
	OG1 / Thr236		C12 (3.34)	
	O / Asp324		C5 (3.87)	
	CB / Leu327	F23 (3.52)	C2 (3.80)	
	CB / Leu327	F25 (3.84)		
	CB / Leu347	F12 (3.53)		
	CD2 / Leu347	F12 (3.76)		
	CD2 / Leu347	F17 (3.87)		
	CB / Ala350	F18 (3.52)	O2 (3.58)	
	CB / Ala350	F20 (3.74)		
	CA / Lys351	F14 (3.87)		
	CB / Lys351	F14 (3.32)		
	CG / Lys351	F14 (3.67)		
	CD / Lys351	F01 (3.58)		
	CD / Glu354	F21 (3.71)		
	CA / Ser480			C1 (3.61)
	CA / Ser480			O1 (2.92)
	CA / Ser480			O1 (3.64)
	C / Ser480			O1 (3.24)
	CB / Ser480	O9 (3.36)		C1 (3.43)

	CB / Ser480			O1 (3.28)
	CB / Ser480			O2 (2.97)
	N / Leu481			C1 (3.47)
	CA / Leu481			O1 (3.86)
	CB / Leu481	O9 (3.69)		
	CD2 / Leu481	F5 (3.84)		
	CG1 / Val482	F1 (3.85)		
FA7 (PFOA3)	CE2 / Tyr150			O2 (3.60)
	CZ / Tyr150			O2 (3.57)
	OH / Tyr150			C1 (3.53)
	OH / Tyr150			C2 (3.58)
	NZ / Lys199		C12 (3.36)	
	CZ3 / Trp214	O8 (3.72)		
	CH2 / Trp214	C7 (3.88)	C12 (3.83)	
	CH2 / Trp214	O8 (3.53)		
	CH2 / Trp214	O9 (3.53)		
	NE / Arg218		C11 (3.68)	
	NE / Arg218		C12 (3.38)	
	CG / Arg218	C4 (3.89)	C11 (3.51)	
	CG / Arg218	C7 (3.75)		
	CG / Arg218	O9 (3.42)		
	CG / Arg218	F5 (3.87)		
	CG / Arg218	F6 (3.48)		
	CG / Leu219	F5 (3.60)		
	CD2 / Leu219	F5 (3.06)		
	CD2 / Leu219	F11 (3.57)		
	CD / Arg222	F3 (3.53)		
	CD / Arg222	F6 (3.49)		
	NH1 / Arg222		C10 (3.82)	
	CZ / Arg222	F6 (3.26)		
	CD1 / Leu238	F12 (3.80)		
	CD1 / Leu238	F14 (3.44)		
	CD1 / Leu238	F18 (3.81)		
	CD1 / Leu238	F24 (3.85)		
	CD2 / Leu238	O8 (3.76)	C1 (3.55)	
	CD2 / Leu238	F12 (3.03)		
	NE2 / His242		C1 (3.71)	
	O / Ala254			C2 (3.45)
	CZ / Arg257		C2 (3.79)	O2 (3.87)
	NH1 / Arg257		C2 (3.83)	
	CB / Arg257	F23 (3.83)		O2 (3.76)
	CB / Leu260	F25 (3.34)		
	CG / Leu260	F25 (3.28)		
	CD2 / Leu260	F18 (3.38)		
	CD2 / Leu260	F25 (3.28)		
	CD1 / Ile264	F17 (3.75)		
	O / Leu283			C3 (3.72)
	CD1 / Leu284			C4 (3.67)
	CB / Ser287	F23 (3.10)		O1 (3.52)
	CB / Ser287			O2 (3.88)

	OG / Ser287			C1 (3.02)
	CG2 / Ile290	F17 (3.16)	C6 (3.80)	
	CG2 / Ile290	F21 (3.74)		
	CA / Ala291	F1 (3.82)	C6 (3.84)	
	CA / Ala291	F3 (3.85)		
	CA / Ala291	F15 (3.25)		
	CB / Ala291	F1 (3.78)		
	CB / Ala291	F15 (3.01)		
	CB / Ala291	F20 (3.72)		
crevice (PFOA4)	CB / Asp187	F20 (3.65)		O1 (3.56)
	CG / Asp187	F20 (3.55)		O1 (3.76)
	CA / Lys190			C10 (3.77)
	C / Lys190	F6 (3.44)		
	O / Lys190			C9 (3.29)
	O / Lys190			C10 (3.36)
	CB / Lys190	F5 (3.42)		C10 (3.89)
	CD / Lys190			C8 (3.87)
	CE / Lys190	F5 (3.68)		
	CA / Ala191	F6 (3.51)		
	CA / Ala191	F12 (3.60)		
	CB / Ala191	F12 (3.56)		
	OG / Ser193			C10 (3.88)
	CB / Ala194			C9 (3.84)
	CB / Asn429	F15 (3.46)		O2 (3.89)
	CG / Asn429	F1 (3.64)		
	CG / Asn429	F15 (3.11)		
	C / Lys432	F21 (3.85)		
	C / Lys432	F23 (3.79)		
	O / Lys432	C22 (3.80)		
	CB / Lys432	F21 (3.27)		
	CB / Lys432	F23 (3.64)		
	CG / Lys436	C22 (3.87)		
	CG / Lys436	F23 (3.42)		
	CG / Lys436	F24 (3.54)		
	NZ / Lys436			C1 (3.69)
	CD1 / Tyr452	F17 (3.82)		
	CD1 / Tyr452	F24 (3.64)		
	CE1 / Tyr452	F25 (3.87)		
	CG2 / Val455	F11 (3.02)		
	CA / Val456	F3 (3.85)		
	CG2 / Val456	F3 (3.81)		
	CG2 / Val456	F11 (3.80)		
	CG2 / Val456	F17 (3.89)		
	CB / Gln459	O8 (3.18)		
	CG / Gln459	O8 (3.58)		C7 (3.43)
	CD / Gln459			C7 (3.54)
	NE2 / Gln459			C7 (3.26)
	NE2 / Gln459			C8 (3.88)
	NE2 / Gln459			C9 (3.80)

|4

Applying delipidated hSA in impedimetric sensors: A portable strategy

Adapted from G. Moro, F. Bottari, S. Liberi, S. Covaceuszach, A. Casetta, A. Angelini, K. De Wael, L. M. Moretto, Covalent Immobilisation of Delipidated Human Serum Albumin on Poly(Pyrrole-2-Carboxylic) Acid Film for the Impedimetric Detection of Perfluorooctanoic Acid,
Bioelectrochemistry, 2020, *134, 107540*

Abstract

The study of PFOA-dhSA complex reported in **Chapter 3** *shows that delipidated human serum albumin (dhSA) might represent a suitable bioreceptor for perfluorooctanoic acid (PFOA) recognition. Because of the non-electroactive nature of both bioreceptor and analyte, the formation of the complex was first followed at a confined surface (the electrode surface) by considering the changes in the impendence of the surface/solution interface. The design of this impedimetric biosensing strategy aimed to: i) develop an affordable, label-free and portable sensing device, ii) operate a critical data interpretation supported by other analytical techniques (used as controls) and iii) assure an easy and accessible read-out of electrochemical impedance spectroscopy (EIS) data.*

The impedimetric platform described in this chapter was developed at graphite screen printed electrodes (G-SPE). The G-SPE were first modified with an electropolymerised film of pyrrole-2-carboxylic acid (Py-2-COOH), a polymer rich in free carboxylic moieties. These functionalities allowed the covalent immobilisation of the dhSA biomolecular recognition layer through EDC/NHS coupling. Once the sensing platform was fully characterised, we focused on the analytical protocol. The changes in dhSA in presence of increasing concentrations of PFOA were followed by electrochemical impedance spectroscopy (EIS) and the data interpretation was supported by the size exclusion chromatography- small-angle X-rays scattering analysis (SEC-SAXS) of dhSA-PFOA complexe. The results show the applicability of dhSA in PFOA monitoring when considering the high nanomolar range (from 100 nM to 2 µM), with the possibility to discriminate it from other class-related compounds (i.e., PFOS and HFPO-DA). However, further optimisations are required to reach the levels of maximum residue limits.

Our focus on the sensor design can be explained considering that: i) the immobilization of biomolecules at the electrode surfaces, particularly screen-printed ones, via EDC/NHS chemistry is often considered as an open-challenge; ii) most impedance sensors do not provide an easy read-out (requiring to fit the data with electrochemical equivalent circuits, EEC). To enrich the toolbox of electrochemists with a new biomolecule immobilization strategy, we examined Py-2-COOH electropolymerisation at G-SPE providing an optimised protocol. The issue related to the impedance data read-out were solved by considering the Bode plot instead of the Nyquist one. A direct evaluation of the signal variations was possible without the need of EEC. However, EIS is not the only option for PFOA dhSA-based biosensing, as we will see in **Chapter 5** *and* **6**.

4.1. Introduction

In the previous chapter, a complete description of the stability, the thermodynamic parameters and the structural characteristics of dhSA-PFOA complexes was provided suggesting the possibility to use dhSA as a bioreceptor for the detection of PFOA in water plants and waste waters [1,2]. Concerning the detection of PFOA, only few examples of electrochemical sensors have been reported up to now and they mainly use electrochemiluminescence [3], potentiometric [4] and photoelectrochemical [5] methods. All these sensors are based on biomimetic receptors, such as the molecularly imprinted polymers (MIP), which are employed also in PFOA removal [6] and non-electrochemical sensing devices [7], as further described in **Chapter 7**. Bioreceptors can play an important role in PFOA sensing, as shown by the immunosensor developed by Cennamo *et al.* [8]. In this example, mono-specific antibodies were produced via standard immunization protocol using a bovine serum albumin (BSA) – PFOA conjugate. However, **protein-based bioreceptors** have not been considered for the detection of this class of analytes, here represented by PFOA, yet. As described in **Chapter 3**, serum proteins-PFAS interactions were largely investigated [9]. Several toxicological studies clearly demonstrated the PFOA capability to interact with albumin thanks to its fatty-acid mimic behaviour [10,11], suggesting the possibility to use these common proteins as bioreceptors for PFOA sensing.

Albumin-based electrochemical, optical and SPR sensors have already reached good performances in the highly selective and sensitive detection of metal ions [12,13], small molecules [14] as well as larger analytes, i.e. antigens [15]. Albumin, especially isoelectric BSA, is a well-known blocking agent able to prevent nonspecific adsorption phenomena in DNA/RNA sensors and immunosensors [16,17]. Lately, it was largely applied in hybridized materials, in the formation of monolayers for probe carries in DNA biosensors showing a high compatibility with other biomolecules/bioreceptors (from peptides to DNA probes)[18,19]. The stability of albumin, especially BSA, in the biosensing platforms was investigated considering variables such as temperature, light radiations, etc. [20]. Therefore, the literature offers a rich background of experimental data, sensor design protocols and characterisation techniques for albumin application in biosensing. Albumin is often combined with **impedimetric affinity-based sensors**, where the bioreceptor is first immobilised on the electrode surface, detecting the protein-target interaction as a localized change in the electrode/solution interface [21].

The **immobilisation of the bioreceptor** is usually a bottleneck in the development of biosensors, particularly at screen-printed electrodes (SPE). To overcome this issue, other surface modifiers are often included to guarantee the stability of the immobilisation as well as of the electrode surface conductivity and consequently the device sensitivity. Zamani *et al*. [22] recently reviewed the preeminent role of conductive electropolymerised polymers, especially pyrrole and its derivatives, that were extensively studied and applied as electrode modifiers [23]. Among the pyrrole derivatives, pyrrole-2-carboxylic acid (Py-2-COOH) was less employed in electroanalytical applications [24–26], even possessing many sought-after characteristics compared to the parent compound pyrrole, such as the presence of the carboxylic acid functional group, which can be used to couple amide-bearing molecules to the surface via **EDC/NHS chemistry** [27]. The covalent immobilization of biomolecules via EDC/NHS chemistry at SPE can be operated also by generating carboxylic group at the surface of the working electrode via electrochemical oxidation [28]. However, these electrochemical oxidation protocol alters the properties of commercial G-SPE, thus polymeric modifiers synthetised in aqueous media and rich in -COOH groups are preferrable.

The complete characterisation of the electrochemical polymerisation pathway of Py-2-COOH has been previously reported by Foschini *et al.* [29], which results allowed the conclusion that the electropolymerisation mechanism is very similar to the one of pyrrole [30]. The final polymeric chain presents a torsion angle between subsequent monomeric units of 74°, compared to 54° of pyrrole [29]. Thus, the **electropolymerisation conditions** already reported and studied for pyrrole can also be applied to the polymerisation of Py-2-COOH. Considering the specific electron transfer properties of polypyrrole, the conductivity of the resulting film is influenced by the electrolyte in which the electropolymerisation takes place [30]. The polypyrrole film is doped with about 20-30% of anions coming from the electrolyte, and the conductivity is linked to the exchange of trapped anions between the film and the solution [31]. Moreover, acid anions increase the conductivity, while basic ones decrease it [32]. Also, the size of the anion is important for the growth of the film and its performances, such as stability to overoxidation [33]. All these parameters need to be taken into account to design a suitable poly(Py-2-COOH) modification protocol compatible with graphite SPE (G-SPE).

Aiming to obtain stable and conductive poly(Py-2-COOH) on the electrode surface for the covalent immobilisation of biomolecules, we first optimized the main electropolymerisation parameters based on previously reported data [34–36]. Two different electrolytes, one organic (SDS) and another inorganic ($NaClO_4$) were compared showing *how much* anions can influence the conductivity of the films at G-SPE. The optimized poly(Py-2-COOH) was then tested in an impedimetric biosensing platform, as illustrated in **Figure 4.1.** As anticipated in **Chapter 3**, the delipidation treatment increases the available binding sites for PFOA [37], improving also the batch-to-batch reproducibility of the bioreceptor and the reproducibility of the biosensor response.

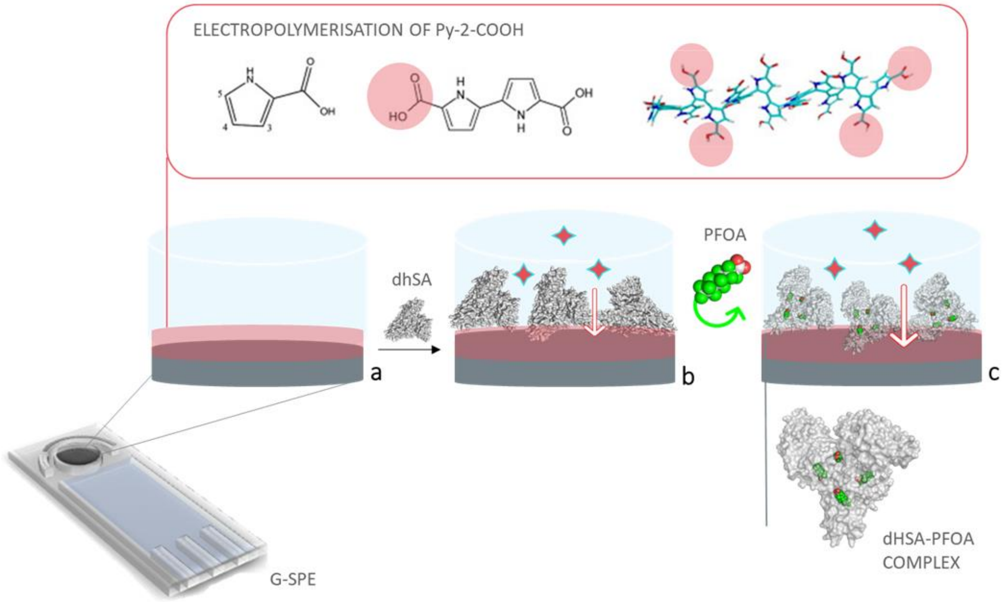

Figure 4.1 *Illustration of the portable biosensing platform designed,* [38]. *The graphite screen-printed electrodes (G-SPE) are modified with:* ***(a)*** *a polymeric layer rich in free carboxylic functional groups (see inset of electropolymerisation mechanism adapted from* [29]*) and* ***(b)*** *delipidated human serum albumin (dhSA). In presence of a redox mediator (red starts) the changes in the interfacial charge transfer resistance are monitored in absence* ***(b)****, and presence* ***(c)*** *of the analyte, namely the PFOA.*

Here, the PFOA-dhSA binding event was followed by electrochemical impedance spectroscopy (EIS) in the presence of a redox probe (**Figure 4.1b-c**) and the changes in the dhSA-PFOA complex conformation were verified by SEC-SAXS (Size Exclusion Chromatography-Small-Angle X-ray Scattering). As a proof-of-concept application, this study confirmed the possibility to develop simple biosensing tools at poly(Py-2-COOH) modified G-SPE for small molecules detection, such as PFOA. The detection strategy reported in this chapter offers two main advantages over the already reported electrochemical biosensors: *i)* it is **label-free**, not requiring any label or co-reactant to perform the detection and *ii)* has the potential to be an easy, fast and robust method of fabrication, based on disposable G-SPE and not requiring complex instrumentations or time-consuming modification protocols.

4.2. Materials and Methods

4.2.1. Reagents and Materials

Pyrrole-2-carboxylic acid (99%) (Py-2-COOH), perfluorooctanoic acid (PFOA, ≥96%), perfluorooctanesulfonic acid potassium salt (PFOS, ≥98%) and hydroxylamine were purchased from Sigma–Aldrich Ltd (Belgium). N-hydroxysulfosuccinimide (NHS) and 1-ethyl-3-(3-dimethylamino) propyl carbodiimide hydrochloride (EDC) were purchased from TCI (Europe). Hexafluoropropylene oxide-dimer acid ammonium salt (HFPO-DA, ≥98%) was purchased from SynQuest Laboratories (USA). Highly purified delipidated human serum albumin (dhSA) was obtained following the protocol reported in [39], as described in **Chapter 3**. Haemoglobin (purity>98%) and ovalbumin (purity>98%) were purchased from Sigma-Aldrich Ltd (Belgium). All the other reagents were of analytical grade and used as received. The 0.1 M phosphate buffer saline solution pH 7.4 with 0.01 NaCl was prepared by mixing stock solutions of 0.1 M NaH_2PO_4 and 0.1 M Na_2HPO_4, purchased from Sigma Aldrich. All aqueous solutions were prepared using MilliQ water (R > 18 MΩ cm). Electrochemical impedance spectroscopy (EIS) and cyclic voltammetry (CV) measurements were performed using an Autolab potentiostat/galvanostat (PGSTAT 302N, ECOCHEMIE, The Netherlands) controlled by NOVA 1.1 software. Disposable graphite screen-printed electrodes (G-SPE) consisting of a graphite working (3 mm diameter) and counter electrode and a silver pseudo reference electrode were purchased from Italsens (Florence, Italy).

4.2.2 G-SPE Py-2-COOH Modification and Characterisation

The electropolymerisation of 10 mM Py-2-COOH was performed by CV, using the following parameters: a potential window between -0.3 V and +1.2 V, at different scan rates (25, 50, 100mV s^{-1}) and number of cycles (5, 10, 20). Two different electrolytes were tested namely 1 M $NaClO_4$ and 0.1 M SDS, both in aqueous solution. EIS measurements were recorded in 0.1 M phosphate buffer pH 7.4 in 1.0 mM of $K_3[Fe(CN)_6]$, 1.0 mM $K_4[Fe(CN)_6]$, in the frequency range between 0.1 MHz and 0.1 Hz, with 0.01 V amplitude and bias potential determined by open circuit potential. Kramers-Kronig transformation was used to verify EIS data for linearity [40,41] and ZView 2 used for the analysis. All the potentials are referred to Ag-pseudo reference electrodes except where otherwise stated. All electrochemical experiments were performed at room temperature.

4.2.3 Covalent Immobilisation of dhSA Bioreceptor

A volume of 50 µL of 10 mM Py-2-COOH in 0.1 M SDS aqueous solution was placed on the G-SPE and the electropolymerisation was performed by CV (5 cycles at 100 mV s^{-1}). The modified G-SPE were first rinsed with 1 mL phosphate buffer pH 7.4. To activate the carboxylic acid groups, 20 µL of an equimolar solution (0.07 M) of EDC/NHS in MilliQ water were incubated at the working electrode for 20 min keeping the G-SPE at 4° C. The solution was removed and 30 µL of 2 mg mL^{-1} dhSA in phosphate buffer pH 7.4 were let in contact with the working electrode for 30 min at 4° C. The dhSA modified G-SPE were rinsed with 1 mL phosphate buffer pH 7.4 to remove the protein excess. Then, the unreacted carboxylic acid groups were blocked with 20 µL of 1 M hydroxylamine incubation for 20 min at 4° C. After dhSA immobilisation, the G-SPE were characterized by EIS before being incubated with PFOA solutions.

4.2.4 Analytical Protocol for PFOA Detection

The modified electrode (dhSA-G-SPE) was incubated with 20 µL of PFOA solution at different concentrations for 20 min at RT. After, the electrode was rinsed with 500 µL of phosphate buffer and EIS spectra were acquired in 80 µL of 1.0 mM of $K_3[Fe(CN)_6]$, 1.0 mM $K_4[Fe(CN)_6]$, in phosphate buffer. The calibration plot was built in the concentration range between 100 nM to 1 µM: the relevant analytical parameter ΔZ is defined as the difference in absolute impedance values, acquired at 10 Hz, between the bare dhSA-G-SPE and after the incubation with PFOA. All measurements were performed in triplicates, unless otherwise indicated.

4.2.5 Micro-FTIR Characterisation

The µFT-IR spectra were collected using the LUMOS II spectrometer from Bruker. The samples were scratched from the electrode using a tungsten needle and deposited in a KBr pellet. Afterwards, they were analysed in transmission mode with an MCT detector, with a spectral range of 4000–700 cm^{-1}, a 4 cm^{-1} resolution, 128 scans, and a 100×100 μm^2 spot size. The spectra have not been corrected in order to not distort the data. The OMNIC and PyMca packages were used for data analysis.

4.2.6 Size Exclusion Chromatography and Small-Angle X-ray Scattering (SEC-SAXS)

The SEC-SAXS experiments were performed at the P12 beamline EMBL SAXS-WAXS at PETRAIII/DESY (Hamburg, Germany) [42]. The size exclusion chromatography (SEC) column (Superdex 200 5/150 column; GE Healthcare Life Sciences) was equilibrated with

SEC-SAXS running buffer A (10 mM sodium phosphate, pH 7.4, 100 mM NaCl, 5% glycerol). A 50 µL aliquot of dhSA (9 mg mL^{-1}) was applied to the column. The SEC column was then equilibrated with SEC-SAXS running solution B (buffer A plus 1 mM PFOA). Before performing the SAXS experiments on the complex, the dhSA was pre-incubated with 1 mM PFOA for 30 min at room temperature and a 50 µL aliquot (9 mg mL^{-1}) was applied to the column. For each run 720 images were recorded using 1 s exposure every 1.25 s at a flow rate of 0.3 mL min^{-1}. For SEC-SAXS data, frames corresponding to dhSA protein peak were identified, blank subtracted and averaged using CHROMIXS [43]. Radii of gyration (Rg), molar mass estimates and distance distribution functions P(r) were computed using the ATSAS package [44], in PRIMUS [45]. Comparison of experimental SAXS data (see **Table A4.1**, **Annex**) and dhSA crystal structure (PDB_ID: 4K2C) [46] was performed using CRYSOL [47].

4.3. Results and Discussion

4.3.1 Electropolymerisation Optimisation

Surface modifications of G-SPE might represent a challenging task and often protocols optimised for other types of electrodes, such as bulk macroelectrodes, are not directly compatible with SPE [48]. To avoid these issues, in this study the monomer electropolymerisation was carried out by CV in aqueous solution avoiding organic solvents that might affect the stability of G-SPE coatings. Taking advantage of the wealth of information already present in literature only **two electrolytes** were tested, an organic anion and an inorganic one, $NaClO_4$ [34] and SDS [35,36], respectively. These two electrolytes were considered because the final poly-pyrrole films obtained were found to have good conductibility and stability, as we would like our Py-2-COOH modifier to be. The optimization of the electropolymerisation protocol and the selection of the most suitable electrolyte among the two mentioned were aimed to maximise the film conductivity, minimise the modification protocol duration and assure the easiness of application.

The electropolymerisation of 10 mM Py-2-COOH at G-SPE was performed in 1 M of $NaClO_4$ [34] and in 0.1 M SDS [35,36] by running five CV cycles at 100 mV s^{-1}. The **electropolymerisation patterns** reported in **Figure 4.2A - B** showed a consistent behaviour for both electrolytes: the monomer oxidation occurred at about +1.1/1.2 V and the intensity of the peak current decreased with increasing the number of CV cycles (see arrows in **Figure 4.2A-B**). The peak currents were comparable for both $NaClO_4$ and SDS (≈ 400 µA for the first cycle). From the polymerisation patterns, the electrolytes differ mainly for the oxidation peak shape (more symmetrical and resolved in $NaClO_4$ solutions) and capacitive contribution (higher for SDS solution). However, the electrochemical properties of the modified electrodes investigated by CV and EIS were found to be completely different in terms of surface conductivity.

In **Figure 4.2C**, the voltammograms recorded in 1.0 mM of $K_3[Fe(CN)_6]$, 1.0 mM $K_4[Fe(CN)_6]$, 0.1 M KNO_3 for bare and both poly(Py-2-COOH) modified G-SPE are compared to describe the **conductive/insulating nature** of these polymeric modifiers. The voltammogram of the G-SPE modified with the Py2-COOH grown in $NaClO_4$ (*blue curve*) showed an almost complete suppression of the redox signals, compared to bare G-SPE (*black curve*). This outcome suggests that the electropolymerisation in $NaClO_4$ passivates the electrode surface leading to the formation of an insulating layer. An opposite behaviour was observed for the Py-2-COOH film obtained in SDS: the voltammograms (*red curve*) present a current increase of about 15% for both anodic and cathodic peaks and a smaller ΔEp (from 202 mV to 112 mV) compared to the bare G-SPE (*black curve*). It is worth noting that the presence of a polymeric layer implies also an increase in the capacitive currents, < 5%. Overall, these characteristics indicate an enhanced electron transfer when carrying out the electropolymerisation in SDS electrolyte.

The striking difference in conductivity of films obtained with the two modification protocols was confirmed by EIS, as shown in **Figure 4.2D**. The electrode modified in $NaClO_4$ solution (*blue dots*) presented a very high charge transfer resistance (Rct) compared to the control (*black dots*) and no diffusion processes were observable from Nyquist plot in the frequency region tested. This data can be fitted with a simplified Randles circuit, excluding Warburg element [49]. Therefore, the formation of an insulating polymer-solution interface was confirmed. On the contrary, the SDS modified electrode presents a Rct lower than the bare G-SPE, as underlined in **Figure 4.2E** (*red dots*). This Nyquist plot is characterised by a double consecutive semicircle (very small initial one) and a large diffusion contribution, which suggest: *i)* the conductive nature of the modifier and *ii)* the presence of multiple processes, which implies the need of an articulated electrochemical equivalent circuit (EEC) for the data fitting. It is possible to conclude that Py-2-COOH electropolymerisation in aqueous solutions is compatible with G-SPE electrodes and the polymer properties can be easily tuned using different electrolytes. In particular, the use of $NaClO_4$ leads to insulating modifiers, while with SDS, poly(Py-2-COOH) conductive films are obtained. Aiming to design a sensitive impedimetric platform, further optimisation was performed only with the 0.1 M SDS electrolyte.

4.3.1.1. Number of cycles and scan rate

The electropolymerisation with SDS was **optimized** in terms of number of CV cycles and scan rate using a *one-variable-at-a-time* approach (OVAT). The monomer solution, 10 mM of Py-2-COOH in 0.1 M SDS, was polymerised using an increasing number of cycles (5, 10, 20) and different scan rates (25, 50, 100 mV s^{-1}). The values tested were selected based on the literature (i.e., pyrrole-based imprinted modifiers [50,51]).

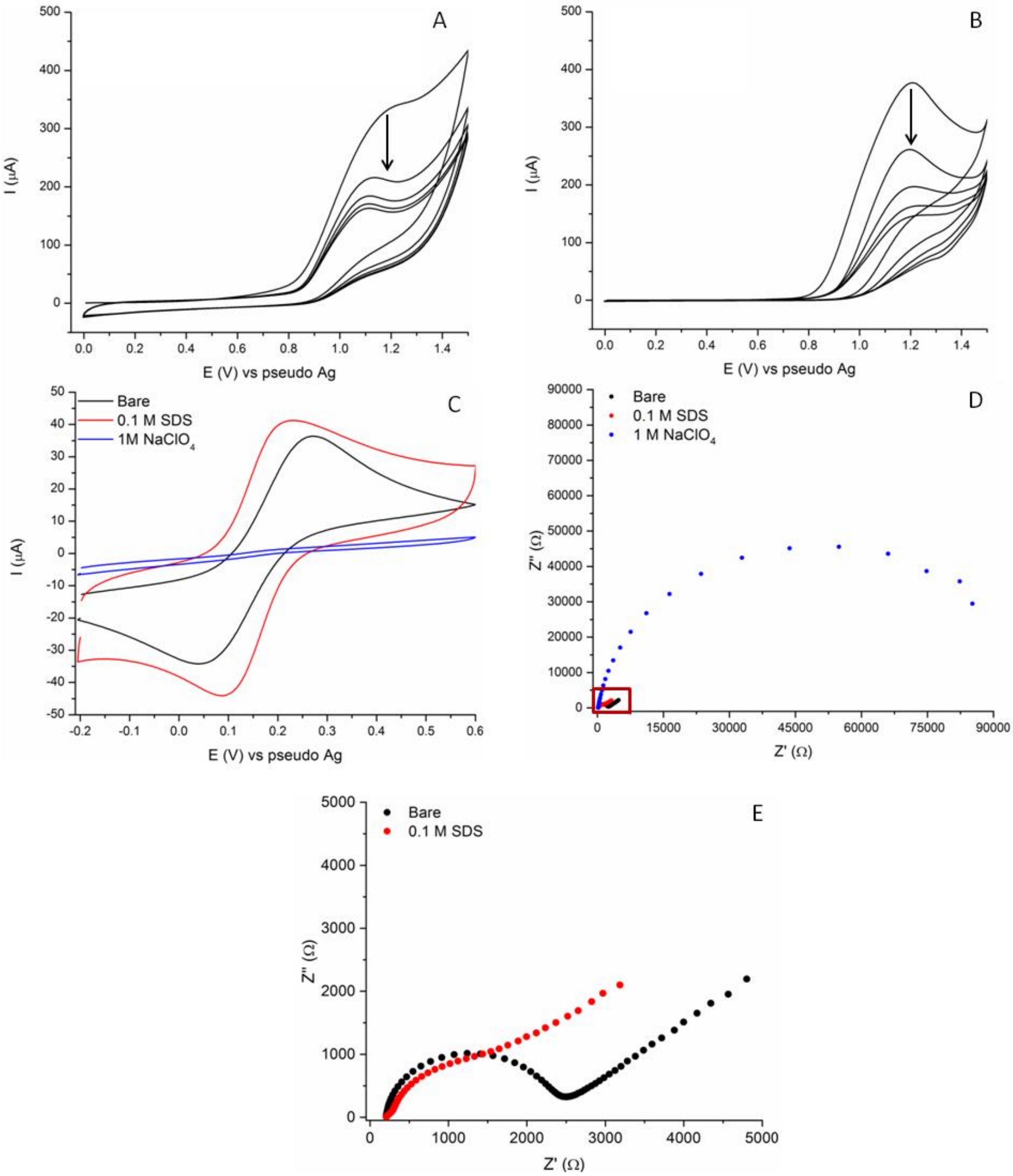

Figure 4.2 *Comparison of different electropolymerisation patterns for 10 mM Py-2-COOH, 5 cycles at 100 mVs-1 between 0 and +1.5 V in 0.1 M SDS (**A**) and 1 M NaClO$_4$ (**B**); (**C**) CVs for bare G-SPE (black line), and after 5 cycles of electropolymerisation with 10 mM Py-2-COOH in 0.1 M SDS (red line) and 1 M NaClO$_4$ (blue line); (**D**) Nyquist plot for bare G-SPE (black line), and after 5 cycles of electropolymerisation with 10 mM Py-2-COOH in 0.1 M SDS (red dots) and 1 M NaClO$_4$ (blue dots); (**E**) Magnification of Nyquist plot in **Figure 4.2D** (region from 0 to 5000 Ω). All the measurements were performed in 0.1 M KNO$_3$ with 1.0 mM of K$_3$[Fe(CN)$_6$], 1.0 mM K$_4$[Fe(CN)$_6$].*

To optimise the number of cycles, the scan rate was kept constant (100 mV s^{-1}) and five cycles of CV were recorded for each different scan rate value. The properties of all the modified G-SPE were characterised by CV and EIS in presence of 1.0 mM of $K_3[Fe(CN)_6]$, 1.0 mM $K_4[Fe(CN)_6]$, 0.1 M KNO_3. Again, the working conditions leading to the more conductive films were considered optimal. When the performances were comparable, other criteria, such as protocol duration, were applied to define the final electropolymerisation protocol. Comparing the performances of the G-SPE modified at different **number of cycles** in **Figure 4.3A-B**, we noticed that poly (Py-2-COOH) modification showed a higher surface conductivity (compared to bare G-SPE) even after 20 consecutive CV cycles. However, the best performances in terms of current intensities and ΔEp were obtained with five CV cycles, as summarised in **Table 4.1**. Increasing two or four times the number of CV cycles, there was an increment in ΔEp from 112 mV for 5 cycles to 173 mV for the 20 cycles.

To operate a rapid modification protocol, a number of five CV cycles was considered optimal for this study. An even lower impact on the modified electrode performances was reported using different scan rates. The results presented in **Figure 4.3C** showed a consistent behaviour with current variations of ± 11% and ΔEp differences of maximum 22 mV. To minimize the protocol duration, a **scan rate value** of 100 mV s^{-1} was selected. The slightly better performances of the electrodes modified with shorter protocols (5 cycles at 100 mV s^{-1}) might be explained by the polymerisation solution. Indeed, the SDS solution has a very low surface tension and tends to spread on the G-SPE surface. Longer electropolymerisation times might result in an uneven deposition since the monomer has more time to diffuse away from the WE surface.

Table 4.1 *Electrochemical parameters of the different poly (Py-2-COOH) modified electrodes: 5, 10 and 20 CV electropolymerisation cycles recorded at 100 mV s^{-1} or 5 CV electropolymerisation cycles recorded at 25, 50 and 100 mV s^{-1}. Average and STD were calculated from triplicate measurements.*

	ΔEp (mV)	**Ipa/Ipc**
Bare	202 ± 8	1.23
5 cycles	112 ± 4	1.03
10 cycle	122 ± 2	1.14
20 cycles	173 ± 5	1.16
--		
25 mV/s	134 ± 6	1.11
50 mV/s	124 ± 3	1.10
100 mV/s	112 ± 4	1.03

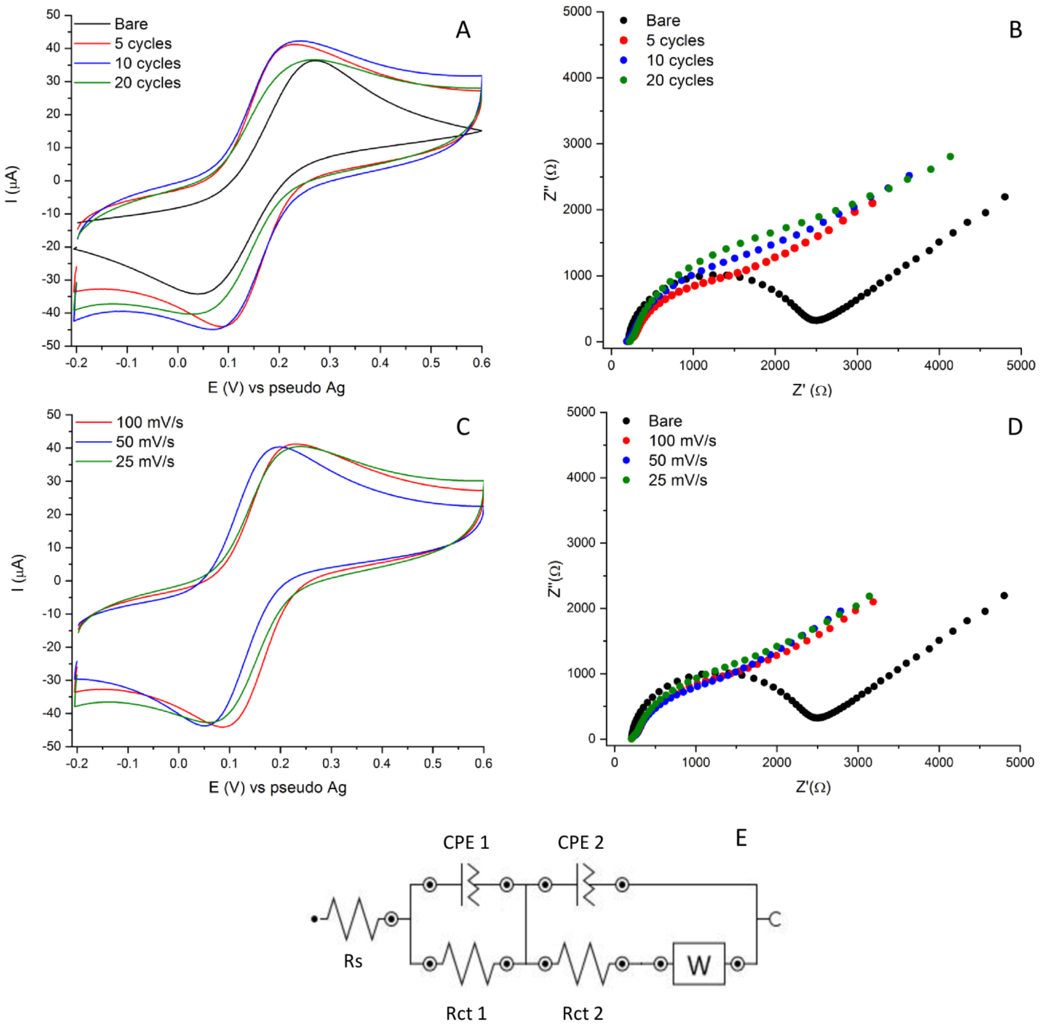

Figure 4.3 *Comparison of different electropolymerisation parameters for 10 mM Py-2-COOH in 0.1 M SDS: CVs (**A**) and Nyquist plots (**B**) of G-SPEs after 5, 10 and 20 CV electropolymerisation cycles at 100 mV s^{-1}; CVs (**C**) and Nyquist plots (**D**) of G-SPEs after 5 CV cycles electropolymerisation at 25, 50 and 100 mV s^{-1}; (**E**) Schematic representation of the EEC used to fit the data.*

The EIS data proved once again that the modified electrodes are still very conductive and indirectly report the successful modification of the electrode surface. The Nyquist plot for the modified electrodes can be fitted by EEC reported in **Figure 4.3E**. Two blocks of circuit elements can be identified; *Rs* is the uncompensated solution resistance while the first block [*CPE 1, Rct 1*] models the poly (Py-2-COOH) film and the second [*CPE 2 (Rct 2; W*)] is related to the electrode surface underneath the polymer. This circuit has been previously reported as a model for electrodes modified with materials (mostly poly-pyrrole films) with different conductivities and morphology of the underlying working electrode [52–54].

The final modification protocol encompasses the electropolymerisation of 10 mM of Py-2-COOH in 0.1 M SDS for 5 CV cycles at 100 mV s^{-1}; all the protocol specifications are summarised in **Section 4.2.3**. The resulting polymeric film provides the carboxylic acid functional groups needed for the covalent immobilisation of biomolecules and improves the conductivity of the working electrode, as evidenced also by the EIS characterisation.

4.3.2. Impedimetric Characterisation of dhSA-PFOA Binding and IR Check

The possibility of following the formation of the dhSA-PFOA complex was studied by EIS at the surface of the Py-2-COOH-G-SPE. The electrode surface rich in free carboxylic acid moieties were activated by EDC/NHS for the covalent immobilisation of dhSA. The protocol was adapted from the one reported by Rengaraj *et al.* for lectin immobilisation at portable screen-printed carbon paper electrodes [28]. The dhSA loading was optimized to a final value of 2 mg mL^{-1} in **Table 4.2**. In this study, a limited range of **dhSA concentrations** was considered: from 0.5 to 5 mg mL^{-1}. The optimisation was based on the comparison of the dhSA-Rct values calculated by fitting the data with the EEC reported in **Figure 4.5**. We observed that for dhSA concentrations lower than 2 mg mL^{-1}, the Rct values were affected by relatively high errors suggesting a non-stable modification. With 2 mg mL^{-1} a good reproducibility was obtained, while for higher concentrations of dhSA the Rct did not change significantly. With 5 mg mL^{-1} we recorded an increase in the Rct but with a much higher associated error. Based on this data, a dhSA-loading of 2 mg mL^{-1} was selected.

Table 4.2 *Average values of dhSA-Rct, recorded at increasing concentrations of dhSA immobilised at the Py-2-COOH-G-SPE surface. Average and STD were calculated from triplicate measurements.*

[dhSA] (mg mL^{-1})	dhSA-Rct (Ω)
0.5	25 ± 11
1.0	50 ± 13
2.0	100 ± 9
3.5	110 ± 16
5.0	150 ± 25

Once the protocol was optimised, the modification and its stability were further characterised with the help of micro-FTIR, as summarised by the spectra comparison in **Figure 4.4**. The **IR spectra** of pure lyophilised dhSA, Py-2-COOH modified G-SPE and dhSA-Py-2-COOH-G-SPE were first collected. The IR spectrum of dhSA is characterised mainly by two intense bands: the *amide I* band at 1655 cm^{-1} and the *amide II* band 1543 cm^{-1} [55,56]. This so-called *amide region* can provide additional information about the secondary structure of albumin [57,58], such information can be useful to check the bioreceptor stability over time and different working conditions (future studies). Despite Py-2-COOH presents some bands with very low intensity in *dhSA amide region*, it is still possible to clearly observed *amide I* and *II* bands in the spectra of the "*modified G-SPE"*. The **stability of the modification** was probed by subjecting the dhSA-Py-2-COOH-G-SPE to up to 10 washing cycles with PBS solution and then collect their IR spectra (data not shown). This simple test shows that dhSA was still present even after several rinsing/drying steps because the IR spectra showed the same feature of the "*modified G-SPE"* and albumin bands (at about 1655 and 1543 cm^{-1}). The spectra recorded prior and after these washing steps overlap. The absence of band shifts might suggest that the secondary structure of dhSA was not altered meaningfully during this test. Here, micro-FTIR was applied as a control technique to verify the stability of the dhSA immobilisation, but it might be further considered for the routine check of dhSA-Py-2-COOH-G-SPE or other protein-modified SPE.

4.3.2.1 Characterisation of the dhSA-Py-2-COOH Modified G-SPE

The Nyquist plots obtained at the bare G-SPE (bare, *black dots*) and after Py-2-COOH acid electropolymerisation (Py-2-COOH, *red dots*), dhSA immobilisation (dhSA, *blue dots*) and PFOA incubation (PFOA 1 µM, *green dots*) are reported in **Figure 4.4**. To extract qualitative and quantitative information about the processes occurring at the electrode surface, the Nyquist plots were fitted with EEC reported in **Figure 4.4B- C**.

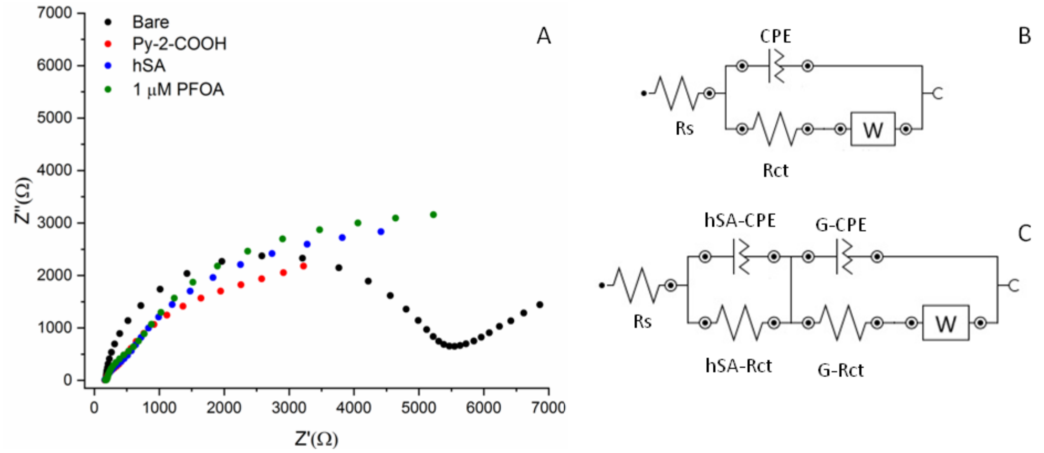

Figure 4.4 *(**A**) Nyquist plots for bare (black dots), poly (Py-2-COOH) modified G-SPE (red dots) and dhSA poly(Py-2-COOH) modified G-SPE in absence (blue dots) and presence of 1 µM PFOA (green dots), (**B**) modified Randles EEC; (**C**) dhSA modified electrode EEC. All the measurements were performed in 0.1 M KNO$_3$ with 1.0 mM of K$_3$[Fe (CN)$_6$], 1.0 mM K$_4$[Fe(CN)$_6$] in 0.1 M KNO$_3$.*

The Nyquist plot for the bare G-SPE was fitted with the modified Randles circuit, reported in **Figure 4.4B.** In this circuit, the migration of charge through the electrolyte solution is described by the solution resistance (Rs), the double-layer formation at the electrode surface is modelled by a constant phase element (CPE), the charge-transfer reaction at the electrode corresponds to the Rct, and the linear diffusion from the bulk of the solution is modelled by the Warburg impedance element (W). The bare G-SPE presented a relatively high Rct (2.12 kΩ). After the electropolymerisation of the conductive pyrrole-2-carboxylic acid film, the Rct was halved (1.02 kΩ). Moreover, the polymeric layer resulted to be highly reproducible and even G-SPEs with different initial Rct values showed comparable performance after the electropolymerisation.

The immobilisation of the dhSA led to the formation of a conductive layer. To model this modification, a different EEC, reported in **Figure 4.4C**, with an additional resistor and capacitor in parallel was used. A similar EEC was previously reported by Xie *et al.* in the EIS study of bovine serum albumin absorption at platinum electrodes [59]. The additional elements (dhSA-CPE and dhSA-Rct) model the resistance and capacitance of the conductive dhSA film. Indeed, the charge must pass through the protein film before accessing the electrode surface (the part consisting of G-CPE, G-Rct and W). The Nyquist plot obtained after the incubation of 1 µM PFOA (green dots) presents an increase in the semicircle part of the plot at lower frequencies which is linked to an increase in Rct of the layer. Thus, it is possible to hypothesize a direct influence of the PFOA on the dhSA structure on the electrode surface. The **conformational changes** of dhSA in presence of PFOA were further investigated by SEC-SAXS.

4.3.2.2. SEC-SAXS Analysis of hSA-PFOA Complexes

SEC-SAXS measurements were performed on dhSA in the unbound state, known as *apo form*, and in complex with 1 mM PFOA (see **Figure A4.1**, **Annex A**). The experimental SAXS curves are compared in **Figure 4.5A** and the size parameters calculated from the raw data are summarised in **Table A4.1**, **Annex A**. From these latter, it is possible to observe that the molecular masses (MM), calculated from the hydrated particle volumes (Vp), were consistent with values expected for monomeric species and in agreement with the MM estimated from the primary sequences. Even if the overall distance distribution function and therefore the calculated D_{max} are not affected by the interaction with PFOA, there is a meaningful change in the radius of gyration, Rg. This difference (about 0.8 Å) is clearly visible in the plots reported in **Figure 4.5B-C**, suggesting a conformational change of dhSA in presence of PFOA. In particular, PFOA-dhSA complexes assumed a more compact shape in respect to the apo form, with a significant decrease in the Rg values (from 27.900 ± 0.006 Å for the apo protein to 27.100 ± 0.008 Å for the complex with PFOA).

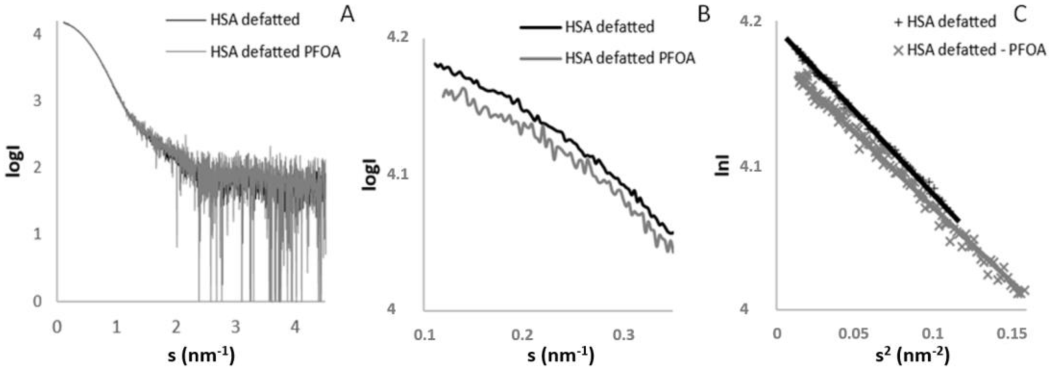

*Figure 4.5 (**A**) Comparison of the experimental SEC-SAXS data obtained for the apo form of dhSA and the complex with PFOA and (**B**) the zoomed regions of these graphs at low angles; the plots display the logarithm of the scattering intensity (log I) as a function of momentum transfer (s); (**C**) Comparison of Guinier plots and fits of the SEC-SAXS data for the apo form of dhSA and the complex with PFOA.*

The observed conformational changes are confirmed by the comparison of the experimental scattering data with theoretical scattering curves computed by CRYSOL [47] from the crystal structure of dhSA [46]. A poor fit with a χ^2 of 3.79 was obtained for the apo form. This result is ascribed to the packing stabilizing interactions that take place in the crystal lattice, resulting in a crystallographic structure more compact than the respective conformation in solution. On the contrary, PFOA binding induces a more compact conformation of dhSA that is very close to the crystal structure with a good agreement (χ^2 of 1.54) between the calculated and measured scattering intensities.

These results suggest that **PFOA compacts the structure of albumin** leading to a meaningful decrease of the radius of gyration (*Rg*). However, it is worth noting that no denaturation or protein unfolding was observed for dhSA after incubation with PFOA. These data can be explained by considering the fatty-acid mimic behaviour of this contaminant that in presence of a completely delipidated protein is able to create strong interactions in the cavities that normally host lipids, hormones or drugs, as described in **Chapter 3** [60,61]. The structure assumed by the dhSA in presence of PFOA might be responsible for the increase in Rct of the modified electrode; the redox mediator in solution should find its path towards the electrode surface hindered by the more compact dhSA layer and thus resulting in an increased charge transfer resistance.

4.3.3. PFOA Impedimetric Analytical Detection Strategy

To simplify the detection strategy and improve the sensitivity of the sensors, a direct evaluation of the impedance signal changes was performed by considering the Bode phase plots instead of analysing the EEC parameters after fitting the Nyquist plots.

In **Figure 4.6A**, the Bode phase plot of dhSA-Py-2-COOH-G-SPE (*blue dots*), it was possible to identify two peaks, with Θ_{max} at 1 and 10 Hz, respectively. Each peak corresponds to a separate kinetic process with different time constants [62]. These processes were ascribed to the interaction of the redox mediator with the dhSA and the polymeric film on the electrode surface. They appear after the Py-2-COOH electropolymerisation, see comparison of bare G-SPE (*black dots*) and Py-2-COOH-G-SPE (*red dots*).

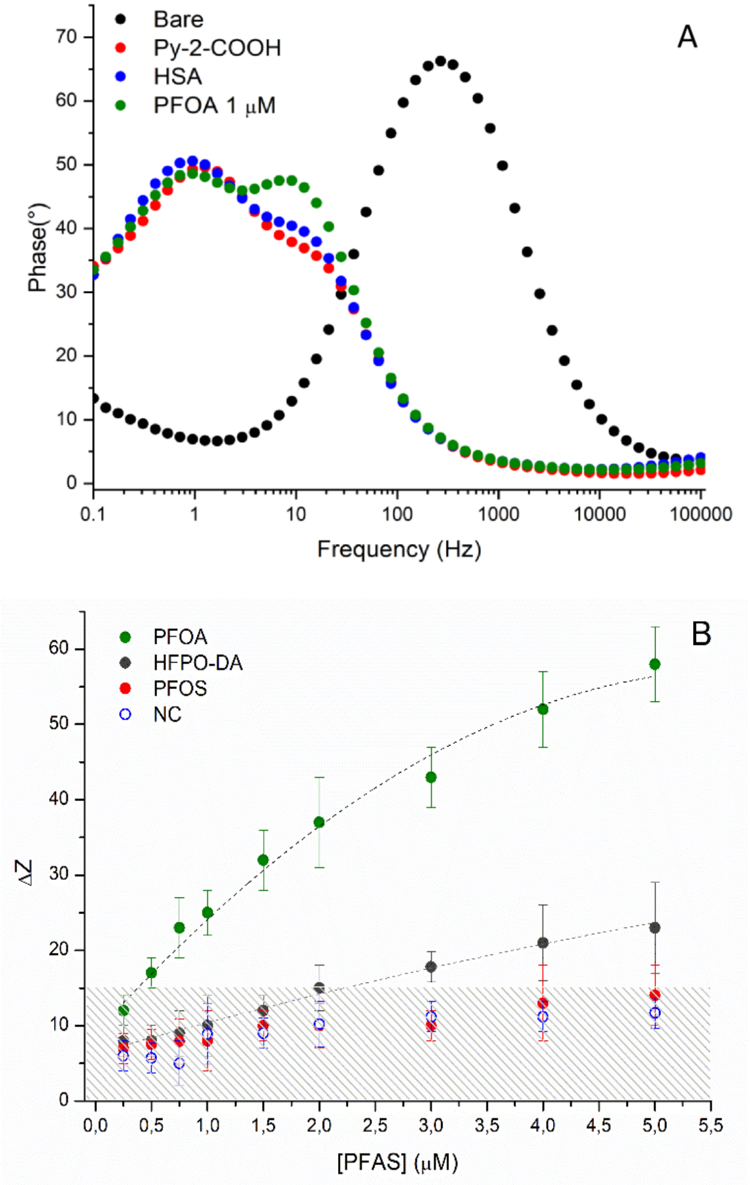

Figure 4.6. *(**A**) Bode phase plot for the dhSA-Py-2-COOH-G-SPE recorded in 0.1 M phosphate buffer pH 7.4 with 1.0 mM of* K_3*[Fe (CN)*$_6$*], 1.0 mM* K_4*[Fe(CN)*$_6$*], bare (black dots), after Py-2-COOH electropolymerisation (red dots), after dhSA immobilisation (blue dots) and after incubation with 1 μM PFOA (green dots); (**B**) Calibration plot for the dhSA-Py-2-COOH-G-SPE biosensors between 100 nM and 5 μM PFOA (green dots), HFPO-DA (grey dots), PFOS (red dots) and buffer solution (white/blue dots), polynomial fitting equation of PFOA calibration plot:* $y = 11.20 + 14.97x^1 - 1.23x^2$*. Error bars calculated on triplicates.*

From the analysis of the Bode phase plots the modification showed a good reproducibility: the maximum phase values of both processes present a relatively low s.d. (50.7 ± 1.1° for the *process I* at 1 Hz and 38.7 ± 0.87° for *process II* at 10 Hz). After **incubation of PFOA** spiked solutions, the Θ_{max} of *process II* at 10 Hz increased (Δ≈11°; *green dots*). This change suggests that the presence of PFOA influences the interfacial region G-SPE/dhSA/solution allowing the redox mediator to access the electrode surface more easily (increase in the phase value). To use this event as an analytical signal, the changes in the absolute impedance IZI, recorded at a fixed frequency of 10 Hz, were plotted against different PFOA (and PFAS) concentrations incubated at dhSA-G-SPE, as shown in **Figure 4.6B**. The analytical parameter used is ΔZ, which is defined as the difference between the Z value of the dhSA modified electrode at 10 Hz and the same value recorded after incubation with different PFOA solutions ($\Delta Z = |Z|_{PFOA/PFAS} - |Z|_{dhSA}$).

PFAS calibration plots in **Figure 4.6B** were built in the range from 100 nM to 5 µM for all analytes tested, namely: our target (PFOA), other two possible interfering compounds from PFAS class (PFOS and HFPO-DA) and the buffer solution. It is worth noting that the other PFAS were selected to: *i)* test another fluorinated substance with the same chain length of PFOA and a different head group (PFOS) and *ii)* test a shorter-chain PFAS with a carboxylic group (HFPO-DA).

For PFOA, a polynomial fitting of the data points (*dotted line*) was applied with a R^2 of 0.997. For PFOA concentrations higher than 2 µM, the trend of the data seems to suggest a progressive saturation of the biorecognition layer. However, a linear interval between 100 nM and 2 µM was observed, and additional optimization might help extending this range down to the low nM range. The reproducibility of the impedimetric biosensors was found to be about 89%, which is considered acceptable for a first proof-of-concept.

The dhSA-Py-2-COOH-G-SPEs were also incubated with: HFPO-DA (*grey dots*), PFOS (*red dots*) and the buffer solution (*white/blue dots*). These negative control experiments were performed in triplicate and the average values with the relative error (expressed as *s.d.*) were plotted in **Figure 4.6B**. The results show clearly that the properties of the electro/solution interface are altered by both the PFAS (PFOS and HFPO-DA) and the blank (buffer solution). With buffer solution additions, the ΔZ ranged from 7-15 (*grey area*) and no trend was observed, as expected for a blank. The signal for 100 nM of PFOA falls below the threshold value (ΔZ≈15) and, thus, cannot be considered specific.

After incubation with increasing concentration of PFOS, the change in ΔZ were of the same magnitude of the one observed with blank additions (from7 to 15) suggesting that PFOS interacts with the layer but without leading to stable conformational changes as for PFOA. Considering the structural similarity of PFOA and PFOS, we could have expected a similar trend in the biosensor response. The behaviour observed can be ascribe to their different affinity for dhSA and the possible differences in PFOA/PFOS-dhSA binding mechanism (as described in **Chapter 3**). Unfortunately, the impedimetric response do not allow to understand more in detail the reason of this different behaviour. Compared to PFOS data, the incubation of HFPO-DA led to a more meaningful change in the ΔZ, with a trend similar to the one observed for PFOA. These findings suggest that also HFPO-DA interacts with the biorecognition layer but its effect is not as evident as for PFOA. This might depend on the HFPO-DA solubility (higher than PFOA one), interaction mechanism, affinity for dhSA (lower than PFOA one), etc. Overall, these negative controls experiments confirmed that the biorecognition layer of our impedimetric platform is highly sensitive (undergoes traceable changes even after blank additions) and particularly suitable for PFOA detection (for other PFAS the ΔZ are not meaningful and/or proportional to the analyte concentration). The results highlight also the need to further improve this impedimetric platform to determine lower PFOA values and suppress the interfering signals. This would be possible using only the albumin domains which bear the FA sites of interest for PFOA instead than the whole dhSA, as anticipated in **Chapter 3** and further discussed in the next ones.

To evaluate the role of dhSA in this platform, additional negative controls were performed using other non-delipidated proteins instead of human serum albumin: ovalbumin (OVA) and haemoglobin (Hb). The G-SPE modification protocol was applied without any optimization of the protein concentrations. In this frame, these proteins were selected simply because their MW is similar to the one of dhSA (OVA≈45kD and Hb≈64.5 kDa). The results of these tests are exemplified in **Figure 4.7**, where the Bode plot of the modified electrodes prior/after incubation of 1 µM PFOA are compared for both OVA and Hb. The results of OVA-Py-2-COOH-G-SPEs show no changes upon incubation of PFOA. As for dhSA, here two processes with different kinetics were observed (dotted lines) even though the frequencies of the Θmax resulted to be shifted towards higher values.

For *Hb-Py-2-COOH-G-SPEs*, the profile of the Bode plot before PFOA incubation was characterised by a broad peak (overlapped peaks) suggesting the presence of multiple processes with similar kinetics. This difference can be ascribed to the completely different nature of Hb compared to dhSA and OVA, as described in **Chapter 2**, Hb is an electroactive protein. Therefore, the equilibria of the interfacial region are more complex to follow. Despite this discrepancy, also this second control experiment showed that PFOA incubation do no alter the biorecognition layer in an observable way. Both controls confirm that the possibility to detect increasing PFOA concentrations with *protein-Py-2-COOH-G-SPEs* depends on the specific changes in the biorecognition layer immobilised at the G-SPE surface. Only dhSA, with its high affinity for PFOA and its capacity to undergo a meaningful conformational change when complexed with this compound, is suitable for PFOA biosensing. Other kinds of protein bioreceptors, such as OVA (not delipidated) and Hb, did not show any traceable changes. In particular, the comparison of OVA and dhSA suggest the importance of albumin delipidation and purification prior to apply the protein in biosensing platforms. Moreover, these controls indirectly prove the applicability of Py-2-COOH in the covalent immobilisation of proteins at G-SPEs, because all experiments showed a good reproducibility.

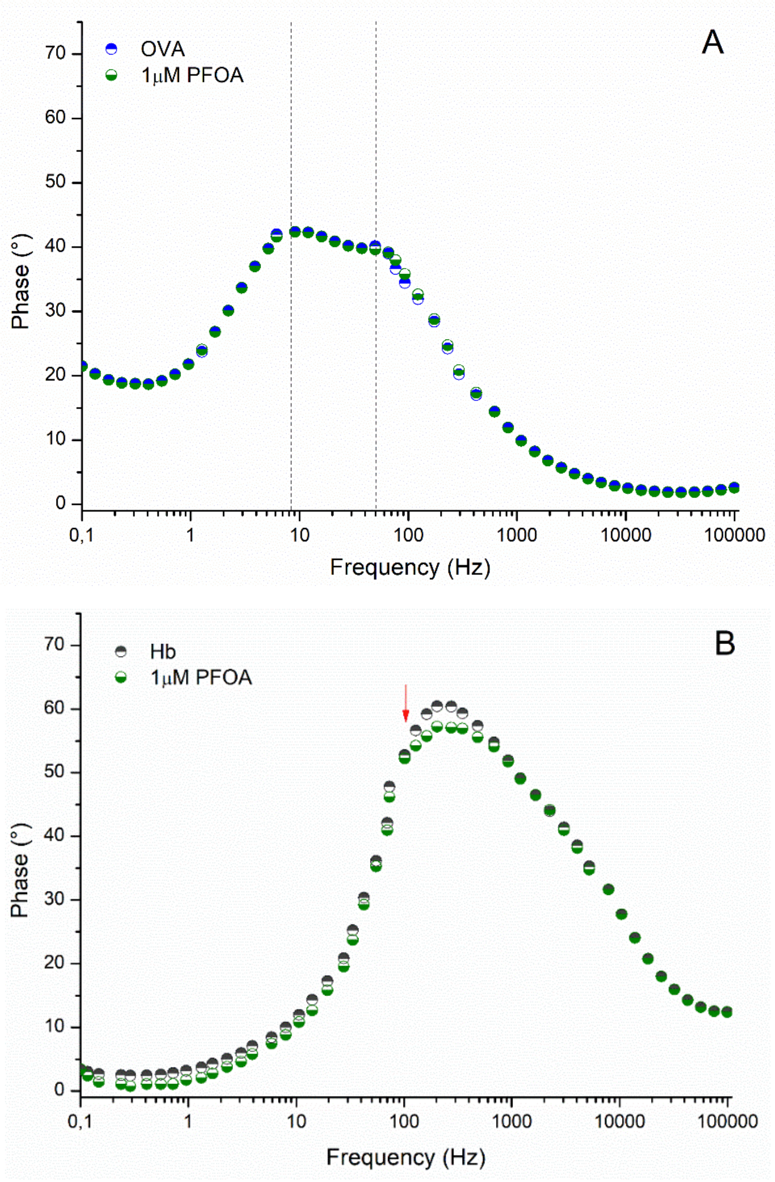

Figure 4.7. *Bode phase plot for the: (**A**) OVA-Py-2-COOH-G-SPE and (**B**) Hb-Py-2-COOH-G-SPE. Both biosensors were tested in 0.1 M phosphate buffer pH 7.4 with 1.0 mM of* $K_3[Fe(CN)_6]$*, 1.0 mM* $K_4[Fe(CN)_6]$ *after incubation with 1 µM PFOA (green dots).*

From these preliminary experiments, we can conclude that dhSA can be applied as a PFOA bioreceptor in portable, affordable sensing platforms. The covalent immobilisation of the protein assures a good reproducibility of the biorecognition layer responses and the high sensitivity of impedance outcomes allow to follow dhSA-PFOA complex formation. All tests aimed to probe the possibility to regenerate the platform after use where not included in this preliminary study.

4.4 Conclusions

With this chapter, we aimed to answer three main questions: *i)* would it be possible to apply dhSA in PFOA detection designing an impedance biosensor? *ii)* shall we optimise a protocol for the covalent immobilisation of our protein bioreceptor at G-SPE avoiding the drawbacks of electrochemical oxidation protocols? *iii)* can we further support impedance data interpretation by the help of other complementary techniques?

The preliminary data obtained with our biosensing platform suggest the possibility to develop a **sensing strategy using dhSA-PFOA complex formation as recognition event**. Indeed, this platform was tested in presence of increasing concentrations of PFOA and the changes at interfacial electron transfer were correlated to the formation of dhSA-PFOA complex, no comparable trends were observed in the negative control experiments (using other PFAS or different protein bioreceptors). When working with dhSA and PFOA, by extracting the absolute impedance values at 10 Hz from the Bode phase plot it was possible to build a calibration plot in the nanomolar range (from 100 nM). Despite the sensitivity should be further improve to reach the LMR prescribed, **this proof-of-concept study showed the ease of combining proteins bioreceptors with poly *Py-2-COOH-G-SPE*** for PFOA monitoring in water samples.

To better answer question *ii),* we first optimised a protocol for the electrosynthesis of conductive poly (Py-2-COOH) modifiers at G-SPE in 0.1 M SDS. The preliminary study of Py-2-COOH electropolymerisation show the key-role of the working conditions applied in the determination of the final properties of the polymer. By performing this polymerisation in SDS conductive modifiers were obtained, while using $NaClO_4$ insulating polymers were synthesised at the electrode surfaces. Delipidated hSA was covalently immobilised at the modified electrode via EDC/NHS coupling taking advantage from the free-carboxylic moieties of the polymer and the biorecognition layer was fully characterised by EIS. Py-2-COOH applicability in protein immobilisation strategies were further confirmed by the tests performed with OVA and Hb. The interpretation of the impedimetric data suggest that PFOA additions compacted the protein bioreceptor and facilitate the redox mediator access to the electrode surface, lowering the impedance of the solution/electrode interfacial region. To answer question *iii)*, this hypothesis was supported by the results obtained with SEC-SAXS analysis of the dhSA-PFOA complex. The applicability of this sensing strategy can be further improved by adding other surface electrode modifiers, such as nanomaterials or electroactive labels, to enhance the sensitivity or modifying the dhSA receptor with protein engineering techniques, as anticipated in **Chapter 3**.

Acknowledgments and Collaborations

*We gratefully acknowledge Sonia Covaceuszach and Alberto Cassetta from the CNR for the SEC-SAXS analysis and data elaboration. Thanks to Fabio Bottari for having followed all steps and challenges of the design of this impedimetric sensing strategy. I am thankful to all professors and colleagues who took part in the **9th International Workshop on Surface Modification for Chemical and Biochemical Sensing** (Poland) in 2019 and in particular the scientific commission that awarded this poster communication motivating me to finalise this work. Special thanks to Prof. L. Jeuken, Prof. A. Kuhn, Prof. E. Lojou, Prof. F. Lisdat, Dr. F. Conzuelo, Prof. I. Palchetti and Dr. A. Giannetti for the precious tips!*

References

[1] L. Maso, M. Trande, S. Liberi, G. Moro, E. Daems, S. Linciano, F. Sobott, S. Covaceuszach, A. Cassetta, S. Fasolato, L.M. Moretto, K. De Wael, L. Cendron, A. Angelini, Unveiling the binding mode of perfluorooctanoic acid to human serum albumin, Protein Sci. (2021). https://doi.org/10.1002/pro.4036.

[2] E. Daems, G. Moro, H. Berghmans, L.M. Moretto, S. Dewilde, A. Angelini, F. Sobott, K. De Wael, Native mass spectrometry for the design and selection of protein bioreceptors for perfluorinated compounds, Analyst. 146 (2021) 2065–2073. https://doi.org/10.1039/D0AN02005B.

[3] S. Chen, A. Li, L. Zhang, J. Gong, Molecularly imprinted ultrathin graphitic carbon nitride nanosheets-Based electrochemiluminescence sensing probe for sensitive detection of perfluorooctanoic acid, Anal. Chim. Acta. 896 (2015). https://doi.org/10.1016/j.aca.2015.09.022.

[4] C. Fang, Z. Chen, M. Megharaj, R. Naidu, Potentiometric detection of AFFFs based on MIP, Environ. Technol. Innov. 5 (2016) 52–59. https://doi.org/https://doi.org/10.1016/j.eti.2015.12.003.

[5] J. Gong, T. Fang, D. Peng, A. Li, L. Zhang, A highly sensitive photoelectrochemical detection of perfluorooctanic acid with molecularly imprined polymer-functionalized nanoarchitectured hybrid of AgI–BiOI composite, Biosens. Bioelectron. 73 (2015) 256–263. https://doi.org/https://doi.org/10.1016/j.bios.2015.06.008.

[6] F. Cao, L. Wang, Y. Tian, F. Wu, C. Deng, Q. Guo, H. Sun, S. Lu, Synthesis and evaluation of molecularly imprinted polymers with binary functional monomers for the selective removal of perfluorooctanesulfonic acid and perfluorooctanoic acid, J. Chromatogr. A. 1516 (2017) 42–53. https://doi.org/https://doi.org/10.1016/j.chroma.2017.08.023.

[7] L. Zheng, Y. Zheng, Y. Liu, S. Long, L. Du, J. Liang, C. Huang, M.T. Swihart, K. Tan, Core-shell quantum dots coated with molecularly imprinted polymer for selective photoluminescence sensing of perfluorooctanoic acid, Talanta. 194 (2019) 1–6. https://doi.org/https://doi.org/10.1016/j.talanta.2018.09.106.

[8] N. Cennamo, G. D'Agostino, F. Sequeira, F. Mattiello, G. Porto, A. Biasiolo, R. Nogueira, L. Bilro, L. Zeni, A Simple and Low-Cost Optical Fiber Intensity-Based Configuration for Perfluorinated Compounds in Water Solution, Sensors (Basel). 18 (2018) 3009. https://doi.org/10.3390/s18093009.

[9] X. Liu, M. Fang, F. Xu, D. Chen, Characterization of the binding of per- and poly-fluorinated substances to proteins: A methodological review, TrAC - Trends Anal. Chem. 116 (2019) 177–185. https://doi.org/10.1016/j.trac.2019.05.017.

[10] M. Salvalaglio, I. Muscionico, C. Cavallotti, Determination of energies and sites of binding of PFOA and PFOS to human serum albumin, J. Phys. Chem. B. 114 (2010) 14860–14874. https://doi.org/10.1021/jp106584b.

[11] Q. Chi, Z. Li, J. Huang, J. Ma, X. Wang, Interactions of perfluorooctanoic acid and perfluorooctanesulfonic acid with serum albumins by native mass spectrometry, fluorescence and molecular docking, Chemosphere. 198 (2018) 442–449. https://doi.org/10.1016/j.chemosphere.2018.01.152.

[12] C.-M. Wu, L.-Y. Lin, Utilization of albumin-based sensor chips for the detection of metal content and characterization of metal–protein interaction by surface plasmon resonance, Sensors Actuators B Chem. 110 (2005) 231–238. https://doi.org/https://doi.org/10.1016/j.snb.2005.01.047.

[13] N.U. Amin, H.M. Siddiqi, Y. Kun Lin, Z. Hussain, N. Majeed, Bovine Serum Albumin Protein-Based Liquid Crystal Biosensors for Optical Detection of Toxic Heavy Metals in Water, Sensors . 20 (2020). https://doi.org/10.3390/s20010298.

[14] C. He, M. Xie, F. Hong, X. Chai, H. Mi, X. Zhou, L. Fan, Q. Zhang, T. Ngai, J. Liu, A highly sensitive glucose biosensor based on gold nanoparticles/bovine serum albumin/Fe3O4 biocomposite nanoparticles, Electrochim. Acta. 222 (2016) 1709–1715. https://doi.org/https://doi.org/10.1016/j.electacta.2016.11.162.

[15] Z. Tang, Y. Fu, Z. Ma, Bovine serum albumin as an effective sensitivity enhancer for peptide-based amperometric biosensor for ultrasensitive detection of prostate specific antigen, Biosens. Bioelectron. 94 (2017) 394–399. https://doi.org/https://doi.org/10.1016/j.bios.2017.03.030.

[16] R. Wang, X. Zhou, X. Zhu, C. Yang, L. Liu, H. Shi, Isoelectric Bovine Serum Albumin: Robust Blocking Agent for Enhanced Performance in Optical-Fiber Based DNA Sensing, ACS Sensors. 2 (2017) 257–

262. https://doi.org/10.1021/acssensors.6b00746.

[17] M. V Riquelme, H. Zhao, V. Srinivasaraghavan, A. Pruden, P. Vikesland, M. Agah, Optimizing blocking of nonspecific bacterial attachment to impedimetric biosensors, Sens. Bio-Sensing Res. 8 (2016) 47–54. https://doi.org/https://doi.org/10.1016/j.sbsr.2016.04.003.

[18] Y.-H. Liu, H.-N. Li, W. Chen, A.-L. Liu, X.-H. Lin, Y.-Z. Chen, Bovine Serum Albumin-Based Probe Carrier Platform for Electrochemical DNA Biosensing, Anal. Chem. 85 (2013) 273–277. https://doi.org/10.1021/ac303397f.

[19] Y. He, Y. Liu, L. Cheng, Y. Yang, B. Qiu, L. Guo, Y. Wang, Z. Lin, G. Hong, Highly Reproducible and Sensitive Electrochemiluminescence Biosensors for HPV Detection Based on Bovine Serum Albumin Carrier Platforms and Hyperbranched Rolling Circle Amplification, ACS Appl. Mater. Interfaces. 13 (2021) 298–305. https://doi.org/10.1021/acsami.0c20742.

[20] A. Kłos-Witkowska, B. Akhmetov, N. Zhumangalieva, V. Karpinskyi, T. Gancarczyk, Bovine Serum Albumin stability in the context of biosensors, in: 2016 16th Int. Conf. Control. Autom. Syst., 2016: pp. 976–980. https://doi.org/10.1109/ICCAS.2016.7832427.

[21] J.S. Daniels, N. Pourmand, Label-free impedance biosensors: opportunities and challenges, Electroanalysis. 19 (2007) 1239–1257. https://doi.org/10.1002/elan.200603855.

[22] F. Ghorbani Zamani, H. Moulahoum, M. Ak, D. Odaci Demirkol, S. Timur, Current trends in the development of conducting polymers-based biosensors, TrAC Trends Anal. Chem. 118 (2019) 264–276. https://doi.org/https://doi.org/10.1016/j.trac.2019.05.031.

[23] M.H. Naveen, N.G. Gurudatt, Y.B. Shim, Applications of conducting polymer composites to electrochemical sensors: a review, Appl. Mater. Today. 9 (2017) 419–433. https://doi.org/10.1016/j.apmt.2017.09.001.

[24] A.C. Gálvez-Iriqui, M.O. Cortez-Rocha, A. Burgos-Hernández, M. Calderón-Santoyo, W.M. Argüelles-Monal, M. Plascencia-Jatomea, Synthesis of chitosan biocomposites loaded with pyrrole-2-carboxylic acid and assessment of their antifungal activity against Aspergillus niger, Appl. Microbiol. Biotechnol. 103 (2019) 2985–3000. https://doi.org/10.1007/s00253-019-09670-w.

[25] J. Qin, D.G. Jo, M. Cho, Y. Lee, Monitoring of early diagnosis of Alzheimer's disease using the cellular prion protein and poly(pyrrole-2-carboxylic acid) modified electrode, Biosens. Bioelectron. 113 (2018) 82–87. https://doi.org/10.1016/j.bios.2018.04.061.

[26] A. Kausaite-Minkstimiene, L. Glumbokaite, A. Ramanaviciene, E. Dauksaite, A. Ramanavicius, An Amperometric Glucose Biosensor Based on Poly (Pyrrole-2-Carboxylic Acid)/Glucose Oxidase Biocomposite, Electroanalysis. 30 (2018) 1642–1652. https://doi.org/10.1002/elan.201800044.

[27] M.J.E. Fischer, Amine Coupling Through EDC/NHS: A Practical Approach BT - Surface Plasmon Resonance: Methods and Protocols, in: N.J. Mol, M.J.E. Fischer (Eds.), Humana Press, Totowa, NJ, 2010: pp. 55–73. https://doi.org/10.1007/978-1-60761-670-2_3.

[28] S. Rengaraj, Á. Cruz-Izquierdo, J.L. Scott, M. Di Lorenzo, Impedimetric paper-based biosensor for the detection of bacterial contamination in water, Sensors Actuators B Chem. 265 (2018) 50–58. https://doi.org/https://doi.org/10.1016/j.snb.2018.03.020.

[29] M. Foschini, H.S. Silva, R.A. Silva, A. Marletta, D. Gonçalves, Theoretical and experimental studies on the electronic, optical, and structural properties of poly-pyrrole-2-carboxylic acid films, Chem. Phys. 425 (2013) 91–95. https://doi.org/https://doi.org/10.1016/j.chemphys.2013.08.006.

[30] S. Sadki, P. Schottland, N. Brodie, G. Sabouraud, The mechanisms of pyrrole electropolymerization, Chem. Soc. Rev. 29 (2000) 283–293. https://doi.org/10.1039/A807124A.

[31] G.K. Chandler, D. Pletcher, The electrodeposition of metals onto polypyrrole films from aqueous solution, J. Appl. Electrochem. 16 (1986) 62–68. https://doi.org/10.1007/BF01015984.

[32] T.F. Otero, J. Rodríguez, Parallel kinetic studies of the electrogeneration of conducting polymers: mixed materials, composition and properties control, Electrochim. Acta. 39 (1994) 245–253. https://doi.org/https://doi.org/10.1016/0013-4686(94)80060-X.

[33] L.F. Warren, D.P. Anderson, Polypyrrole Films from Aqueous Electrolytes: The Effect of Anions upon Order, J. Electrochem. Soc. 134 (1987) 101–105. https://doi.org/10.1149/1.2100383.

[34] Y. Li, J. Yang, Effect of electrolyte concentration on the properties of the electropolymerized polypyrrole films, J. Appl. Polym. Sci. 65 (1997) 2739–2744. https://doi.org/10.1002/(sici)1097-4628(19970926)65:13<2739::aid-app16>3.3.co;2-u.

[35] J.M. Pernaut, R.C.D. Peres, V.F. Juliano, M.-A. De Paoli, Electrochemical study of polypyrrole/dodecyl

sulphate, J. Electroanal. Chem. Interfacial Electrochem. 274 (1989) 225–233. https://doi.org/https://doi.org/10.1016/0022-0728(89)87043-3.

[36] D.-H. Han, H.J. Lee, S.-M. Park, Electrochemistry of conductive polymers XXXV: Electrical and morphological characteristics of polypyrrole films prepared in aqueous media studied by current sensing atomic force microscopy, Electrochim. Acta. 50 (2005) 3085–3092. https://doi.org/https://doi.org/10.1016/j.electacta.2004.10.085.

[37] H. Chen, P. He, H. Rao, F. Wang, H. Liu, J. Yao, Systematic investigation of the toxic mechanism of PFOA and PFOS on bovine serum albumin by spectroscopic and molecular modeling, Chemosphere. 129 (2015) 217–224. https://doi.org/10.1016/j.chemosphere.2014.11.040.

[38] G. Moro, F. Bottari, S. Liberi, S. Covaceuszach, A. Cassetta, A. Angelini, K. De Wael, L. Maria, Covalent immobilization of delipidated human serum albumin on poly (pyrrole-2-carboxylic) acid film for the impedimetric detection of perfluorooctanoic acid, Bioelectrochemistry. 134 (2020) 107540. https://doi.org/10.1016/j.bioelechem.2020.107540.

[39] R.F. Chen, Removal of Fatty Acids from Serum Albumin by Charcoal Treatment, J. Biol. Chem. 242 (1967) 173–181. https://doi.org/https://doi.org/10.1016/S0021-9258(19)81445-X.

[40] B.A. Boukamp, Practical application of the Kramers-Kronig transformation on impedance measurements in solid state electrochemistry, Solid State Ionics. 62 (1993) 131–141. https://doi.org/10.1016/0167-2738(93)90261-Z.

[41] P. Agarwal, Application of Measurement Models to Impedance Spectroscopy, J. Electrochem. Soc. 142 (1995) 4159. https://doi.org/10.1149/1.2048479.

[42] C.E. Blanchet, A. Spilotros, F. Schwemmer, M.A. Graewert, A. Kikhney, C.M. Jeffries, D. Franke, D. Mark, R. Zengerle, F. Cipriani, S. Fiedler, M. Roessle, D.I. Svergun, Versatile sample environments and automation for biological solution X-ray scattering experiments at the P12 beamline (PETRA III, DESY), J. Appl. Crystallogr. 48 (2015) 431–443. https://doi.org/10.1107/S160057671500254X.

[43] A. Panjkovich, D.I. Svergun, CHROMIXS: automatic and interactive analysis of chromatography-coupled small-angle X-ray scattering data, Bioinformatics. 34 (2018) 1944–1946. https://doi.org/10.1093/bioinformatics/btx846.

[44] D. Franke, M. V. Petoukhov, P. V. Konarev, A. Panjkovich, A. Tuukkanen, H.D.T. Mertens, A.G. Kikhney, N.R. Hajizadeh, J.M. Franklin, C.M. Jeffries, D.I. Svergun, ATSAS 2.8: A comprehensive data analysis suite for small-angle scattering from macromolecular solutions, J. Appl. Crystallogr. 50 (2017) 1212–1225. https://doi.org/10.1107/S1600576717007786.

[45] P. V. Konarev, V. V. Volkov, A. V. Sokolova, M.H.J. Koch, D.I. Svergun, PRIMUS: A Windows PC-based system for small-angle scattering data analysis, J. Appl. Crystallogr. 36 (2003) 1277–1282. https://doi.org/10.1107/S0021889803012779.

[46] Y. Wang, H. Yu, X. Shi, Z. Luo, D. Lin, M. Huang, Structural mechanism of ring-opening reaction of glucose by human serum albumin, J. Biol. Chem. 288 (2013) 15980–15987. https://doi.org/10.1074/jbc.M113.467027.

[47] D. Svergun, C. Barberato, M.H.J. Koch, CRYSOL - a Program to Evaluate X-ray Solution Scattering of Biological Macromolecules from Atomic Coordinates, J. Appl. Crystallogr. 28 (1995) 768–773. https://doi.org/10.1107/S0021889895007047.

[48] G. Moro, D. Cristofori, F. Bottari, E. Cattaruzza, K. De Wael, L.M. Moretto, Redesigning an electrochemical MIP sensor for PFOS: Practicalities and pitfalls, Sensors (Switzerland). 19 (2019). https://doi.org/10.3390/s19204433.

[49] Y.F. Xing, S.J. O'Shea, S.F.Y. Li, Electron transfer kinetics across a dodecanethiol monolayer self assembled on gold, J. Electroanal. Chem. 542 (2003) 7–11. https://doi.org/10.1016/S0022-0728(02)01440-7.

[50] Y. Kong, W. Zhao, S. Yao, J. Xu, W. Wang, Z. Chen, Molecularly imprinted polypyrrole prepared by electrodeposition for the selective recognition of tryptophan enantiomers, J. Appl. Polym. Sci. 115 (2010). https://doi.org/10.1002/app.31165.

[51] K.K. Tadi, R.V. Motghare, V. Ganesh, Electrochemical Detection of Sulfanilamide Using Pencil Graphite Electrode Based on Molecular Imprinting Technology, Electroanalysis. 26 (2014). https://doi.org/10.1002/elan.201400251.

[52] C. Deslouis, M.M. Musiani, B. Tribollet, Free-Standing Membranes for the Study of Electrochemical Reactions Occurring at Conducting Polymer/Electrolyte Interfaces, J. Phys. Chem. 100 (1996) 8994–

8999. https://doi.org/10.1021/jp953154n.

[53] A. Ramanavicius, A. Finkelsteinas, H. Cesiulis, A. Ramanaviciene, Electrochemical impedance spectroscopy of polypyrrole based electrochemical immunosensor, Bioelectrochemistry. 79 (2010) 11–16. https://doi.org/https://doi.org/10.1016/j.bioelechem.2009.09.013.

[54] C. Deslouis, M.M. Musiani, B. Tribollet, M.A. Vorotyntsev, Comparison of the AC Impedance of Conducting Polymer Films Studied as Electrode - Supported and Freestanding Membranes Comparison of the AC Impedance of Conducting Polymer Films Studied as Electrode-Supported and Freestanding Membranes, (1995) 0–7.

[55] S. Jokar, A. Pourjavadi, M. Adeli, Albumin–graphene oxide conjugates; carriers for anticancer drugs, RSC Adv. 4 (2014) 33001–33006. https://doi.org/10.1039/C4RA05752J.

[56] V. Militello, C. Casarino, A. Emanuele, A. Giostra, F. Pullara, M. Leone, Aggregation kinetics of bovine serum albumin studied by FTIR spectroscopy and light scattering, Biophys. Chem. 107 (2004) 175–187. https://doi.org/https://doi.org/10.1016/j.bpc.2003.09.004.

[57] R. Lu, W.-W. Li, A. Katzir, Y. Raichlin, H.-Q. Yu, B. Mizaikoff, Probing the secondary structure of bovine serum albumin during heat-induced denaturation using mid-infrared fiberoptic sensors, Analyst. 140 (2015) 765–770. https://doi.org/10.1039/C4AN01495B.

[58] N. Ardiarini, S. Harimurti, FTIR study of secondary structure of bovine serum albumin and ovalbumin FTIR study of secondary structure of bovine serum albumin and ovalbumin, (2016) 0–6. https://doi.org/10.1088/1742-6596/769/1/012016.

[59] Q. Xie, C. Xiang, Y. Yuan, Y. Zhang, L. Nie, S. Yao, A novel dual-impedance-analysis EQCM system—investigation of bovine serum albumin adsorption on gold and platinum electrode surfaces, J. Colloid Interface Sci. 262 (2003) 107–115. https://doi.org/https://doi.org/10.1016/S0021-9797(03)00196-6.

[60] J. Ghuman, P.A. Zunszain, I. Petitpas, A.A. Bhattacharya, M. Otagiri, S. Curry, Structural basis of the drug-binding specificity of human serum albumin, J. Mol. Biol. 353 (2005) 38–52. https://doi.org/10.1016/j.jmb.2005.07.075.

[61] A.A. Bhattacharya, T. Grüne, S. Curry, Crystallographic analysis reveals common modes of binding of medium and long-chain fatty acids to human serum albumin, J. Mol. Biol. 303 (2000) 721–732. https://doi.org/10.1006/jmbi.2000.4158.

[62] E. Casero, A.M. Parra-Alfambra, M.D. Petit-Domínguez, F. Pariente, E. Lorenzo, C. Alonso, Differentiation between graphene oxide and reduced graphene by electrochemical impedance spectroscopy (EIS), Electrochem. Commun. 20 (2012) 63–66. https://doi.org/https://doi.org/10.1016/j.elecom.2012.04.002.

4.1 Annex A

Details of the SEC-SAXS analysis

Table A4.1. *SAXS structural parameters: radius of gyration (Rg), maximum dimension (Dmax), Porod volume (Vp), and Molecular Mass (MM). Dmax was obtained from the distribution function using GNOM; I(0) (scattering intensity) was obtained from the scattering data by the Guinier analysis.*

Data collection parameters	dhSA	dhSA/PFOA
Instrument	P12 (PETRA III)	
Beam geometry (mm^2)	0.2 x 0.12	
Wavelength (Å)	1.24	
s range (Å^{-1})	0.003–0.445	
Concentration (mg/ mL)	9	
Temperature (K)	283	
Structural parameters		
I(0) (A.U.) [from Guinier]	15584±10	7634±12
Rg (A) [from Guinier]	**27.900±0.005**	**27.000±0.004**
Guinier sRg limits	0.986	1.11
Dmax (Å)	80±4	
Vp Porod volume estimate (Å^3)	110390±10000	109550±10000
Molecular mass determination (Da)		
MM [from Porod volume]	64900±6000	64400±6000
Calculated monomeric MM from sequence	66500	

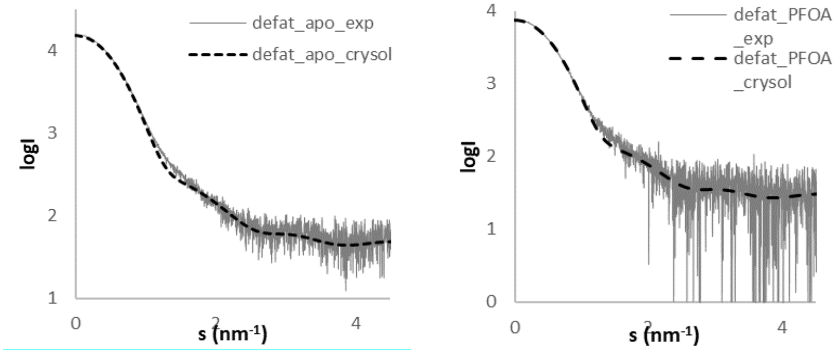

Figure A4.1. *Comparison of the crystallographic dhSA (dashed line) with experimental SEC-SAXS data for the apo form (left) and for the complex with PFOA (right), data analysis performed with CRYSOL* [47].

|5

Applying dhSA in electrochemical sensing: A haem-mediated strategy

Abstract

An in-depth understanding of protein-ligand interactions can help identifying new bioreceptors as well as potential electroactive probes for indirect detection strategies. Therefore, after designing an impedimetric-based sensor in ***Chapter 4****, we searched for possible redox probes to develop a voltammetric sensing strategy again using albumin as PFOA bioreceptor. Among the endogenous ligands carried by albumin, we have the haem group with its well-known reversible redox behaviour (described also in* ***Chapter 2****).*

In this chapter, we compared PFOA-albumin complex with haem-albumin one observing that the two ligands bind differentcorrelated FA sites. Once the PFOA binding pocket FA7 is occupied, the haem-binding site undergo a conformational change which hinders haem binding. These findings suggest the possibility to apply haem as redox probe in PFOA-albumin detection strategies. Haem-albumin complexes in presence/absence of PFOA were first screened by UV-Vis spectroscopy. Once verified the complex formation, haem was further characterised using electrochemical methods. The haem-albumin-PFOA system was studied in solution aiming to understand: the complexity of the multiple equilibria, the changes in binding kinetics and how these latter can be followed by considering the probe redox activity, the non-specific adsorption phenomena at stake, etc. The preliminary results suggest the possibility to apply haem as redox probe.

The approach proposed in this study consisted mainly of three steps: i) a comparative analysis of albumin-ligands crystallographic structures which provided the theoretical basis of our hypothesis; ii) a screening of the complexes in solution performed with UV-Vis spectroscopy and iii) an electrochemical study of haem redox behaviour in presence of different equilibria (haem-albumin, PFOA-albumin, etc.).

5.1 Introduction

The nonelectroactive nature of dhSA does not hinder the possibility of combining this bioreceptor with electrochemical sensing strategies other than the impedance-based one presented in **Chapter 4**. To design alternative strategies, we can include electroactive labels or probes, whose electrochemical behaviour can be easily recorded and directly linked to the presence/absence of dhSA-PFOA complex [1]. For instance, electroactive peptides with lower affinity for dhSA pockets than the target molecule can be designed and loaded in the protein bioreceptor [2]. When loaded inside the protein pockets, these peptides will not show any electrochemical signal because they are *buried* among the hydrophobic chains of dhSA. In presence of the target, the peptides will be gradually released and this event can be followed by recording their electrochemical response, allowing a semi-quantitative detection of the analyte.

This biosensing platform, as well as the impedimetric and optical ones (**Chapter 4** and **Chapter 6**), required a high control of **non-specific** and **bio-specific protein adsorption processes**, which occur at the electrode surface and can affect deeply the signal recorded [3]. It is worth noting that most sensing surfaces (from SPR to electrode ones) are prone to non-specific adsorption (NSA) of proteins [4]. NSA happens when a molecule adsorbs to the surface of a sensing platform in an irreversible way. This leads to a high background signal which is indiscernible from the specific binding one, affecting the sensor in terms of sensitivity, selectivity and reproducibility [5]. In the other strategies described the albumin bioreceptors were immobilised at an electrode (**Chapter 4**) or an optical fiber surface (**Chapter 6**) and NSA effects were limited by including several washings and rinsing steps and covering the bare surfaces with polymeric layers which partially prevent these phenomena. Therefore, for the impedimetric and optical platform the contribution of NSA will be further considered during the optimisation steps. We introduce NSA in this chapter because the proof-of-concept voltammetric study reported here was carried out in solution, without immobilising the dhSA. In these conditions, NSA-related contributions need to be carefully evaluated since the first preliminary experiments and eventually reduced by the help of electrode surface modifiers. In the last decades, Vörös and co-workers dedicated many efforts to the description of NSA physisorption mechanism with different methods following its kinetics and proving *how* the introduction of surface-active copolymers as well as peptides arrays can limit NSA phenomena [6–8]. A complete overview of *how* NSA was characterised and overcome in the last five decades was recently published by Frutiger *et al.*, underling that NSA is still a **bottleneck** in sensing and **biosensing design** [9].

Before considering designing synthetic probes, naturally occurring and commercially available electroactive labels, such as hemin, should be tested. **Hemin [iron (III) protoporphyrin (IX) chloride]** is a coordination complex structurally equivalent to the prosthetic group of haemoglobins (*haem b*): it has a ferric centre (Fe^{3+}) coordinated with a tetradentate protoporphyrin ring and an axial chloride atom (**Figure 5.1A**).

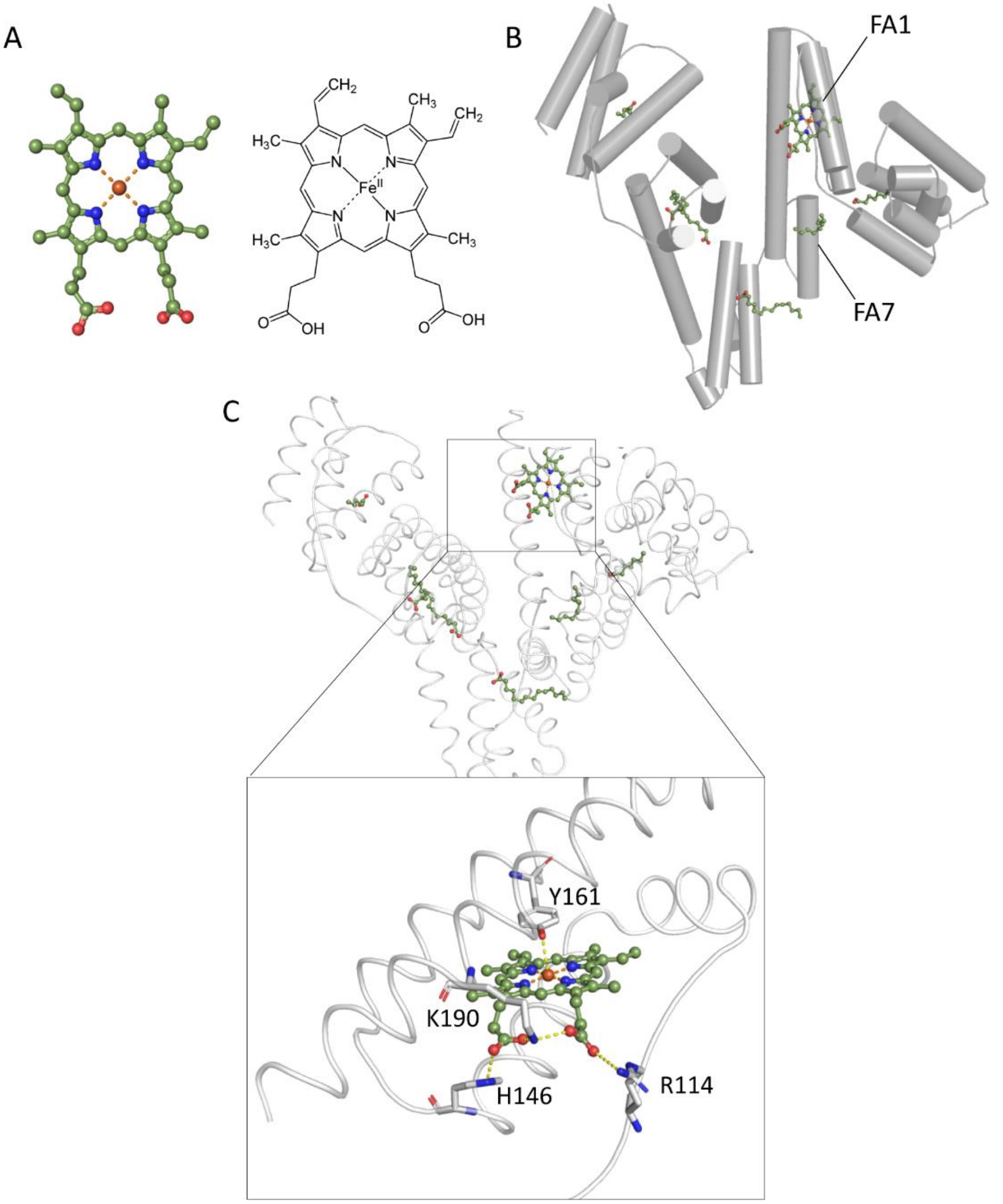

Figure 5.1 *Structure of hemin-albumin complex (PDB ID: 1O9X): (**A**) detail of hemin structure and (**B)** hemin bound to the site FA1 in the subdomain IB of hSA. (**C**) Structure of hemin-albumin complex with a close-up view of hemin interactions with the hydrophobic residues of pocket FA1 according to Zunszain et al.* [10]. *The three-dimensional structure model was generated and rendered using PyMOL*[11].

Endogenously produced in our body, hemin can bind several proteins, such as hemopexin [12] and albumin [13]. High purity hemin is obtained from bovine substance salt. It possesses a chloride ligand in the fifth coordination site of Fe(III) in place of histidine in the natural protein and is involved in binding interactions with serum proteins, such as albumins, to form methemalbumin [14]. In medical treatments, hemin is mostly applied in the management of porphyria attacks in formulation such as *Human Hemin,* particularly suggested for acute intermittent porphyria [15]. Pharmacological studies confirmed that most **porphyrin compounds** are able to form **strong intermolecular complexes with proteins** [16]. Porphyrins show a poor water-solubility, thus the binding to serum proteins can increase their solubility.

According to Komatsu *et al.* [10], the features of the α-helical pockets of albumin are similar, in terms of hydrophobicity, to those of haem-binding sites of haemoglobin and myoglobin. This promotes hemin binding to the site **FA1 of albumin**, a narrow D-shaped hydrophobic cavity located in subdomain IB [17], as shown in **Figure 5.1B**. The crystallographic analysis of hemin-albumin complexes showed that the protoporphyrin ring interacts with the hydrophobic side-chains of the pocket residues [18].

In **Figure 5.1C**, we can observe that the central Fe^{3+} atom coordinates with the hydroxyl group of tyrosine 161 (Y161) and the two propionate groups are co-coordinated by three basic residues oriented towards the pocket entrance (R114, H146 and K190). The binding event is followed by a slight expansion of subdomain IB (1.4 Å separation increase in helices 8 and 10) that was observed also in presence of fatty acids, so hemin binding does not alter the conformation (no deep/specific changes in the protein quaternary structure). On the contrary, Baroni *et al.* [19] first observed that the binding of certain drugs, such as warfarin and ibuprofen, to the hSA induces conformational changes, which **affect haem transfer kinetics** with meaningful variations of the K_D values going from $(1.3 \pm 0.2) \times 10^{-8}$ M^{-1} in absence of the drugs to $(1.5 \pm 0.2) \times 10^{-7}$ M^{-1} in presence of both warfarin and ibuprofen. These drugs are known to bind to Sudlow's site I (FA7) and II (FA3-4), respectively, inducing the N (normal) or the B (basic) conformation transition in hSA. Their molecular interactions with hSA were fully elucidated in literature and the comparison of warfarin-albumin and hemin-albumin complexes is reported in **Figure 5.2**, as an example [20–22].

Why this comparison is interesting to us? In 2005, Ascenzi *et al.* [23] performed an extensive study showing that the presence of drugs (particularly the ones binding site Sudlow's I) leads to a **decrease in the association equilibrium constants** of haem binding by one order of magnitude (K_A varies from about 8×10^7 M^{-1} to 7×10^6 M^{-1}). This behaviour was ascribed to the ligand-dependent allosteric changes particularly self-evident because of the spatial proximity between the FA1 (haem cleft) and site Sudlow's I (see **Figure 5.2 A-D**). In **Figure 5.2 D**, we can clearly see a differences in the helices distances between hemin-albumin and warfarin-albumin complexes. It is worth noting that two residues (H146 and R114) are not visible in warfarin-albumin structure, as they are not coordinated and possibly exposed to the solvent.

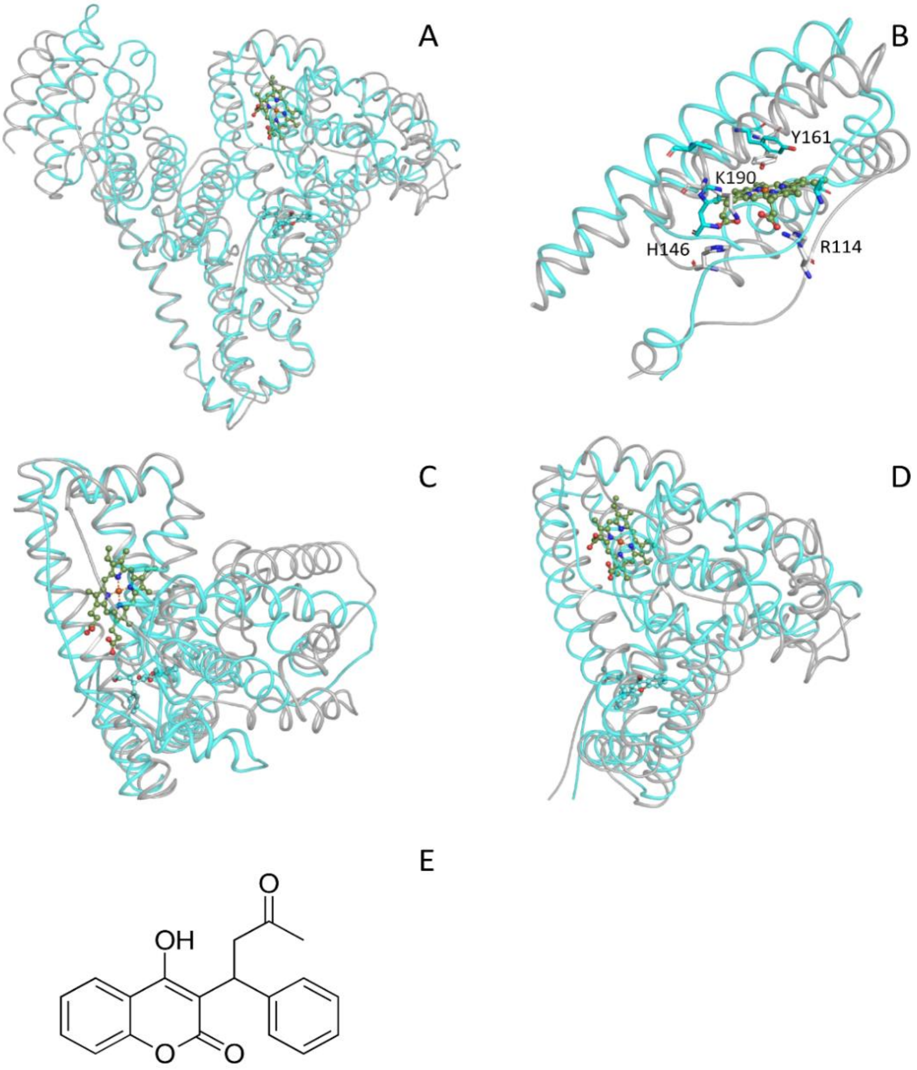

Figure 5.2 *(**A-C-D**) Structure of has-warfarin complex with different orientation, (PDB ID: 2BXD); (**B**) Visual comparison of the spatial distribution of the chains of subdomains IB, IA and IIA in hSA-warfarin complex (light blue) and hemin-hSA (light grey) obtained by PyMOL (sequence alignment, PDB: 2BXD and 1O9X)*[11]. *In all structures, hemin was reported as a reference to underline the changes in FA1 pocket folding* [20,24]. *(**E**) Warfarin structure.*

Their increased mobility can explain the lack of a well-defined electron density of these amino acid residues. Further studies were carried out to characterise the changes in the enzymatic activity of haem-albumin in presence of common therapeutics leading to a complete description of these systems instrumental to design medical treatments and pharmacokinetics studies [24].

In our study, these findings can be partially transposed by considering the similarity between the drugs reported and our contaminant, the PFOA, in terms of albumin-binding mechanism/sites. Indeed, in **Chapter 3** we saw that PFOA can bind FA7 as well as FA3-4, therefore also PFOA might affect the kinetic of hemin binding to dhSA, as observed for warfarin.

If **haem-albumin binding kinetic is affected by the presence of PFOA**, as in the case of warfarin [19], hemin could possibly be used as an electroactive label in PFOA biosensing by recording the changes in its electrochemical behaviour when dhSA or dhSA-PFOA are in solution. On one hand, we expect to observe a variation (a current decrease in the best-case scenario) after the addition of dhSA to hemin solution because haem-albumin complex will be easily formed and the electron transfer of hemin iron centre will be partially hindered by dhSA hydrophobic pocket. On the other hand, when dhSA-PFOA complex is added (loading dhSA with PFOA in a previous step), hemin binding will be affected by the presence of PFOA and hemin electrochemical signals will possibly decrease less than with dhSA only. Of course, these equilibria can be affected by other phenomena, such as NSA. To clearly correlate the hemin signal changes to the formation of complexes with dhSA or PFOA-dhSA, hemin electrochemistry needs to be carefully characterised using different analytical methods.

So far hemin-albumin complexes have been studied mainly via crystallography, NMR, EPR, UV-Vis and fluorescence spectroscopy [25], thus there are many analytical techniques we can possibly apply in this study, complementary to electrochemical ones. Among these, **UV-Vis spectroscopy** allows to follow albumin-hemin complex formation in solution with all the advantages of an easily-available analytical method. The changes in the equilibria in solution can also be followed considering the quasi-reversible electrochemical behaviour of hemin, which was previously described in **Chapter 2** [26].

Aiming to verify these hypotheses and to evaluate the applicability of hemin in dhSA-PFOA sensing, a preliminary study was carried out. Firstly, the influence of PFOA on hemin-dhSA binding kinetics was monitored by UV-Vis spectroscopy. Secondly, the quasi-reversible electrochemical behaviour of hemin was fully characterised and the electron transfer kinetics was estimated using the Laviron formalism [27]. Thirdly, the possibility to follow hemin-dhSA complex formation through hemin electrochemistry was evaluated in solution. To mimic the working conditions of the UV-Vis tests, dhSA and dhSA-PFOA aliquots were added to a hemin solution monitoring the changes in voltammetric response. This setup allowed avoiding the possible drawbacks of dhSA confinement at the electrode surface that will be considered in a second phase of this study.

5.2 Materials and Methods

5.2.1 Chemicals

Perfluorooctanoic acid (PFOA, ≥96%), perfluorooctanesulfonic acid potassium salt (PFOS, ≥98%) and hemin (from bovine, ≥90%) were purchased from Sigma−Aldrich Ltd (Belgium). Highly purified delipidated human serum albumin (dhSA) was obtained as described in **Chapter 3**. All the other reagents were of analytical grade and used as received. The 0.1 M phosphate buffer saline solution pH 7.4 with 0.01 NaCl was prepared by mixing stock solutions of 0.1 M NaH_2PO_4 and 0.1 M Na_2HPO_4, purchased from Sigma Aldrich. All aqueous solutions were prepared using MilliQ water (R > 18 MΩ cm).

5.2.2 UV-Vis and Electrochemical Setup

The electronic absorption spectra in the UV-visible region were acquired using an AvaLight-DH-S-BAL deuterium-halogen light source, coupled with an Avaspec-2048L detector with a 20 μm slit, using a fibre optics set-up. All measurements were recorded in 15 mL solution, using a 10 mm pathlength quartz cuvette (100-QS cuvette, Hellma Analytics). Blank solvent corrections were made before recording the spectra of each sample and all measurements were recorded under gentle stirring. For the kinetic study, a fixed volume of dhSA or dhSA-PFOA solutions was added to the hemin solution and let equilibrate for five minutes (300 s) recording a spectrum every second. Data were collected within the wavelength range 250-900 nm, considering that the primary region of interest is the Soret band of porphyrin centred at about 400 nm. All spectra were treated with Orange and Origin 2018 software.

5.2.3 Electrochemical Study

All electrochemical measurements were carried out using a Metrohm Autolab potentiostat/galvanostat (PGSTAT 302 N, Metrohm Autolab, Utrecht, The Netherlands) controlled by NOVA 2.1 software. A standard three electrode configuration was used with glassy carbon electrode (GCE, diameter 3 mm) as working electrode, platinum wire as counter electrode and saturated calomel (KCl sat.) as reference. The GCE were polished using alumina slurries (0.3, 0.1, 0.05 µm) with intermediate rinsing steps using Milli Q water immediately before the experiment. Hemin stock solution (5 mM) was prepared in 100 mM NaOH (porphyrins solubility increases at basic pHs) and diluted to 5 µM in 5 mL of phosphate buffered saline at pH 7. The solutions were bubbled with Ar for 20 minutes before starting the measurements and throughout measurements a Ar blanket was kept above the solution. A negative initial scan polarity was used for all voltammograms recorded because in these working conditions the reduction of hemin

Fe^{3+} to Fe^{2+} is the first process occurring, so the addition of electrons to the system in the initial scan step (negative polarity) facilitates the reduction. All CV were recorded in the potential window between -1.00 V and +0.2 V, with a starting potential of -0.01 V, at different scan rates (from 0.01 to 100 V s^{-1}). SWV scans were recorded at 8-18 Hz with a pulse amplitude of 25 mV and a step potential of 1 mV going from 0.0 V to -1.00 V (*forward scan*) and vice versa (*backward scan*). All voltammograms were collected at RT inside the Faraday cage.

5.3 Results and Discussion

To verify the hypothesis described in the introduction, we first followed the hemin binding in presence of dhSA and dhSA-PFOA by UV-Vis spectroscopy, confirming the complex formation in both cases and evidencing different kinetics. Afterwards, hemin electrochemical behaviour was studied via CV determining the electron transfer kinetics and, finally, the changes in SWV signal of hemin in presence/absence of dhSA and dhSA-PFOA were investigated.

5.3.1 UV-Vis Spectroscopy: Hemin-dhSA Complex

The macrocycle of porphyrin based-compounds, such as hemin, has a fully conjugated aromatic π-electron system which is responsible for: *i)* the characteristic strong absorption bands in near UV, namely *Soret* or *B band* (at about 400 nm) and *ii)* the lower bands in the visible region, namely *α* and *β Q-band* (at about 490-650 nm). All these electronic transitions are assigned using the four-orbital model of Gouteman as described by Dayer *et al.* [28]. The formation of porphyrin-protein complexes influences the electronic transitions of both, ligand and protein, and can be followed by considering the shifts in the absorption bands. Thus, UV–Vis absorption spectroscopy is particularly suitable for studying the structural changes and binding interactions in protein-aromatic compound systems. Here, the changes in the absorption spectra during the titration of hemin with albumin and albumin-PFOA were analysed considering the shifts in hemin characteristic bands, especially Soret one. For all these experiments, hemin solutions in PBS buffer were prepared by dilution of a stock in DMSO (100 µM). In **Figure 5.3** the spectra of a 10 µM hemin solution (see spectra *H*, *red line*) shows:

i) a low intensity band at about 265 nm,

ii) a band with a wavelength of maximum absorbance, λ_{max}, of 350 nm,

iii) a broad Soret band with a λ_{max} of 385 nm and

iv) a large, undefined band at about 600 nm.

According to Makarska-Bialokoz, the first band can be ascribed to the traces of the protein structure, as the hemin is extracted from bovine blood (with a purity > 90%) [25]. In organic solutions, the Soret band is more intense, defined and Gaussian-shaped because of the hydrophobic nature of hemin (*spectra not shown*), while in aqueous media hemin tends to aggregate [17]. The formation of hemin dimers and the occurrence of vibrionic coupling phenomena were previously correlated with the broadening of UV bands (which can even lead to a complete overlap of the band at 350 nm with the Soret one) [18]. Hemin spectrum presents a unique Q band at about 600 nm suggesting that α and β bands are merged due to vibrionic coupling. Because of their lower intensities, Q bands will not be further considered; the λ-region of interest for our study is the one reported in the inset of **Figure 5.3**.

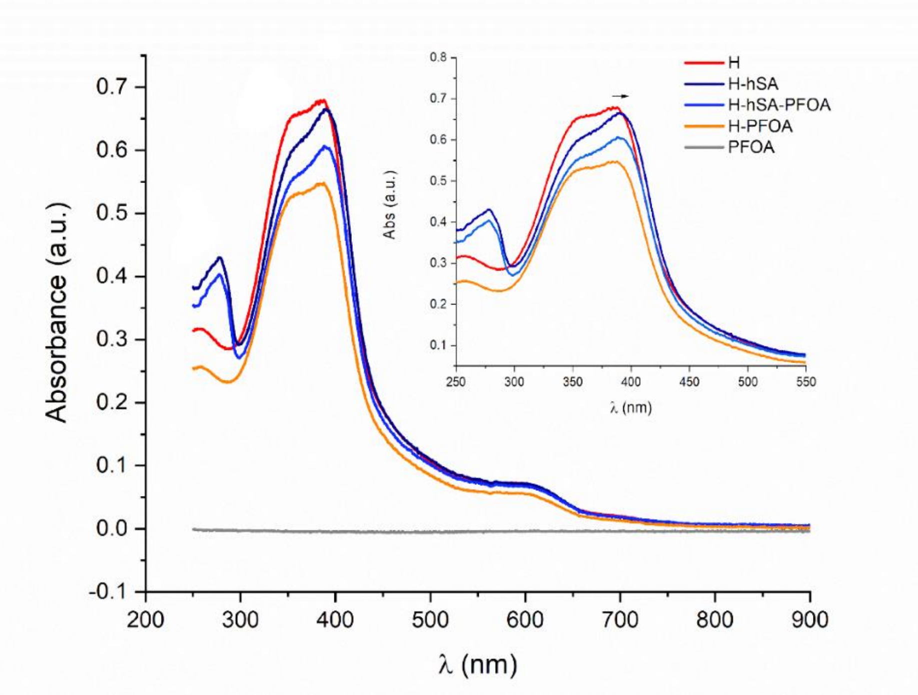

Figure 5.3 *UV-Vis absorption spectra of: 10 µM of hemin (H, red), 5:1 hemin: human serum albumin complex (H-hSA, navy blue), 5:1:50 hemin:dhSA:perflurooctanoic acid (H-hSA-PFOA, light blue) complex and negative control spectra of 1:2 hemin:PFOA (H-PFOA, orange) and PFOA (PFOA, grey). Inset: the region between 250 and 550 nm with the Soret absorption band of hemin.*

The intensity of hemin Soret band increased linearly with the concentration in the range tested, going from 0.5 µM to 35 µM. This trend confirmed the validity of Lambert-Beer's law in the concentration range under study and, therefore, the possibility to perform a kinetic study of hemin-serum proteins binding.

The addition of dhSA to the hemin solution with a hemin:dhSA ratio of 5:1 (see *H-hSA*, *blue navy line*, **Figure 5.3**) is followed by:

i) a **bathochromic shift**, also known as *red shift*, of the **Soret band** and

ii) the appearance of another well-defined band with λ_{max} at 278 nm.

The red shift of about 15 nm suggests the complex formation, also observed for hemin-α-microglobulin complexes [17]. In the UV-Vis study reported by Makarska-

Bialokoz, the hemin-bovine serum albumin (BSA) complex formation was followed by a more meaningful red shift of Soret band of about 26 nm (from 385 to 411 nm) [25]. Such shift was ascribed to the complex formation and the simultaneous change of the iron oxidation state in hemin. Indeed, the Soret band of hemin at 385 nm is associated with the ferric iron form of hemin, while when the ferrous iron form is present Soret band is at about 411 nm [29,30]. In our case, the λ_{max} obtained for the hemin-dhSA complex is of 400 nm, therefore the change in oxidation form of hemin iron cannot be clearly followed via UV-Vis spectroscopy. Further details about this aspect will be provided in the following electrochemical study. The band at 278 nm is ascribed to the intrinsic fluorescence of proteins determined by the presence of aromatic amino acids (such as tryptophan, tyrosine and phenylalanine). The presence of this band confirmed that dhSA is in its native state. When dhSA interacts with hemin, the intensity of this band increases (hyperchromatic shift) undergoing a blue shift of few nm (*data not shown*), as previously described for BSA. Our data are in good agreement with the previous literature.

Then, the screening of hemin-dhSA-PFOA complex was performed. Prior to add hemin solution, PFOA was incubated with dhSA (1:50 ratio) for 15 min, aiming to assure the formation of PFOA-dhSA complex. The UV-Vis spectrum recorded afterwards (see *H-dhSA-PFOA*, light blue, **Figure 5.3**) showed features similar to ones of hemin-dhSA complex. These findings confirmed the formation of the hemin-dhSA complex even in presence of PFOA, as expected. Indeed, the presence of the contaminant is not preventing the hemin to bind albumin but lowering the binding rate and kinetics. It is worth noting that Baroni *et al.* [7] were able to observe a blue shift in hemin Soret band in presence of warfarin and ibuprofen using relatively high concentrations of these drugs (about 0.05 M). However, in this test PFOA concentrations were between 100 and 500 µM because of the analytical context of interest and for consistency with the characterisation study presented in **Chapter 3**. As a negative control, hemin-PFOA (1:10) and PFOA solution were tested (*H-PFOA, orange* and *H*, grey **Figure 5.3**) showing that PFOA does not affect the typical Soret absorption band of hemin because no meaningful changes in the band λ_{max} were recorded. Also, DMSO and PBS spectra were recorded showing no contribution in the spectral region tested, as expected from the literature.

The kinetics of hemin binding to dhSA and dhSA-PFOA was followed by recording the absorbance at a fixed wavelength, corresponding to the maximum of the complex band, over a time-frame of 300 s starting from the t_0 (corresponding to the protein addition in hemin solution).

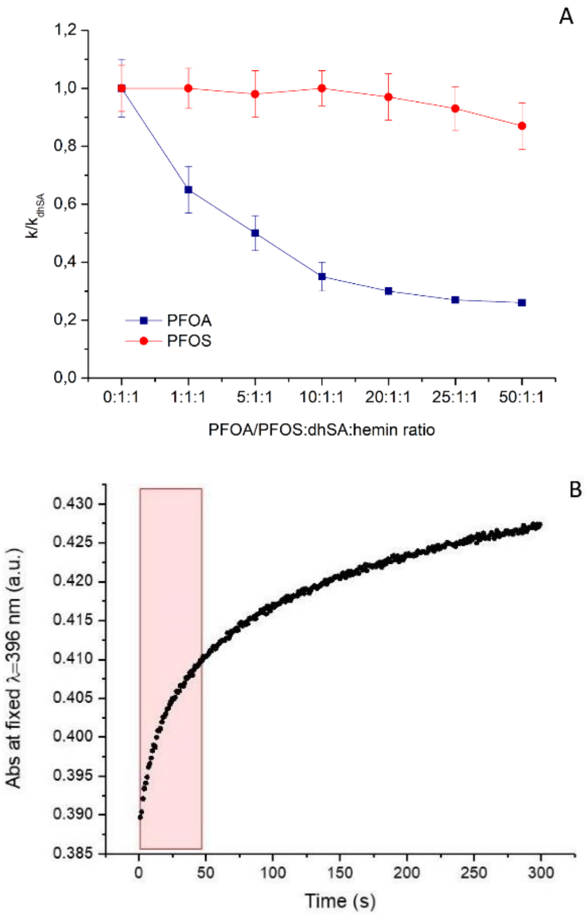

Figure 5.4 *Overview of the data obtained in the kinetics study at different PFOA ratios (**A**) with an example of the plots obtained during the hemin-dhSA (1:1 ratio) kinetic study (**B**): starting from the addition of dhSA to hemin solution the absorbance of the dhSA-hemin complex was followed over time (300s). The curve obtained (**B**) is characterised by a linear growth (0-50 s; inset: light red area) before going to saturation.*

The Abs *vs* time plots recorded at different PFOA ratios (exemplified in **Figure 5.4B**) are characterised by a consistent trend: a first linear increase (0-30 s) of the signal that goes toward saturation for t >30 s. The curves recorded in presence hemin with dhSA alone or dhSA-PFOA (where dhSA was previously incubated with different concentrations of PFOA) differed mainly in the first linear region. To simplify the data elaboration, only the linear region (0-30 s) was considered. The data were analysed using a first order kinetic reaction model. The kinetic constants were then normalized on the hemin-dhSA one to evaluate the changes in the complex formation “speed” upon different ratios of PFOA (these constants are not directly related to the K_D). In **Figure 5.4A**, a comparison of the k/k_{dhSA} values vs the different PFOA:dhSA:hemin ratios is reported. The results show a decrease in the k/k_{dhSA} upon increasing concentrations of PFOA. These finding seems to suggest that the formation of PFOA-dhSA complex and the presence of an excess of PFOA in solution are lowering the kinetic of hemin binding to dhSA. The 1:1:1 PFOA:dhSA:hemin ratio was found to lead to a decrease in the hemin binding kinetics of about 35%. Concerning the λ_{max}, blue shifts of 2-6 nm were observed for PFOA:dhSA:hemin ratios higher than 25:1:1. These findings confirmed that PFOA as well as warfarin and ibuprofen can affect the kinetics of hemin binding to albumin [19]. Thus, our first hypothesis is verified. As a control, also PFOS was tested to further prove that the reduction in the kinetic constant is associated to PFOA ability to bind the albumin pocket FA7 and alter the conformation of FA1 where hemin binds. PFOS has a different binding mechanism and affinity for albumin, as described in **Chapter 3**. As expected, in presence of PFOS no meaningful changes in the k/k_{dhSA} were observed upon increased PFOS ratios, as summarized in **Figure 5.4A**.

After these preliminary tests confirming the influence of PFOA on hemin-dhSA binding kinetics, we investigated if these multiple equilibria (hemin-albumin, albumin-PFOA, hemin-albumin-PFOA) can be followed considering hemin electroactive behaviour.

5.3.2 Probing the probe: hemin electrochemistry

Prior to correlate the changes in hemin electrochemical signal to the presence of dhSA, PFOA and the corresponding complexes, the electrochemistry of hemin in deaerated aqueous solutions was studied. This screening was very important because it allowed a first evaluation of the phenomena that might affect the redox signal of hemin probe, namely: *i)* the presence of oxygen traces leading to the formation of hemin adducts and, as consequence, to a more complex voltammetric pattern, as previously described [31,32], and *ii)* the NSA, particularly common when working with carbonaceous materials, such as glassy carbon electrodes [33]. The working conditions reported in **Section 5.2.3** were chosen to assure dhSA stability, but are not optimal for hemin, which is poorly soluble in aqueous media. For these reasons, it was fundamental to "*probe the probe"* by analysing the main features of its voltammetric responses (ΔE, $E_{1/2}$, etc.) as well as its electron transfer (ET) kinetic constants.

The cyclic voltammograms of hemin in PBS pH 7.4 under Ar atmosphere reported in **Figure 5.5A** show the reversibility of ferric–ferrous redox couple with a $E_{½}$ of about -0.56 V vs SCE and a ΔE between the cathodic (Fe^{3+} to Fe^{2+}) and anodic (Fe^{2+} to Fe^{3+}) peaks of ≈ 100 mV at 0.100 V s^{-1}. The one-electron, quasi-reversible nature of the redox process was confirmed [26]. From **Figure 5.5A**, it is possible to observe that the peak separation is increasing with the scan rate. To characterise the kinetic of the ET process and determine the electron-transfer rate constant (ks) of hemin, an extensive scan rate study was performed by CV in the range between 0.010 V s^{-1} and 100 V s^{-1}. A linear dependence of the cathodic and anodic peak current intensities (I_p) with the scan rate (*v*) was observed with r^2> 0.985 and r^2> 0.992, respectively (**Figure 5.5B**). By plotting Ip values vs the square root of the scan rate ($v^{1/2}$) a linear fit with r^2<0.89 was obtained.

For the application of Laviron formalism, the electrochemical process is required to be diffusionless [27,34] and consistent with Butler-Volmer model. This last requirement can be verified by checking the linearity of E_{peak} vs log v dependence at high scan rates. Once all requirements were found to be fulfilled, we elaborated the characteristic *trumpet* plot reported in **Figure 5.5C** by plotting the cathodic and anodic peak potentials vs the logarithm of the scan rate (log v).

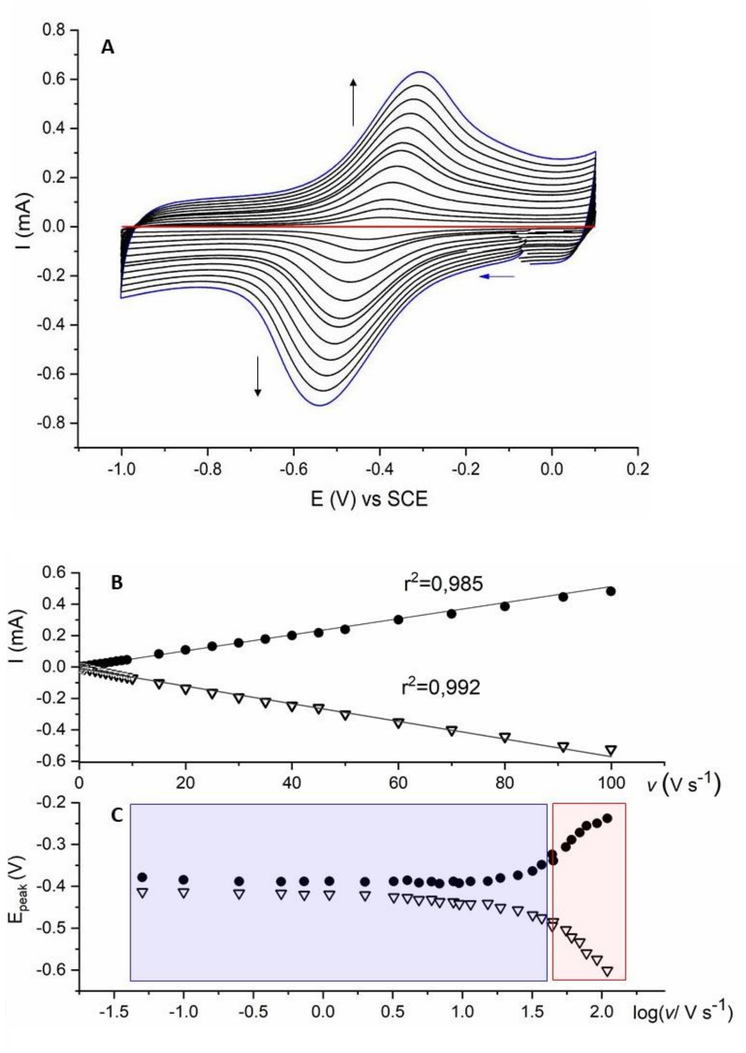

Figure 5.5 *(**A**) Overlap of the cyclic voltammograms recorded in 0.5 mM of hemin in PBS pH 7.4 at increasing scan rates (from red to blue: 0.01, 0.05, 0.1, 0.25, 0.5, 0.75, 1.0, 2.0, 3.0, 4.0, 5.0, 6.0, 7.0, 8.0, 9.0, 10.0, then with 5 V s^{-1} increments until 50 V s^{-1} and with 10 V s^{-1} increments until 100 V s^{-1} in blue); (**B**) Linear dependence of the cathodic (triangle) and anodic (dots) peak potential values on the scan rate; (**C**) Laviron trumpet plot showing the dependence of the cathodic (triangle) and anodic (dots) peak potential values on the logarithm of the scan rate, in light red data region in which the ΔE> 200/n mV condition is verified.*

The application of Laviron formalism offers two possible ways to determine the k_s of a quasi-reversible ET:
i) for ΔE > 200/n mV,
ii) for ΔE < 200/n mV, where n is the number of electrons involved in the ET.

For ΔE > 200/n mV, the ks is determined by:

$$ks = \frac{\alpha nFvc}{RT} = (1-\alpha)\frac{nFva}{RT} \qquad \text{(Equation 5.1)}$$

where α is the transfer coefficient describing the symmetry of the energy barrier of the redox reaction while R, T, F and n have their usual significance. The values of v_c and v_a are extrapolated from the linear part of E_p vs log v plot and correspond to the scan rate values (respectively cathodic, v_c, and anodic, v_a) at which the linear fittings of the cathodic and anodic branches intersect. In these conditions, the transfer coefficient can also be estimated from the cathodic or anodic branches considering the slope of their linear fitting [15]. Here, for simplicity, only the analysis of the cathodic branch will be reported, considering that:

$$\alpha = \frac{-2.3RT}{nF*slope} \qquad \text{(Equation 5.2)}$$

For ΔE < 200/n mV, the k_s can be calculated using **Equation 3**, in which m^{-1} values are tabulated [27] and depend on the average peak separation and the number of electrons involved in the ET process (ΔEn). Here, the scan rate, *v,* corresponds the point of intersection of the cathodic and anodic branches linear fitting ($v_a = v_c$) in the Ep vs log v plot of **Figure 5.5C**.

$$k_s = m\,(nv\frac{F}{RT}) \qquad \text{(Equation 5.3)}$$

In the present study, most Ep values present a ΔE < 200/n mV (blue box in **Figure 5.5C**). Considering these values, it was possible to estimate a k_s value for the ET of hemin of 15.5 ± 2.5 s^{-1}. The k_s was calculated also for the Ep values fulfilling condition ΔE > 200/n (red box in **Figure 5.5C**) obtaining a value of 19.4 ± 7.3 s^{-1}. In general, the k_s calculated from the trumpet plot by considering ΔE > 200/n values are higher than the one extrapolated using Eq. 3 as was previously reported [35]. In this particular case, it is worth noting that the k_s calculated using ΔE > 200/n values have an associate error higher than when calculated using values of ΔE < 200/n. This result can be ascribed to the limited range of data and the fact that, for scan rates higher than 50 V s^{-1}, the redox peaks are broader and less defined. Therefore, in the next steps the k_s values of hemin

ET in presence of dhSA and/or PFOA will be estimated considering only Ep values calculated for ΔE < 200/n mV.

5.3.3 Probing PFOA: is it possible?

Following the characterisation of hemin voltammetric behaviour, it is now time to see how the presence of dhSA and the formation of the hemin-dhSA complex affect the probe response and if other changes occur when dhSA is previously incubated with PFOA. This study was performed by CV and SWV keeping a fixed hemin concentration of 5 µM considering the hemin:dhSA, dhSA:PFOA, dhSA:PFOS ratios previously tested. The changes in the ET kinetics summarized in **Figure 5.6A** were evaluated using a 1:1 hemin:dhSA and a 1:1:10 hemin:dhSA:PFOA/PFOS ratios. Hemin:PFOA/PFOS (1:10 ratio) solutions were used as negative control system.

Figure 5.6A underlines that in presence of dhSA and dhSA:PFOA/PFOS the k_s of hemin underwent a meaningful decrease. This variation cannot be explained considering the formation of hemin-albumin complexes because even if part of the hemin in solution will bind the dhSA FA1 pockets and less hemin will be available in solution, the k_s of the ET process should not be affected. Indeed, the free-hemin in solution should have the ability to exchange electrons with the electrode surface at the same rate as before. Unfortunately, we are not working in ideal conditions: this decrease in the k_s can be ascribed to NSA processes taking place at the electrode surface. Thanks to their hydrophobic nature hemin-dhSA and hemin-dhSA:PFOA/PFOS complexes tends to adsorb at the electrode preventing the ET of hemin in solution. Therefore, what we record is not the k_s of hemin but, most luckily an average value of the k_s of hemin and hemin-albumin complexes. No meaningful k_s variations were observed by adding only PFOA or PFOS to the hemin solution confirming that the major changes in the k_s were observed in presence of dhSA. The contributions of dhSA NSA were further evaluated comparing the electrochemical signal of a redox probe (1.0 mM of $K_3[Fe(CN)_6]$, 1.0 mM $K_4[Fe(CN)_6]$) in solution with just hemin and just dhSA. The results showed a progressive decrease in the current intensities probe signal at increasing concentrations of dhSA with shift in the E_p values toward higher potentials, while hemin did not affect the probe voltammetric response (*negative control data not shown*). It is worth noting that when dhSA:PFOA was added to the hemin solution a decrease in the k_s value of about 60% was observed. However, these data are all deeply affected from NSA contributions. This first test allowed us estimating the impact of NSA in our system and underlined the necessity of minimise this contribution in the next steps of this study.

These findings did not allow any consideration about PFOA capability of reducing the kinetic of the hemin binding to dhSA. To evaluate this phenomenon, a preliminary SWV study was performed. It is worth noting that the kinetic of hemin electron transfer is expected to be independent from the hemin-albumin complex formation. This latter will simply decrease hemin availability in solution and its final concentration, which can be followed considering the changes in hemin faradic signal (especially in terms of current intensities).

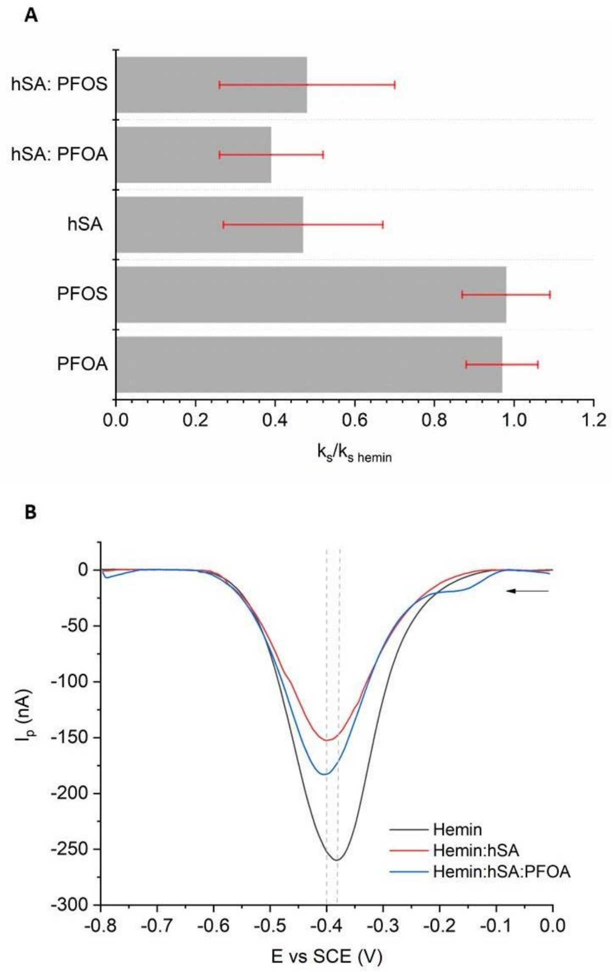

***Figure 5.6** (**A**) Overview of the values of the electron transfer kinetic constants (k_s) normalized toward the k_s of hemin for hemin solutions (5 µM) with additions of PFOA (50 µM), PFOS (50 µM), dhSA (5 µM) and dhSA:PFOA/PFOS (1:10); the associated errors were calculated on triplicates (error bars in red). (**B**) SWV voltammograms of hemin (black line), hemin:dhSA (red line) and hemin:dhSA:PFOA (ratio 1:1:50; blue line).*

Figure 5.6B provides an example of hemin, hemin:dhSA and hemin:dhSA:PFOA voltammograms recorded via SWV. Hemin presents a unique, symmetric cathodic peak with an E_p of -0.383 V vs SCE that shifts to -0.404 V vs SCE when delipidated dhSA is added with a 1:1 hemin:dhSA ratio. This shift toward higher potentials (ΔE_p= 20 mV) is followed by a decrease in hemin peak current intensity of 41%. Both the shift in E_p and the current decrease can be ascribed to: *i)* NSA and *ii)* the complex formation (responsible of decreasing the free hemin *available* for ET). These contributions cannot be distinguished in the system under study; but we can expect NSA ones to be constant when working with equal dhSA concentrations (because they are proportional to dhSA concentration).

When instead of dhSA, hemin:dhSA:PFOA (ratio 1:1:50, **Figure 5.6B**) is added to hemin solution a current decrement of about 30% is recorded. This lower decrease in hemin I_p in presence of PFOA is possibly due to the slower kinetic of hemin:dhSA complex formation. Indeed, the PFOA, which was previously loaded in dhSA hydrophobic pockets, is expected to induce an allosteric change in dhSA FA1 hampering hemin binding to dhSA and leading to a major availability of free hemin compare to dhSA only. Here, it is possible to made some more considerations about the dataset by considering NSA contributions equal for hemin:dhSA and hemin:dhSA:PFOA.

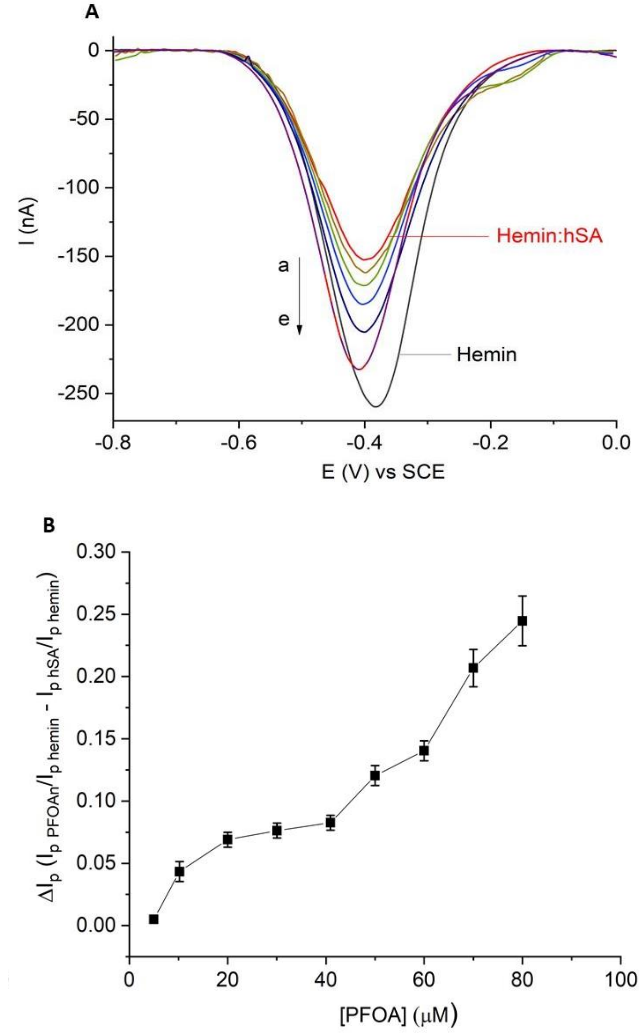

Figure 5.7 *(**A**) SWV voltammograms of hemin (black line), hemin:dhSA (red line) and hemin:dhSA:PFOA at increasing PFOA ratios: from 1:1:20 (**a**) to 1:1:90 (**f**); (**B**) Plot of the signal variations of hemin Ip at increasing*

PFOA concentrations; for comparison the triplicate values were first normalized towards Ip hemin value and then the normalized value obtained in presence of dhSA only was subtracted.

The influence of increasing PFOA:dhSA ratios on hemin voltammetric response was further explored in the range between 1:1 and 1:100. The voltammograms in **Figure 5.7A** shows a decrease in hemin I_p current at increasing ratios of PFOA (going from **a**, 1:10, to **f**, 1:90). All hemin I_p values recorded in presence of dhSA and dhSA:PFOA were normalised towards the I_p value of hemin alone (*black line* in **Figure 5.7A**) to compare different datasets. The normalized values of hemin:dhSA:PFOA at different PFOA concentrations are presented in **Figure 5.7B**. We can observe that, with PFOA concentrations lower than 20 µM, there are variations in hemin I_p of 40% on average of triplicate measurements.

PFOA concentrations higher than 40 µM induce a variation in the I_p with current decreases going from 30% to 16.9% (following a linear trend). These results suggest the possibility of monitoring indirectly increasing PFOA concentrations by following the changes in hemin reduction peak in presence of dhSA:PFOA complex with the assumption that NSA contributions are constant and, therefore, negligible. To draw a sensing strategy from these preliminary data, we need to consider that: *i)* PFOA contaminated samples need to be incubated first with dhSA (to assure the dhSA:PFOA complex formation) and then with hemin probe; *ii)* only high ratio of dhSA:PFOA will be detectable; *iii)* hemin electrochemistry in aqueous solution can be affected by numerous factors (oxygen traces and NSA processes need to be further evaluated). Despite these constraints, the data showed the possibility to combine commercially available electroactive labels, such as hemin, to delipidated dhSA-based sensing strategies for nonelectroactive contaminants.

5.4 Conclusions

Evaluating hemin applicability as a probe in PFOA voltammetric sensing allowed us to further investigate the possible connections between pharmacokinetic studies and biosensing design. Indeed, well-known conformational changes in albumin pockets caused by certain drugs, which affect haem (hemin) binding, might occur even when another molecule, PFOA in this case, binds to the same sites. Aiming to verify this hypothesis a UV-Vis study was carried out. The hemin-dhSA complex kinetic results were affected by the presence of the contaminant. Therefore, it was possible to move forward and try to follow these variations through electrochemistry, considering the changes in the voltammetric behaviour of hemin.

The preliminary data confirmed the possibility to **correlate the changes in the intensity of hemin reduction peak to increasing PFOA:dhSA ratios**. It is worth to note that the ratios considered here were relatively high compared to the ones of real samples. Nevertheless, for this preliminary study, it was necessary to evaluate the magnitude of the signal changes testing in presence of relative high ratios of PFAS. Of course, this is only a first step to investigate the possibility of designing analytical devices for PFAS detection based on dhSA and hemin. Prior to continue this study, the design of the platform needs to be planned considering how to minimise NSA. For instance, by protecting the electrode surface with anti-fouling agents (self-assembled monolayers, etc.) or immobilizing the dhSA. Even though PFOA sensing with hemin probe seems difficult to combine with a real analytical context (oxygen-free conditions are difficult to obtain in-situ with portable devices), the development of a sensor by combining nonelectroactive target and bioreceptor with an electroactive probe paved the way for further studies where optimisation of conditions could lead to a sensor that has application on real analytical contexts.

Acknowledgments

A special thanks to S. Trashin, R. Campos and O. Voet who helped me designing this study and followed all the steps of these study. It was very enriching to discuss with the them the possibility to apply structural biology finding in the design of novel electrochemical strategies.

References

[1] G. Moro, K. De Wael, L.M. Moretto, Challenges in the electrochemical (bio)sensing of nonelectroactive food and environmental contaminants, Curr. Opin. Electrochem. 16 (2019) 57–65. https://doi.org/10.1016/j.coelec.2019.04.019.

[2] H. Shinohara, H. Kuramitz, K. Sugawara, Design of an electroactive peptide probe for sensing of a protein, Anal. Chim. Acta. 890 (2015) 143–149. https://doi.org/https://doi.org/10.1016/j.aca.2015.07.052.

[3] R. Heuberger, G. Sukhorukov, J. Vörös, M. Textor, H. Möhwald, Biofunctional Polyelectrolyte Multilayers and Microcapsules: Control of Non-Specific and Bio-Specific Protein Adsorption, Adv. Funct. Mater. 15 (2005) 357–366. https://doi.org/https://doi.org/10.1002/adfm.200400063.

[4] R.R. Seigel, P. Harder, R. Dahint, M. Grunze, F. Josse, M. Mrksich, G.M. Whitesides, On-Line Detection of Nonspecific Protein Adsorption at Artificial Surfaces, Anal. Chem. 69 (1997) 3321–3328. https://doi.org/10.1021/ac970047b.

[5] J.Y. Lichtenberg, Y. Ling, S. Kim, Non-Specific Adsorption Reduction Methods in Biosensing, Sensors . 19 (2019). https://doi.org/10.3390/s19112488.

[6] M. Beyer, T. Felgenhauer, F. Ralf Bischoff, F. Breitling, V. Stadler, A novel glass slide-based peptide array support with high functionality resisting non-specific protein adsorption, Biomaterials. 27 (2006) 3505–3514. https://doi.org/https://doi.org/10.1016/j.biomaterials.2006.01.046.

[7] F. Höök, J. Vörös, M. Rodahl, R. Kurrat, P. Böni, J.J. Ramsden, M. Textor, N.D. Spencer, P. Tengvall, J. Gold, B. Kasemo, A comparative study of protein adsorption on titanium oxide surfaces using in situ ellipsometry, optical waveguide lightmode spectroscopy, and quartz crystal microbalance/dissipation, Colloids Surfaces B Biointerfaces. 24 (2002) 155–170. https://doi.org/https://doi.org/10.1016/S0927-7765(01)00236-3.

[8] S. VandeVondele, J. Vörös, J.A. Hubbell, RGD-grafted poly-l-lysine-graft-(polyethylene glycol) copolymers block non-specific protein adsorption while promoting cell adhesion, Biotechnol. Bioeng. 82 (2003) 784–790. https://doi.org/https://doi.org/10.1002/bit.10625.

[9] A. Frutiger, A. Tanno, S. Hwu, R.F. Tiefenauer, J. Vörös, N. Nakatsuka, Nonspecific Binding—Fundamental Concepts and Consequences for Biosensing Applications, Chem. Rev. 121 (2021) 8095–8160. https://doi.org/10.1021/acs.chemrev.1c00044.

[10] T. Komatsu, N. Ohmichi, P.A. Zunszain, S. Curry, E. Tsuchida, Dioxygenation of human serum albumin having a prosthetic heme group in a tailor-made heme pocket, J. Am. Chem. Soc. 126 (2004) 14304–14305. https://doi.org/10.1021/ja046022t.

[11] G. Janson, C. Zhang, M.G. Prado, A. Paiardini, PyMod 2.0: improvements in protein sequence-structure analysis and homology modeling within PyMOL, Bioinformatics. 33 (2017) 444–446. https://doi.org/10.1093/bioinformatics/btw638.

[12] M. Paoli, B.F. Anderson, H.M. Baker, W.T. Morgan, A. Smith, E.N. Baker, Crystal structure of hemopexin reveals a novel high-affinity heme site formed between two β-propeller domains, Nat. Struct. Biol. 6 (1999) 926–931. https://doi.org/10.1038/13294.

[13] P.A. Adams, M.C. Berman, Kinetics and mechanism of the interaction between human serum albumin and monomeric haemin., Biochem. J. 191 (1980) 95–102. https://doi.org/10.1042/bj1910095.

[14] M. Rosenfeld, D.M. Surgenor, METHEMALBUMIN: INTERACTION BETWEEN HUMAN SERUM ALBUMIN AND FERRIPROTOPORPHYRIN IX, J. Biol. Chem. 183 (1950) 663–677. https://doi.org/https://doi.org/10.1016/S0021-9258(19)51193-0.

[15] U. Baruah, N. Gogoi, G. Majumdar, D. Chowdhury, Capped Fluorescent Carbon Dots for Detection of Hemin: Role of Number of –OH Groups of Capping Agent in Fluorescence Quenching, Sci. World J. 2013 (2013) 529159. https://doi.org/10.1155/2013/529159.

[16] A. V Solomonov, E. V Rumyantsev, E. V Antina, Serum albumin and its bilirubin complex as drug-carrier proteins for water-soluble porphyrin: a spectroscopic study, Monatshefte Für Chemie - Chem. Mon. 144 (2013) 1743–1749. https://doi.org/10.1007/s00706-013-1062-z.

[17] S. Curry, Beyond expansion: structural studies on the transport roles of human serum albumin., Vox Sang. 83 Suppl 1 (2002) 315–319. https://doi.org/10.1111/j.1423-0410.2002.tb05326.x.

[18] P.A. Zunszain, J. Ghuman, T. Komatsu, E. Tsuchida, S. Curry, Crystal structural analysis of human serum albumin complexed with hemin and fatty acid, 9 (2003) 1–9.

[19] S. Baroni, M. Mattu, A. Vannini, R. Cipollone, S. Aime, P. Ascenzi, Effect of ibuprofen and warfarin on the allosteric properties of haem – human serum albumin A spectroscopic study, 6220 (2001) 6214–6220.

[20] I. Petitpas, A.A. Bhattacharya, S. Twine, M. East, S. Curry, Crystal structure analysis of warfarin binding to human serum albumin. Anatomy of drug site I, J. Biol. Chem. 276 (2001) 22804–22809. https://doi.org/10.1074/jbc.M100575200.

[21] I. Fitos, J. Visy, J. Kardos, Stereoselective kinetics of warfarin binding to human serum albumin: Effect of an allosteric interaction, Chirality. 14 (2002) 442–448. https://doi.org/10.1002/chir.10113.

[22] J. Wilting, W.F. van der Giesen, L.H.M. Janssen, The effect of human albumin conformation on the binding of warfarin, Acta Pharm. Suec. 17 (1980) 74–75.

[23] P. Ascenzi, A. Bocedi, S. Notari, E. Menegatti, M. Fasano, Heme impairs allosterically drug binding to human serum albumin Sudlow's site I, Biochem. Biophys. Res. Commun. 334 (2005) 481–486. https://doi.org/10.1016/j.bbrc.2005.06.127.

[24] P. Ascenzi, A. Bocedi, M. Gioia, G. Fanali, M. Fasano, M. Coletta, Warfarin inhibits allosterically the reductive nitrosylation of ferric human serum heme-albumin, J. Inorg. Biochem. 177 (2017) 63–75. https://doi.org/10.1016/j.jinorgbio.2017.08.030.

[25] M. Makarska-Bialokoz, Interactions of hemin with bovine serum albumin and human hemoglobin: A fluorescence quenching study, Spectrochim. Acta - Part A Mol. Biomol. Spectrosc. 193 (2018) 23–32. https://doi.org/10.1016/j.saa.2017.11.063.

[26] S.Y. and A.J.B. Rudra N. Samajdar, Dhivya Manogaran, Using Porphyrin - Amino Acid Pairs to Model the Electrochemistry of of Heme Proteins: Experimental and Theoretical Investigations, Phys. Chem. Chem. Phys. (2018). https://doi.org/10.1039/C8CP00605A.

[27] E. Laviron, General expression of the linear potential sweep voltrammogram in teh case of diffusionless electrochemical systems, J. Electroanal. Chem. 101 (1979) 19–28.

[28] M.R. Dayer, A.A. Moosavi-movahedi, M.S. Dayer, Band Assignment in Hemoglobin Porphyrin Ring Spectrum : Using Four- Orbital Model of Gouterman, (2010) 473–479.

[29] N. Nanzyo, S. Sano, Type c Ferri- and Ferrohemochrome Formation between Hemin c, Amino Acids, and Peptides, J. Biol. Chem. 243 (1968) 3431–3440. https://doi.org/https://doi.org/10.1016/S0021-9258(18)93327-2.

[30] D.T.-Y. Chiu, J. Van Den Berg, F.A. Kuypers, I.-J. Hung, J.-S. Wei, T.-Z. Liu, Correlation of membrane lipid peroxidation with oxidation of hemoglobin variants: Possibly related to the rates of hemin release, Free Radic. Biol. Med. 21 (1996) 89–95. https://doi.org/https://doi.org/10.1016/0891-5849(96)00035-4.

[31] Z. Jahromi, T. Shamspur, A. Mostafavi, M. Mohamadi, Separation and preconcentration of hemin from serum samples followed by voltammetric determination, J. Mol. Liq. 242 (2017) 91–97. https://doi.org/10.1016/j.molliq.2017.07.008.

[32] R.S. Tieman, L.A. Coury, J.R. Kirchhoff, W.R. Heineman, The electrochemistry of hemin in dimethylsulfoxide, J. Electroanal. Chem. 281 (1990) 133–145. https://doi.org/10.1016/S0022-0728(73)80377-8.

[33] M.T. De Groot, M. Merkx, A.H. Wonders, M.T.M. Koper, Electrochemical reduction of NO by hemin adsorbed at pyrolitic graphite, J. Am. Chem. Soc. 127 (2005) 7579–7586. https://doi.org/10.1021/ja051151a.

[34] R. Campos, E.E. Ferapontova, Electrochemistry of weakly adsorbed species: Voltammetric analysis of electron transfer between gold electrodes and Ru hexaamine electrostatically interacting with DNA duplexes, Electrochim. Acta. 126 (2014) 151–157. https://doi.org/https://doi.org/10.1016/j.electacta.2013.07.083.

[35] R. Campos, E.E. Ferapontova, Electrochimica Acta Electrochemistry of weakly adsorbed species : Voltammetric analysis of electron transfer between gold electrodes and Ru hexaamine electrostatically interacting with DNA duplexes, Electrochim. Acta. 126 (2014) 151–157. https://doi.org/10.1016/j.electacta.2013.07.083.

|6

Applying dhSA in Optical Biosensors: A Label-free Strategy

Adapted from G. Moro, F. Chiavaioli, S. Liberi, P. Zubiate, I. Del Villar, A. Angelini, K. De Wael, F. Baldini, L. M. Moretto, A. Giannetti, Nanocoated Fiber Label-Free Biosensor for PFOA monitoring via Lossy Mode Resonance,

***Results in Optics**, **2021**, 5, 100123*

Abstract

After confirming that the formation of albumin (dhSA)- perfluorooctanoic acid (PFOA) complex is a suitable recognition event for the design of impedimetric sensors, we extended our investigations to optical sensing platforms. A proof-of-concept label-free optical sensor based on fiber optics (FO) was developed aiming to: i) test the applicability of albumin as PFOA bioreceptors in FO-based sensors and ii) compare the performance of impedimetric and optical biosensors. Among FO-based sensors, those based on lossy mode resonance (LMR) phenomenon are showing promising results in terms of sensitivity, detection limit (down to fM and pM range), and reproducibility. So far, the determination of small-molecules, such as PFOA, with LMR-sensors have not been studied extensively. However, it can be achieved by means of a well-designed biological recognition layer, as in our study.

In this chapter, the performances of a label-free LMR-assisted optical biosensor based on tin oxide nanocoated D-shaped fiber are described. As for **Chapter 4** *and* **5***, dhSA was used as bioreceptor for PFOA after immobilisation onto the FO surface. Different protocols for dhSA covalent immobilisation were tested to identify the optimal working conditions based on the performance of the final platform. The conformational changes related to the formation of dhSA-PFOA complex, previously described in* **Chapter 4***, were monitored following the LMR spectral shifts, due to the refractive index (RI) change at the surface of the FO. The results showed a trend that can be modelled with Langmuir adsorption isotherm and confirmed the applicability of dhSA as bioreceptor even in LMR-sensors. In these preliminary experiments, PFOA was detected in synthetic aqueous samples down to 0.156 ng mL^{-1} (0.374 nM), but the performance of these platforms will be further improved.*

From a methodological point of view, the study presented in this chapter was instrumental in broadening our perspective in sensing platform design, proving the importance of comparing multiple strategies before focusing on the optimization of one of them. This choice needs to be made in a critical way considering the analytical questions to which we aimed to answer, as discussed in the conclusions of this chapter.

6.1. Introduction

Fiber optic (FO)-based sensors for water pollutants monitoring are successfully employed in the detection of pesticides, heavy metals, toxic substances and PFAS providing highly sensitive, selective and reproducible responses [1–3]. FOs can be easily combined with other sensing elements, (i.e., metal nanoparticles, quantum dots or inorganic/polymeric nanocoatings) allowing the design of a wide variety of sensing architectures, modifying the optical features and, as a result, the performance of the final device[4–8]. These optics were coupled with miniaturized and microfluidic systems (i.e., microfluidic chips [9]) as well as *Lab-on-Fiber* tools (i.e. [10,11]) for the detection of small-molecules and biomolecules, from nucleic acids to cells. As previously mentioned, (**Chapter 1**), miniaturized devices compatible with on-flow or microfluidic systems are often required for water monitoring to tackle the levels of small-molecules pollutants in continuous (i.e., water plans, tap water) [12,13].

FO-based sensors adopt different strategies to allow the interaction of light traveling inside a FO with the surrounding environment where target-receptor recognition event takes place: from the etching of the fiber cladding to its entire removal, extending the evanescent wave of fiber mode (electromagnetic field) out of the fiber [14,15]. It is worth noting that depending on the sensing concept, the deposited coating, and FO features, surface plasmon polaritons, Bloch or lossy/leaky mode waves can be generated to exploit the excitation of **resonance-based phenomena** [16]. All optical resonances allow measuring the changes in the fiber-surrounding refractive index (RI) on the basis of induced shift of the resonance wavelength which is correlated to the analyte recognition event, as we will further explain in this section [17,18].

In the last decades, the deposition of thin films, micro or nanocoating, at optical materials has led to the development of **surface-plasmon resonance** (SPR) sensors (first described as polarisonation resonance-based sensors) as well as **lossy-mode resonance** (LMR) sensors. In 1982, Naylander *et al.* developed an SPR-sensor for gas detection using a prism in Kretschmann-Reather configuration with a silver nanocoating on the upper side, as depicted in **Figure 1A** [19]. The position of the resonance, expressed in wavelength (λ), was found to be sensitive to film thickness and surrounding medium/media. Therefore, by applying a layer sensitive to the analyte (i.e., biological recognition layer) on top of the metallic nanocoating, it was possible to correlate the changes in the resonance position (resonance angle shift [20]) with the analyte presence and, even, its concentration.

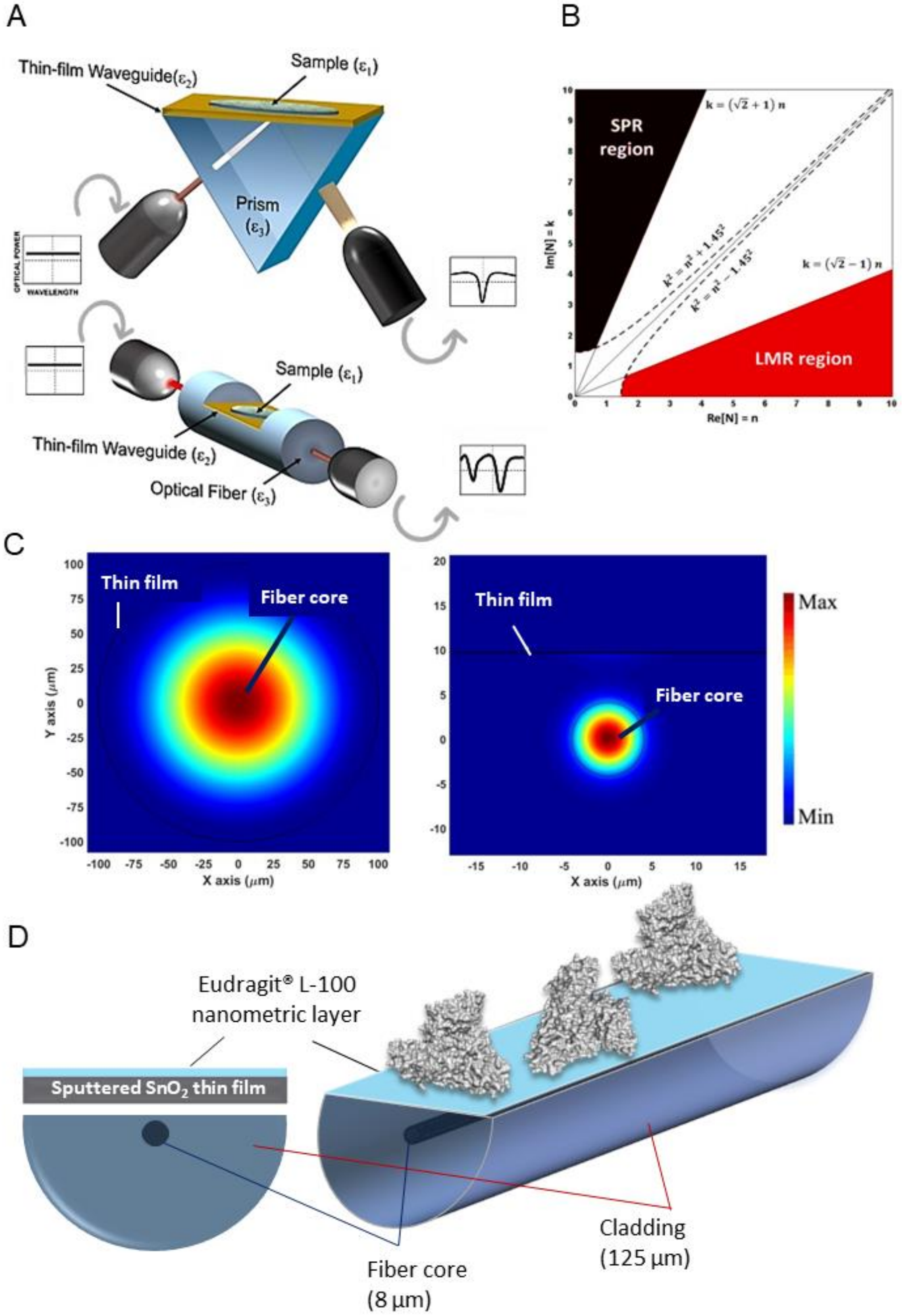

*Figure 6.1 Configurations used in LMR and SPR-based sensors: (**A**) a nanocoated optical prism, known as Kretschmann configuration, and a nanocoated D-shaped optical fiber, (**B**) map of the conditions for LMR and SPR generation expressed considering the imaginary and real parts of thin film RI, ([N] means the complex RI), (**C**) distribution of the optical field intensity of $HE_{1,1}$ mode in the cross-section of an unclad fiber (right) and a D-shaped fiber (left) both modified with Eudragit polymer, (**D**) schematic of the D-shaped fiber modified with Eudragit and dhSA for PFOA detection used in this chapter. All images were adapted from previous publications: (**A-B**) from* [21] *(**C**) from* [22] *and (**D**) from* [23].

These changes, expressed in resonance spectral shift [24], were monitored in real time within flow cell systems, generating sensorgrams where all the steps of the molecular interaction can be followed: from target-receptor association, to steady state equilibrium to dissociations. Once the sensorgram is recorded, SPR-chips surfaces can be regenerated and reused. Real-time monitoring as well as reusability, high-output performance and robustness are ideal characteristics for a sensing platform. Therefore, SPR-sensors entered the market showing their applicability in a wide variety of fields, from food-safety to biomedical one [25]. The evolution of SPR-sensors was boosted till the theoretical limits, which are ascribed mainly to the noise associated with light source and detector characteristics [25]. These limits affect SPR-based devices sensitivity, but other resonance modes can make up to detect the analyte down to femtomolar levels, such as LMR [22].

Among resonance phenomena, LMR was described in the same period of SPR, but its application in optical sensor design dates only 2005 [26]. In this example a D-shaped optical fiber configuration was used (**Figure 6.1A**). The changes in optical signal were expressed in function of wavelength: the input light results in a transmitted signal and the shifts of the curve minimum were recorded and plotted versus the time. It is worth noting that the conditions to generate LMR differs deeply from SPR ones, as summarized in the plot of **Figure 6.1B**. Here, a substrate and a medium with a refractive index of 1.45 and 1, respectively, are considered. SPR and LMR regions are identified as functions of the complex RI of the thin film material.

LMR can be induced from different materials (except for pure metals, which are used in SPR) as long as the real part of the thin-film permittivity (ε) is positive and the extinction coefficient (k) is maintained to low values [27]. Working with D-shaped optical fibers allowed to enlarge the evanescent field (**Figure 6.1C**) and, as a consequence, record narrower resonances compared to uncladded optical fibers improving the surface sensitivity. To maximise the sensitivity in LMR sensing, the waveguide modes need to be coupled with a particular lossy mode of the semiconductor nanocoating and an optimal film thickness value can allow obtaining a maximum attenuation in the transmission spectrum. Therefore, the control and characterisation of the nanocoating thickness play a key-role in LMR-based sensors, as described by Del Villar et al. [28]. In this context metal oxides were largely tested and the one that showed the highest RI sensitivity was tin dioxide (SnO_{2-x}) [29,30]. Also, the FO geometry is doubtless another feature to take into account in the design of high-performance sensing platforms [18,22]. Until now, the configuration that gave the best performance was the D-shaped (also called side-polished) single-mode FO one. A schematic of a D-shaped FO nanocoated with a layer of SnO_{2-x} and an additional polymeric nano-film for surface functionalization is reported in **Figure 6.1D**, as a schematic of the type of fibers and modification used in the present work. Despite the versatility of these FO platforms in label-free biosensing, their capability to detect small molecules is extremely limited due to the non-chromogenic/fluorescent nature of the analyte (in this case a labelled-based approach must be used as single molecule array methodology [31]) or its low molecular weight. So far, this challenge was addressed by implementing the instrumentation and methodologies in use, including immobilisation steps or receptors, as overviewed by Peltomaa *et al.* [32].

LMR-sensors for small-molecules detection need to be further investigated keeping in mind that LMR-devices have several advantages over the well-established SPR-based ones, such as: *i*) easy tunability of the LMR wavelength in the optical spectrum as a function of the coating thickness, *ii*) cheaper material used as coating (metal-oxides or polymers with respect to noble metals), *iii*) possibility of exciting both polarization states of light and capability of multiple LMR generation above all. Despite the complexity of resonance modes, Arregui *et al.* [27] underlined that once the nanocoating and the working conditions are optimized the devices work as simple **refractometer sensors**.

Here, dhSA was applied as biorecognition layer in a D-shaped FO LMR-platform and the changes observed in dhSA structure/conformation upon PFOA binding (followed via EIS in **Chapter 4**) were studied in a series of preliminary experiments. The covalent immobilisation of dhSA at SnO_{2-x} nanocoated D-shaped FO was first optimized. Then, PFOA solutions at different concentrations were tested in real-time confirming the possibility to detect very small molecules, such as PFAS, with LMR-sensors.

6.2 Materials and methods

6.2.1 Reagents

D- shaped fiber samples were purchased from Phoenix Photonics Ltd (Birchington, UK.) For the nanocoating deposition, a tin oxide target (SnO_{2-x}) with 99.99% purity was purchased from ZhongNuo Advanced Material Technology Co. (Beijing, China). UV-polymerizing optical adhesive (NOA 68), Norland Products Inc. (East Windsor, NJ, US) was used for the FO immobilisation. Methacrylic acid/methacrylate copolymer, commercially known as Eudragit L100, was purchased from Evonik Degussa GmbH (Dusseldorf, Germany). As a biological recognition layer, the delipidated albumin was used and prepared, as described in **Chapter 3**. The covalent immobilisation of albumin at the SnO_{2-x} fibers was done via EDC/NHS chemistry with 1-Ethyl-3-(3-(dimethylamino)-propyl) carbodiimide hydrochloride (EDC), and N-hydroxy succinimide (NHS) purchased from Pierce (Illinois, US). As for the previous chapters, perfluorooctanoic acid (PFOA), hydroxylamine, NaH_2PO_4, Na_2HPO_4 and NaCl of analytical grade were purchased from Sigma-Aldrich (Milan, Italy). The 0.1 M phosphate saline buffer at pH 7.4 was prepared by mixing stock solutions of 0.1 M NaH_2PO_4 and 0.1 M Na_2HPO_4 and adding 0.1 M NaCl. All other reagents were of analytical grade and solutions were prepared using double distilled deionized water and filtered prior to use to avoid contaminations of the systems.

6.2.2 Fiber manufacturing and integration in the microfluidic system

Tin oxide nanocoating was deposited on the starting D-shaped fibers, which consisted of a standard single-mode fiber (i.e., Corning SMF-28e) with a side-polished region with a length of roughly 17 mm. The manufacturing procedure to polish and coat these FOs was previously reported by Zubiate *et al.* [30]. Once the polished surface of the fiber is cleaned, the SnO_{2-x} nanocoating deposition is carried out by placing the fiber onto a suitable glassy substrate and then inserting it in a DC sputter machine (ND-SCS200, Nadetech Innovations, Navarra, Spain). The deposition required a constant pressure of Ar of about 9×10^{-2} mbar and the application of a current with intensity of 90 mA. The size of the sputtering target was 57 mm in diameter and 3 mm in thickness. These working conditions guarantee a thickness of the nanomaterial ranging from 150 nm to 180 nm [30], which is suitable for the excitation of LMR [4].

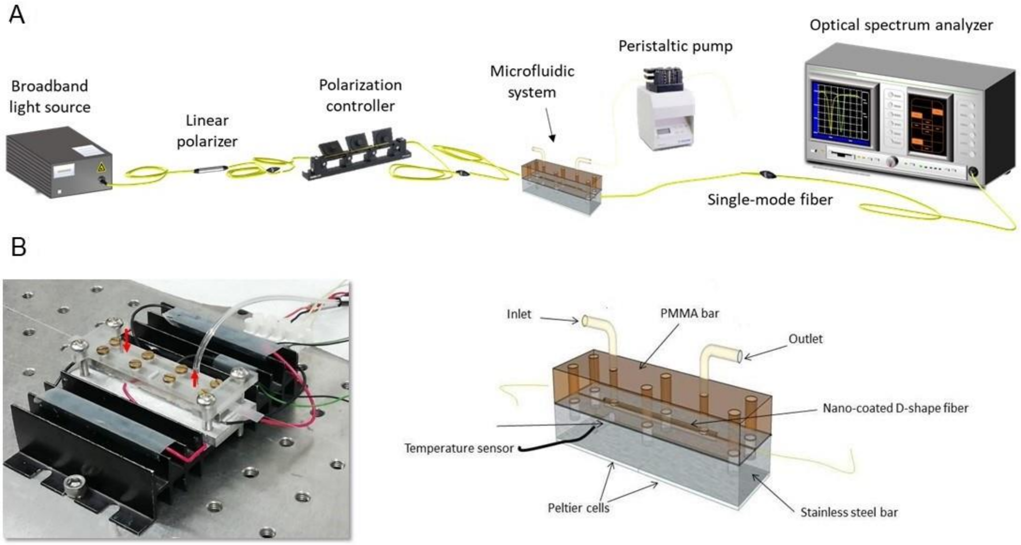

Figure 6.2 *(**A**) Schematic of the main components of the customised experimental setup in use, (**B**) picture and details of the flow cell with temperature stabilization system. Illustration adapted from* [24,33].

An *ad-hoc* experimental setup shown in **Figure 6.2A** was assembled to monitor the transmission spectrum of the fiber during the biosensing tests. The setup included: *i*) a broadband multi-LED light source (SLD- 1310/1430/1550/1690; FiberLabs, Inc., Saitama, Japan), which was instrumental to guide the light through the fiber, *ii*) an optical spectrum analyser (OSA, Anritsu MS9030A-MS9701B; Kanagawa, Japan) to monitor the LMR in the range from 1250 to 1700 nm, *iii*) a FO in-line polarizer and *vi*) a polarization controller, which permits to adjust the polarization state of light (transverse electric, TE, or transverse magnetic, TM), which was placed between the optical source and the D-shaped fiber (**Figure 6.2A**). After the deposition process, the fiber was placed inside a thermo-stabilised microfluidic system, previously described by Trono *et al.* [33]. This system allowed working with microvolumes of samples and to stabilise temperature variations (error of ±0.05 °C). The flow cell depicted in **Figure 6.2B** was made up of two equal-size pieces (74 mm long, 15 mm wide and 5 mm high each bar), which were assembled and entrapped with Parafilm® sheets to assure the water-proofing. The two bars consisted of polymethylmethacrylate PMMA (top) and of stainless steel (bottom). The flow channel with a cross-sectional square size of 1 mm^2 and a length of 40 mm were on both bars. The flow cell inlet and outlet were made of two stainless-steel tubes (1.2 mm outer diameter and 1 mm inner diameter) placed on the PMMA bar and connected to the flow channel. To fix the D-shaped portion of the fiber, a V-groove of 0.5 mm deep was engraved on both ends of the top bar. The optical fiber was glued to the V- groove edges using the UV-polymerizing optical adhesive.

The steel bar was thermally stabilised by the help of two Peltier cells (ILX Lightwave LDC-3722B TEC controller, ILX Lightwave Corporation, Bozeman, MT, US) and the temperature was monitored in continuous thank to a thermistor inserted in the PMMA bar and coupled with a thermometric measuring unit (Lutron TM-917). The microfluidic system was connected to a peristaltic pump (GILSON Minipulse 3, Middleton, WI, US) with a premium medical grade plastic tubing, which allows controlling the flow rate. The flow rate changed according to the biosensing protocol, as detailed in **Section 6.2.3**.

6.2.3 Fiber Surface Functionalization with dhSA and PFOA determination

Once manufactured, the nanocoated D-shaped fibers were modified with a polymeric layer, namely Eudragit L100. The choice of this polymer was driven by the fact that it is rich in free carboxylic moieties, that as for Py-2-COOH in **Chapter 4**, can be used for the covalent immobilisation of a protein bioreceptor via EDC/NHS chemistry. The optimization of Eudragit L100 deposition was previously reported [17,30]. In brief, the deposition was carried out via immersion of the D-shape region in a 0.04% (w/v) Eudragit L100 solution in ethanol for about 1 min. The polymeric layer was dried at room temperature for 15 min to assure its complete reticulation and ethanol evaporation. The FO was glued in the flow channel of the microfluidic system, described in **Section 6.2.2**. The temperature was stabilised to a constant value of 15 °C, which is remarkably different from the routinely temperature values reported in literature ranging from 22 °C up to 30 °C [17,30].

First, the carboxylic moieties of Eudragit L100 were activated with EDC/NHS (2 mM/5 mM, respectively) solution injected at 25 µL min^{-1} for 30 min. Second, a 1 mg mL^{-1} solution of dhSA was injected at different flow rates (as described in **Section 6.3.1**) for 30 min or 1 h. Third, a washing step in PBS running buffer at a flow rate of 250 µL min^{-1} for 10 min. All solutions mentioned below were freshly prepared in PBS pH 7.4. The assays were performed injecting increasing concentrations of PFOA, considering two ranges of concentrations: from 15.6 ng mL^{-1}to 625 ng mL^{-1} (first range, Protocol A) and from 0.156 ng mL^{-1}to 15.6 ng mL^{-1} (second range, Protocol B). The PFOA concentrations tested are summarized in **Table 1**, expressed with different units to facilitate the comparison with other values in the previous chapters. The tested values were higher than the ones prescribed by PFAS regulations (i.e., the maximum residue levels of PFOA in drinking waters for the Veneto region since 2017 is 60 ng/L) but close to the PFOA levels monitored in real samples, as described in **Chapter 1**.

Table 1 Values of PFOA concentration tested with protocol A and/or B.

[PFOA]				
ng/mL	ng/L	uM	nM	Protocol
0.156	156	0.000374	0.374	B
1.56	1560	0.00374	3.74	B
15.6	15600	0.0374	37.4	A/B
31.2	31200	0.0749	74.9	A
625	625000	1.50	1500	A

In both cases, a flow rate of 25 µL mL^{-1} for roughly 30 min was used. Finally, washing steps were performed with PBS after each PFOA injection, at a flow rate of 250 µL mL^{-1} for 10/20 min when the steady-state condition was reached.

6.2.4 Scanning Electron Microscopy Imaging

The surface of the FO after functionalization with the biorecognition layer and incubation with increasing PFOA concentrations was characterised with scanning electron microscope, a Gaia 3 Tescan FIB-SEM, TESCAN ORSAY HOLDING (Brno-Kohoutovice, Czech Republic) equipped with an in-lens detector at 3 kV and an aperture diameter of 30 µm. The images of fiber morphology were collected using secondary electrons (SE) at 5.0 kV with a magnification of 19.6 kX. The elemental composition of the FO samples, both longitudinal and transversal cross-sections, was investigated via X-ray microanalysis system (EDAX; Octane Elect EDS system; AMETEK, US) comparing the results obtained at nude and modified FOs.

6.3 Results and discussion

6.3.1 Functionalization of the FO

In the SnO_{2-x} nanocoated D-shaped FO manufactured as explained by Zubiate *et al.* [30], the functionalization protocol was designed considering successful strategies for biomolecules immobilisation in literature [18]. Among the latter, Chiavaioli *et al.* [22] developed an immunosensing platform in which the bioreceptor (primary antibody) was covalently immobilised at the surface of SnO_{2-x} nanocoated D-shaped OF with the help of a polymeric layer. This polymer, an acrylic/methacrylic esters polymer (Eudragit L100), was deposited at the polished FO to provide free, exposed carboxylic functional groups to crosslink with the primary amines of the bioreceptors via EDC/NHS chemistry. In this previous study, the thickness of the Eudragit L100 layer after the solvent evaporation was estimated to be 60 ± 7 nm, almost one third of the tin oxide nanocoating thickness (160 ± 5 nm) [22]. The cross-sections of the modified FO were characterised via TEM, SEM and EDS, providing additional information about the morphology and elemental composition of the polymer modified FO [24]. Based on the successful results (in terms of performance and reproducibility) obtained with this protocol, we decided to apply Eudragit L100 at our FO and immobilize dhSA via EDC/NHS coupling. The integration of the biological sensing layer in our flow-cell setup might require time-consuming, one-variable-at-a-time (OVAT) studies (i.e., sensor design with OVAT [34]). Flow parameters (i.e., flow rate and duration), concentrations of the reagents as well as other working conditions (i.e., temperature of the microfluidic system) need to be evaluated to assure a stable and reproducible modification of the FO. However, the elevated costs and limited availability of the OF in use oblige to limit these optimisation steps.

For these reasons, we decided to: *i)* work with the polymeric modifier previously studied, *ii)* adapt the antibodies immobilisation protocol [22] to our dhSA biorecognition layer (**Section 6.2.3**), *iii)* test only two different flow rates for dhSA using the OVAT approach. We focused on the duration of the dhSA immobilisation step, because it plays a crucial role: short modification protocols (<2 h) can result in unstable modifications due to the low number of biomolecules immobilised, while long modification protocols (>2 h) might be difficult to reproduce due to the partial alteration of the protein bioreceptor (i.e., conformational changes, unfolding) [35]. These considerations are instrumental to deal with the complexity of biosensor design where immobilisation/collection rates, equilibration steps and flow rate values influence not only the success of bioreceptor immobilisation step, but also in the target recognition process. The importance of considering all these parameters was emphasised even by Squires *et al.* [36], who proposed a computational method to model the analyte transport in biosensors based on surface capture recognition. The application of such computational methods to investigate the system behaviour in given conditions and study parameters of interest (i.e., fluxes, collection rates and equilibration times) will be further considered in the optimisation of the PFOA-sensing platform.

The values of flow rate used in dhSA immobilisation step were 25 µL min^{-1} and 10 µL min^{-1} for protocols A and B, respectively. In **Figure 6.3A**, the sensorgrams allow comparing the outcome of the two protocols. Using protocol A, dhSA immobilisation experienced a steeper change in the LMR signal and reached the stabilization in less than 30 min. For protocol B, the immobilisation step of dhSA lasted 1 h with a slower stabilization trend compared to A. We can expect the reduced flow rate used in protocol B to result in a slower immobilisation of the protein bioreceptor. The label-free might benefit from a slower immobilisation step as previously observed [30].

In this study, the best conditions were selected considering the response of the biosensors upon addition of increasing concentrations of PFOA in the low ng mL^{-1} range. An addition of 15.6 ng mL^{-1} resulted in a LMR residual shift (i.e., the shift of the baseline in PBS running buffer taken before and after the analyte injection) of 0.03 nm and of 3.7 nm with protocol A and B, respectively.

- **Protocol A** was found to lead to the formation of a **non-suitable** biological recognition layer: incubating PFOA spiked solutions with increasing concentrations (from 15.6 ng mL^{-1} to 31.2 and 625 ng mL^{-1}), no meaningful correlation with LMR residual shifts was observed as shown in **Figure 6.3A**. Even after incubation with high excess of PFOA (625 ng mL^{-1}) only a minimal LMR residual shift of 0.17 nm was recorded. These outcomes were ascribed to biological recognition layer dysfunctionalities. However, better performance could be obtained even with this protocol by changing the PFOA flow rate and increasing the collection time together with the system equilibration time [17].
- **Protocol B** provided a **stable and functional** modification, and even the incubation of a very low concentration of PFOA (0.156 ng mL^{-1}) resulted in a clear LMR shift, while the following additions of PFOA (1.56 and 15.6 ng mL^{-1}) exhibited increasing and larger shifts of the LMR wavelength. Therefore, protocol B was considered suitable for the proposed application because it allows recording meaningful LMR residual shifts upon the incubation of increasing PFOA concentrations.

Once functionalized with dhSA, the flat surface of the D-shaped fiber portion was analysed via SEM-EDS to check the morphology and the elemental composition of the region. In **Figure 6.3B** we can observe a layer brighter than the silica fiber (coloured in green for the sake of clarity). The layer comprises the biological layer, the polymeric one (*recognition layer*) and tin dioxide nanocoating (*LMR-exciting layer*). Overall, the combined layers showed an average thickness of about 200±15 nm as shown in **Figure 6.3C**. Afterwards, the biosensor performance in following real-time the PFOA/dhSA binding was screened.

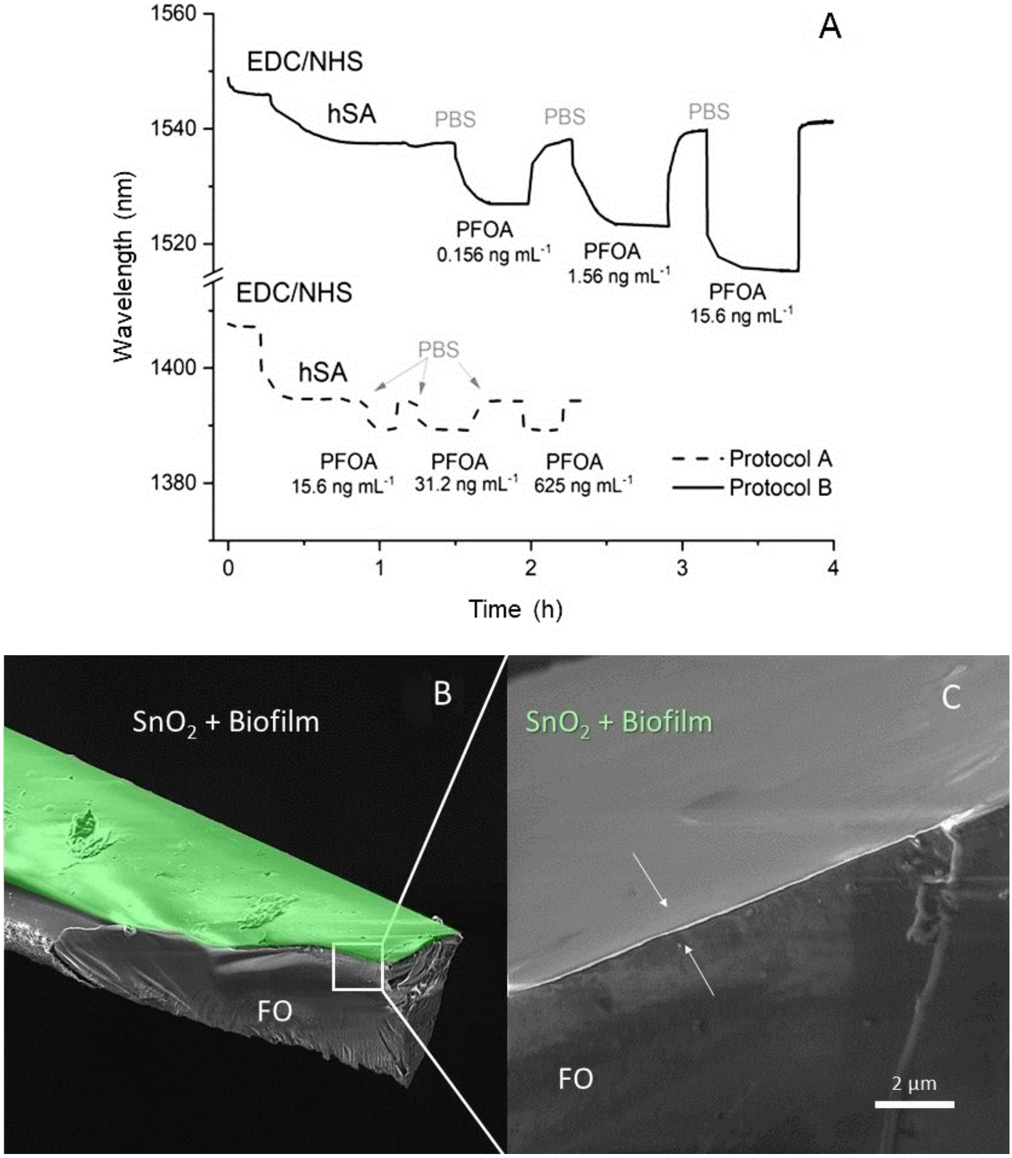

Figure 6.3 *Comparison of the sensorgrams of the SnO$_{2-x}$ nanocoated D-shaped fiber biosensors highlighting the modification steps using protocol A (dashed line) and B (continuous line): starting from the addition of EDC/NHS to the immobilisation of dhSA, the washing steps in PBS running buffer and the addition of the target, PFOA (**A**). SEM images of both the longitudinal (**B**) and cross-sectional (**C**) views of the functionalized silica fiber: the D-shaped region of the fiber with the modified surface (light green) and a zoom in the interface between the silica fiber (FO) and the SnO$_{2-x}$ nanocoating modified with the biofilm.*

6.3.2 PFOA Determination: Preliminary Tests

Increasing concentrations of PFOA spiked in PBS solutions were injected using the peristaltic pump, within the microfluidic system where the functionalized FO was previously located. For these preliminary experiments, PFOA concentrations of 0.156 ng mL^{-1} (PFOA 1), 1.56 ng mL^{-1} (PFOA 2) and 15.6 ng mL^{-1} (PFOA 3) were tested aiming to probe the range of applicability of the biosensor and its effectiveness with synthetic water samples. An example of PFOA real-time monitoring is reported in **Figure 6.4A** that represents the part of the entire sensorgram shown in **Figure 6.3A** (protocol B) related to the interaction of PFOA with dhSA-modified sensing layer: it starts with PBS addition, then the blank measurement (i.e., zero analyte concentration), followed by increasing PFOA concentrations.

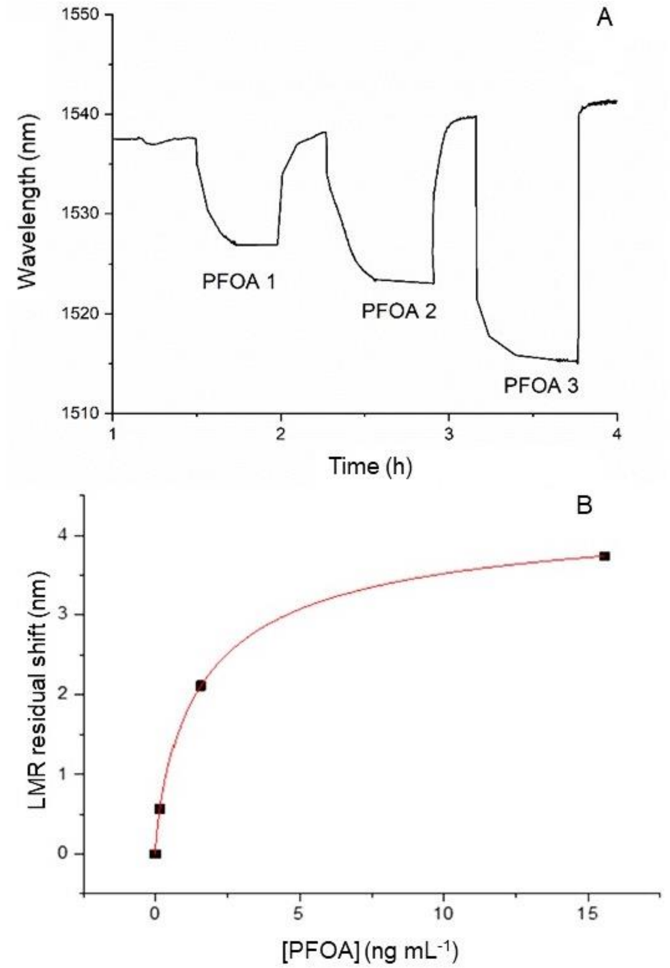

Figure 6.4 Example of part of the sensorgram of the SnO_{2-x} *nanocoated LMR fiber biosensor as a function of increasing concentrations of PFOA: 0.156 ng mL^{-1} (PFOA 1), 1.56 ng mL^{-1} (PFOA 2), 15.6 ng mL^{-1} (PFOA 3) (**A**). Calibration curve fitted with a Langmuir adsorption isotherm (sigmoidal curve) based on Hill equation (**B**).*

Each sample incubation was followed by an intermediate washing step with PBS as well, to prevent nonspecific binding and/or analyte aggregation [17]. The trend of LMR shift vs PFOA concentration is reported in **Figure 6.4B**. The experimental data were fitted using a Langmuir adsorption isotherm making use of Hill equation. This latter can model reversible association, such as complex formation, among a protein and a small size molecule ligand giving information about the degree of interaction [37]. It is worth noticing that Hill equation was previously applied in LMR-based biosensors [30] and other types of biosensors [38].

The sigmoidal fit in **Figure 6.4B** showed a correlation coefficient R^2 of 0.9989 with a maximum standard deviation of about 0.06 nm (hence the standard deviation bars are not visible in the plot). The values of the standard deviation were obtained by considering consecutive acquisitions for each experimental point under the same working conditions at flow stopped and after reaching the equilibrium. By using the approach described in [18,22], where the maximum standard deviation of the experimental points can be considered (conservative approach), an estimation of the limit of detection by a concentration value below 0.1 ng mL^{-1}, is provided. This value is very close to the PFOA concentration limits required by the current regulation. These preliminary results suggest the possibility to detect PFOA concentrations even below 0.156 ng mL^{-1}.

After the addition of PFOA, the presence of fluorine caused by the PFOA binding to dhSA was further confirmed via SEM-EDS–based analysis, considering the central flat surface of the SnO_{2-x} nanocoated D-shaped FO, as shown in the inset of **Figure 6.5**. Fluorine is found to be 3.72 wt%, as reported in **Table 2**, while the functionalization layer (biofilm plus tin dioxide layer) is responsible for the presence of both carbon (14.31 wt%) and tin dioxide (30 wt%).

Table 2 *Chemical composition of the dhSA-modified* SnO_{2-x} *nanocoated D-shaped FO after PFOA tests and comparison with a pristine FO sample (no PFOA tests).*

	Element	Carbon (K)	Oxygen (K)	Silicon (K)	Fluorine (K)	Tin (L)
No PFOA	wt %	17.44	32.79	21.87	0.00	27.90
PFOA	wt %	14.31	32.74	19.23	3.72	30.00

These data clearly confirmed that after the incubation step, PFOA was confined at the FO surface even after the washing steps in the running buffer. Therefore, it is possible to conclude that the analyte is not non-specifically bound to the protein layer of the FO surface, but it is able to give high-affinity non-covalent interactions with the biofilm that allow a stable confinement of the PFOA itself onto the FO surface. This was further confirmed with the absence of fluorine in SEM-EDS–based analysis from a pristine SnO_{2-x} nanocoated D-shaped FO sample (see **Table 2**, row named “No PFOA”). Once we tested the different concentrations of PFOA, we investigated the possibility of regenerating the biosensing platform using hydroxylamine. Unfortunately, this step resulted in a strong red shift and led to the destabilization of the biorecognition layer, and other alternatives need to be tested. Considering the high-affinity of dhSA-PFOA binding, it is difficult to design a regeneration protocol operating the analyte removal (via competition mechanism or playing on PFOA affinity for organic solvents). However, even a one-step removal of the biosensing layer which allows reusing the OFs would be instrumental to limit the costs of these sensing strategy. These preliminary findings suggest that there is an interest in improving this sensing strategy and support the current dataset with negative control experiments and a complete interference study including both PFAS and other small-molecules, such as pesticides or antibiotics (*ongoing project*).

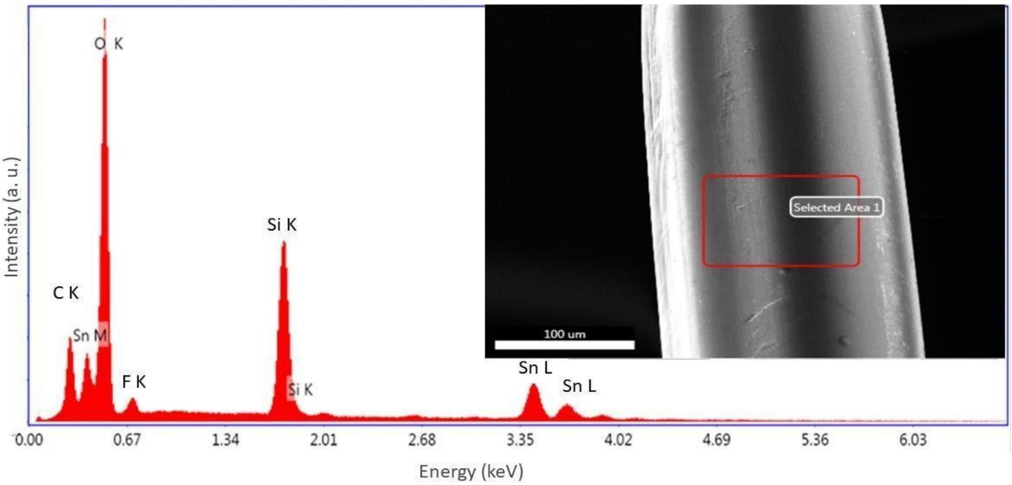

Figure 6.5 *EDS spectrum of an area of the flat surface of dhSA-modified SnO_{2-x} nanocoated D-shaped FO after incubation of PFOA synthetic solutions; the area selected is highlighted in the SEM image reported in the inset (red box).*

6.4 Conclusions

This proof-of-concept study focused on the design of an LMR-based optical sensor for PFOA detection using dhSA as a biorecognition layer. The preliminary results showed the importance of optimising the biological layer immobilisation protocol and confirming the possibility to determine PFOA down to the low ng mL^{-1} range, reaching values close to the current maximum residual limits.

Our primary aim was to test the compatibility of *"dhSA/PFOA recognition mechanism"* within optical sensing strategies, as previously done with the impedimetric approach described in **Chapter 4** [34]. Despite the optical and impedimetric strategies not being directly comparable (optical ones still need to be subjected to an extensive interference study), the LMR-based sensor showed better performances in terms of sensitivity if compared with the impedimetric one. The lower detectable concentration for this latter was of 100 nM, while the optical platform allows us to record meaningful signal variation even upon incubation of 0.374 nM of PFOA. These promising results need to be critically evaluated considering that this OF-based setup is not portable and the costs are not affordable for large scale applications so far. The rapid evolution of OF-based technologies will help to overcome this limiting step.

As anticipated in **Chapter 4**, dhSA can be further engineered by selecting just the domains that show the highest affinity for PFOA based on the crystallographic studies or modifying the protein structure to increase the bioreceptor affinity. Implementing the bioreceptor affinity for the target or amplifying its conformation changes in the presence of these small-size molecules will help improve the sensor selectivity.

The application of LMR-based sensing strategies can be extended to other compounds of the PFAS family by using different protein biological layers or engineered albumins (different domains or modification can lead to different selectivity in the final bioreceptor). These latter present all the advantages of highly stable, reproducible, and cost-affordable bioreceptors. We believe that this preliminary but disruptive study highlights how LMR-based sensing technology can rapidly evolve answering the need of small-size molecules monitoring, thus paving the way for a remarkable and almost-unique approach able to sense any kind of biological target (small, medium and large size molecules) with high-performance outcomes.

Acknowledgments

The idea of testing this biosensing strategy was born in November 2019 at the ***9th International Workshop on Surface Modification for Chemical and Biochemical Sensing*** *(Poland) in a discussion with Ambra Giannetti and Prof. Ilaria Palchetti in front of my poster. After that friendly chat, Prof. Moretto and I were invited to Florence where we started a fruitful collaboration with the Institute of Applied Physics "Nello Carrara", National Research Council of Italy (CNR), 50019 Sesto Fiorentino. We had the chance to develop these first preliminary experiments in January 2020 and our collaboration is now ongoing to improve this study and develop new projects. I would like to thank Francesco Chiavaioli, Ambra Giannetti and Francesco Baldini for this great opportunity and for sharing their expertise in optical platforms, particularly LMR-based ones. For me, as PhD student, carrying out these preliminary experiments and comparing optical and impedimetric platforms was a great chance to broaden my knowledge and think outside the box.*

References

[1] Y. Zhang, Y. Sun, L. Cai, Y. Gao, Y. Cai, Optical fiber sensors for measurement of heavy metal ion concentration: A review, Measurement. 158 (2020) 107742. https://doi.org/https://doi.org/10.1016/j.measurement.2020.107742.

[2] L. Jiao, N. Zhong, X. Zhao, S. Ma, X. Fu, D. Dong, Recent advances in fiber-optic evanescent wave sensors for monitoring organic and inorganic pollutants in water, TrAC Trends Anal. Chem. 127 (2020) 115892. https://doi.org/https://doi.org/10.1016/j.trac.2020.115892.

[3] N. Khansili, G. Rattu, P.M. Krishna, Label-free optical biosensors for food and biological sensor applications, Sensors Actuators B. Chem. 265 (2018) 35–49. https://doi.org/10.1016/j.snb.2018.03.004.

[4] N.A.A. Nazri, N.H. Azeman, Y. Luo, A.A. A Bakar, Carbon quantum dots for optical sensor applications: A review, Opt. Laser Technol. 139 (2021) 106928. https://doi.org/https://doi.org/10.1016/j.optlastec.2021.106928.

[5] S.K. Shukla, C.S. Kushwaha, T. Guner, M.M. Demir, Chemically modified optical fibers in advanced technology: An overview, Opt. Laser Technol. 115 (2019) 404–432. https://doi.org/https://doi.org/10.1016/j.optlastec.2019.02.025.

[6] X. Wang, O.S. Wolfbeis, Fiber-Optic Chemical Sensors and Biosensors (2015–2019), Anal. Chem. 92 (2020) 397–430. https://doi.org/10.1021/acs.analchem.9b04708.

[7] Z. Li, X. Yang, H. Zhu, F. Chiavaioli, Sensing Performance of Fiber-Optic Combs Tuned by Nanometric Films: New Insights and Limits, IEEE Sens. J. XX (2021) 1–12. https://doi.org/10.1109/JSEN.2021.3068445.

[8] F. Esposito, L. Sansone, A. Srivastava, F. Baldini, S. Campopiano, F. Chiavaioli, M. Giordano, A. Giannetti, A. Iadicicco, Long period grating in double cladding fiber coated with graphene oxide as high-performance optical platform for biosensing, Biosens. Bioelectron. 172 (2021) 112747. https://doi.org/10.1016/j.bios.2020.112747.

[9] Y. Zhao, X. Hu, S. Hu, Y. Peng, Applications of fiber-optic biochemical sensor in microfluidic chips: A review, Biosens. Bioelectron. 166 (2020) 112447. https://doi.org/https://doi.org/10.1016/j.bios.2020.112447.

[10] C. Riccardi, A. Meyer, J.J. Vasseur, I. Russo Krauss, L. Paduano, R. Oliva, L. Petraccone, F. Morvan, D. Montesarchio, Stability Is Not Everything: The Case of the Cyclisation of a Thrombin-Binding Aptamer, ChemBioChem. 20 (2019) 1789–1794. https://doi.org/10.1002/cbic.201900045.

[11] S. Pissadakis, Lab-in-a-fiber sensors: A review, Microelectron. Eng. 217 (2019) 111105. https://doi.org/https://doi.org/10.1016/j.mee.2019.111105.

[12] A.M. Meyer, C. Klein, E. Fünfrocken, R. Kautenburger, H.P. Beck, Real-time monitoring of water quality to identify pollution pathways in small and middle scale rivers, Sci. Total Environ. 651 (2019) 2323–2333. https://doi.org/https://doi.org/10.1016/j.scitotenv.2018.10.069.

[13] I. Yaroshenko, D. Kirsanov, M. Marjanovic, P.A. Lieberzeit, O. Korostynska, A. Mason, I. Frau, A. Legin, Real-Time Water Quality Monitoring with Chemical Sensors, Sensor. 20 (2020) 3432.

[14] Y. Cardona-Maya, A.B. Socorro, I. Del Villar, J.L. Cruz, J.M. Corres, J.F. Botero-Cadavid, Label-free wavelength and phase detection based SMS fiber immunosensors optimized with cladding etching, Sensors Actuators B Chem. 265 (2018) 10–19. https://doi.org/https://doi.org/10.1016/j.snb.2018.03.002.

[15] M. Śmietana, M. Koba, P. Mikulic, W.J. Bock, Towards refractive index sensitivity of long-period gratings at level of tens of µm per refractive index unit: fiber cladding etching and nano-coating deposition, Opt. Express. 24 (2016) 11897–11904. https://doi.org/10.1364/OE.24.011897.

[16] F. Chiavaioli, Recent Development of Resonance-Based Optical Sensors and Biosensors, Opt. . 1 (2020). https://doi.org/10.3390/opt1030019.

[17] F. Chiavaioli, C.A.J. Gouveia, P.A.S. Jorge, F. Baldini, Towards a Uniform Metrological Assessment of Grating-Based Optical Fiber Sensors: From Refractometers to Biosensors, Biosens. . 7 (2017). https://doi.org/10.3390/bios7020023.

[18] F. Chiavaioli, D. Janner, Fiber Optics Sensing with Lossy Mode Resonances: Applications and Perspectives, J. Light. Technol. 8724 (2021). https://doi.org/10.1109/JLT.2021.3052137.

[19] C. Nylander, B. Liedberg, T. Lind, Gas detection by means of surface plasmon resonance, Sensors and Actuators. 3 (1982) 79–88. https://doi.org/https://doi.org/10.1016/0250-6874(82)80008-5.

[20] R.B.M. Schasfoort, Chapter 2 History and Physics of Surface Plasmon Resonance, in: Handb. Surf. Plasmon Reson., The Royal Society of Chemistry, 2017: pp. 27–59. https://doi.org/10.1039/9781788010283-00027.

[21] I. Del Villar, F.J. Arregui, C.R. Zamarreño, J.M. Corres, C. Bariain, J. Goicoechea, C. Elosua, M. Hernaez, P.J. Rivero, A.B. Socorro, A. Urrutia, P. Sanchez, P. Zubiate, D. Lopez, N. De Acha, J. Ascorbe, I.R. Matias, Optical sensors based on lossy-mode resonances, Sensors Actuators B Chem. 240 (2017) 174–185. https://doi.org/https://doi.org/10.1016/j.snb.2016.08.126.

[22] F. Chiavaioli, P. Zubiate, I. Del Villar, C.R. ZamarrenÌo, A. Giannetti, S. Tombelli, C. Trono, F.J. Arregui, I.R. Matias, F. Baldini, Femtomolar Detection by Nanocoated Fiber Label-Free Biosensors, ACS Sensors. 3 (2018) 936–943. https://doi.org/10.1021/acssensors.7b00918.

[23] G. Moro, F. Chiavaioli, S. Liberi, P. Zubiate, I. Del Villar, A. Angelini, K. De Wael, F. Baldini, L.M. Moretto, A. Giannetti, Nanocoated fiber label-free biosensing for perfluorooctanoic acid detection by lossy mode resonance, Results Opt. 5 (2021) 100123. https://doi.org/https://doi.org/10.1016/j.rio.2021.100123.

[24] R.B.M. Schasfoort, Chapter 1 Introduction to Surface Plasmon Resonance, in: Handb. Surf. Plasmon Reson., The Royal Society of Chemistry, 2017: pp. 1–26. https://doi.org/10.1039/9781788010283-00001.

[25] M. Piliarik, J. Homola, Surface plasmon resonance (SPR) sensors: approaching their limits?, Opt. Express. 17 (2009) 16505–16517. https://doi.org/10.1364/OE.17.016505.

[26] A. Andreev, B. Pantchev, P. Danesh, B. Zafirova, E. Karakoleva, E. Vlaikova, E. Alipieva, A refractometric sensor using index-sensitive mode resonance between single-mode fiber and thin film amorphous silicon waveguide, Sensors Actuators B Chem. 106 (2005) 484–488. https://doi.org/https://doi.org/10.1016/j.snb.2004.09.002.

[27] F.J. Arregui, I. Del Villar, J.M. Corres, J. Goicoechea, C.R. Zamarreño, C. Elosua, M. Hernaez, P.J. Rivero, A.B. Socorro, A. Urrutia, P. Sanchez, P. Zubiate, D. Lopez, N. De Acha, I.R. Matias, Fiber-optic Lossy Mode Resonance Sensors, Procedia Eng. 87 (2014) 3–8. https://doi.org/https://doi.org/10.1016/j.proeng.2014.11.253.

[28] I. Del Villar, M. Hernaez, C.R. Zamarreño, P. Sánchez, C. Fernández-Valdivielso, F.J. Arregui, I.R. Matias, Design rules for lossy mode resonance based sensors, Appl. Opt. 51 (2012) 4298–4307. https://doi.org/10.1364/AO.51.004298.

[29] K. Kosiel, M. Koba, M. Masiewicz, M. Śmietana, Tailoring properties of lossy-mode resonance optical fiber sensors with atomic layer deposition technique, Opt. Laser Technol. 102 (2018) 213–221. https://doi.org/https://doi.org/10.1016/j.optlastec.2018.01.002.

[30] P. Zubiate, A. Urrutia, C.R. Zamarreño, J. Egea-Urra, J. Fernández-Irigoyen, A. Giannetti, F. Baldini, S. Díaz, I.R. Matias, F.J. Arregui, E. Santamaría, F. Chiavaioli, I. Del Villar, Fiber-based early diagnosis of venous thromboembolic disease by label-free D-dimer detection, Biosens. Bioelectron. X. 2 (2019) 100026. https://doi.org/10.1016/j.biosx.2019.100026.

[31] S.M. Schubert, L.M. Arendt, W. Zhou, S. Baig, S.R. Walter, R.J. Buchsbaum, C. Kuperwasser, D.R.

Walt, Ultra-sensitive protein detection via Single Molecule Arrays towards early stage cancer monitoring, Sci. Rep. 5 (2015) 11034. https://doi.org/10.1038/srep11034.

[32] R. Peltomaa, B. Glahn-Martínez, E. Benito-Peña, M.C. Moreno-Bondi, Optical Biosensors for Label-Free Detection of Small Molecules, Sensors . 18 (2018). https://doi.org/10.3390/s18124126.

[33] C. Trono, F. Baldini, M. Brenci, F. Chiavaioli, M. Mugnaini, Flow cell for strain- and temperature-compensated refractive index measurements by means of cascaded optical fibre long period and Bragg gratings, Meas. Sci. Technol. 22 (2011). https://doi.org/10.1088/0957-0233/22/7/075204.

[34] G. Moro, F. Bottari, S. Liberi, S. Covaceuszach, A. Cassetta, A. Angelini, K. De Wael, L. Maria, Covalent immobilization of delipidated human serum albumin on poly (pyrrole-2-carboxylic) acid film for the impedimetric detection of perfluorooctanoic acid, Bioelectrochemistry. 134 (2020) 107540. https://doi.org/10.1016/j.bioelechem.2020.107540.

[35] S.M. Borisov, O.S. Wolfbeis, Optical Biosensors, Chem. Rev. 108 (2008) 423–461. https://doi.org/10.1021/cr068105t.

[36] T.M. Squires, R.J. Messinger, S.R. Manalis, Making it stick: convection, reaction and diffusion in surface-based biosensors, Nat. Biotechnol. 26 (2008) 417–426. https://doi.org/10.1038/nbt1388.

[37] R. Gesztelyi, J. Zsuga, A. Kemeny-Beke, B. Varga, B. Juhasz, A. Tosaki, The Hill equation and the origin of quantitative pharmacology, Arch. Hist. Exact Sci. 66 (2012) 427–438. https://doi.org/10.1007/s00407-012-0098-5.

[38] N. Cennamo, G. D'Agostino, F. Sequeira, F. Mattiello, G. Porto, A. Biasiolo, R. Nogueira, L. Bilro, L. Zeni, A Simple and Low-Cost Optical Fiber Intensity-Based Configuration for Perfluorinated Compounds in Water Solution, Sensors (Basel). 18 (2018) 3009. https://doi.org/10.3390/s18093009.

|7

Molecularly Imprinted Polymers-based Sensor: Practicalities and Pitfalls

Adapted from *G. Moro**, D. Cristofori, F. Bottari, E. Cattaruzza, K. De Wael, L. M. Moretto, Redesigning an Electrochemical MIP Sensor for PFOS: Practicalities and Pitfalls, Special Issue "Advanced Electrochemical Sensors and Environmental Monitoring"*
***Sensors**, **2019**, 19, 4433.*

Abstract

Recently, biomimetic electrochemical sensors based-on synthetic modifiers, such as molecularly imprinted polymers (MIP) were successfully applied to PFAS monitoring in waters. The transfer of technology (TOT) of these electrochemical sensors within miniaturized, low-cost, fully portable analytical devices for the in-situ monitoring of PFAS as well as other environmental contaminants is still an open challenge.

Despite the numerous examples of PFAS sensors reported in literature, most of these analytical tools cannot advance in the TOT till reaching the market and get stuck in the engineering process. The redesign of a sensing strategy is often limiting its performance and, therefore, its applicability. In the redesign of MIP sensors, many parameters should be taken into account from the working conditions to the electrode characteristics (i.e., surface roughness). A complete characterisation of the surface modifiers can help to avoid time-consuming optimisations. It would allow a better understanding of the reasons why certain redesign steps affect the sensor performances.

In this chapter, a MIP electrochemical sensor for PFOS developed on gold disk electrodes was redesigned on commercial gold screen-printed electrodes (Au-SPE), as a case-study. Its initial performances were found to be poor. Prior to proceeding with further optimisation, a morphological study of the bare and modified electrode surfaces was carried out. Scanning electron microscopy–energy-dispersive X-ray spectrometry (FE-SEM–EDS), atomic force microscopy (AFM) and profilometry revealed a heterogeneous distribution of the polymer. The MIP growth resulted strongly influenced by the electrode roughness. The high content of fluorine of the target-template molecule allowed to map the distribution of the MIP and to define a characterisation protocol for this biomimetic modifier. Overall, the case study shows the importance of a multi-analytical characterisation approach to identify the factors that limit the redesign process and the TOT advances.

The study, further extended to the use of sputtered gold working electrodes and sputtered customized Au-SPE, is still ongoing. So far, it provides a methodological example of how to characterise MIP-modified SPE surfaces and use this information to guide MIP design or redesign steps.

7.1. Introduction

Lately, considerable efforts have been dedicated to the development of biomimetic electrochemical sensors for the indirect detection[1] of nonelectroactive targets (i.e., drugs of abuse, antibiotics, environmental contaminants, etc.) [1,2].

Molecularly imprinted polymers (MIP) have been largely applied as recognition layers in chemical sensors [3,4]. MIP are bio-inspired synthetic materials with target-mimetic cavities able to operate the selective recognition of a defined target molecule [5]. Their target-mimetic cavities enable the pre-concentration of the target on the electrode surface, improving the sensor sensitivity (LODs down to nanomolar or picomolar range) and the selectivity [6–9]. It was observed that MIP **target-mimetic cavities** provide a stable and highly selective recognition, reaching the performances of enzymatic receptors with all the advantages of a synthetic material. Indeed, compared to bioreceptors (i.e., enzymes, aptamers antibodies, etc.), MIP present all the characteristics of polymeric modifiers: a good chemico-physical stability, long shelf-life, affordable costs, ease of preparation and large scale productions [10,11].

The **synthesis of MIP** is characterized by three main steps: *i)* the formation of a pre-polymerisation complex between the template, which can be with the target molecule itself, and the functional monomer/s (*pre-arrangement step*), *ii)* the polymerisation of the monomer and *iii)* the subsequent removal of the template (*extraction step*) that leads to the formation of target-specific cavities within the polymeric network. It is worth noting that these cavities are complementary in size, shape and chemical functionalities with the template. They selectively bind the target molecules via covalent or non-covalent interactions allowing discriminating structurally related compounds (even enantiomers! [12,13]). MIP are extremely tuneable modifiers. Their synthesis can occur via different polymerisation mechanisms (i.e., free radical polymerisation, nitroxide-mediated radical polymerisation, etc.) and methods (i.e., bulk polymerisation, surface imprinting, precipitation, etc.), as recently summarised by Villa *et al*. [14]. In the design of electrochemical sensors, MIPs are integrated with the transducer (namely, the electrode surface) through immobilisation after bulk polymerisation [15,16], solid-state synthesis [17,18] or direct electropolymerisation [10,19,20]. Electropolymerisation conditions (i.e., monomer concentration, solution pH, etc.) determine the characteristics of MIP network: its insulation or conductive properties, its rate of nucleation and growth, its film thickness and morphology. The rational design can be instrumental to define the optimal parameters for MIP electrogeneration and maximise

---

[1] The concept of *"indirect detection"* strategy in electrochemical sensors is described in Moro et al., Current Opinions in Electrochemistry, 2019.

the monomer/template affinity based on the interaction at stake, as discussed by Fernando *et al.* [21]. Despite of the design approach, electropolymerisation shows all the advantages of a one-step process and requires the use of electroactive functional monomers [22]. Once an electroactive target is entrapped in the cavities its electron transfer can be followed directly on the electrode, as for [19]. For nonelectroactive targets, such as PFAS, the detection is mostly followed by considering two types of variations before/after the recognition event:

i) the changes in the diffusional permeability of an electroactive probe through thin MIP film (voltammetric sensors);

ii) the variation of charge transfer resistance at the MIP/solution interface (impedimetric sensors).

Both readout strategies imply the generation of an overall signal, which is due to the contribution of nonspecific interactions with the nonimprinted surface and adsorption at the electrode surface, as discussed by Yarman *et al.* [23]. To limit these contributions, extensive optimisation of the analytical protocols is required. Despite MIP capability of suppressing interferences (by acting as shape-selective filters), the changes in the polymeric network due to experimental conditions or the interaction with the sample (contaminated and not) needs to be carefully evaluated.

The sensitivity of MIP can be further enhanced by immobilising them on **hierarchical nanomaterials** [24] which often represent an additional challenge in TOT. Recently, the synthesis of the magnetic MIP (MMIP) and its combination with portable electrochemical sensors showed promising results, together with the imprinting of two template molecules in a single polymer matrix, the so-called dual MIP (DMIP) strategy [25–27]. **Several MIP sensors have been developed for the determination of PFAS**, particularly PFOS and HFPO-DA, as summarized in **Figure 7.1A-D**. In 2018, Karimian *et al.* reported a MIP-sensor for PFOS, which will be consider as a case-study for the redesign study presented in this chapter [28]. In this sensor (**Figure 7.1A**), the MIP were electrosynthesised at gold disk electrodes using ortho-phenylenediamine (*o*-PD) as a monomer. Poly-o-PD is one of the most common electronically conductive polymer (ECP) in use, together with pyrrole, 3-aminophenylboronic acid, phenol, thiophenol and aniline [29]. Its electrosynthesis have been largely investigated. Camurri *et al.* modelled the initial stages of o-PD electropolymerisation, while Vanossi *et al.* elucidated the correlation of its structural characteristic and its interfacial capacitive behavior [30,31].

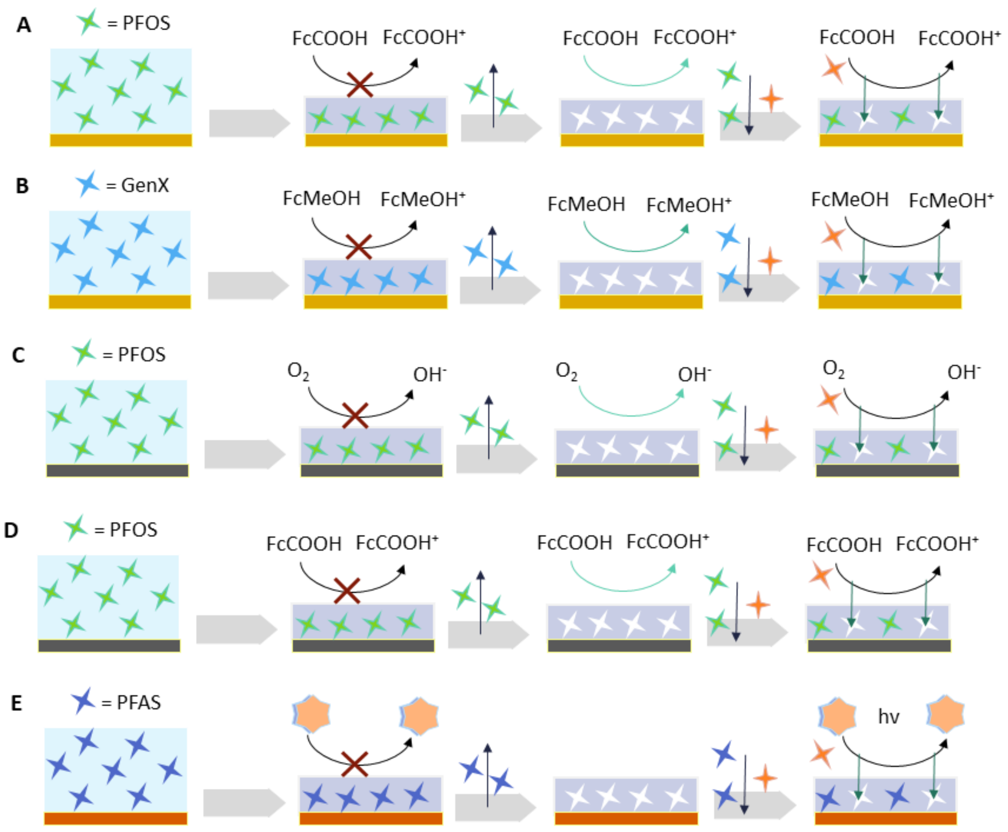

Figure 7.1 *Schematic of MIP-based sensors for PFAS, whit details of MIP preparation pathway: from the electrosynthesis to the template removal and the target rebinding step. The redox active probes are reported on each path. (**A**) PFOS sensor with poly-o-PD MIP on Au-DE* [28], *(**B**) HFPO-DA (GenX) sensor with poly-o-PD MIP on Au microelectrodes* [32], *(**C**) PFOS sens or with poly-o-PD MIP on glassy carbon electrodes* [33], *(**D-E**) PFAS sensor MIP combined with photoelectroactive materials* [34,35].

Poly-o-PD has been used by Glasscott *et al*. [33] to develop a MIP- sensor for the determination of HFPO-DA in river waters (**Figure 7.1B**). The MIP were integrated on gold microelectrode and ferrocene methanol was applied, as redox probe. The same research group developed also a MIP-sensor on glassy carbon for PFOS, and a MIP impedimetric sensor for PFOS using ambient oxygen as redox probe (**Figure 7.B-C**) [33,36]. MIP were applied also in photoelectrochemical (PEC) detection of PFAS. Here, the competition between PFAS and an electron donor led to a decrease in the photoelectrocurrent in presence of PFAS. Li *et al.* reported a MIP-graphite screen-printed electrode for photoelectrochemical detection of perfluorooctane sulfonyl fluoride [34]. They modified a commercial screen-printed electrode by electrodepositing bismuth oxyiodide nanoflakes, then a MIP layer was grafted on the surface by deposition of a drip of MIP dispersion followed by solvent evaporation. A PEC sensor for PFOA has been described by Gong *et al.*, they used a photoactive glass functionalized with a poly

2,2-azobis-2-methylpropionitrile molecularly imprinted polymer [35]. A drop of MIP dispersion was casted and then dried on the photoactive glass coated with bismuth oxyiodide nanoflakes and silver iodide nanoparticles which served as matrix to graft the MIP. These examples of PEC sensors are summarized in the schematic of **Figure 7.1E**.

In spite of these examples and their outstanding performances (good reproducibility, LODs in subnanomolar level, etc.), the majority of these sensors do not reach the market and remain mere proof-of-concept studies. The main challenges in their TOT concerns: the miniaturisation of the devices, the automation of sensor production, the development of user-friendly protocols and their applicability and reproducibility in real sample analysis. Often the conceptualization and the first optimisation of these sensors are carried out on bulk electrodes, such as gold disk or glassy carbon electrodes (as in **Figure 7.1**). However, for routinary *in-situ* applications screen-printed electrodes (SPE) are more suited. In this frame, the redesign of these sensing platforms from bulk electrodes to SPE plays a key role. Aiming to improve redesign approaches, **the MIP-PFOS sensors** reported in [28] **was chosen as case-study**. The biomimetic sensor on gold disk electrodes (Au-DE) showed excellent performance (LOD lower than the health advisory limit of 0.04 nM [37]) and was successfully applied in water sample analysis. Ferrocene carboxylic acid (FcCOOH) is used as a probe. Once the PFOS is entrapped in the cavities of the non-conductive molecularly imprinted receptor, a decrease in the redox probe signal is observed. It is related to the concentration of PFOS (*inversely proportional*). To assure the correct functioning of this indirect detection-based sensor, the MIP modifier has to form a homogenous, non-conductive layer with good reproducibility. In an ideal system, the imprinted film should allow the exchange of electrons between the electroactive probe and the electrode surface only through the target-mimetic cavities. The optimised MIP film obtained on the gold disk electrodes presents a thickness of about 200 nm [28] and its non-conductive nature was verified via cyclic voltammetry. However, the morphology and the properties of MIP do not depend only on the synthesis protocol (i.e., pre-complex mixture, electropolymerisation conditions, etc.) but also on the electrode surface features (i.e., roughness, conductivity, etc.) [38,39].

In this chapter, the possibility to apply a MIP synthesis protocol, developed on Au-DE, to gold screen-printed electrodes (Au-SPE) was investigated focusing on a case-study, the MIP-sensor for PFOS developed by Karimian *et al.* [28]. Commercial Au-SPE were first considered for the development of a portable and low-cost device. Our approach to sensor redesign was based mainly on the use of electrochemical techniques: *i)* to investigate the charge transfer process on the modified electrode surface and *ii)* to gather information about the imprinting process and the overall performances of the sensor [40,41]. Imaging techniques were applied to map the morphology and properties of the bare and MIP-modified Au-SPE [39,42]. The highly fluorinated structure of the target/template molecules allowed us **visualising the MIP distribution** with field-emission scanning electron microscopy–energy-dispersive X-ray spectrometry (FE-SEM–EDS) imaging. At the best of our knowledge, this is the first report of indirect visualisation of molecularly imprinted film on electrode surfaces via elemental mapping. From a **methodological point of view**, the main goals of this study were: *i)* to provide useful guidelines to easily redesign MIP sensors, *ii)* to propose multi-analytical approaches for MIP characterisation, *iii)* to stimulate the technological transfer of already existing biomimetic sensors.

The first part of the study was dedicated to the electrochemical study of commercial Au-SPE and the evaluation of their performances. The second part focused on the FE-SEM–EDS study of the bare and MIP-modified Au-SPE, investigating the impact of electrode surface features on the MIP morphology and distribution. The results allow defining a multi-analytical characterisation protocol applicable also to other PFAS-sensors redesign processes. From this analysis, the importance of the electrode surface features emerged clearly. The relatively high roughness of Au-SPE was found to be a limiting factor for the formation of non-conductive MIP for PFOS recognition. To further confirm these findings also sputtered gold electrodes were tested. The results of this third part of the study suggested the possibility to advance in the TOT of MIP-PFOS sensors using suitable SPE with limited surface roughness.

7.2 Materials and Methods

7.2.1. Materials, Apparatus and Analytical Techniques

Perfluorooctanesulfonic acid potassium salt (PFOS ≥ 98%), ferrocenecarboxylic acid and (FcCOOH ≥ 97%) o-phenylenediamine (o-PD ≥ 98%), were purchased from Sigma-Aldrich. All other reagents were of analytical grade and solutions were prepared using MilliQ water. Gold screen-printed electrodes 220AT (Au-SPE) were purchased from DropSens (Metrohm, Antwerp, Belgium) are composed of a gold working electrode (3 mm diameter), a gold counter electrode and a silver pseudo reference electrode. For the third part of the study (**Section 7.3.4**), gold electrodes plates (squared, 0.5 x 0.5 cm) were used as working electrodes performing all measurement in 10 mL cells, with an Ag/AgCl (sat. KCl) as reference and a Pt coil counter electrode.

Cyclic voltammetry (CV), differential pulse voltammetry (DPV) and electrochemical impedance spectroscopy (EIS) were carried out using a Metrohm Autolab potentiostat/galvanostat (PGSTAT 302 N, Metrohm Autolab) controlled by NOVA 1.1 software. A field emission scanning electron microscope (FE-SEM) Zeiss Sigma|VP was operated with 20 kV accelerating voltage to collect electron micrographs of the samples;

the instrument is equipped with an energy-dispersive X-ray spectrometer (EDS) Bruker Quantax 200, a system of the silicon drift detector (SDD) type with a 30 mm^2 collection window. The element ratios were calculated with a standardless approach using the Bruker ESPRIT v.1.9 software, with the Interactive PB-ZAF algorithm.

Roughness parameters were calculated from data obtained with an AlphaStep 500 stylus-based surface profiler. Different scans, recorded at different scan speed, sampling frequency, scan length, stylus force and the position on the sample surface were analysed. Scan length was always between 500 and 1000 µm.

Atomic force microscopy (AFM) images were obtained with an Asylum Research (Oxford Instruments Company, Abingdon, UK) Cypher instrument, used for both the topographical signal (collected in intermittent-contact mode) and the conductivity map collected with the conductive-AFM mode (C-AFM).

7.2.2 Molecularly Imprinted Polymer (MIP): From Synthesis to Template Removal

Au-SPE were washed with MilliQ water before use. The r MIP pre-complex solution was prepared by mixing 10 mM o-PD and 1 mM PFOS in 0.1 M acetate buffer pH 5.8 with 10% methanol (1:10 monomer:template ratio) and kept at 4 °C before use. The MIP electropolymerisation was performed in 100 µL drop of pre-complex solution deposited on the SPE surface, by cyclic voltammetry, scanning 25 consecutive cycles in the potential window from 0.0 V to +1.0 V vs. pseudo-Ag at a scan rate of 50 mV s^{-1}. The non-imprinted polymer (NIP), used as a control experiment, was prepared using the same protocol without adding PFOS in the pre-complex solution. All solutions were fresh prepared and stored at 4 °C for no more than 12 h. After the electropolymerisation, the MIP-electrodes were rinsed with 5 mL of MilliQ water, dried under air flow and stored at room temperature. The template was removed by letting 50 µL drops of methanol/MilliQ water (1:3, *v*/*v*) solution in contact with the working electrode for 5 min for three times reaching a total extraction time of 15 min. The electrode was rinsed with 1 mL of MilliQ water after the two first extraction steps and with 1 mL of methanol/MilliQ water (1:2, *v*/*v*) after the last one. The MIP/NIP electrodes were dried under air flow and kept at room temperature before use.

7.2.3. Electrochemical Characterisation and Performance of MIP Sensors

The electrochemical characterisation was carried out in 0.5 mM FcCOOH, 0.01 M ammonia buffer pH 8.4 by CV and EIS. The CVs were performed between −0.4 V and 0.6 V vs. pseudo-Ag, 50 mV s^{-1} scan rate, 2 to 4 scans. The EIS measurements were performed between 0.1 MHz and 0.1 Hz, 0.01 V amplitude and bias potential determined by open circuit potential (OCP). Equivalent circuit fitting was performed with NOVA 1.1 software and all the data were verified with the Kronig-Kramers transformation for consistency [43,44]. The electrochemical measurements of PFOS were carried out in 100 µL drops. A series of 0.01 M ammonia buffer pH 8.4 solutions spiked with different concentrations of PFOS (from 50 nM to 500 nM) were prepared. In this rebinding step, the 100 µL drops of PFOS solutions were left in contact with the modified electrodes for 15 min. After this incubation, the drops were washed away using 1 mL of methanol/MilliQ water (1:2, *v/v*) and the electrodes were tested in 100 µL of 0.5 mM FcCOOH, 0.01 M ammonia buffer pH 8.4 by performing CV and DPV. For the CV, the conditions mentioned above were applied, while for DPV the following parameters were used (previously optimised [28]) potential window between 0.0 V and 0.5 V vs. pseudo Ag, pulse width 25.0 ms, pulse amplitude 25.0 mV, increment potential 4.0 mV and scan rate 20 mV s^{-1}. The calibration plots were obtained by performing the rebinding step of four different solutions at increasing concentration of PFOS (50, 100, 250 and 500 nM). In between each step, the modified electrodes were accurately rinsed with 1 mL of methanol/MilliQ water (1:2, *v/v*). A baseline correction using the moving average (n = 1) tool within the NOVA 1.1 software was operated on the DPV voltammograms obtained. All the analyses were performed in triplicates. Except where otherwise stated, all the potentials are referred to an Ag pseudo reference (about −200 mV compared to SCE). All electrochemical experiments were performed at room temperature.

7.3 Results and discussion

7.3.1. Electrochemical Characterisation of MIP-Gold Screen-Printed Electrodes

The original protocol reported by Karimian *et al.* [28] was adapted to the commercial Au-SPE. The electropolymerisation was carried out in a drop of 100 µL to reduce the pre-complex solution volume. The percentages of methanol in the pre-complex solution and in the template removal step were drastically decreased. An excessive methanol content was found to affect the electrode performance, as shown in **Figure 7.2**. With 50% methanol the first CV cycle of the electropolymerisation presents a broad oxidation peak with a relatively low current intensity (about 200 µA); the working electrode (WE) appears darker at the end of the process. With 25% methanol the WE is slightly darker and the electropolymerisation pattern presents a more defined oxidation peak. Only reducing the methanol concentration to 10%, the expected electropolymerisation pattern with a first CV cycle characterised by multiple oxidation peaks was recorded. This was also the minimal methanol concentration applicable to assure the complete dissolution of the target-template (PFOS).

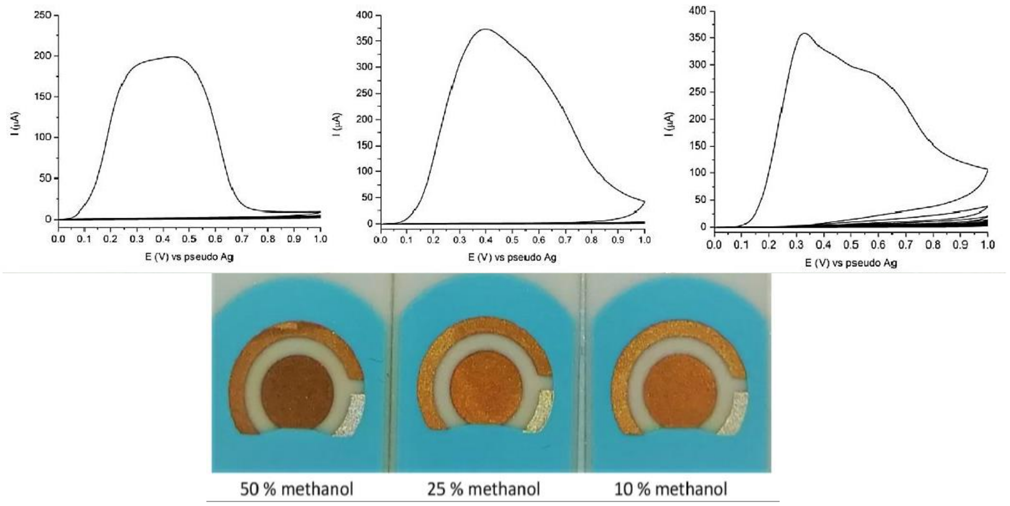

50 % methanol 25 % methanol 10 % methanol

Figure 7.2 *Effect of methanol content on the performances of Au-SPE: (upper part) CVs of the electropolymerisation recorded at different percentages of methanol* **and (lower part)** *photographs of the electrodes after the polymerisation.*

After these first changes, the adapted protocol (fully described in **Section 7.2.2**) was utilized to obtain imprinted (MIP) and non-imprinted (NIP) polymers. An electrochemical characterisation of the modified sensors was performed by CV and EIS. For these preliminary tests, the electropolymerisation patterns of both MIP and NIP polymers (compared in **Figure 7.3**) were found to be consistent with the ones previously reported in [28]. The voltammograms of NIP electropolymerisation in **Figure 7.3B** showed in the first CV cycle multiple oxidation peaks (two main ones at +0.3 V and +0.6 V vs pseudo-Ag), as previously observed [45]. For the MIP, the first cycle presented a unique peak at +0.3 V. These differences in MIP/NIP the electropolymerisation pattern indirectly confirmed the complete dissolution of the PFOS in the pre-complex solution even in presence of a reduced methanol content.

The step-by-step characterisation reported in **Figure 7.4** allowed to follow the formation of the imprinted film on the electrode surface. After the electropolymerisation, both MIP and NIP modified electrodes showed a non-conductive behaviour as expected for the formation of a non-conductive polymer on their surfaces.

The redox behaviour of the mediator (FcCOOH) is completely suppressed for both the MIP (blue curve in **Figure 7.4A**) and the NIP (blue curve in **Figure 7.4B**). However, the capacitive current of MIP and NIP electrodes present a different intensity: for the MIP it was about 6 ± 0.9 nA while for the NIP a value of about 17 ± 0.8 nA was recorded. This difference was simply ascribed to the different composition of the electropolymerisation solution and to the presence of the PFOS template in the MIP, which influences the properties of the final polymer.

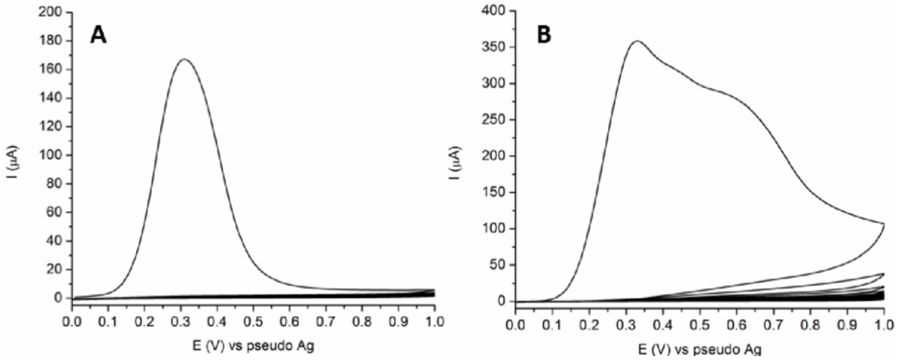

***Figure 7.3**. Comparison of the electropolymerisation pattern of imprinted (**A**) and non-imprinted (**B**) polymers on Au-SPE.*

After the template extraction, the redox activity of the mediator was again visible on MIP (green curve in **Figure 7.4A**) while it was still not present on NIP (green curve in **Figure 7.4B**, overlapped with red and blue curves). This behaviour is consistent with the fact that after extraction of the template the imprinted cavities are free again, allowing the electron exchange between the electrode surface and the mediator in solution. However, this electron transfer (ET) was heavily influenced by the presence of the MIP: the ΔEp increases (from 65 mV to 145 mV), the $E_{1/2}$ shifted (ΔE >100 mV) and the peak current intensities for both anodic and cathodic processes decreased. As expected, for NIP there was no difference before and after extraction since there were no empty imprinted cavities to free. *After the rebinding* of 500 nM PFOS, a decrease in the FcCOOH signal was recorded on MIP-Au-SPE (red curve in **Figure 7.4A**). This can be considered as an indication of the successful recognition event between PFOS target/template molecules and the imprinted cavities, as previously stated [28]. Once the cavities are re-loaded with the PFOS the interaction of the redox mediator with the electrode surface and consequently its signal will decrease again. As expected, no changes were observed on NIP-Au-SPE (red curve in **Figure 7.4B**). This confirmed the MIP recognition capabilities towards PFOS and the success of the imprinting protocol.

EIS results for both MIP and NIP provided additional information about the polymer formation and characteristics. The Nyquist plots for both MIP (**Figure 7.4C**) and NIP (**Figure 7.4D**) showed the successful deposition of the polymer film. The data of the bare Au-SPE electrodes (black dots in **Figure 7.4E-F**) can be fitted to a Randles electrochemical equivalent circuit (EEC, **Figure 7.4G**) where: R_s is the uncompensated solution resistance, CPE the constant phase element used to model the double layer capacitance, R_{ct} the charge transfer resistance and W the Warburg impedance. This latter accounts for the semi-infinite diffusion of the electroactive species from the bulk of the solution towards the surface of the electrode.

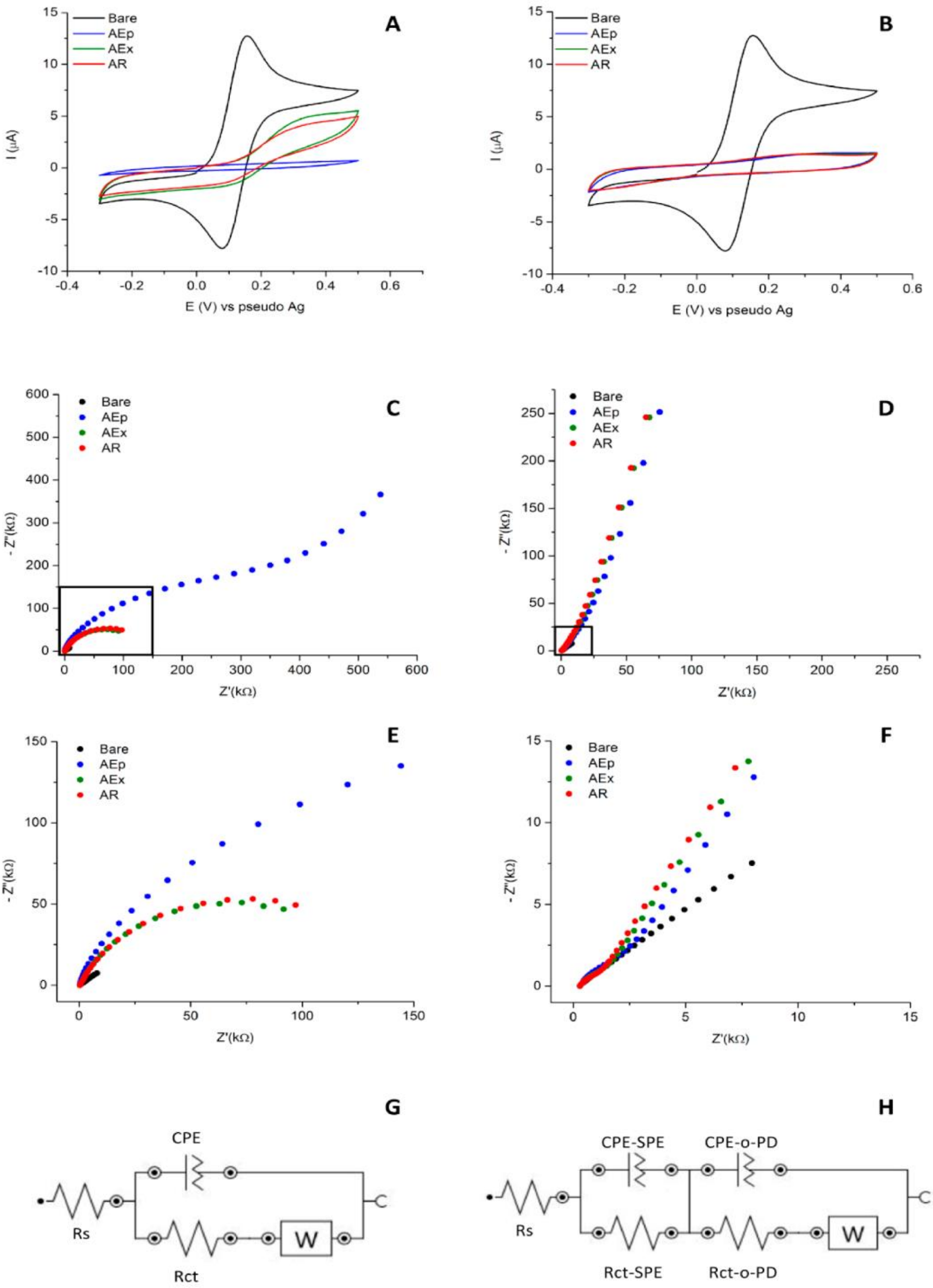

Figure 7.4. *Electrochemical characterisation study of imprinted (MIP) and non-imprinted (NIP) polymers at gold screen-printed electrode (Au-SPE). Cyclic voltammetry (CV) and Nyquist plots obtained after each step of the modified protocol for MIP ((**A**,**C**), respectively) and NIP ((**B**,**D**), respectively). The CVs were scanned at 50 mVs*$^{-1}$*, while EIS spectra were recorded with an amplitude of 0.01 V and a bias potential determined by open circuit potential (OCP). All measurements were performed in 0.5 mM FcCOOH, 0.01 M ammonia buffer (pH 8.4). Zoom in on the Nysquit plot for MIP (**E**) and NIP (**F**) and equivalent circuits*

*used to fit the EIS data (**G,H**). The abbreviations used in the legend indicate the following steps: Bare, unmodified Au-SPE (in black); AEp, after electropolymerisation (in blue); AEx, after template extraction (in green); AR, after target rebinding (in red).*

After the electropolymerisation, the impedance behaviour of the MIP changes: the blue curve in **Figure 7.4C** shows a very depressed semicircle at higher frequencies and a linear trend at lower frequencies. The radius of the semicircle is linked to the R_{ct}. Since there is a non-conductive modifier on the surface of the electrode, the ET between the mediator and the electrode is heavily impaired. *After the extraction* (green curve in **Figure 7.4C**), the semicircle radius decreases again, as now the cavities are free and the probe can reach the electrode surface. After rebinding of 500 nM of PFOS the Nyquist plot for the MIP (red curve in **Figure 7.4C-E**) does not show meaningful changes even though an increase in R_{ct} was expected since the cavities are again occupied. However, the PFOS concentration is very low compared to the original pre-complex solution (1 mM). For the NIP, instead, the Nyquist plot after electropolymerisation (blue curve in **Figure 7.4D**) shows a modest increase in the semi-circular part at higher frequencies (see also blue curve in **Figure 7.4F**) while the linear part is very steep and starts at relatively high frequencies compared to the MIP. Again, no sensible changes are present after extraction and rebinding of 500 nM of PFOS as already shown by CV (see **Figure 7.4B**). The impedance data for both the MIP and NIP sensors could be fitted by the equivalent circuit reported in **Figure 7.4H**. The circuit accounts for the presence of a non-conductive polymeric layer on top of a conductive electrode surface [46,47]. CPE-SPE and R_{ct}-SPE are, respectively, the constant phase element and the charge transfer resistance of the Au-SPE, while CPE-o-PD and R_{ct}–o-PD refer to the o-PD polymer film. The values of the charge transfer resistance (summarized in **Table 1**) for both MIP and NIP confirm this interpretation.

***Table 1** Charge transfer resistances (Rct-o-PD) for the MIP and NIP: AEp after electropolymerisation, AEx, after extraction, AR, after rebinding.*

MIP	Rct-o-PD (kΩ)	χ2
AEp	125	0.03
AEx	21.7	0.02
AR	20.5	0.005
NIP	Rct-o-PD (kΩ)	χ2
AEp	2.37	0.005
AEx	2.15	0.03
AR	2.32	0.005

While the R_{ct}–o-PD of the NIP remains constant for each step (c.a. 2 kΩ), the MIP presents very high values after electropolymerisation (125 kΩ), that diminish sensibly after extraction (around 20 kΩ). This first characterisation of the MIP-Au-SPE gave positive results suggesting the feasibility of the optimisation of the original protocol [28] on SPE. To validate the proposed protocol, the analytical performance of the imprinted sensors was tested and compared to the original sensor.

7.3.2. Performance of MIP-Au-SPE

The performance of the imprinted sensors was evaluated by differential pulse voltammetry (DPV), using NIP-Au-SPE as a control experiment. Four different concentrations of PFOS (50, 100, 250 and 500 nM) within the linear range previously reported [28] (from 0.1 nM to 1.5 µM) were selected. The calibration plot shown in **Figure 7.5**, obtained from triplicate measurements, using MIP-Au-SPE showed a poor reproducibility and an unexpected trend. Instead of a linear decrease in signal at increasing PFOS concentration, a non-linear evolution with a net signal increase at 500 nM was observed.

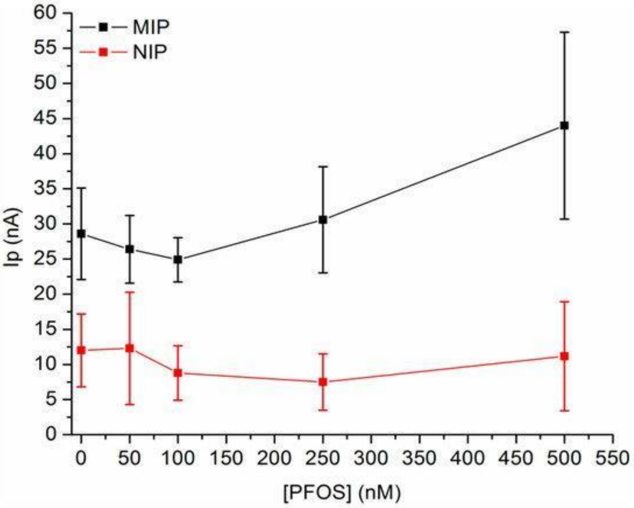

Figure 7.5 Calibration plots of imprinted (MIP, black) and non-imprinted (NIP, red) polymers at Au-SPE obtained after the rebinding of 0, 50, 100, 250 and 500 nM of PFOS. The values presented are the average of three measurements and the error associated to the standard deviation.

For 50 and 100 nM, signals with current intensities slightly lower than the unloaded MIP were recorded and these variations were not considered relevant because of the high error associated. For 250 and 500 nM, the increased signals and associated errors might suggest the instability of the obtained modification and the partial removal of the polymer from the electrode surface. The relatively high errors associated with the measurements depend mainly on the highly variable responses of the different MIP-Au-SPE sensors and can possibly be ascribed to the variability in the electrode surface properties. As a control experiment, NIP-Au-SPE were also tested showing no relevant variations in the signal intensity after the different rebinding, as expected. The high error associated with the values presented can be explained with the lack of target-template cavities and the occurrence of adsorption phenomena [28]. No net signal increases were observed for 250 and 500 nM and this was ascribed to the higher stability of the non-imprinted polymer itself.

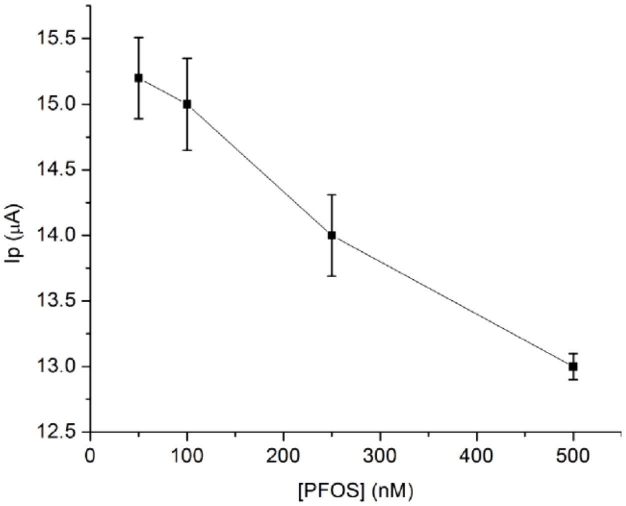

Figure 7.6 *Calibration plot of PFOS at bare Au-SPE. The values presented are the average of three measurements and the error associated to the standard deviation.*

Also, the PFOS affinity for the bare Au-SPE was tested, operating the rebinding on unmodified electrodes. From the calibration plot obtained (**Figure 7.6**), minimal signal variations (with a Δi for 50 and 500 nM PFOS solutions of about 2.5 ± 0.5 μA) were recorded with an inversely proportional trend between the target concentration and the mediator signal. The affinity of PFAS for gold substrates will be further discussed in **Chapter 8**, where the results of molecular dynamics simulations allowed quantifying the attraction energies at stake between our fluorinated compounds and this electrode material. The higher reproducibility of the measurements at bare Au-SPE in comparison to MIP/NIP-Au-SPE ones, indirectly suggest the low reproducibility and instability of polymeric modifiers. The trend showed in **Figure 7.6** confirmed PFOS affinity for the Au-SPE surface and the importance of considering these interactions in further optimisations.

The analysis of the MIP-Au-SPE performances underline the need of further redesign the protocol and identifying the factors that limit the sensor performance. Aiming to understand the reasons behind its poor performances, the morphological characterisation of the bare electrode surface and the MIP and NIP modified sensors was carried out.

7.3.3. Morphological Characterisation

7.3.3.1. Surface Analysis of Unmodified Au-SPE

The roughness and the electrodic properties of the bare Au-SPE were investigated by FE-SEM, profilometry and AFM. From FE-SEM micrographs, it was possible to observe a heterogeneous surface, characterised by swells and holes as can be seen in the secondary electron micrograph reported in **Figure 7.7A-B**.

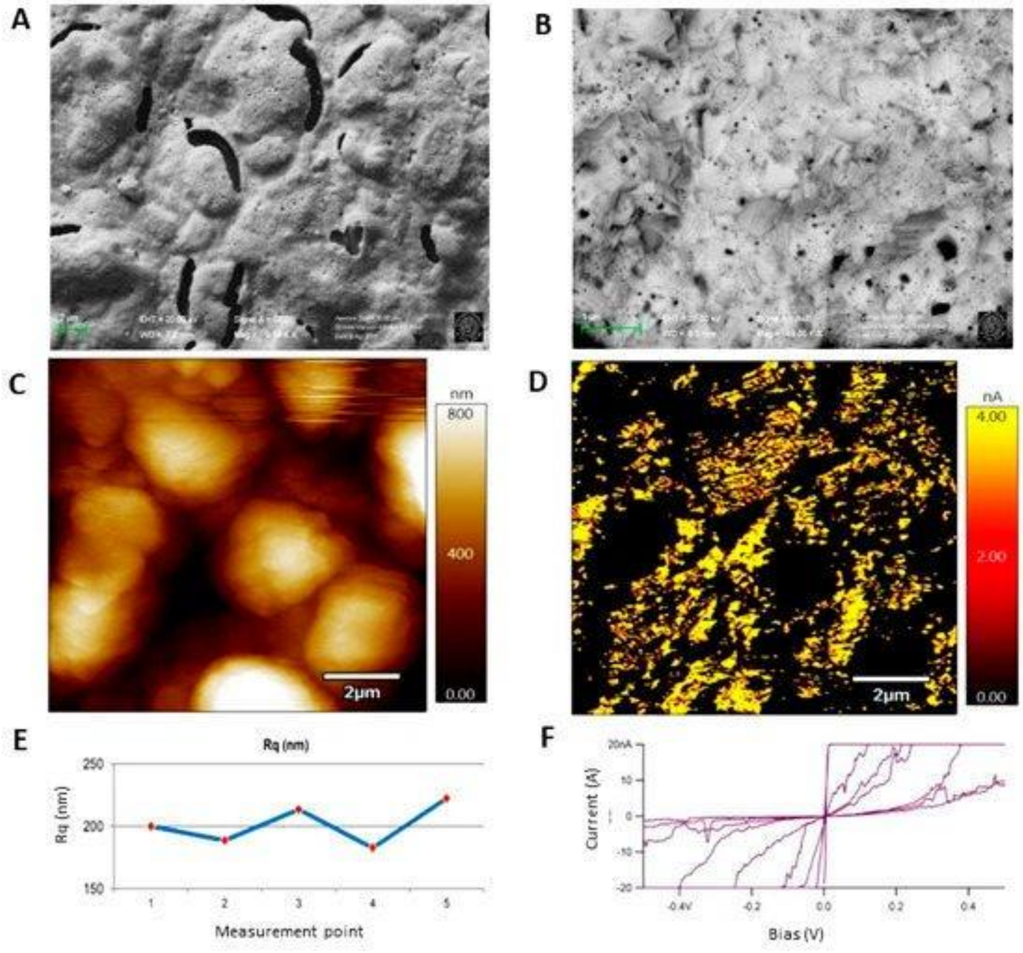

Figure 7.7 *Surface characterisation of unmodified gold screen-printed electrode imaged with: field-emission scanning electron microscopy (FE-SEM) at 9.16 kX using secondary electrons (**A**) and 40 kX using backscattered electrons (**B**), both at 20.00 kV; atomic force microscopy (AFM) topography (**C**) and conductivity (**D**) modes. AFM correlated graphs showing the roughness (**E**) and the conductivity (**F**) measured in different points.*

The estimated Rq < 1 μm suggests the importance of characterising the surface roughness in the nanometric range by AFM topographical analysis.

The roughness of the surface was estimated in the micrometer and nanometer range. By means of the stylus surface profiler, a root mean square roughness, Rq, of

(0.75 ± 0.10) µm was calculated from the raw data, as defined in [48]; the uncertainty is related to a 95% confidence interval. **Figure 7.7C** showed that the total height of the swells is about 0.8 µm. Rq values calculated from AFM results on five different sites imaged gave a mean value of 200 nm. The variation of the R_q value from site to site reported in **Figure 7.7E** was about 15 nm. This R_q value, (200 ± 15) nm, confirmed the meaningful nanoscale roughness of the surface.

Moreover, a platelet-shaped fine structure was imaged with FE-SEM at higher magnification, as shown in **Figure 7.7B**. It was noticed that even though the platelets have different orientation in different sample areas, in a single area they tend to be aligned with each other. In order to verify the possible presence of other metals in amalgam with Au, the elemental composition of the bare electrode surface was investigated by EDS analysis [49], but apart from gold, no other elements were found.

From AFM measurements, it was possible to map the heterogeneous conductivity of these electrodes. Areas with smaller conductivity correspond to the swells in topographical image, while the holes present a relatively higher but non-uniform conductivity, as can be seen by comparing **Figure 7.7 C-D** (acquired during the very same scanning through different channels of the instrument). This behaviour leads to different current-voltage profiles in the different points of the surface, as shown by the curves in **Figure 7.7F**.

The profiles reported have different slopes and ohmic intervals ranging from (12 ± 5) mV to (670 ± 130) mV. These values indicate that the surface characteristics of the Au-SPE (220AT, Dropsens) differ deeply from the homogenous, approximately flat bulk gold disk electrode surface. The heterogeneous conductivity of the surface might be responsible for a heterogeneous growth of the polymer modifier.

7.3.3.2. Surface Analysis of MIP and NIP

The MIP distribution after polymerisation was investigated with backscattered and secondary electrons. By comparing the images of the same area obtained with these two signals it was possible to recognize the polymer distribution on the electrode surface. Since the backscattered electrons (BSE) signal depends on the average atomic number Z of the sample material hit by beam (primary) electrons in BSE micrographs the polymer is darker than higher-Z areas, like bare gold ones [50]. On the other hand, the secondary electrons (SE) signal is much less sensitive to the average atomic number [51]. Therefore, in BSE images it was possible to recognize areas richer in polymer with respect to the surroundings as dark areas. However, each dark area cannot be identified as a polymer, because holes on the bare electrode surface appear dark; nonetheless they also appear dark in SE images, and this allowed discriminating which dark areas in BSE micrographs were holes and which were not. With this approach, the comparison of BSE (**Figure 7.8A**) and SE (**Figure 7.8B**) of the same area of the sample highlighted the presence of low-Z areas, which reasonably were polymer areas (due to the nature of the sample).

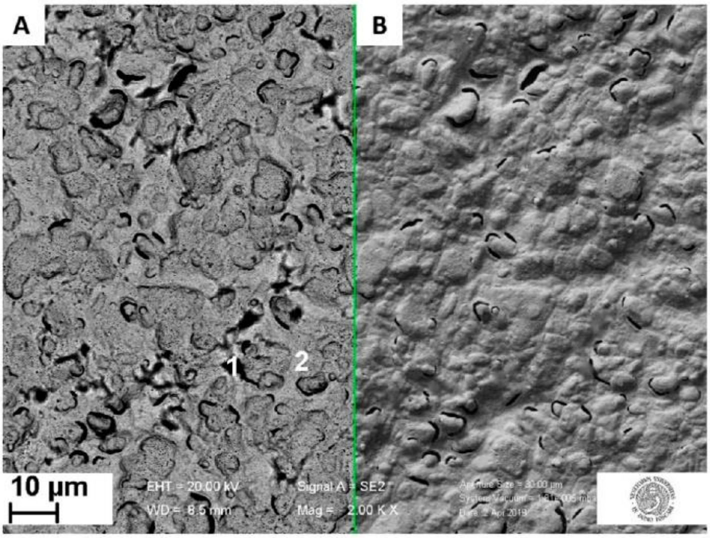

Figure 7.8 *Surface of a MIP modified Au-SPE imaged with FE-SEM using the backscattered electrons (**A**) and secondary electrons (**B**) at 20.0 kV with a magnification of 2 kX; inset: numbers indicating the points where energy-dispersive X-ray spectrometry (EDS) spectra were recorded. Inset: point 1 dark area ascribed to polymer formation and point 2 bare Au surface.*

The EDS confirmed this hypothesis: these dark areas are rich in C and F atoms (wt%[2] of 74% and 42%, respectively, compared to 21% and ≈0% observed on bare Au-SPE), which are present in the MIP, while the surrounding light areas give a lower C peak and almost no F peak at all. Thus, this SEM/EDS analysis showed that the polymer is mainly growing in islands on the surface of the working electrode.

Other examples of these islands are visible in **Figure 7.9**, which shows that in some cases the polymer grows in rod shape, with a length up to almost 30 µm. The relatively regular shape of these islands might be ascribed to the crystalline nature of the polymer in these aggregates (OPD crystals have an orthorhombic lattice [52]).

In **Figure 7.9B**, a close-up image of a single island is reported, and the presence of fluorine in the EDS spectra from the islands (i.e., spectra A-1 and B-1 in **Figure 7.9**) confirm the successful entrapment of the PFOS in the polymer matrix with a weight concentration ratio between F and C, c_F/c_C, of 0.94. In the spectra A-2 and B-2 (**Figure 7.9**) recorded in the region outside the polymer islands a weak fluorine peak was observed, revealing the presence of the PFOS also out of the islands; with a c_F/c_C of 0.07.

---

[2] Where *wt%* is weight percentage of an element: is the weight of that element measured in the sample divided by the weight of all elements in the sample multiplied by 100.

These observations suggested that the pre-complex electropolymerisation is not homogenous and that the PFOS is preferentially associated within polymeric islands.

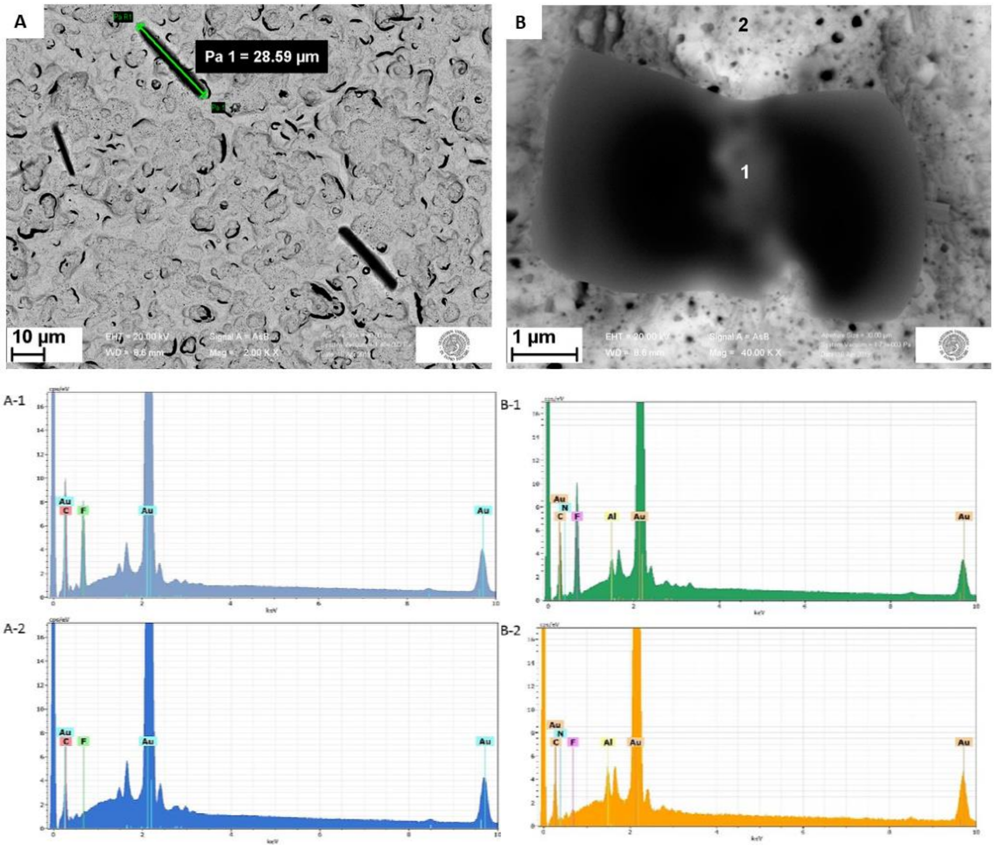

*Figure 7.9 Examples of MIP heterogenous distribution after electropolymerisation with the presence of polymer 'islands-like' aggregates. Overall distribution at 2.00 kX, with green arrow and label indicating the island length of about 28.6 µm (**A**). Zoom on a polymeric island at 40.00 kX, where the numbers indicate the EDS spectra acquisition points (**B**). Both images were obtained using backscattered electrons.*

The highly fluorinated of the template/target molecules allowed mapping the template distribution on the electrode surface by means of an X-ray map of the fluorine peak. In **Figure 7.10**, a backscattered micrograph is compared with the fluorine map of the same area to highlight the correspondence between polymer islands and high fluorine weight percentages, above indicated as wt%. In the X-ray map randomized distribution of lower quantities of F can be observed. It can be partially ascribed to a background noise. But it also confirmed the presence of an inhomogeneous MIP distribution also outside the islands.

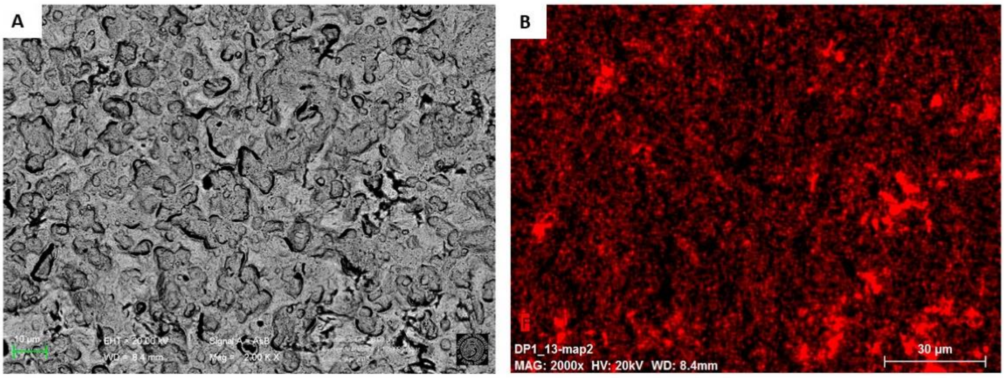

Figure 7.10 *Examples of MIP heterogenous distribution after electropolymerisation: image obtained with backscattered electron (BSE), 20.00 kV and a magnification of 2.00 kX (**A**) and the corresponding fluorine map (**B**), whose most intense areas are at the same locations as low Z island in BSE micrograph. This map was elaborated by applying a smooth filter with kernel size 3 to the data collected by the detector.*

The same set of measurements was performed using NIP-Au-SPE. No traces of fluorine were observed. However, a similar heterogeneous distribution of the polymer was observed in SE and BSE images. In the carbon X-ray maps, higher concentration areas similar to those found in the fluorine map were observed. However, these maps were not further considered because of their high background noise. All these maps were obtained with an acquisition time optimised to 6 min, a reasonably short time for the 30 mm^2 window SDD detector used. The optimisation of the instrument settings helped increase the collection efficiency, reducing the measuring time needed to reach the requested signal-to-noise ratio in the map.

This characterisation allows a better understanding of the data presented in **Section 7.3.1**. The poor reproducibility at Au-SPE can be ascribed to the heterogenous distribution of the MIP polymer due to the roughness of this substrate. Indeed, commercial gold screen-printed electrodes were found to have a highly rough surface which did not allow a homogenous polymerization of MIP. This could be one of the main reasons behind the poor reproducibility of MIP-Au-SPE responses. These results suggested the need to continue this redesign process by focusing on the electrode surface, including a surface activation treatment to improve the conductivity or to test other Au-SPEs produced with different fabrication techniques (i.e., sputtered). For these reasons, a third part of the study was dedicated to the synthesis of MIP at sputtered gold plates, as described in the following section.

7.3.4 Lowering the Roughness: MIP at Sputtered Gold Electrode[3]

Sputtered gold plates (SGP, squared, 0.5 x0.5 cm) were used as working electrodes and the protocol described in **Section 7.2.3** was applied using a standard three-electrode cell setup. SGP roughness, measured using AFM, was found to be much lower than the one of the commercial Au-SPE, with an average value of (10 ± 1) nm compared to the one of (200 ± 15) nm recorded for Au-SPE. The FE-SEM-EDS analysis showed a uniform surface and did not evidence any other element apart from gold. The voltammograms of the electropolymerisation of both MIP and NIP were found to be consistent with the one previously described (**Figure 7.3**). Once the template was removed, MIP-SGP performance were tested using synthetic solution with increasing concentration of PFOS.

The voltammograms in **Figure 7.11A** show that the peak currents decrease as PFOS concentration increases, proving the capability of the MIP to recognize the PFOS molecule. The plot in **Figure 7.11B** shows the correlation between PFOS concentrations and the MIP-PFOS sensor responses. The peak currents ($i - i_0$) were in the order of nanoamperes. The strategy needs to be surely optimised, but a promising trend was observed in respect to the previous sections. NIP modified SGP showed no meaningful changes after PFOS incubations. Despite the very limited linear range, the present experiments suggested: *i)* the potential applicability of SGP as MIP substrate to develop MIP based sensing strategies for PFOS, *ii)* confirmed (indirectly) the importance of controlling the electrode surface features, *iii)* the potential applicability of a miniaturize PFOS sensor in the low nanomolar range (1 – 15 nM).

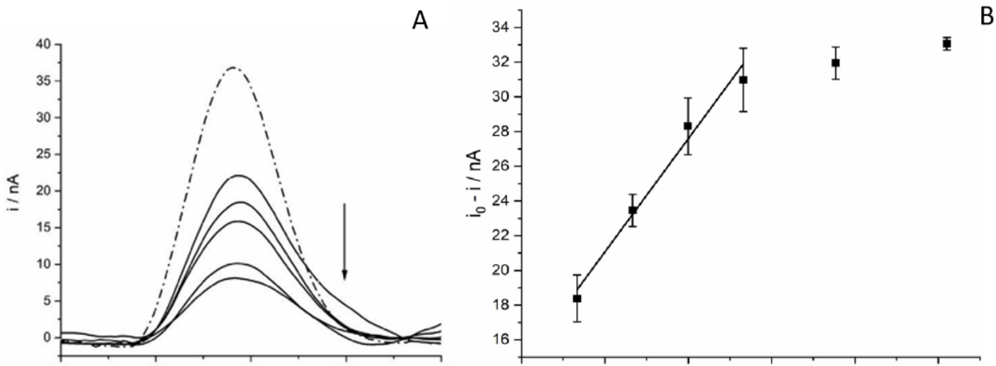

Figure 7.11. (A) Voltammograms recorded via DPV after 15 min incubation in 0.5 mM FcCOOH (pH 8.4) containing increasing concentration of PFOS, dashed line: blank, black lines: PFOS concentrations from 3.3 nM to 18.9 nM. (B) Dependence of the $i_0 - i$ on the PFOS concentration. Regression line in the concentration range 3.3 – 18.9 nM: $i_0 - i = 1.31[PFOS] + 14.53$.

---

[3] The following results have to be considered as preliminary (*ongoing study*).

These preliminary data suggest the need of designing customised Au-SPE with a sputtered gold working electrode, as illustrated in **Figure 7.12**. Here, a sputtered gold plate is first considered carrying out the MIP electropolymerisation and the template extraction within a standard three-electrode cell setup (volumes < 5mL). Once the MIP is formed and the cavities are free, the MIP-SGP can be combined with a screen-printed mask containing the external reference and counter electrodes, obtaining a compact analytical device suitable for *in-situ* applications.

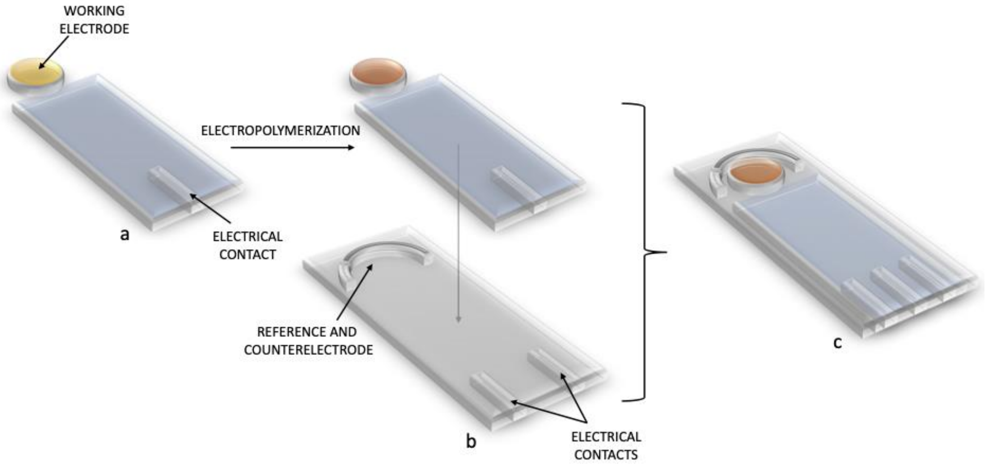

Figure 7.12 *Schematic illustration of the proposed design for MIP-PFOS sensor, (**a**) customised sputter gold plates, (**b**) screen-printed mask, (**c**) assembled platform.*

7.4 Conclusions

The redesign of MIP-electrochemical sensors is often limiting the TOT of electrochemical sensors for *in-situ* environmental monitoring. In this chapter, a MIP-sensor for PFOS detection was redesigned and adapted: from a standard three-electrode cell setup with a gold disk working electrode to a portable gold screen printed electrode device. The possibility to adapt the MIP modification protocol to portable electrodes was first investigated using CV and EIS to characterise the MIP synthesis steps. The results obtained were encouraging even though the final sensor performance was not comparable to the MIP on bulk electrodes.

To better understand these outcomes, an extensive multi-analytical characterisation study was performed. By combining FE-SEM-EDS, profilometry and AFM, we observed that the Au-SPE presented a high surface roughness, which led to a heterogenous distribution of the MIP after electropolymerisation. The SEM–EDS study performed to describe the morphology and distribution of the MIP modifiers allowed to visualize the formation of polymer islands with a higher content of template. This information helped to interpret the data obtained from the first electrochemical study of the sensor. The unique possibility to perform a complete morphological study, visualizing the MIP distribution at the electrode surface, should be further applied in the next optimisation steps of the redesign and extended to the study of other MIP with templates rich in fluorine (particularly for PFAS monitoring).

Here, this characterisation allowed ascribing the poor reproducibility of MIP-Au-SPE to the heterogeneous distribution of the MIP polymer due to the roughness of the substrate. As anticipated, the commercial gold SPE in use showed a highly rough surface which did not permit the formation of a homogeneous imprinted polymer. This hypothesis was further confirmed by the last test carried out at SGP with a lower surface roughness.

In the overall the results underlined the need to continue this redesign process by focusing on the electrode surface, including a surface activation treatment to improve the conductivity and testing customised sputtered SPE.

The redesign study presented here showcased several of the possible issues in the technological transfer of imprinted electrode modifiers, stressing once more the need for a deeper connection between fundamental research done in the laboratory and envisioned commercial applications and TOT processes.

Acknowledgments

I would like to thank all the colleagues that contributed to this work, particularly Fabio Bottari that followed all the steps with a thought-provoking approach to the redesign process, MIP electrosynthesis and characterisation. We got to learn how an appropriate characterisation can avoid time-consuming optimisations, at least this time!

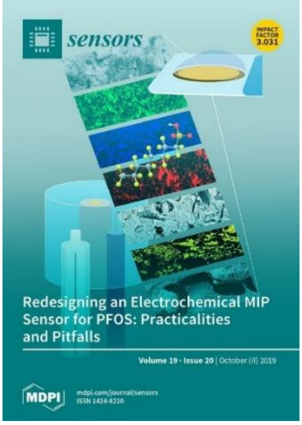

sensors

IMPACT FACTOR 3.031

Redesigning an Electrochemical MIP Sensor for PFOS: Practicalities and Pitfalls

Volume 19 · Issue 20 | October (II) 2019

MDPI mdpi.com/journal/sensors ISSN 1424-8220

A special thank also to Davide Cristofori for introducing me to FE-SEM-EDS and AFM. All the hours spent in tuning the mapping parameters gave me the possibility to get familiar with EDS mapping, its potential and limitations. Davide, I am grateful you got involved in first-person in the project because our discussions opened up my mind, your passion for electron microscopy was really contagious! Thanks to Rafaël Barbattini and Asylum Research for their support and for following us in all AFM measurements and data interpretation. Thanks to our students Ettore and Alessia for carrying on this project. I would like to acknowledge Prof. Elti Cattaruzza for the profilometry measurements, his help and precious time.

Thanks to MDPI editors for selecting our contribution as representative for **Sensor Issue 29***.*

References

[1] S.T. Ovbude, P. Tao, Z. Li, D.S. Hage, High-Performance affinity chromatographic studies of repaglinide and nateglinide interactions with normal and glyoxal- or methylglyoxal-modified human albumin serum, J. Pharm. Biomed. Anal. 201 (2021) 114097. https://doi.org/https://doi.org/10.1016/j.jpba.2021.114097.

[2] N. Tarannum, S. Khatoon, B.B. Dzantiev, Perspective and application of molecular imprinting approach for antibiotic detection in food and environmental samples: A critical review, Food Control. 118 (2020) 107381. https://doi.org/https://doi.org/10.1016/j.foodcont.2020.107381.

[3] N. Leibl, K. Haupt, C. Gonzato, L. Duma, Molecularly Imprinted Polymers for Chemical Sensing: A Tutorial Review, Chemosens. . 9 (2021). https://doi.org/10.3390/chemosensors9060123.

[4] O.S. Ahmad, T.S. Bedwell, C. Esen, A. Garcia-Cruz, S.A. Piletsky, Molecularly imprinted polymers in electrochemical and optical sensors, Trends Biotechnol. (2018) 1–16. https://doi.org/10.1016/j.tibtech.2018.08.009.

[5] C. Malitesta, E. Mazzotta, R.A. Picca, A. Poma, I. Chianella, S.A. Piletsky, MIP sensors - The electrochemical approach, Anal. Bioanal. Chem. 402 (2012) 1827–1846. https://doi.org/10.1007/s00216-011-5405-5.

[6] M. Palanna, I. Mohammed, S. Aralekallu, M. Nemakal, L.K. Sannegowda, Simultaneous detection of paracetamol and 4-aminophenol at nanomolar levels using biocompatible cysteine-substituted phthalocyanine, New J. Chem. 44 (2020) 1294–1306. https://doi.org/10.1039/C9NJ05252F.

[7] M.M. El-Beshlawy, F.M. Abdel-Haleem, A. Barhoum, Molecularly Imprinted Potentiometric Sensor for Nanomolar Determination of Pioglitazone Hydrochloride in Pharmaceutical Formulations, Electroanalysis. 33 (2021) 1244–1254. https://doi.org/https://doi.org/10.1002/elan.202060141.

[8] J. Yang, W. Feng, K. Liang, C. Chen, C. Cai, A novel fluorescence molecularly imprinted sensor for Japanese encephalitis virus detection based on metal organic frameworks and passivation-enhanced selectivity, Talanta. 212 (2020) 120744. https://doi.org/https://doi.org/10.1016/j.talanta.2020.120744.

[9] H. Song, Y. Wang, L. Zhang, L. Tian, J. Luo, N. Zhao, Y. Han, F. Zhao, X. Ying, Y. Li, An ultrasensitive and selective electrochemical sensor for determination of estrone 3-sulfate sodium salt based on molecularly imprinted polymer modified carbon paste electrode, Anal. Bioanal. Chem. 409 (2017) 6509–6519. https://doi.org/10.1007/s00216-017-0598-x.

[10] V. V Shumyantseva, T. V Bulko, L. V Sigolaeva, A. V Kuzikov, A.I. Archakov, Electrosynthesis and binding properties of molecularly imprinted poly-o-phenylenediamine for selective recognition and direct electrochemical detection of myoglobin, Biosens. Bioelectron. 86 (2016) 330–336. https://doi.org/10.1016/j.bios.2016.05.101.

[11] O.S. Ahmad, T.S. Bedwell, C. Esen, A. Garcia-Cruz, S.A. Piletsky, Molecularly Imprinted Polymers in Electrochemical and Optical Sensors, Trends Biotechnol. 37 (2019) 294–309. https://doi.org/https://doi.org/10.1016/j.tibtech.2018.08.009.

[12] S.A. Piletsky, K. Karim, E. V Piletska, C.J. Day, K.W. Freebairn, C. Legge, A.P.F. Turner, Recognition of ephedrine enantiomers by molecularly imprinted polymers designed using a computational approach, Analyst. 126 (2001) 1826–1830. https://doi.org/10.1039/B102426B.

[13] Y. Zhang, H.-Y. Wang, X.-W. He, W.-Y. Li, Y.-K. Zhang, Homochiral fluorescence responsive molecularly imprinted polymer: Highly chiral enantiomer resolution and quantitative detection of L-penicillamine, J. Hazard. Mater. 412 (2021) 125249. https://doi.org/https://doi.org/10.1016/j.jhazmat.2021.125249.

[14] C.C. Villa, L.T. Sánchez, G.A. Valencia, S. Ahmed, T.J. Gutiérrez, Molecularly imprinted polymers for food applications: A review, Trends Food Sci. Technol. 111 (2021) 642–669. https://doi.org/https://doi.org/10.1016/j.tifs.2021.03.003.

[15] H. Song, Y. Wang, L. Zhang, L. Tian, J. Luo, N. Zhao, Y. Han, F. Zhao, X. Ying, Y. Li, An ultrasensitive and selective electrochemical sensor for determination of estrone 3-sulfate sodium salt based on molecularly imprinted polymer modified carbon paste electrode, Anal. Bioanal. Chem. 409 (2017) 6509–6519. https://doi.org/10.1007/s00216-017-0598-x.

[16] M.A. Hammam, H.A. Wagdy, R.M. El Nashar, Moxifloxacin hydrochloride electrochemical detection based on newly designed molecularly imprinted polymer, Sensors Actuators, B Chem. 275 (2018) 127–136. https://doi.org/10.1016/j.snb.2018.08.041.

[17] F. Canfarotta, J. Czulak, A. Guerreiro, A. Garcia, S. Piletsky, G. Ertürk, M. Hedström, B. Mattiasson, A novel capacitive sensor based on molecularly imprinted nanoparticles as recognition elements, Biosens. Bioelectron. 120 (2018) 108–114. https://doi.org/10.1016/j.bios.2018.07.070.

[18] O.S. Ahmad, A. Guerreiro, K. Karim, E. Piletska, S. Piletsky, New potentiometric sensor based on molecularly imprinted nanoparticles for cocaine detection, Biosens. Bioelectron. 96 (2017) 49–54. https://doi.org/10.1016/j.bios.2017.04.034.

[19] G. Moro, F. Bottari, N. Sleegers, A. Florea, T. Cowen, L.M. Moretto, S. Piletsky, K. De Wael, Conductive imprinted polymers for the direct electrochemical detection of β-lactam antibiotics: the case of cefquinome, Sensors Actuators, B Chem. 297 (2019) 126786. https://doi.org/10.1016/j.snb.2019.126786.

[20] J. Zhang, X. Guo, J. Zhou, G. Liu, S. Zhang, Electrochemical preparation of surface molecularly imprinted poly (3- aminophenylboronic acid)/ MWCNTs nanocomposite for sensitive sensing of epinephrine, Mater. Sci. Eng. C. 91 (2018) 696–704. https://doi.org/10.1016/j.msec.2018.06.011.

[21] P.U.A.I. Fernando, M.W. Glasscott, G.K. Kosgei, J.S. Cobb, E.M. Alberts, C.G. Bresnahan, T.C. Schutt, G.W. George, L.C. Moores, Toward Rational Design of Electrogenerated Molecularly Imprinted Polymers (eMIPs): Maximizing Monomer/Template Affinity, ACS Appl. Polym. Mater. 3 (2021) 4523–4533. https://doi.org/10.1021/acsapm.1c00575.

[22] P.S. Sharma, A. Pietrzyk-Le, F. D'Souza, W. Kutner, Electrochemically synthesized polymers in molecular imprinting for chemical sensing, Anal. Bioanal. Chem. 402 (2012). https://doi.org/10.1007/s00216-011-5696-6.

[23] A. Yarman, F.W. Scheller, How Reliable Is the Electrochemical Readout of MIP Sensors?, Sensors . 20 (2020). https://doi.org/10.3390/s20092677.

[24] W. Guo, F. Pi, H. Zhang, J. Sun, Y. Zhang, X. Sun, A novel molecularly imprinted electrochemical sensor modi fi ed with carbon dots , chitosan , gold nanoparticles for the determination of patulin, Biosens. Bioelectron. 98 (2017) 299–304. https://doi.org/10.1016/j.bios.2017.06.036.

[25] S. Ansari, Application of magnetic molecularly imprinted polymer as a versatile and highly selective tool in food and environmental analysis: Recent developments and trends, TrAC - Trends Anal. Chem. 90 (2017) 89–106. https://doi.org/10.1016/j.trac.2017.03.001.

[26] S.Y. Dai, X. Kan, From non-electroactive to electroactive species: highly selective and sensitive detection based on a dual-template molecularly imprinted polymer electrochemical sensor, Chem. Commun. 53 (2017) 11755–11758. https://doi.org/10.1039/c7cc06329f.

[27] S. Fatma, B.B. Prasad, S. Jaiswal, R. Singh, K. Singh, Electrochemical simultaneous analysis of dopamine and epinephrine using double imprinted one monomer acryloylated graphene oxide-carbon black composite polymer, Biosens. Bioelectron. 135 (2019) 36–44. https://doi.org/10.1016/j.bios.2019.04.016.

[28] N. Karimian, A.M. Stortini, L.M. Moretto, C. Costantino, S. Bogialli, P. Ugo, Electrochemosensor for Trace Analysis of Perfluorooctanesulfonate in Water Based on a Molecularly Imprinted Poly(o-phenylenediamine) Polymer, ACS Sensors. 3 (2018) 1291–1298. https://doi.org/10.1021/acssensors.8b00154.

[29] P.S. Sharma, A. Pietrzyk-Le, F. D'Souza, W. Kutner, Electrochemically synthesized polymers in molecular imprinting for chemical sensing, Anal. Bioanal. Chem. 402 (2012) 3177–3204. https://doi.org/10.1007/s00216-011-5696-6.

[30] G. Camurri, P. Ferrarini, R. Giovanardi, R. Benassi, C. Fontanesi, Modelling of the initial stages of the electropolymerization mechanism of o-phenylenediamine, J. Electroanal. Chem. 585 (2005) 181–190. https://doi.org/10.1016/j.jelechem.2005.08.016.

[31] D. Vanossi, L. Pigani, R. Seeber, P. Ferrarini, P. Baraldi, C. Fontanesi, Electropolymerization of ortho-phenylenediamine . Structural characterisation of the resulting polymer film and its interfacial capacitive behaviour, J. Electroanal. Chem. 710 (2013) 22–28. https://doi.org/10.1016/j.jelechem.2013.04.028.

[32] M.W. Glasscott, K.J. Vannoy, R. Kazemi, M.D. Verber, J.E. Dick, μ-MIP: Molecularly Imprinted Polymer-Modified Microelectrodes for the Ultrasensitive Quantification of GenX (HFPO-DA) in River Water, Environ. Sci. Technol. Lett. 7 (2020) 489–495. https://doi.org/10.1021/acs.estlett.0c00341.

[33] R.B. Clark, J.E. Dick, Electrochemical Sensing of Perfluorooctanesulfonate (PFOS) Using Ambient Oxygen in River Water, ACS Sensors. 5 (2020) 3591–3598.

https://doi.org/10.1021/acssensors.0c01894.

[34] X. Li, X. Wang, T. Fang, L. Zhang, J. Gong, Disposable photoelectrochemical sensing strip for highly sensitive determination of perfluorooctane sulfonyl fluoride on functionalized screen-printed carbon electrode, Talanta. 181 (2018) 147–153. https://doi.org/https://doi.org/10.1016/j.talanta.2018.01.005.

[35] J. Gong, T. Fang, D. Peng, A. Li, L. Zhang, A highly sensitive photoelectrochemical detection of perfluorooctanic acid with molecularly imprined polymer-functionalized nanoarchitectured hybrid of AgI–BiOI composite, Biosens. Bioelectron. 73 (2015) 256–263. https://doi.org/https://doi.org/10.1016/j.bios.2015.06.008.

[36] R. Kazemi, E.I. Potts, J.E. Dick, Quantifying Interferent Effects on Molecularly Imprinted Polymer Sensors for Per- and Polyfluoroalkyl Substances (PFAS), Anal. Chem. 92 (2020) 10597–10605. https://doi.org/10.1021/acs.analchem.0c01565.

[37] US EPA, PFOA &PFOS Drinking Water Health Advisories, (2016) 1–4.

[38] Y. Lattach, N. Fourati, C. Zerrouki, J.M. Fougnion, F. Garnier, C. Pernelle, S. Remita, Molecularly imprinted surface acoustic wave sensors: The synergy of electrochemical and gravimetric transductions in chemical recognition processes, Electrochim. Acta. 73 (2012) 36–44. https://doi.org/10.1016/j.electacta.2011.11.119.

[39] A. Turco, S. Corvaglia, E. Mazzotta, Electrochemical sensor for sulfadimethoxine based on molecularly imprinted polypyrrole: Study of imprinting parameters, Biosens. Bioelectron. 63 (2015) 240–247. https://doi.org/10.1016/j.bios.2014.07.045.

[40] C. Peng, J. Jin, G.Z. Chen, A comparative study on electrochemical co-deposition and capacitance of composite films of conducting polymers and carbon nanotubes, Electrochim. Acta. 53 (2007) 525–537. https://doi.org/10.1016/j.electacta.2007.07.004.

[41] G. Fomo, T. Waryo, U. Feleni, P. Baker, E. Iwuoha, Electrochemical Polymerization- Functional Polymers, Springer International Publishing, Cham, 2019. https://doi.org/10.1007/978-3-319-95987-0_3.

[42] H. Wang, L. Yuan, H. Zhu, R. Jin, J. Xing, Comparative study of capsaicin molecularly imprinted polymers prepared by different polymerization methods, J. Polym. Sci. Part A Polym. Chem. 57 (2019) 157–164. https://doi.org/10.1002/pola.29281.

[43] B.A. Boukamp, Practical application of the Kramers-Kronig transformation on impedance measurements in solid state electrochemistry, Solid State Ionics. 62 (1993) 131–141. https://doi.org/10.1016/0167-2738(93)90261-Z.

[44] P. Agarwal, Application of Measurement Models to Impedance Spectroscopy, J. Electrochem. Soc. 142 (1995) 4159. https://doi.org/10.1149/1.2048479.

[45] I. Losito, F. Palmisano, P.G. Zambonin, O-Phenylenediamine Electropolymerization By Cyclic Voltammetry Combined With Electrospray Ionization-Ion Trap Mass Spectrometry, Anal. Chem. 75 (2003) 4988–4995. https://doi.org/10.1021/ac0342424.

[46] M.M. Musiani, Characterization of electroactive polymer layers by electrochemical impedance spectroscopy (EIS), Electrochim. Acta. 35 (1990) 1665–1670. https://doi.org/10.1016/0013-4686(90)80023-H.

[47] C. Deslouis, M.M. Musiani, B. Tribollet, Free-Standing Membranes for the Study of Electrochemical Reactions Occurring at Conducting Polymer/Electrolyte Interfaces, J. Phys. Chem. 100 (1996) 8994–8999. https://doi.org/10.1021/jp953154n.

[48] H.H.S. E.S. Gadelmawla, M.M. Koura, T.M.A. Maksoud, I.M. Elewa, Roughness parameters, J. Mater. Process. Technol. (2002) 133–145.

[49] F. Milano, L. Giotta, D. Chirizzi, S. Papazoglou, C. Kryou, A. De Bartolomeo, V. De Leo, M.R. Guascito, I. Zergioti, Phosphate modified screen printed electrodes by lift treatment for glucose detection, Biosensors. 8 (2018) 1–14. https://doi.org/10.3390/bios8040091.

[50] J. Goldstein, D.E. Newbury, P. Echlin, D.C. Joy, C. Fiori, E. Lifshin, Scanning Electron Microscopy and X-Ray Microanalysis, 4th ed., Springer US, 2018. https://doi.org/10.1007/978-1-4613-3273-2.

[51] L. Reimer, Scanning Electron Microscopy. Physics of Image Formation and Microanalysis, 2nd ed., 1998.

[52] A. Czapik, M. Gdaniec, A new polymorph of benzene-1,2-diamine: Isomorphism with 2-amino-phenol and two-dimensional iso-structurality of polymorphs, Acta Crystallogr. Sect. C Cryst. Struct. Commun. 66 (2010) 198–201. https://doi.org/10.1107/S0108270110008474.

|8

Fluorinated Self-Assembled Monolayers: Different Architectures for PFAS Screening

Adapted from

Giulia Moro, Cedrix J. Dongmo Foumthuim, Marco Spinaci, Ettore Martini, Eleonora Balliana, Dafne Cimino, Rui Campos, Peter Lieberzeit, Flavio Romano, Achille Giacometti, Karolien De Wael, Ligia Maria Moretto, "How perfluoroalkyl substances modify fluorinated self-assembled monolayer architectures: an electrochemical and computational study", submitted to Chimica Analytica Acta.

Abstract

Apart from single-molecule detection strategies also screening ones are urgently required for tacking perfluoroalkyl substances (PFAS) in water matrices to face the ubiquitous nature of these pollutants, their global spreading, and the fast evolution of PFAS towards short-chain branched molecules. To develop new sensing architectures and approaches, the investigation and design of new synthetic recognition layers or electrode modifiers is crucial.

In this chapter, the possibility to play with "fluorophilic interactions" was considered and the changes in fluorinated self-assembled monolayers (SAM) upon long and short-chain PFAS exposure were studied. SAM with different architectures, such as pinholes/defects-free and with randomized pinholes/defects, were first described. Then, the applicability of fluorinated SAM in PFAS sensing was evaluated. The changes in the SAM structures were followed combining electrochemical impedance spectroscopy and voltammetric techniques. The experimental data interpretation was supported by molecular dynamics (MD) simulations for a more in-depth understanding of the possible interaction mechanisms involved, especially fluorine-fluorine ones. This chapter offers a complete characterisation of pinhole- and defect-free fluorinated SAM showing how this latter can be applied in the screening of long-chain PFAS with a switch-on sensing strategy. Only fluorinated SAM with defects/pinholes showed promising results for the screening of both short and long-chain PFAS combined with a switch-off sensing strategy. These modifiers can be further combined in more complex architectures and with other sensing platforms.

Apart from providing important insights about fluorinated SAM applicability in PFAS sensing, this study represents a successful example of how the impedimetric and electrochemical data interpretation can be supported by MD simulations. The agreement between MD simulation data and experimental findings oriented our interpretations and helped us evaluating the reliability of the systems tested.

.

8.1. Introduction

Bio- and biomimetic sensors have shown promising results in PFAS determination even though most of these devices were conceived for the detection of a single-molecule and cannot monitor the whole class of these pollutants simultaneously [1–4]. Therefore, the design of class-selective sensing strategies would be instrumental to follow the fast evolution of these compounds and tackle all generations of PFAS: from long chains (> C_7/C_8) to short ones (< C_7) [5]. It is worth noting that the hydrophobic-lipophilic properties of all generations of PFAS, which are of fundamental interest for industrial and household applications, depend mainly on their fluorinated tails. Thus, PFAS fluorinated chains (different in length and structure) can be used as a target for the development of PFAS screening strategies. To this aim, the high degree of fluorination of PFAS tails should be considered in the choice of suitable molecular recognition layers. In particular, layers able to take advantage from **fluorine-fluorine (F-F) non-covalent interactions** to operate PFAS recognition should be tested as electrode modifiers. For instance, Niu *et al.* designed a colorimetric sensing strategy for perfluorinated compounds based on this type of interactions [6]. Aiming to provide new insights about possible PFAS sensing strategies, also Fang *et al.* described the fluorophilic interaction of C-F chains studying fluorinated self-assembled monolayers (SAM) exposed to perfluorooctanoic acid (PFOA) and perfluorooctanesulfonic acid (PFOS) [7]. The authors proved the applicability of SAM in PFOA sensing design a switch on-off response electrochemical platform [8]. These previous studies together with previous screening of anionic surfactant capability of altering SAM architectures provides strong background for our study. Here, we aim to test and compare different SAM architectures and move from traditional long chain PFAS to the new generations of short chain ones [9].

The use of **organothiols SAM** as sensing elements in electroanalytical applications was introduced in the 1990s [10]. Since then, these modifiers have been successfully applied in numerous electrochemical and impedimetric sensing platforms for the measurement of pH and for the detection of metal ions, small molecules, biomolecules and microorganisms [7,11,12]. SAM were used to study surface-confined molecules and nanostructures at solid/liquid interfaces providing key information about the physicochemical properties of the latter (*i.e.,* wettability, catalytic effects, etc.) [13,14]. The adaptability and high compatibility of SAM with other molecular recognition elements can be also applied in the design of amplified recognition strategies to improve the sensitivity, reproducibility and speed of the resulting sensing device [15,16].

In the design of SAM-based sensing strategies, the dynamic nature of organothiol SAM architecture needs to be taken into account [17]. SAM structural properties depend on the thiol chemical structure, on the conditions of the self-assembly process, and finally on the surface coverage along with the interactions (covalent/noncovalent) taking place at the SAM interface [18,19]. Alkanethiols deposited on gold can result in highly ordered, pinhole/defect-free SAM (*ordered SAM* **Figure 8.1A**) or SAM with randomly-positioned pinholes and defects (*unordered SAM* **Figure 8.1B**) [20]. A pinhole is defined as a site on the substrate that is not covered by the monolayer, while a defect is formed when the thiol chain does not stand in an upright position [20].

The irregularities (pinholes/defects) in the SAM layer enable a direct electron transfer (ET) of the redox probe in solution. Therefor*e, unordered SAM* are often combined with *switch-off* sensing strategies where increasing concentrations of the target lead to an increase in the order of the SAM structure and, as a consequence, to a decrease in the direct ET of the redox probe, as shown in **Figure 8.1B** [21–23]. In these systems, the target molecules which are attracted by the SAM and the gold substrates tend to compete to insert in the pinholes/defects of the monolayer. This interaction mechanisms was applied also in the *switch-off* sensing strategy reported by Fang *et al.* to detect micromolar levels of perfluorooctanoic acid (PFOA) via hydrophobic interactions with 6-(ferrocenyl)-hexanethiol SAM [8]. Non-covalent interactions (*i.e.,* Van der Waals, hydrogen bond, halogen bond, *etc.*) play a key-role in SAM-based strategies and should be considered when designing new SAM recognition elements. These interactions can lead to structural changes in unordered SAMs that can be followed by electrochemistry and electrochemical impedance spectroscopy (EIS), as reported in this work.

When using different self-assembly conditions, the same alkanethiols with a chain length of more than nine carbon atoms can result in compact, well-organised and hydrophobic monolayers, which are modelled as pinhole- and defect-free SAMs [2,4,24]. These SAMs can isolate the electrode surface, blocking the direct ET of electroactive species in solution and so enabling only the ET via tunnelling [21,25]. In principle, this type of SAM can be integrated with *switch-on* sensing strategies, where the target molecules can induce the formation of defects and pinholes as in **Figure 8.1A**.

Through these irregularities, the redox probe can undergo a direct ET followed by an increase of current signal. This latter PFAS sensing strategy based on fluorophilic interactions has been explored and is reported below. The study of these systems were supported by molecular dynamics (MD) simulations that allow the prediction of interaction mechanisms and the estimation of the non-covalent energetics involved [22].

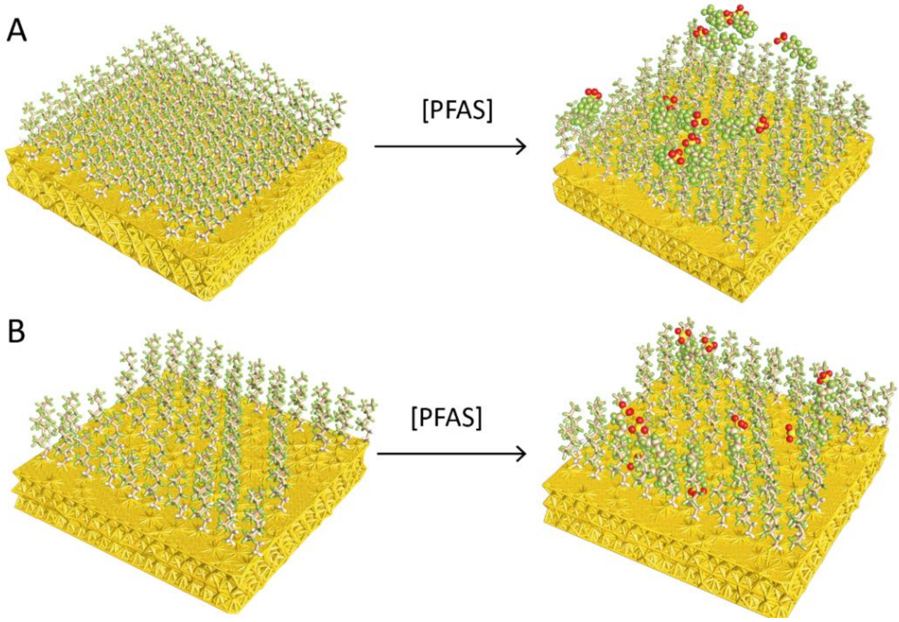

Figure 8.1. *Schematic of a possible switch-on (**A**) and switch-off (**B**) sensing strategies for the screening of PFAS based on fluorinated SAM at gold electrodes. The SAM are characterised by different architectures: an ordered one modelled as pinhole- and defect-free (**A**), and an unordered structure with pinholes and defects (**B**). Upon PFAS exposure ordered SAM might undergo the formation of pinholes/defects (followed by an increase in the redox probe currents, switch-on), while in unordered SAM PFAS molecules "fill the gaps" (followed by a decrease in the redox probe currents, switch-off).*

Indeed, the use of MD simulations in the study of SAMs on inorganic surfaces is increasingly gaining importance [26–31], thanks to the continuous development of reliable and accurate empirical force fields [32–34].Furthermore, beyond providing a complementary input to the interpretation of wet lab experiments, MD simulations and more generally molecular simulation methods can reliably predict the preferential adsorption modes and phase segregation of alkanethiol mixtures on Au(111) slabs [35]. Vemparala and Karki have employed MD simulations to unravel the structural properties of SAMs alkanethiol as a function of temperature, lattice spacing, and molecular chain length [36]. Similarly, Devi used MD simulations to provide insightful knowledge on the thermal and wetting behaviour of alkanethiol SAM on Au(111) surface, suggesting that the wetting behaviour of the gold SAM surface can be modified by altering the terminal functional group of the SAM chains [37]. Moreover, MD simulations have proven important to underpin the correlation between the chemical structures of functionalized alkanethiol SAMs on gold surfaces and their underlying molecular motion at the picosecond time scale, thus demonstrating how the alkyl chain motions correlate with the dynamics of the head group [38]. Here, MD simulations have provided an atomistic details of the interaction modes of fluorinated pinhole- and defect-free SAM architectures build on Au(111) monolayer, thereby enabling to dissect the main driving forces.

In this work, the structural changes of different types of fluorinated SAM (FDT-SAM) upon long and short chain PFAS exposure were investigated via electrochemical and impedance-based methods supporting the data analysis with MD simulations. *Unordered* and *ordered* FDT-SAM were characterised via voltammetric techniques, electrochemical impedance spectroscopy (EIS) and infrared spectroscopy. For pinhole- and defect-free SAM, the ET kinetic constants were studied via EIS potential scan, while the electrode surface coverage was estimated via linear sweep voltammetry (LSV). Different trends were observed under long and short chain exposure for ordered FDT-SAM while a consistent response was obtained in presence of FDT-SAM with pinholes and defects. These preliminary results suggest the applicability of FDT-SAM in sensing strategies for PFAS screening and the interest of combining electrochemical and computational approaches.

8.2 Materials and Methods

8.2.1. Chemicals and Materials

Dodecanethiol (DDT), 1H,1H,2H,2H-perfluorodecanethiol (FDT), 2,3,3,3-tetrafluoro-2-(heptafluoropropoxy)-propanoate ammonium salt (HFPO-DA), perfluorooctanoic acid (PFOA), perfluorooctanesulfonic acid potassium salt (PFOS), perfluoropentanoic acid (PFPA), perfluorhexanesulfonic acid (PFHxS) were purchased from Sigma Aldrich. All PFAS chemical structures are summarised in **Figure A8.1A**. All other reagents were of analytical grade. Diamond slurry (3 µm), alumina powder (1 and 0.05 µm), nylon polishing cloths, Microcloth PSA 2-7/8, were from Buehler.

8.2.2. Protocols for SAM Preparation

Prior to thiol chemisorption, polycrystalline gold disk electrodes (Au-DE) (BAS, area 0.020 cm^2) were firstly treated by scanning ten cyclic voltammetry (CV) cycles in 0.1 M KOH, in the potential window from -0.4 V to -1.6 V vs Ag/AgCl (KCl sat.), at a scan rate of 50 mV s^{-1}. All potentials are reported vs Ag/AgCl (KCl sat.). Secondly, they were mechanically polished for 2 min in a figure-eight pattern on Buehler Microcloth with successive finer grades (15, 3 and 1 µm), diamond (3 µm) and alumina (1 and 0.05 µm), respectively, followed by a sonication in ethanol/water (1:1) for 10 min. Thirdly, the electrodes were treated by scanning ten CV cycles in 1 M H_2SO_4, in the potential window from -0.3 V to 1.7 V at a scan rate of 300 mV s^{-1}. Then, ten cycles in 0.5 H_2SO_4, 0.01 M KCl, in the potential window from 0 V to 1.7 V, at a scan rate of 300 mV s^{-1}. Finally, the potential was cycled between 0 and 1.7 V in 1 M H_2SO_4 until a stable CV was obtained.

Au-DE were modified with FDT and DDT-SAM by overnight (> 14 h) or 6 h incubation in 0.5 or 5 mM thiol solution in absolute ethanol at room temperature depending on the desired properties. For highly ordered SAM, overnight incubation and an initial concentration of 5 mM were found to be optimal to assure the formation of a stable monolayer with good blocking properties. For the less ordered SAM, the incubation time was reduced to 6 h and the concentration was 0.5 mM. When using this second set of conditions, SAM with a reproducible density of pinholes/defects were obtained as explained in **Section 8.3.2**. To assure the reproducibility of both SAM architectures, the incubation steps were carried out in temperature/pressure-controlled conditions (room temperature and atmospheric pressure). Prior to use, modified Au-DE were rinsed to remove the thiols adsorbed at the interface (nonspecific binding). Then, they were conditioned by soaking in 0.1 M KNO_3 for about 30 min.

8.2.3. Voltammetric and Impedimetric Study

Electrochemical measurements were carried out using a three-electrode cell setup equipped with: an Ag/AgCl (KCl sat.) reference electrode, a Pt coil counter electrode and SAM-modified Au-DE as working electrodes. All potentials are expressed vs Ag/AgCl (KCl sat.) electrode. CV and Square Wave Voltammetry (SWV) were carried out using different potentiostat/galvanostat: the CH model 660B and the Autolab Model 204 controlled by NOVA 1.1 software. CVs were recorded within the potential window from -0.2 to +0.6 V vs Ag/AgCl (KCl sat.) at a scan rate of 50 mV s^{-1}. DPV experiments were recorded in the potential window from −0.2 V to + 0.7 V Ag/AgCl (KCl sat.), using the following parameters: potential increment of 0.002 V, amplitude of 0.025 V, pulse width of 0.025 s, sample width of 0.0125 s and pulse period of 0.05 s. Electrochemical impedance spectroscopy (EIS) measurements were carried out in the frequency range from 0.1 Hz to 100 KHz (12 points per decade), with 0.01 V amplitude and an initial potential in the range from -0.4 to 0.6 V vs Ag/AgCl (KCl sat.). Measurements were carried out in 0.1 M KNO_3, 1.0 mM of $K_3[Fe(CN)_6]$, 1.0 mM $K_4[Fe(CN)_6]$. To investigate the changes in SAM after PFAS exposure via EIS, SAM modified AU-DE were incubated in 100 nM aqueous solution of PFAS for one hour, then rinsed with distilled water and the impedimetric measurements were recorded as described above. ZPlot software was used to fit impedimetric data. SAM changes after PFAS exposure were investigated via DPV in 0.1 M KNO_3, 1.0 mM $K_4[Fe(CN)_6]$ and increasing concentration of PFAS (from 5 nM to 2 µM), incubating the SAM modified AU-DE in the measurement solution for 30 min for each concentration prior to acquiring the voltammetric responses.

8.2.4 ATR- FTIR Control Procedure

Infrared spectra were acquired by a single-reflection attenuated total reflection (ATR) accessory (MIRacle ATR, PIKE Technologies), with a diamond crystal coupled to a Fourier Transform Infrared (FTIR) spectrometer (Equinox 70 FT-IR, Bruker). Spectra were recorded in the range from 400 to 4000 cm^{-1} with a resolution of 4 cm^{-1}, accumulating 256 scans. Three analyses were performed for each sample to ensure the reproducibility of obtained spectra. Both bulk reagents and modified gold surfaces were analysed.

8.2.5 Simulation Model Setup

Molecular dynamics simulations were performed with the Gromacs (v2018.7) molecular package [10]. The force field GolP-Charmm22* [11] was used for the gold slab meanwhile parameters for the poly- and per-fluorinated alkylated compounds (FDT, PFOS, HFPO-DA, see **Figure A8.1A-B**) were obtained from the Amber-compatible parameters of Gaff2 using Antechamber module of AmberTools [39,40], and then converted to Gromacs-like format using the acypipy.py script [41]. Charge optimisation was computed using the AM1-BCC charge model [42,43]. All simulations were performed in an aqueous medium by filling a rectangular box with the 3-site rigid TIP3P water model [44] see **Figure A8.1C**. Potassium ions were subsequently added to account for the overall negative charge and achieve a concentration of 0.1 nM. Minimisation of the solvent was performed keeping frozen the positions of the organic moieties and gold atoms.

MD simulations were performed on two PFAS, namely PFOS and HFPO-DA. FDT molecules were used to construct the SAM on a gold substrate (**Figure A8.1B**). All the chemical structures of these compounds were drawn with the Avogadro software [5], and each of them was simulated in its deprotonated form. A gold (111) slab with a surface area of (58.6 x 60.9) $Å^2$ and with a thickness given by five atomic layers was used as a substrate [45] (**Figure A8.1D**). The gold slab was frozen throughout the simulations, while a harmonic restraining potential of 1000 kJ mol^{-1} nm^{-2} was applied to FDT-sulphur atoms in the case of the full SAM surface coverage simulations. In the case of the simulations mimicking the system with pinhole defects, the restraining potential was also applied to the FDT heavy atoms, to prevent the molecules from lying down on the gold slab.

The base of the 3D simulation box was set equal to the surface of the gold substrate, while the z-component was set equal to 80.0 Å. The distance between the FDT molecules and the substrate, taken as the distance between the sulphur atom and the upper external layer of the substrate was set equal to 2.42 Å, within the limit of Au-S covalent bond formation. The chemical structure of FDT was obtained from 1 ns of MD simulation, thereby optimizing the geometry. To increase the probability of sampling more binding/interaction events, an additional FDT-SAM was added on the opposite side of the simulation box, leading to a double fluorinated SAM layer (**Figure A8.1B-C**). Finally, in order to keep the FDT-SAM molecular assembly fixed at the bottom and top of the simulation box, the FDT-sulphur atoms along with the gold substrate were restrained throughout the simulation timescale.

Two different SAM architectures were simulated, as summarized in **Figure A8.1E-F**. In the first one, (**E**), the ordered FDT-SAM was arranged so that 110 FDT molecules are placed perpendicularly to the substrate. The distance between these molecules, measured as the separation distance between their sulphur atoms, was set equal to 5.87 Å, which is compatible with the occupation sites of the hexagonal lattice [17]. In this way, the substrate was uniformly and fully covered by FDT molecules, schematizing a defect-free SAM. In the second one, (**F**), the substrate is partially covered by FDT molecules to mimic a pinhole scheme, with a surface coverage of 50%. This value was chosen in order to have a system that closely matches the experimental one, in which the surface coverage was less than half that of the ordered SAM.

Subsequently, ten PFOS or HFPO-DA molecules initially placed in the middle of the simulation box, were added to both setups, in order to study how they interact with the FDT-SAM monolayers and, eventually, modify arrangement of these latter (see **Figure A8.1G**).

Finally, for the sake of completeness, a complementary setup including 10 target molecules (PFOS or HFPO-DA) and 10 FDT moieties was simulated in a periodic box of water embedding a single gold layer at one end of the simulation box. This enables the estimation of the non-covalent interactions along with the visualisation of the preferential binding modes upon binding to the Au (111) surface (see **Figure A8.1H**).

8.2.6 Numerical Protocol

MD simulations of at least 250 ns for each system were performed in the canonical NVT ensemble. However, it should be mentioned that the production runs were preceded by 5 ns NVT equilibration in which the positions of all the heavy atoms were restrained. Moreover, it should be mentioned that the parameters of the MD simulations were set according to the force field authors recommendations [11]. Finally, the rigid-rod-dipole method for gold atom polarisation was implemented following [11].

The temperature was equilibrated to the reference value of 300 K using the Nose-Hoover thermostat [46,47] with a coupling constant of 0.2 ps. The leap-frog integrator with integration time-step of 1 fs was employed. The Particle Mesh Ewald summation was used to account for long-range electrostatics, with a real space cut-off of 10 Å. Lastly, simulations have employed a periodic box and a force-switched cut-off starting at 9 Å and ending at 10 Å for the Van der Waals non-bonded interactions.

8.3 Results and discussion

8.3.1. Testing *Ordered* Fluorinated SAM Applicability to Switch-on Sensing

8.3.1.1 Electrochemical Characterisation of FDT-SAM

The electrochemical characterisation of highly ordered, pinholes/defects-free SAM of FDT was carried out aiming at describing the blocking properties and, when possible, the electron tunnelling kinetics of FDT-SAM. The study of FDT-SAM was developed using pinhole/defect free DDT SAM as a reference system [18]. **Figure 8.2** summarises and compares the results obtained for FDT and DDT monolayers. Both SAM were formed at Au-DE aiming to block the direct electron transfer at the electrodes surface by creating highly ordered, pinholes/defects-free monolayers. For FDT-SAM, the self-assembly process was optimized to maximise the blocking properties of the final modifiers, as described in **Section 2.2**. For the preparation of DDT-SAM the protocol reported by Aguiar *et al.* was applied [18].

The blocking properties of both modifiers were characterised via CV and EIS in the potential window from -0.2 to +0.6 V vs Ag/AgCl (KCl sat.), in 1.0 mM of $K_3[Fe(CN)_6]$, 1.0 mM $K_4[Fe(CN)_6]$ in 0.1 M KNO_3 (**Figure 8.2**). It is worth noting that ferro-ferricyanide redox couple was chosen as redox probe because of its anionic nature, while cationic probes were excluded to avoid side-phenomena related to their electrostatic attraction for the fluorinated-chains of FDT [16]. The voltammograms recorded in presence of the redox probe (**Figure 8.2A**) showed the inhibition of the direct electron transfer. This implies the absence of defined redox peaks. These features are highlighted by the comparison of these voltammograms with the ones recorded at bare gold electrodes reported in **Figure A8.2A**. The sigmoidal shape of the voltammograms is commonly interpreted as a sign of microelectrode behaviour (radial diffusion process), when working with micro/nanoelectrodes array [48,49]. However, in this context, this shape suggests the occurrence of electron tunnelling processes. Sigmoidal voltammograms with low capacitive current contributions (< 5 nA) were previously observed when using pinhole/defect free SAM, particularly DDT-SAM, as shown in **Figure A8.2B** [18]. In respect to the DDT monolayers, FDT ones showed doubled capacitive contributions (5 nA vs 2 nA) and higher faradic currents in presence of the redox probe (average Δi = 30 nA). These differences are related to the chemical structure of the thiols, which partially determines the SAM arrangement, density and features.

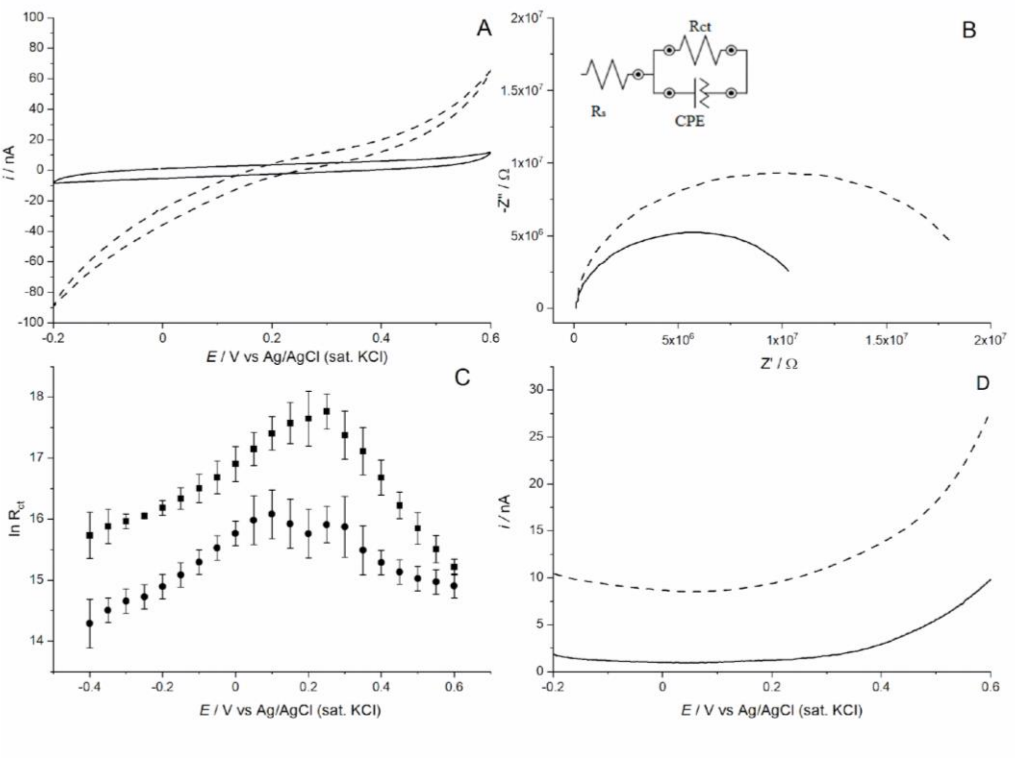

Figure 8.2. *(**A**) Cyclic voltammograms of ordered FDT-SAM in 1.0 mM of $K_3[Fe(CN)_6]$, 1.0 mM $K_4[Fe(CN)_6]$ (solid line), 0.1 M KNO_3 aqueous solution (dotted line for the blank), (**B**) Nyquist plot of FDT-SAM (solid line) and DDT-SAM (dotted line) in presence of the redox probe; inset: simplified Randles EEC, (**C**) Variation in the ln R_{ct} values in respect to the potential for FDT-SAM (dots) and DDT-SAM (squares) recorded via EIS potential scan, (**D**) DPV of FDT-SAM (dotted line) and DDT-SAM (solid line) in presence of the redox probe.*

In **Figure 8.2B,** the EIS measurements are reported as Nyquist plots fitted with a simplified Randles electrochemical equivalent circuit (EEC). The EEC includes three terms: the uncompensated solution resistance (R_s), the constant phase element used to model the double layer capacitance (CPE) and the charge transfer resistance (R_{ct}). The semicircular shape of the Nyquist plots confirmed the absence of diffusion-driven process and blocking properties of the SAM [9,50,51]. FDT-SAM shows a lower resistance to charge transfer than DDT one (**Figure 8.2B**). Again, this difference can be ascribed to the thiol chains, which differs in conductivity and length [7].

These voltammetric and impedimetric data confirm the blocking properties of FDT monolayers. The FDT surface coverage was further studied by following the thiols desorption via liner sweep voltammetry (LSV, **Figure A8.2C-D**). An estimation of the monolayer density can be obtained by integration of the reduction peak [52,53]. For FDT, a coverage value of about 3.5 nmol cm^{-2} was observed. This latter was higher than the theoretical value (0.4 nmol cm^{-2}) calculated assuming a hexagonal pattern like the one reported by Zenasni *et al.* for fluorinated SAM [17]. This discrepancy can be ascribed to the methodology in use: the FDT desorption peak (**Figure A8. 2D**) is broader than DDT one (**Figure A8. 2C**) suggesting the possible presence of multiple-processes that cannot be discriminated prior to integrating the peak. Despite this, the LSV desorption tests confirmed the high density of the monolayers and can be further applied to verify the presence of SAM at Au-DE in routinary experiments. To further attest SAM chemisorption, attenuated total reflection infrared spectroscopy (ATR-FTIR) was applied [54,55]. The details of ATR-FTIR characterisation are discussed in the Annex A with few examples of infrared spectra (**Figure A8.3A-D**). From the analysis of the IR spectra the presence of FDT-SAM was clearly verifiable.

Once having described FDT-SAM general features, we studied the kinetics of electron transfer through tunneling via EIS potential scans in the presence of the redox probe, again with DDT-SAM as the reference system (**Figure A8.2E-F**). Overpotentials (η, relative to the formal potential of the couple which is 0.22 V vs Ag/AgCl) were imposed to the system in the range from -0.62 V to 0.38 V vs Ag/AgCl and the variations, expressed as ln R_{ct}, in function of η were considered for both monolayers confirming that FDT-SAM have lower resistance values than DDT-SAM in the range of potentials tested [19,20,24]. The values of R_{ct} as a function of η reported in **Figure 8.2C** were used to calculate the kinetics parameters of tunneling electron transfer in **Table 8.1**.

Table 8.1. *Variation of transfer coefficient α with negative overpotentials for electrodes modified with FDT- and DDT-SAM, in data obtained in presence of 1.0 mM of $K_3[Fe(CN)_6]$, 1.0 mM $K_4[Fe(CN)_6]$ in 0.1 M KNO_3. Values calculated using the equations reported in* [18].

	FDT		**DDT**	
η (V)	α	$k°_{app}$ (cm s^{-1})	α	$k°_{app}$ (cm s^{-1})
-0.62	0.145	1.79 x10^{-3}	0.158	5.34 x10^{-4}
-0.57	0.146	1.11 x10^{-3}	0.164	3.72 x10^{-4}
-0.52	0.150	7.63 x10^{-4}	0.173	2.83 x10^{-4}
-0.47	0.160	5.95 x10^{-4}	0.183	2.12 x10^{-4}
-0.42	0.170	4.09 x10^{-4}	0.194	1.45 x10^{-4}

-0.37	0.174	2.51 x10^{-4}	0.205	9.51 x10^{-5}
-0.32	0.181	1.52 x10^{-4}	0.219	6.00 x10^{-5}
-0.27	0.189	8.83 x10^{-5}	0.235	3.63 x10^{-5}
-0.22	0.198	4.96 x10^{-5}	0.254	2.00 x10^{-5}
-0.17	0.212	2.79 x10^{-5}	0.278	1.02 x10^{-5}
-0.12	0.240	1.68 x10^{-5}	0.313	4.83 x10^{-6}

Also, the electron transfer coefficient (α) and the apparent rate transfer constant a) (k°*app*) were calculated as previously reported [20]. The value of α decreases with increasing overpotential, while k°_{app} increases with increasing overpotential. These results are in good agreement with what reported by Aguiar *et al.* [18] for pinhole/defect-free DDT-SAM. It was possible to observe that FDT-SAM allows a faster electron transfer having higher k°_{app} values compared to DDT-SAM. This information will be considered while studying the changes in these SAM systems upon PFAS exposure.

8.3.1.2 Changes in Ordered FDT-SAM upon PFAS Exposure

Once characterised, fluorinated SAM were tested as electrode modifiers for the development of *switch-on sensing* strategies using DPV to maximize the signal-to-noise ratio, as anticipated in Figure 8.2D. The changes in the structure of FDT and DDT-SAM after exposure to both long-chain and short-chain PFAS were studied (summary of PFAS chemical structure in Figure A8.1). We aimed at verifying whether, and eventually, to which extent the hydrophobic, non-covalent interactions between SAM interface and PFAS molecules alter the SAM architectures (i.e., partial destabilization, compacting, etc.). For this preliminary test, the long-chain PFAS considered were PFOA and PFOS, while the short-chain PFAS tested were PFHXS, HFPO-DA and PFPA.

Incubation with increasing concentrations of PFOS or PFOA (ranging from 50 to 1000 nM) was found to affect the insulating properties of FDT-SAM. Upon exposure to these long-chain PFAS, increasing oxidation currents were recorded at FDT-SAM modified electrodes, as shown in Figure 8.3A-B. These results can be explained considering that once the SAM architecture is altered and pinholes/defects are formed, the redox probe can approach the electrode surface and undergo a direct electron transfer. This results in current intensities much higher than those recorded when only electron tunneling processes occurred (Figure 8.2D). These currents showed values lower than 10 nA in the potential region between 0.25 and 0.3 V vs Ag/AgCl sat. KCl, while currents of about 20 nA were observed after incubation with 50 nM PFOA/PFOS (Figure 8.3A-B). Currents increased linearly with analyte concentrations in the range from 50 up to 1000 nM. For PFOA/PFOS concentration higher than 1μM one can observe a progressive decrease in current values. These changes in the FDT-SAM showed good reproducibility and were not observed during negative control experiments (results summarised in **Figure A8.4A-F**). In particular, no changes were recorded upon additions of blank solutions (0.1 M KNO_3) for both FDT-SAM and DDT-SAM, used as control system. The incubation of PFOS/PFOA at DDT-SAM using the same working conditions did not affect the insulating properties of the SAM (results summarised in **Figure A8.4C-D**). This experiment indirectly confirmed that the variations observed at FDT-SAM can be ascribed mainly to F-F interaction between the PFAS molecules and FDT tails. The observations above are limited to long-chain PFAS: the incubation of short-chain PFAS (PFHXS, HFPO-DA and PFPA) did not lead to any recordable change in the FDT SAM structure, examples of the voltammograms recorded in **Figure A8.5**. In **Figure 8.3C**, the current values were reported as a function of different PFAS concentrations after blank subtraction at a fixed potential of 0.3 V vs Ag/AgCl (sat. KCl) and expressed as Δi. The variations observed after blank additions (0.1 M KNO_3) were found to be lower than 10 nA, thus Δi values of <10 nA were considered not meaningful in the present analysis.

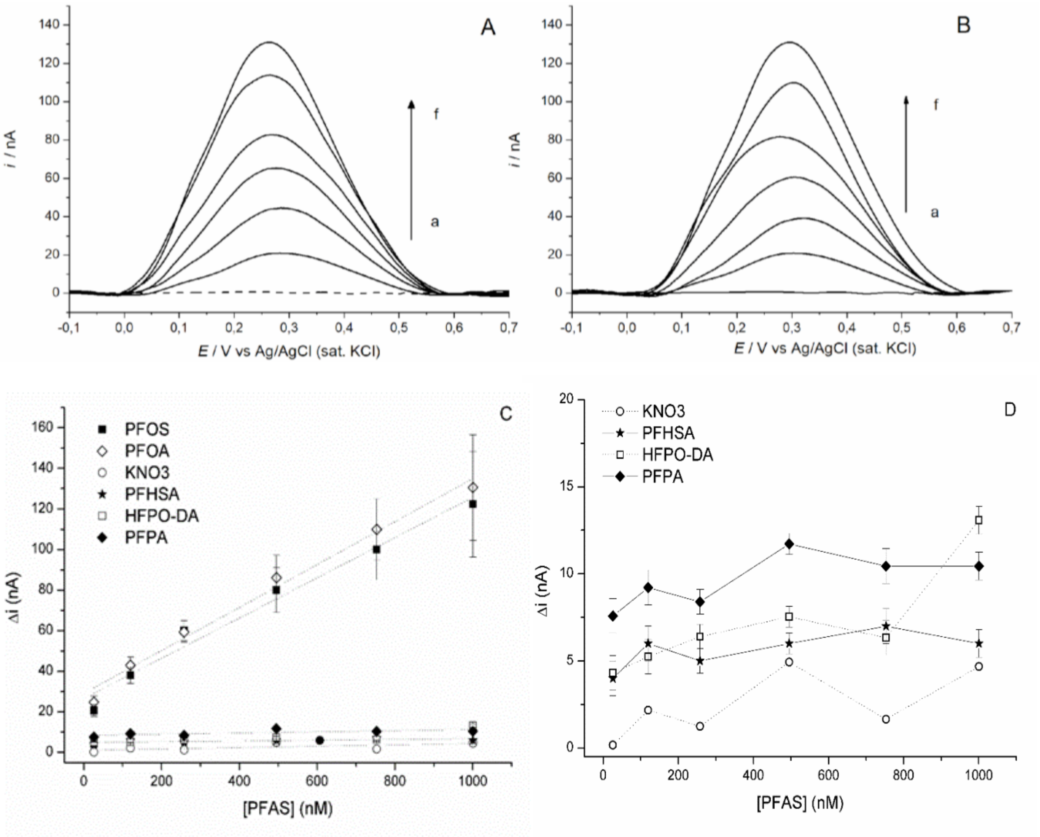

*Figure 8.3. Representative DPV of FDT-SAM recorded upon increasing concentrations, from 50 to 1000 nM (a to f), of PFOS (**A**) and PFOA (**B**) compared to blank (dotted line). Peak current vs increasing concentrations*

*of PFAS (PFOS, PFOA, PFHXSA, HFPO-DA and PFPA) (**C**), and of only short chain PFAS - PFHXSA, HFPO-DA and PFPA (**D**).*

Figure 8.3C highlights that PFOS/PFOA exposure leads to changes in the FDT structure which are linearly proportional to PFAS concentrations (linear fitting equations: $y=0.12x+26.5$, $R^2=0.97$ for PFOS and $y=0.09$ c $+29.1$, $R^2=0.98$ for PFOA). The long-chain PFAS shows a consistent behaviour, which differs deeply from the short-chain one. Indeed, PFHXS, HFPO-DA and PFPA do not alter the FDT-SAM structure in a significant way. Their Δi values are on average <10 nA as shown in **Figure 8.3D**. This comparison underlines that there are no clear trends and even the exposure to short-chain PFAS >1000 nM did not alter the blocking properties of FDT SAM. Short-PFAS are potentially contributing to compact SAM structure by laying in the interfacial region. The relatively higher solubility of short-chain PFAS, as discussed in the following section, together with their shorter length might be responsible for the behaviour observed. Overall, PFHXS, HFPO-DA and PFPA show consistent trends. A similar behaviour was observed for DDT-SAM, again tested as a negative control.

The differences observed in FDT-SAM blocking properties upon exposure to long and short-chain PFAS cannot be simply explained by the fluorinated tail length. For this reason, prior to further applying FDT-SAM in PFOS/PFOA monitoring, it would be necessary to elucidate the interactions involved. However, these results provide evidence that the screening of PFAS at pinholes/defects-free FDT-SAM via a switch-on strategy is not applicable to short-chain PFAS.

8.3.1.3 MD Simulations vs Experimental Outcomes

MD simulations showed that both PFOS and HFPO-DA adhere at the FDT-SAM interface without altering the monolayer arrangement, as shown in **Figure 8.4**. These arrangements are driven by an attractive force, rather than a repulsive one, as suggested by the negative values of the interaction energies observed.

To assess whether there is any difference between the affinities of the two target molecules, i.e., the short- and long-chain PFAS, with the SAM, we analyse MD simulations as follows: for each of the molecules, we compute the number of contacts between the target molecule atoms and the atoms of the SAM. We define two atoms to be in contact if their separation is within 0.6 nm (**Figure A8.6 A-B**). In turn, we deem the target molecule as (reversibly) bound to the SAM if its number of contacts is $\geqq 16$ for the short-chain HFPO-DA, and $\geqq 27$ for the long-chain PFOS (**Figure A8.6 E-F**). Finally, to extract the affinity to the SAM, we computed the average potential energy of the two interacting molecules when bound according to the above criterion. These energies were found to be -36 KJ/mol for the system with PFOS and -23 KJ/mol for the one with HFPO-DA, where non-interacting molecules would have zero interaction energy. We find that both targets display a negative interaction energy with the SAM monolayer, albeit the affinity of the long-chain PFOS being significantly (13 KJ/mol) more favourable.

This difference in PFOS/HFPO-DA behaviour can be explained considering the chemical structures of these pollutants and, as a consequence, their different physicochemical properties. According to Nixon *et al.*, HFPO-DA is considered to be infinitely soluble in aqueous solutions with a low adsorption potential and a high mobility [56,57]. On the contrary, PFOS shows a solubility in pure water of about 680 mg/L at 25 °C, according to 3M assessment in pure water (while in natural seawater a solubility of 12.4 mg/L at 22-23 °C was measured [58]).

As a consequence of their chemical nature, PFOS molecules in aqueous solution will be strongly attracted by the fluorinated SAM and even by the gold substrate, as further discussed in **Section 8.3.2**. They will get involved in stable interactions with the SAM interfacial region, thereby increasing their number of contacts with the fluorinated surface. During this process, driven by an attractive force, the insertion of PFOS in the SAM arrangement might occur even though it was not clearly observed in our classical simulations. If we assume the occurrence of similar events in the experimental setup, it would be possible to partially explain the results observed in the previous section. However, the deep alteration of the FDT-SAM structure suggested from the experimental data was not observed in the MD simulations despite the complexity of the system. In general, the discrepancy observed suggests that the results in **Section 8.3.1.2** might not be correlated to an alteration of the SAM structure caused by the exposure to PFOA/PFOS but to other side-processes which destabilise the monolayer. Although further studies will be needed to elucidate this phenomenon, the results collected so far and the comparison between experimental and simulation data allow to exclude the applicability of pinhole/defect-free FDT-SAM in long-chain PFAS screening strategies.

The scenario changes when HFPO-DA is considered: for this compound MD simulation and experimental data are fully consistent. **Figure 8.4** helps to explain why no changes in the values of the current were observed upon HFPO-DA exposure in **Section 8.3.1.2**, because the target molecules are partially interacting with the surface. The higher solubility of HFPO-DA compared to PFOS is responsible for the weaker attraction of this compound with the FDT SAM interfacial region. The FDT SAM structure is not altered and not even compacted by the interaction with short-chain PFAS. In this case, the MD simulations allowed an in-depth understanding of the mechanisms at stake.

Since the FDT/HFPO-DA attractive forces are not prevalent and HFPO-DA is involved in multiple equilibria (HFPO-DA/HFPO-DA, HFPO-DA/FDT interaction, etc.) which are strongly affected by the working conditions, this part of the study allowed to understand why these highly-ordered fluorinated monolayers are not suitable for PFAS sensing.

These findings do not imply that fluorinated SAM with different architectures combined with other sensing strategies (different from *switch on*) should not be considered. For this reason, in the next section a different FDT and DDT-SAM architecture will be discussed.

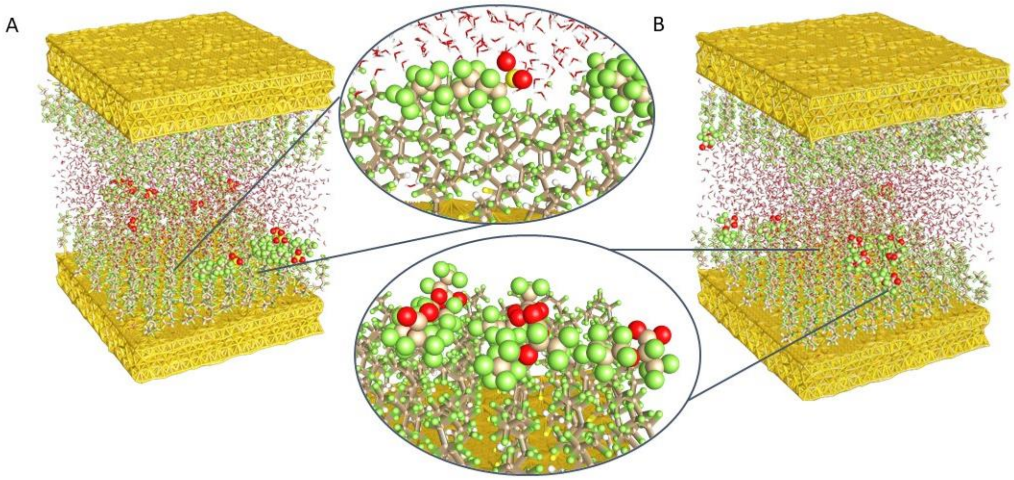

Figure 8.4. *Framework of the MD simulations box with two gold substrates modified with an ordered SAM facing each other. FDT-SAM upon exposure to: (**A**) PFOS and (**B**) HFPO-DA. Zoom in: interaction of molecules with the interfacial region of the SAM.*

8.3.2. Testing *Unordered* Fluorinated SAM Applicability to Switch-off Sensing

8.3.2.1 *SAM Characterisation and Changes upon PFAS Exposure*

SAM with a controlled density of pinholes and defects are often used in *switch off* sensing of small-organic molecules, as anticipated in **Section 8.1**. After having tested highly ordered SAM, the investigation of possible fluorinated modifiers for the design of PFAS sensors moved towards less-ordered monolayer arrangements with partial blocking properties. In the presence of such modifiers, electron transfer can occur directly with no need to study the kinetics of other transfer processes, as in **Section 8.3.1.1**. FDT-SAM containing pinholes/defects can be obtained by lowering both initial thiol concentration and incubation time as described **Section 8.2.2**. For the sake of simplicity these FDT-SAM will be referred to as *unordered* in this work. Such FDT-SAM obtained showed reproducible results after introducing suitable rinsing/soaking steps in

0.1 M KNO_3 solutions (details in **Section 8.2.2**), which remove thiols that are not bound to the gold substrate. Voltammetric characterization of these FDT-SAM took place at the conditions described in **Section 8.3.1**. Such modifiers allow for direct electron transfer via their pinholes/defects, as suggested by the well-defined redox process observable in the voltammograms of **Figure 8.5 A-B**. The voltammograms parameters ($E_{1/2}$ and ΔE_p) are in agreement with what is expected for a one-electron reversible redox process. Oxidation (**Figure 8.5B**) results in a sharp Gaussian peak with E_{pa}=+0.22 V vs Ag/AgCl (sat. KCl) contrary to previous observations for *switch on* FDT-SAM system, where broad oxidation peaks were recorded covering multiple processes. The Faradaic currents here are in the order of hundreds of nA confirming that even *unordered* FDT-SAM show obvious blocking properties (at a bare Au-DE these currents will be in the µA range). Also, for this second FDT-SAM architecture, surface coverage was estimated via LSV resulting in an experimental value of 1.3 nmol cm^{-2}. Keeping in mind the above-mentioned considerations about the possible error factors of this methodology, it is still possible to compare *ordered* and *unordered* FDT-SAM systems qualitatively. This comparison suggests that for *unordered* SAM the surface coverage is less than half of the *ordered* one.

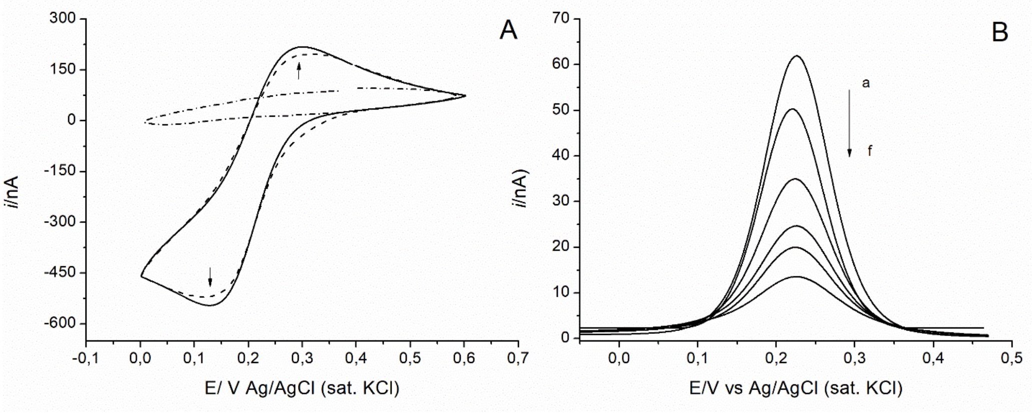

Figure 8.5. *(**A**) Cyclic voltammograms of unordered FDT-SAM in 1.0 mM of $K_3[Fe(CN)_6]$, 1.0 mM $K_4[Fe(CN)_6]$ (solid line), 0.1 M KNO_3 aqueous solution (dotted line for the blank) and upon exposure to a 500 nM HFPO-DA solution (dashed line); inset: arrows pointing the changes in redox peak currents prior/after HFPO-DA incubation. (**B**) DPV of FDT-SAM in presence of the redox probe after incubation with increasing concentrations of HFPO-DA (0, 0.5, 1.5, 5, 7,5, 10 µM, from a to f). HFPO-DA was considered representative for both long and short chain PFAS.*

Figure 8.5B shows the drop in the E_{pa} currents upon exposure to increasing concentrations of HFPO-DA (from 0.5 to 10 µM) this trend was observed for all PFAS tested, as further explained in this section. This first screening carried out in a wide range of PFAS concentrations confirm that it is possible to follow increasing PFAS concentration at *unordered* FDT-SAM and no signal saturation was observed in the range tested. The decreases in the oxidation peak currents were first observed via CV and, then, followed with DPV (**Figure 8.5A-B**).

The differences in oxidation peak currents at increasing PFOA/PFOS concentrations show a linear trend (linear fitting $R^2 > 0.98$), as reported in **Figure 8.6A**. As a control experiment, FDT-modified Au-DE were incubated with KNO_3 to evaluate the possible alteration of the SAM upon successive incubations. These results clearly demonstrate that no meaningful variations occurred. Furthermore, adding the electrolyte solution did not lead to the trends observed upon incubating with the pollutants. Therefore, *unordered* FDT-SAM show a good stability. Changes in their blocking properties can be correlated with the presence and insertion of long-chain PFAS into their structure. The error bars, calculated from triplicate measurements, suggest good reproducibility of the results. PFOA insertion in pristine SAM was previously observed by Fang *et al.* using µM concentration of this pollutant [15]. The authors explained the tendency of PFOA to intercalate into SAM defects/pinholes by considering the formation of partial-micelles and its highly fluorinated nature, without elucidating the respective interactions (mainly attractive repulsive forces). Therefore, one can assume that other short and long chain PFAS will also insert into monolayers, compacting them and thus increasing their blocking properties leading to meaningful decrease in probe oxidation currents. Such changes in FDT-SAM architectures allow one to detect PFOS and PFOA in the low nM range as well as µM range (up to 10 µM). Contrary to what was observed in **Section 8.3.1**, the results after incubation of long-chain and short-chain PFAS at *unordered* FDT-SAM show a consistent trend.

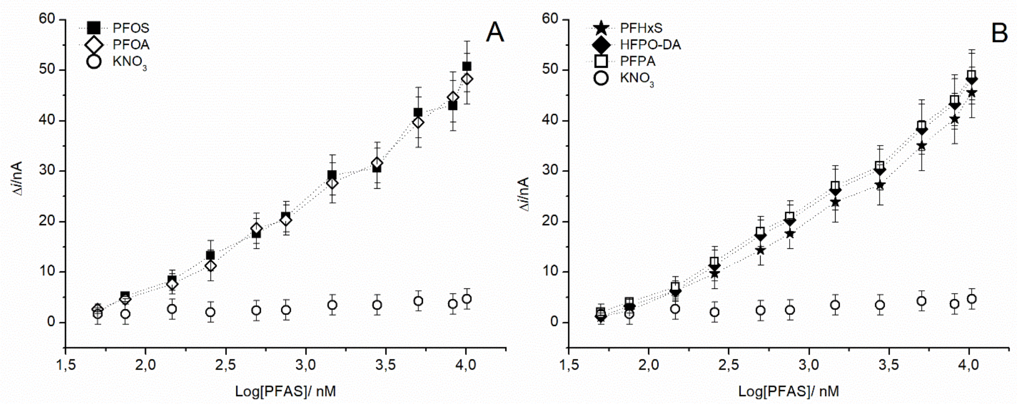

Figure 8.6. *Calibration plots of log (**A**) and short (**B**) chain PFAS after incubation at unordered FDT-SAM. The changes in the peak currents are plotted versus the logarithm of the PFAS concentrations: PFOS and PFOA*

*(**A**) and PFHXS/HFPO-DA/PFPA (**B**). In both plots, the addition of the electrolyte solution (KNO$_3$), considered as the blank, were included for comparison.*

Incubating with increasing concentrations of PFHxS, HFPO-DA and PFPA leads to progressive decrease in probe oxidation current (**Figure 8.6B**). The results suggest that also short-chain PFAS intercalate into FDT-SAM pinholes and defects, compacting the monolayer structure. Due to their different physicochemical properties (especially their increased solubility compared to long-chain PFAS), PFHxS, HFPO-DA and PFPA may have undergone interactions other than insertion. These findings confirm the possibility to apply FDT-SAM-based sensing to screen and estimate the total amount of both long- and short-chain PFAS in aqueous samples. Comparing the data in **Figure 8.6A-B**, one can see that the trends for PFOA/PFOS and PFHxS/HFPO-DA/PFPA are consistent. Further modifications of these monolayers might allow for obtaining intra-class selectivity. However, this is beyond the scope of this preliminary study. The consistency of PFAS interactions with FDT-SAM needed to be further explained from a molecular point of view. Furthermore, a complete series of negative control experiments in the study of unordered FDT-SAM confirmed that: adding blanks does not alter FDT and DDT unordered SAM in a meaningful way; trends observed at unordered DDT-SAM after PFAS incubation differ from those at FDT-SAM (overview in **Figure A8. 7**).

8.3.2.2 MD Simulations vs Experimental Outcomes

To better understand the mechanism of interaction of PFAS within FDT SAM pinholes/defects, MD simulations were run considering an *unordered* monolayer. As for the previously simulated systems, ten PFOS and ten HFPO-DA molecules were considered as representative compounds for long-chain PFAS and short-chain PFAS, respectively. The gold slab was placed at the bottom of the simulation box, and its surface at the interface with the solvent was only 50% covered by FDT molecules, in order to mimic the pinholes in the fluorinated SAM architecture. As described in **Section 8.3.1.3**, an additional fluorinated SAM with the same characteristics as the former was added to the top of the simulation box to increase the probability of sampling more binding/interacting events.

During MD simulations of both systems the insertion of the targets in the FDT-SAM pinholes was observed, as shown in the snapshots reported in **Figure 8.7**. The close-up look of the system **Figure 8.7A** shows that for HFPO-DA the insertion occurs with the hydrophilic head group (-COOH) pointing towards the gold substrate instead of facing the FDT-SAM/aqueous solution interface. This behaviour can be ascribed to the relatively short length of the HFPO-DA, and to the strong affinity of these fluorinated target molecules (i.e., PFOS and HFPO-DA) to the gold substrate. Indeed, different simulation snapshots show that for sufficiently large pinholes HFPO-DA tends to lie on the gold substrate. On the contrary, PFOS molecules can fit in the pinholes with the hydrophilic head group oriented towards the interfacial region of the FDT-SAM. In this case, there is no way for them to lie on the gold substrate, likely due to their relatively linear and long chains that restrict their conformational freedom once trapped into the FDT-SAM pinhole.

To estimate non-covalent interaction energies (computed as Lennard-Jones and van der Waals) of these target molecules with the gold substrate, a different simulation model setup was implemented. Ten FDT molecules and ten target molecules (PFOS and HFPO-DA) were placed in solution in a periodic simulation box having only one gold substrate at one end. The average energies obtained for a single molecule are equal to -86 KJ/mol for long-chains PFOS molecules, and to -57 KJ/mol for short chains HPFO-DA molecules. These energies were calculated following the same procedure as described in **Section 8.3.1.3**, by determining the numbers of contact, and by considering only the energies corresponding to time windows where the number of contacts was greater than or equal to the chosen threshold (≧ 15 for the HFPO-DA molecules, and ≧ 23 for the PFOS molecules).

We further studied the affinity of both target moieties with unordered SAM with the same methods described in **Section 8.3.1.3**. The plots of the number of contacts (**Figure A8.8A-B**) show that PFOS molecules can insert into the pinholes by forming more stable non-covalent bonds with the FDT molecules of the monolayer, than the bonds formed by the HFPO-DA counterpart. In this case, we set the threshold of the number of contacts ≧ 19 for the short-chain PFAS, and ≧ 28 for the long-chain PFAS, see **Figure A8.8E-F**. The corresponding average interacting energies computed according to this threshold are equal to -51 KJ/mol for the system with PFOS and -38 KJ/mol for the one with HFPO-DA. Even in this case, the affinity of long-chain PFOS is significantly (13 KJ/mol) more favourable. However, it is worth noting that the HFPO-DA single molecules that form more stable bonds with FDT-SAM have energies of the same order of magnitude (-50 KJ/mol) as those determined by the PFOS system. Besides, the literature does not provide quantitative data for the interaction energy to compare with. Thus, the values reported herein should be taken with due care and likely be viewed as a general order of magnitude for PFAS interacting entities considered here in general, and fluoro-fluoro tails, in particular. Nonetheless, these values are consistent with those reported in [17] for small organic moieties adsorbed onto Au(111) monolayers.

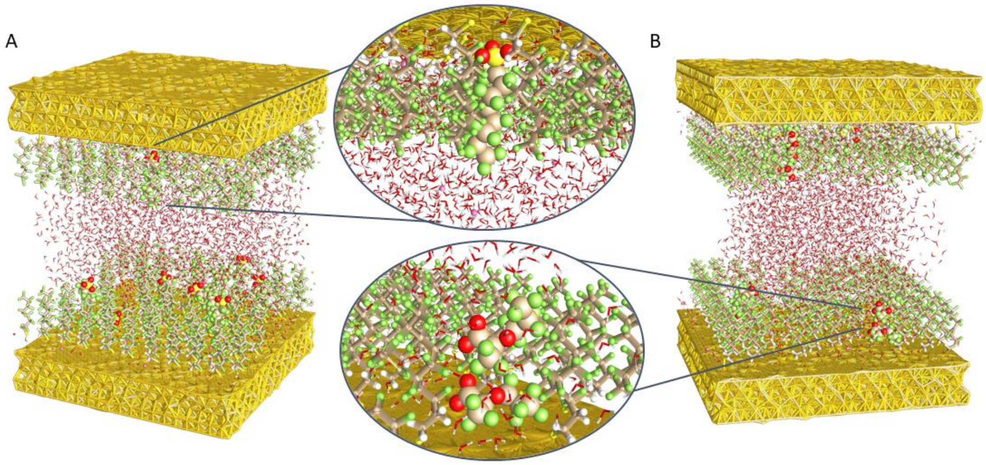

Figure 8.7. *Framework of the MD simulations box with two gold substrates modified with an unordered SAM facing each other. FDT-SAM upon exposure to: (**A**) PFOS and (**B**) HFPO-DA. Zoom in: orientation of the PFAS molecules in the interaction with the interfacial region of the SAM.*

In conclusion, FDT-SAM with pinholes/defects were found to be suitable for PFAS screening. The linear trends were observed in concentration range from 100-1000 nM. The sensitivity of these *switch-off* sensing strategies can be further improved with additional optimizations steps or combining FDT-SAM with other modifiers. The results described in this section proved the importance of a complete characterization of the SAM modifiers, the need of a complete series of negative control experiments and the interest of supporting electrochemical data interpretation via MD simulations.

8.4 Conclusions

The changes in FDT-SAM with a pinholes/defects-free structure (*ordered SAM*) or randomized pinholes/defects architecture (*unordered SAM*) were studied upon long- and short-chain PFAS exposure. We aimed to evaluate fluorinated SAM applicability in the development of *switch-on* or *switch-off* sensing strategies for PFAS. The changes in the SAM structures were studied considering variations in the blocking properties of the monolayers via a combination of electrochemical impedance spectroscopy and voltammetry. Experimental data interpretation went hand in hand with molecular dynamics (MD) simulations for understanding the possible interaction mechanisms involved, especially fluorine-fluorine ones, in a more in-depth manner.

During the first part of the study, *ordered SAM* were investigated characterising their blocking properties (in particular, the kinetics of the electron tunneling) and surface coverage. These findings can be further applied in the design of *ordered* FDT-SAM for other sensing applications. Complete electrochemical and impedimetric characterisation serves this purpose. *Ordered* FDT-SAM were found to be unsuitable for PFAS screening due to the fact that short chain PFAS did not lead to any traceable change in SAM properties. Changes in the ordered FDT-SAM structures were observed for long chain PFAS (PFOS and PFOA). However, the experimental results showed poor reproducibility. These data were not supported by MD simulations: those showed that all long- and short-chain PFAS should deposit at the FDT-SAM interface without altering its structure or intercalate. PFAS molecules were found to minimise their energy by arranging themselves at the monolayer/solution interface. Therefore, changes in current intensities recorded for PFOA/PFOS were ascribed to other side-phenomena; this type of fluorinated SAM architecture was not further considered for sensing applications.

Another FDT-SAM architecture (*unordered*), was tested in the second part of the study. Upon PFAS exposure, *unordered* FDT-SAM showed increased blocking properties enabling sensing increasing PFAS concentration from nM to low µM range. This system turned out compatible with a *switch-off* sensing strategy for both long- and short-chain PFAS screening. For this second FDT-SAM architecture, experimental data and MD simulations lead to the same conclusions. Hence, it was possible to confirm and elucidate the insertion process of PFAS molecules interacting with *unordered* SAM. This mechanism was previously proposed in hypotheses, but not described in a quantitative way (estimating energies) yet. Overall, the present work underlines the importance of: *i*) characterizing and comparing different SAM architectures, *ii*) supporting interpretation of electrochemical data with MD simulations to describe the interactions involved, and *iii*) using a reference system to operate a complete series of negative controls (DDT-SAM) and evaluate the contributions expected (FDT-SAM, F-F interactions). In both parts of this preliminary study, negative controls played a key role: they allowed us to indirectly prove that the interactions observed depend on the presence of a fluorinate monolayer and, as a consequence, can be defined as fluorophilic. The application of fluorophilic interactions in the design of PFAS recognition elements for the development of sensing strategies is promising. Based-on these interactions, it is possible to realize a new generation of sensing platform for screening of PFAS (all generations) thus answering the urgent need for portable and rapid analytical tools for PFAS monitoring in waste waters. For this purpose, fluorinated SAM modifiers can be further combined with other electrode surface materials to enhance the sensitivity and develop original sensing devices.

In respect to the MIP-based sensor described in **Chapter 7**, the SAM-based sensing strategies investigated here showed the potential of a PFAS screening platform easy to implement. Fluorinated SAM modifiers or other type of highly fluorinated electrode surface modifiers can be further considered for the development of a new generation of sensors for PFAS monitoring (photoelectrochemical, electrochemiluminescence-based, etc.).

Acknowledgments

This work started after a fruitful and critical discussion about the future of PFAS sensors and the need to design tuneable platform able to follow the fast diversification of these class of contaminants. I am grateful to Prof. Peter Lieberzeit and both my supervisors for the discussion and for their engagement in this topic. With this preliminary work we aimed to explore a "way out" from single-molecule designed sensors and move towards fast PFAS screening electrochemical platforms. I am thankful to Cedrix, Marco, Prof. Flavio Romano and Prof. Achille Giacometti for having accepted the challenge to support electrochemical data with MD simulation. This collaboration took months and taught me a lot about the importance of building a common knowledge in between our different fields (…we should continue at this point)! Thanks to Elenora and Dafne for helping us characterising our SAM with ATR and getting involved in the project (their curiosity was contagious!). A big thank to Ettore Martini, our master student, who follow most of this project and faced all the challenges and pitfalls with me, I was proud of what you did! Thank to Rui Campos for having taught me all I need to know about SAM when I started and for having always the right question or a trump card to share! The computational resources were provided by the SCSCF multiprocessor cluster at the University Ca' Foscari of Venice. We further acknowledge the CINECA project HP10CGFUDT for the availability of high-performance computing resources through the ISCRA initiative. This work was supported by MIUR PRIN-COFIN2017 "Soft Adaptive Networks" (grant code 2017Z55KCW acknowledged to A.G.) and by Marie Skłodowska-Curie Actions (grant number 842219 acknowledged to R.C.). Molecular graphics and analyses performed with UCSF Chimera, developed by the Resource for Biocomputing, Visualization, and Informatics at the University of California, San Francisco, with support from NIH P41-GM103311.

References

[1] M.M. McCabe, P. Hala, A. Rojas-Pena, O. Lautner-Csorba, T.C. Major, H. Ren, R.H. Bartlett, E.J. Brisbois, M.E. Meyerhoff, Enhancing analytical accuracy of intravascular electrochemical oxygen sensors via nitric oxide release using S-nitroso-N-acetyl-penicillamine (SNAP) impregnated catheter tubing, Talanta. 205 (2019) 120077. https://doi.org/https://doi.org/10.1016/j.talanta.2019.06.077.

[2] M.W. Glasscott, K.J. Vannoy, R. Kazemi, M.D. Verber, J.E. Dick, μ-MIP: Molecularly Imprinted Polymer-Modified Microelectrodes for the Ultrasensitive Quantification of GenX (HFPO-DA) in River Water, Environ. Sci. Technol. Lett. 7 (2020) 489–495. https://doi.org/10.1021/acs.estlett.0c00341.

[3] K.L. Rodriguez, J.H. Hwang, A.R. Esfahani, A.H.M.A. Sadmani, W.H. Lee, Recent developments of PFAS-detecting sensors and future direction: A review, Micromachines. 11 (2020). https://doi.org/10.3390/mi11070667.

[4] G. Moro, K. De Wael, L.M. Moretto, Challenges in the electrochemical (bio)sensing of nonelectroactive food and environmental contaminants, Curr. Opin. Electrochem. 16 (2019) 57–65. https://doi.org/10.1016/j.coelec.2019.04.019.

[5] M.D. Hanwell, D.E. Curtis, D.C. Lonie, T. Vandermeersch, E. Zurek, G.R. Hutchison, Avogadro: an advanced semantic chemical editor, visualization, and analysis platform, J. Cheminform. 4 (2012) 17. https://doi.org/10.1186/1758-2946-4-17.

[6] H. Niu, S. Wang, Z. Zhou, Y. Ma, X. Ma, Y. Cai, Sensitive Colorimetric Visualization of Perfluorinated Compounds Using Poly(ethylene glycol) and Perfluorinated Thiols Modified Gold Nanoparticles, Anal. Chem. 86 (2014) 4170–4177. https://doi.org/10.1021/ac403406d.

[7] C. Fang, Z. Sobhani, M. Megharaj, R. Naidu, Electrochemical Proof of Fluorophilic Interaction among Fluoro-Carbon Chains, Electroanalysis. 30 (2018) 2349–2355. https://doi.org/10.1002/elan.201800190.

[8] C. Fang, M. Megharaj, R. Naidu, Electrochemical switch on-off response of a self-assembled monolayer (SAM) upon exposure to per fl uorooctanoic acid (PFOA), J. Electroanal. Chem. 785 (2017) 249–254. https://doi.org/10.1016/j.jelechem.2016.12.040.

[9] C. Fang, M. Megharaj, R. Naidu, Electrochemical Studies on Self-assembled Monolayer (SAM) Upon Exposure to Anionic Surfactants: PFOA, PFOS, SDS and SDBS, Electroanalysis. 29 (2017) 2155–2160. https://doi.org/10.1002/elan.201700108.

[10] M.J. Abraham, T. Murtola, R. Schulz, S. Páll, J.C. Smith, B. Hess, E. Lindah, Gromacs: High performance molecular simulations through multi-level parallelism from laptops to supercomputers, SoftwareX. 1–2 (2015). https://doi.org/10.1016/j.softx.2015.06.001.

[11] L.B. Wright, P.M. Rodger, S. Corni, T.R. Walsh, GolP-CHARMM: First-Principles Based Force Fields for the Interaction of Proteins with Au(111) and Au(100), J. Chem. Theory Comput. 9 (2013) 1616–1630. https://doi.org/10.1021/ct301018m.

[12] R. Campos, E.E. Ferapontova, Electrochimica Acta Electrochemistry of weakly adsorbed species : Voltammetric analysis of electron transfer between gold electrodes and Ru hexaamine electrostatically interacting with DNA duplexes, Electrochim. Acta. 126 (2014) 151–157. https://doi.org/10.1016/j.electacta.2013.07.083.

[13] Y.F. Xing, S.F.Y. Li, A.K.H. Lau, S.J. O'Shea, Electrochemical impedance spectroscopy study of mixed thiol monolayers on gold, J. Electroanal. Chem. 583 (2005) 124–132. https://doi.org/10.1016/j.jelechem.2005.05.010.

[14] Y.S. Shon, R. Colorado, C.T. Williams, C.D. Bain, T.R. Lee, Low-density self-assembled monolayers on gold derived from chelating 2-monoalkylpropane-1,3-dithiols, Langmuir. 16 (2000) 541–548. https://doi.org/10.1021/la981698l.

[15] H. Sahalov, B. O'Brien, K.J. Stebe, K. Hristova, P.C. Searson, Influence of applied potential on the impedance of alkanethiol SAMs, Langmuir. 23 (2007) 9681–9685. https://doi.org/10.1021/la701398u.

[16] P. Diao, M. Guo, D. Jiang, Z. Jia, X. Cui, D. Gu, R. Tong, B. Zhong, Fractional coverage of defects in

self-assembled thiol monolayers on gold, J. Electroanal. Chem. 480 (2000) 59–63. https://doi.org/10.1016/S0022-0728(99)00445-3.

[17] O. Zenasni, A.C. Jamison, T.R. Lee, The impact of fluorination on the structure and properties of self-assembled monolayer films, Soft Matter. 9 (2013) 6356–6370. https://doi.org/10.1039/C3SM00054K.

[18] F.A. Aguiar, R. Campos, C. Wang, R. Jitchati, A.S. Batsanov, M.R. Bryce, R. Kataky, Comparative electrochemical and impedance studies of self-assembled rigid-rod molecular wires and alkanethiols on gold substrates, Phys. Chem. Chem. Phys. 12 (2010) 14804–14811. https://doi.org/10.1039/c005402j.

[19] H.O. Finklea, Consequences of a potential-dependent transfer coefficient in ac voltammetry and in coupled electron-proton transfer for attached redox couples, J. Electroanal. Chem. 495 (2001) 79–86. https://doi.org/10.1016/S0022-0728(00)00399-5.

[20] Y.F. Xing, S.J. O'Shea, S.F.Y. Li, Electron transfer kinetics across a dodecanethiol monolayer self assembled on gold, J. Electroanal. Chem. 542 (2003) 7–11. https://doi.org/10.1016/S0022-0728(02)01440-7.

[21] J.N. Meegoda, J.A. Kewalramani, B. Li, R.W. Marsh, A review of the applications, environmental release, and remediation technologies of per-and polyfluoroalkyl substances, Int. J. Environ. Res. Public Health. 17 (2020) 1–26. https://doi.org/10.3390/ijerph17218117.

[22] M. Al Amin, Z. Sobhani, Y. Liu, R. Dharmaraja, S. Chadalavada, R. Naidu, J.M. Chalker, C. Fang, Recent advances in the analysis of per- and polyfluoroalkyl substances (PFAS)—A review, Environ. Technol. Innov. 19 (2020) 100879. https://doi.org/10.1016/j.eti.2020.100879.

[23] D. Barceló, T. Ruan, Challenges and perspectives on the analysis of traditional perfluoroalkyl substances and emerging alternatives, TrAC - Trends Anal. Chem. 121 (2019) 2–3. https://doi.org/10.1016/j.trac.2019.07.016.

[24] H.O. Finklea, S. Avery, M. Lynch, T. Furtsch, Blocking Oriented Monolayers of Alkyl Mercaptans on Gold Electrodes, Langmuir. 3 (1987) 409–413. https://doi.org/10.1021/la00075a024.

[25] R.C. Buck, J. Franklin, U. Berger, J.M. Conder, I.T. Cousins, P. De Voogt, A.A. Jensen, K. Kannan, S.A. Mabury, S.P.J. van Leeuwen, Perfluoroalkyl and polyfluoroalkyl substances in the environment: Terminology, classification, and origins, Integr. Environ. Assess. Manag. 7 (2011) 513–541. https://doi.org/10.1002/ieam.258.

[26] J. Hautman, M.L. Klein, Simulation of a monolayer of alkyl thiol chains, J. Chem. Phys. 91 (1989) 4994–5001. https://doi.org/10.1063/1.457621.

[27] A. Ulman, J.E. Eilers, N. Tillman, Packing and molecular orientation of alkanethiol monolayers on gold surfaces, Langmuir. 5 (1989) 1147–1152. https://doi.org/10.1021/la00089a003.

[28] B. Rai, S. P., C.P. Malhotra, Pradip, K.G. Ayappa, Molecular Dynamic Simulations of Self-Assembled Alkylthiolate Monolayers on an Au(111) Surface, Langmuir. 20 (2004) 3138–3144. https://doi.org/10.1021/la0357256.

[29] J. Wen, W. Li, S. Chen, J. Ma, Simulations of molecular self-assembled monolayers on surfaces: packing structures, formation processes and functions tuned by intermolecular and interfacial interactions, Phys. Chem. Chem. Phys. 18 (2016) 22757–22771. https://doi.org/10.1039/C6CP01049K.

[30] T. Utesch, M. Sezer, I.M. Weidinger, M.A. Mroginski, Adsorption of Sulfite Oxidase on Self-Assembled Monolayers from Molecular Dynamics Simulations, Langmuir. 28 (2012) 5761–5769. https://doi.org/10.1021/la205055g.

[31] P.K. Ghorai, S.C. Glotzer, Molecular Dynamics Simulation Study of Self-Assembled Monolayers of Alkanethiol Surfactants on Spherical Gold Nanoparticles, J. Phys. Chem. C. 111 (2007) 15857–15862. https://doi.org/10.1021/jp0746289.

[32] V.P. Raut, M.A. Agashe, S.J. Stuart, R.A. Latour, Molecular Dynamics Simulations of Peptide−Surface Interactions, Langmuir. 21 (2005) 1629–1639. https://doi.org/10.1021/la047807f.

[33] F. Iori, R. Di Felice, E. Molinari, S. Corni, GolP: An atomistic force-field to describe the interaction of proteins with Au(111) surfaces in water, J. Comput. Chem. 30 (2009) 1465–1476. https://doi.org/https://doi.org/10.1002/jcc.21165.

[34] P. Bhadra, S.W.I. Siu, Comparison of Biomolecular Force Fields for Alkanethiol Self-Assembled

Monolayer Simulations, J. Phys. Chem. C. 121 (2017) 26340–26349. https://doi.org/10.1021/acs.jpcc.7b08092.

[35] Y. Jiang, X. Zhang, L. Pei, S. Yue, L. Ma, L. Zhou, Z. Huang, Silver nanoparticles modi fi ed two-dimensional transition metal carbides as nanocarriers to fabricate acetycholinesterase-based electrochemical biosensor, 339 (2018) 547–556. https://doi.org/10.1016/j.cej.2018.01.111.

[36] S. Vemparala, B.B. Karki, R.K. Kalia, A. Nakano, P. Vashishta, Large-scale molecular dynamics simulations of alkanethiol self-assembled monolayers, J. Chem. Phys. 121 (2004) 4323–4330. https://doi.org/10.1063/1.1775779.

[37] J. Meena Devi, A simulation study on the thermal and wetting behavior of alkane thiol SAM on gold (111) surface, Prog. Nat. Sci. Mater. Int. 24 (2014) 405–411. https://doi.org/https://doi.org/10.1016/j.pnsc.2014.06.009.

[38] C. Yan, R. Yuan, W.C. Pfalzgraff, J. Nishida, L. Wang, T.E. Markland, M.D. Fayer, Unraveling the dynamics and structure of functionalized self-assembled monolayers on gold using 2D IR spectroscopy and MD simulations, Proc. Natl. Acad. Sci. 113 (2016) 4929 LP – 4934. https://doi.org/10.1073/pnas.1603080113.

[39] J. Wang, R.M. Wolf, J.W. Caldwell, P.A. Kollman, D.A. Case, Development and testing of a general amber force field, J. Comput. Chem. 25 (2004) 1157–1174. https://doi.org/https://doi.org/10.1002/jcc.20035.

[40] J. Wang, W. Wang, P.A. Kollman, D.A. Case, Automatic atom type and bond type perception in molecular mechanical calculations, J. Mol. Graph. Model. 25 (2006) 247–260. https://doi.org/https://doi.org/10.1016/j.jmgm.2005.12.005.

[41] A.W. Sousa da Silva, W.F. Vranken, ACPYPE - AnteChamber PYthon Parser interfacE, BMC Res. Notes. 5 (2012) 367. https://doi.org/10.1186/1756-0500-5-367.

[42] A. Jakalian, B.L. Bush, D.B. Jack, C.I. Bayly, Fast, efficient generation of high-quality atomic charges. AM1-BCC model: I. Method, J. Comput. Chem. 21 (2000) 132–146. https://doi.org/https://doi.org/10.1002/(SICI)1096-987X(20000130)21:2<132::AID-JCC5>3.0.CO;2-P.

[43] A. Jakalian, D.B. Jack, C.I. Bayly, Fast, efficient generation of high-quality atomic charges. AM1-BCC model: II. Parameterization and validation, J. Comput. Chem. 23 (2002) 1623–1641. https://doi.org/https://doi.org/10.1002/jcc.10128.

[44] W.L. Jorgensen, J. Chandrasekhar, J.D. Madura, R.W. Impey, M.L. Klein, Comparison of simple potential functions for simulating liquid water, J. Chem. Phys. 79 (1983) 926–935. https://doi.org/10.1063/1.445869.

[45] J.-A. Huang, M.Z. Mousavi, G. Giovannini, Y. Zhao, A. Hubarevich, M.A. Soler, W. Rocchia, D. Garoli, F. De Angelis, Multiplexed Discrimination of Single Amino Acid Residues in Polypeptides in a Single SERS Hot Spot, Angew. Chemie Int. Ed. 59 (2020) 11423–11431. https://doi.org/https://doi.org/10.1002/anie.202000489.

[46] S. Nosé, A molecular dynamics method for simulations in the canonical ensemble, Mol. Phys. 52 (1984) 255–268. https://doi.org/10.1080/00268978400101201.

[47] W.G. Hoover, Canonical dynamics: Equilibrium phase-space distributions, Phys. Rev. A. 31 (1985) 1695–1697. https://doi.org/10.1103/PhysRevA.31.1695.

[48] Y. Tu, Y. Lin, W. Yantasee, Z. Ren, Carbon Nanotubes Based Nanoelectrode Arrays: Fabrication, Evaluation, and Application in Voltammetric Analysis, Electroanalysis. 17 (2005) 79–84. https://doi.org/https://doi.org/10.1002/elan.200403122.

[49] F.L.R. Bard A.J., Electrochemial methods fundamentals and applications, 2nd ed., 2004.

[50] E. Sabatini, I. Rubinstein, R. Maoz, J. Sagiv, Organized self-assembling monolayers on electrodes. Part I. Octadecyl derivatives on gold, J. Electroanal. Chem. 219 (1987) 365–371.

[51] L.Y.S. Lee, R.B. Lennox, Ferrocenylalkylthiolate labeling of defects in alkylthiol self-assembled monolayers on gold, Phys. Chem. Chem. Phys. 9 (2007) 1013–1020. https://doi.org/10.1039/b613598f.

[52] J.C. Love, L.A. Estroff, J.K. Kriebel, R.G. Nuzzo, G.M. Whitesides, Self-Assembled Monolayers of Thiolates on Metals as a Form of Nanotechnology, Chem. Rev. 105 (2005) 1103–1170. https://doi.org/10.1021/cr0300789.

[53] C.A. Widrig, C. Chung, M.D. Porter, The electrochemical desorption of n-alkanethiol monolayers from polycrystalline Au and Ag electrodes, J. Electroanal. Chem. Interfacial Electrochem. 310 (1991) 335–359. https://doi.org/https://doi.org/10.1016/0022-0728(91)85271-P.

[54] C.E.D. Chidsey, D.N. Loiacono, Chemical Functionality in Self-Assembled Monolayers: Structural and Electrochemical Properties, Langmuir. 6 (1990) 682–691. https://doi.org/10.1021/la00093a026.

[55] M.D. Porter, T.B. Bright, D.L. Allara, C.E.D. Chidsey, Spontaneously organized molecular assemblies. 4. Structural characterization of n-alkyl thiol monolayers on gold by optical ellipsometry, infrared spectroscopy, and electrochemistry, J. Am. Chem. Soc. 109 (1987) 3559–3568. https://doi.org/10.1021/ja00246a011.

[56] P.D. Willard B. Nixon, B.S. Frank J. Lezotte, Determination of the water solubility and vapor pressure of H-28308, 2008.

[57] R.A. Hoke, B.D. Ferrell, T.L. Sloman, R.C. Buck, L.W. Buxton, Aquatic hazard, bioaccumulation and screening risk assessment for ammonium 2,3,3,3-tetrafluoro-2-(heptafluoropropoxy)-propanoate, Chemosphere. 149 (2016) 336–342. https://doi.org/https://doi.org/10.1016/j.chemosphere.2016.01.009.

[58] D. Brooke, A. Footitt, T. Nwaogu, Environmental Risk Evaluation Report: Perfluorooctanesulphonate (PFOS), 2004. https://www.gov.uk/government/uploads/system/uploads/attachment_data/file/290857/scho1009brbl-e-e.pdf.

8.1 Annex A

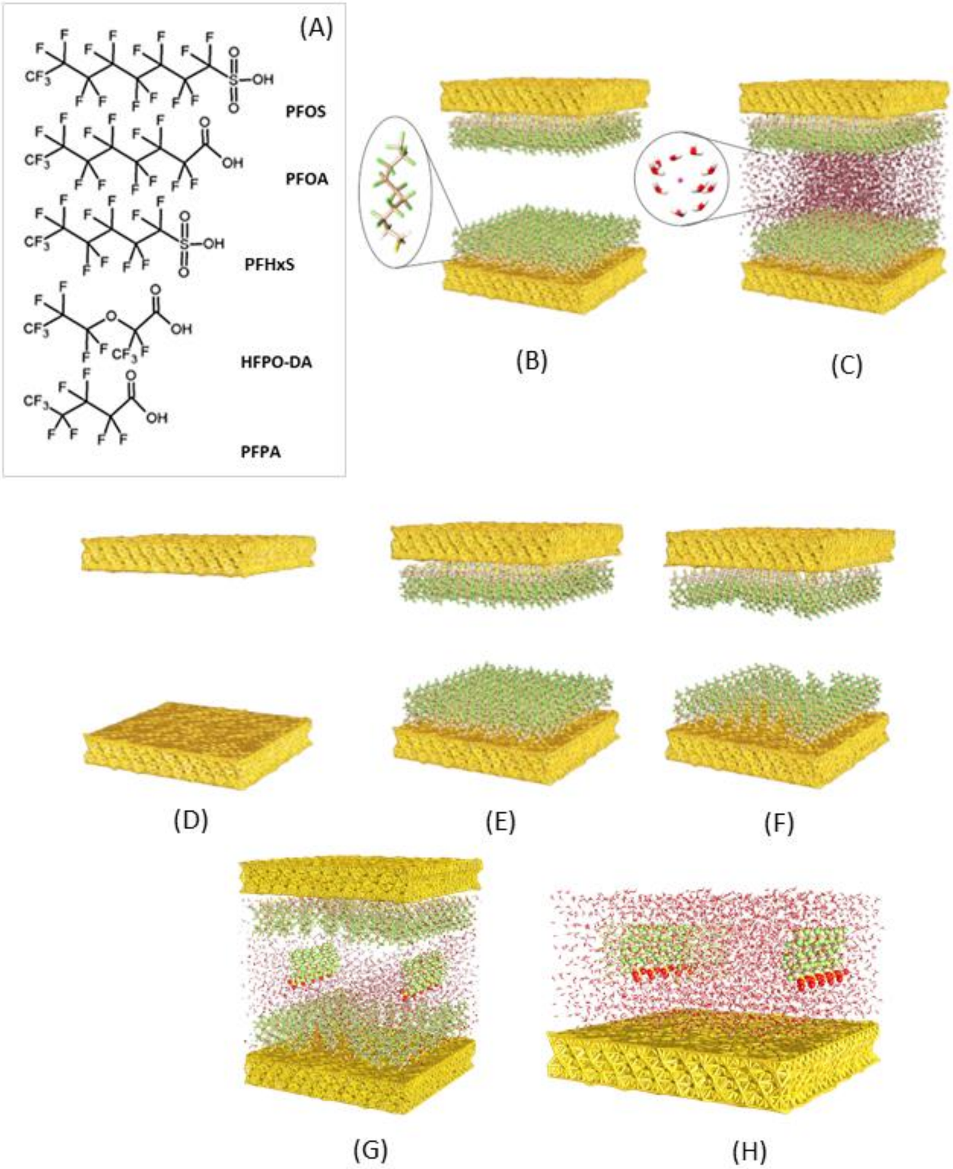

Figure A8.1. MD simulations setup: *(**A**) Chemical structures of long- and short-chain PFASs, (**B**) periodic simulation box embedding two ordered and mirrored FDT-SAMs, inset: zoom of FDT molecule. (**C**) periodic simulation box embedding two ordered and mirrored FDT-SAMs filled with the 3-site rigid TIP3P water model; inset: water molecules and potassium ions. (**D**) Periodic simulation box embedding two gold (111) slabs. Simulation box embedding: (**E**) two ordered and mirrored FDT-SAMs and (**F**) two unordered and mirrored FDT-SAMs. (**G**) Periodic simulation box embedding FDT-SAMs and ten PFOS molecules in solution. (**H**) Half periodic simulation box embedding ten FDT and ten PFOS molecules in aqueous solution with potassium ions.*

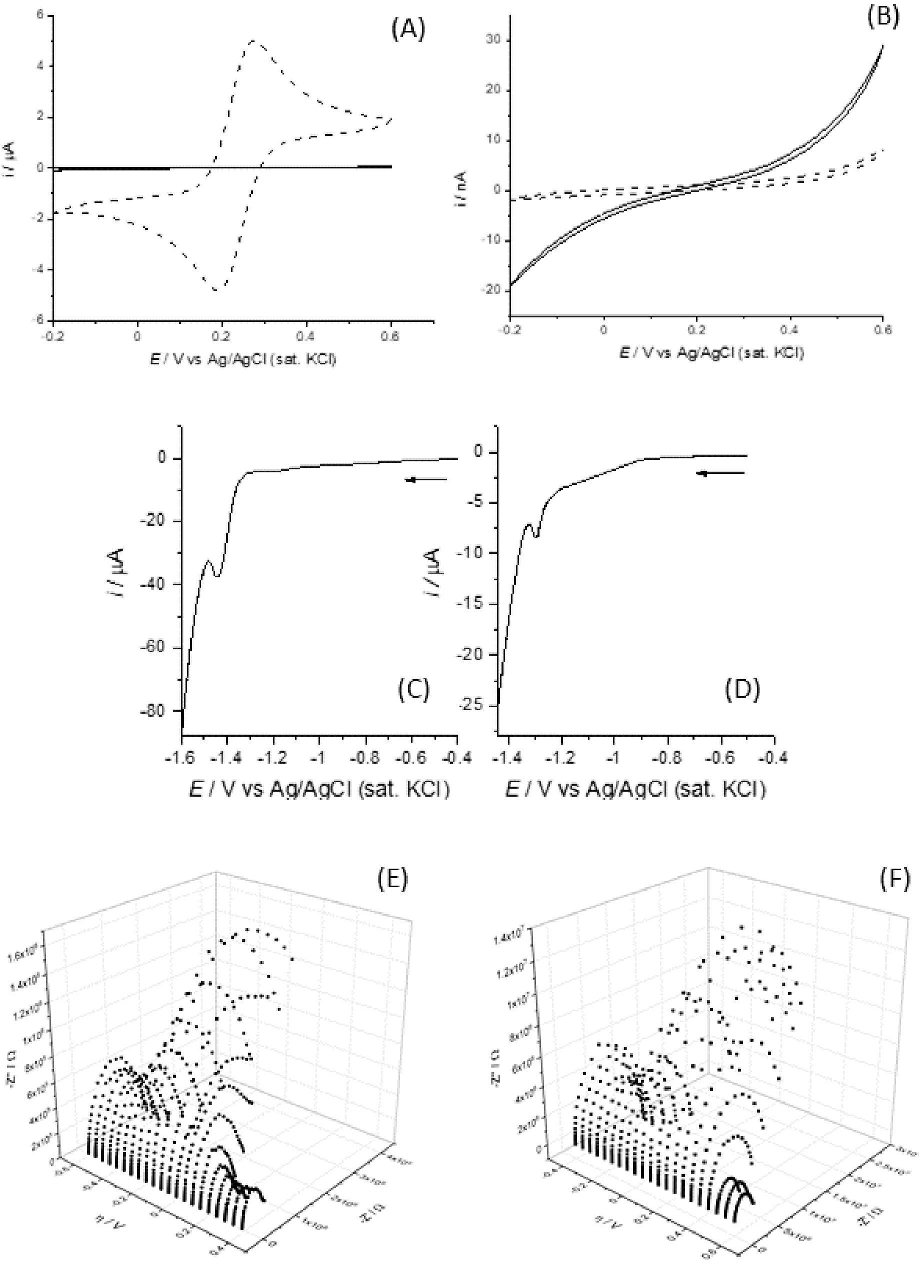

Figure A8.2. ***Electrochemical characterization of ordered FDT and DDT-SAM***: *(**A**) Cyclic voltammogram of FDT SAM (continuous line) and bare electrode (dashed line) recorded in redox probe solution; CVs of (**B**) DDT SAM recorded in redox probe (black line) and background electrolyte (dashed line). (**C-D**) Linear sweep voltammogram showing a cathodic process corresponding to the desorption of the FDT-SAM (**C**) and DDT-SAM (**D**) from the GDE surface recorded in KOH 0.05 M. (**E-F**) EIS potential scan data overview for FDT-SAM (**E**) and DDT-SAM (**F**).*

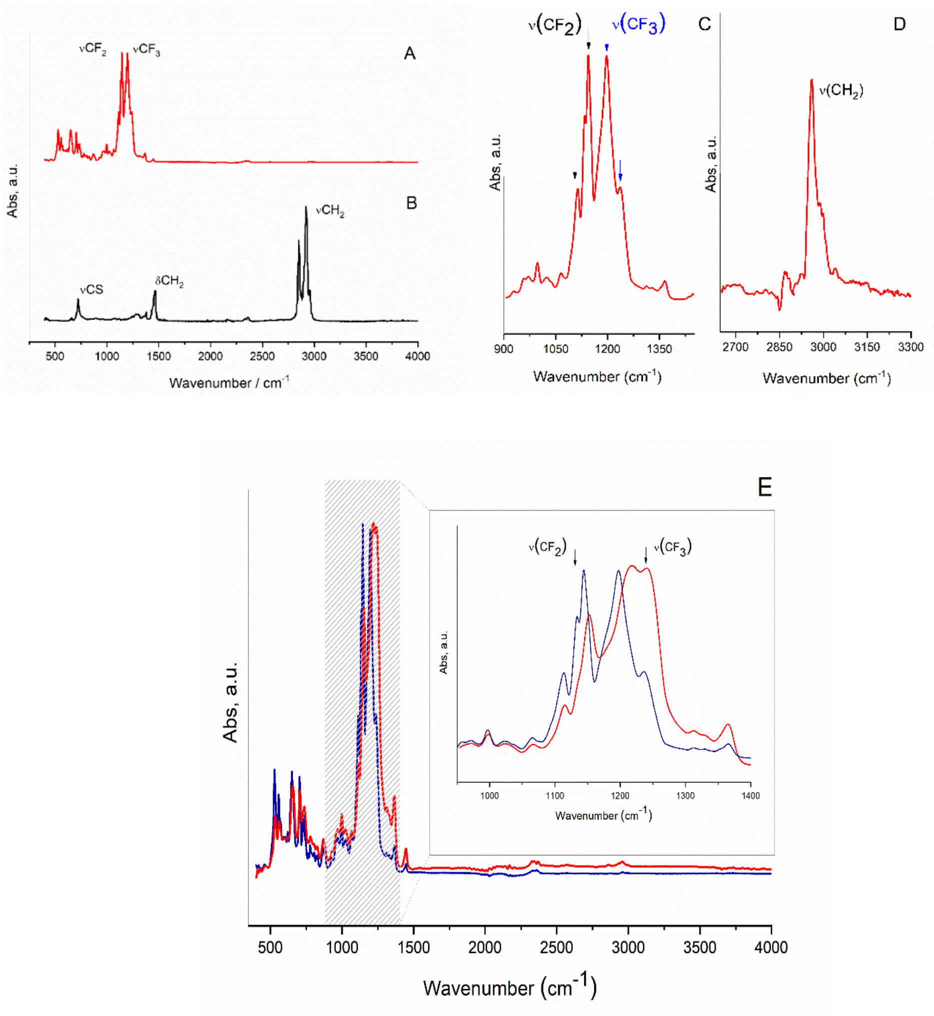

*Figure A8.3. IR characterization of FDT and DDT-SAM: (**A**) Infrared spectra of FDT and (**B**) DDT recorded in the spectral range between 400 and 4000 cm^{-1}, the label identify the main stretching and bending signals; (**C**) Characteristic regions of the FDT spectra: CF_3 anDd CF_2 stretching region in the spectral range from 900 to 1350 cm^{-1}; (**D**) Zoom in the CH_2 stretching region of FDT spectrum ranging from 2700 to 3300 cm^{-1}; (**E**) Overlay of infrared spectra of FDT bulk (blue line) an FDT-SAM on gold (red line); inset: zoom of CF stretching region.*

The spectra of FDT and DDT were first compared (**Figure A8.3A-B**). It was possible to observe that FDT spectra is characterized by very strong signals in the region between 1100 and 1350 cm^{-1} (**Figure A8.3C**). These signals can be ascribed to the stretching of CF_2 between 1113 and 1144 cm^{-1} and the stretching of CF_3 between 1198 and 1239 cm^{-1} [54,55]. The relative intensities and distribution of these signals are relevant for the identification of fluorinated compounds, as we will see in the following paragraphs. In particular, the ratio between CF_2 and CF_3 main signals was found to be 1:2. From the analysis of the FDT spectra, we were expecting additional signals in the region of symmetric and asymmetric methylene stretching (vCH_2) between 2851 and 2919 cm^{-1}, respectively [54]. These signals were clearly observed in DDT (**Figure A8.3D**). Considering the two $–CH_2$ groups of FDT, we might expect to observe vCH_2 with an intensity of approximately 20-30% relative to the $–CF_2$. This is not confirmed by the empirical data where these modes are apparently absent. Further analysis of the FDT spectrum, zooming the $–CH_2$ stretching region reveals the presence of these modes with a very low intensity. This spectral feature, can be justified by the effect of the neighbouring fluorine and thiol groups, as suggested by Chidsey et al. [54] (**Figure A8.3D**). The overlay of the bulk thiol and the thiol on gold spectra is reported in **Figure A8.3E**. The spectrum of FDT on gold is slightly shifted to higher wavenumber. The deconvolution process of the CF region revealed a CF_2:CF_3 ratio of 1:4. The increment in this ratio, compared to the bulk compound, can be due to the reduced mobility of the CF_2 moieties in an ordered SAM. On the contrary, the increase observed in the vCF_3 area can be explained considering the relatively high mobility of this group because of its the terminal position [53].

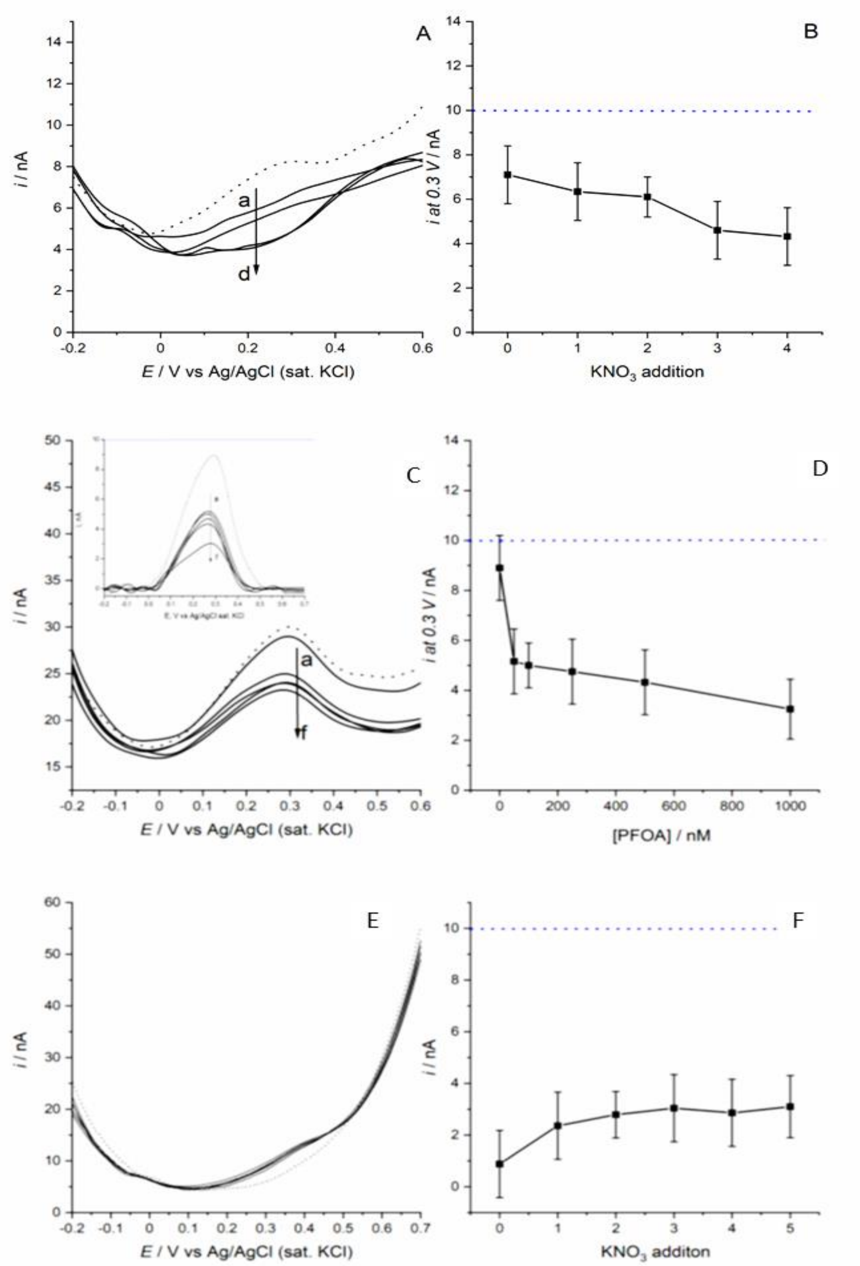

***Figure A8. 4. Negative controls of ordered FDT-SAM**: (**A**) Voltammograms of FDT-SAM recorded after KNO$_3$ additions (full lines from a to d) compared to the blank (dotted line). (**B**) Current at 0.3 V vs KNO$_3$ additions relative to (**A**) (blue dotted line: 10 nA). (**C**) Example of voltammograms of DDT-SAM recorded upon exposure to increasing PFOA concentrations from 50 to 1000 nM (full lines from a to f) compared to the blank (dotted line), inset: baseline corrected voltammograms. (**D**) Current at 0.3 V vs PFOA concentration relative to (**C**). (**E**) Voltammograms of DDT-SAM recorded after KNO3 additions (full lines) compared to the blank (dotted line). (**F**) Current at 0.3 V vs KNO3 additions relative to (**E**) (blue dotted line: 10 nA).*

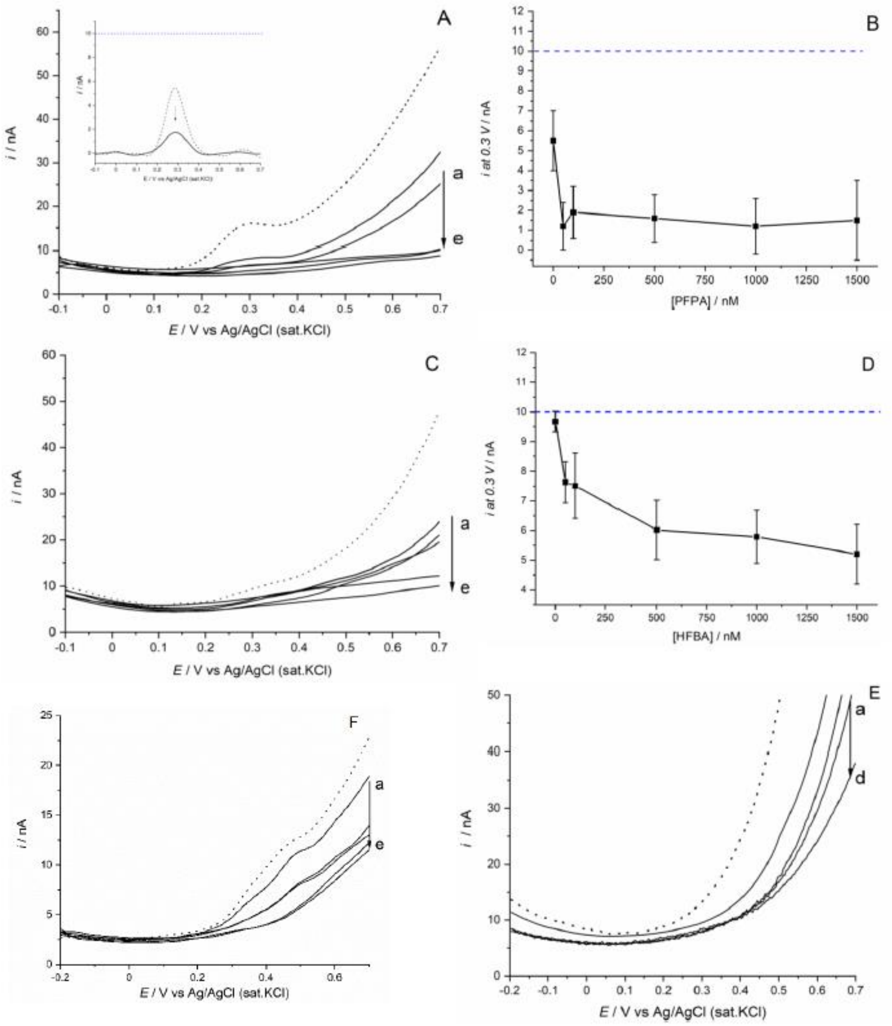

Figure A8.5. Experiments ordered FDT-SAM: *Examples of the results obtained after incubating FDT-SAM with short chain PFAS: (**A**) Voltammograms of FDT-SAM recorded upon exposure to increasing PFPA concentrations from 50 to 1500 nM (**a** to **e**) (full lines) compared to the blank (dotted line), inset: baseline corrected voltammograms of blank and 50 nM. (**B**) Current at 0.3 V vs PFPA concentration relative to **A**). (**C**) Voltammograms of FDT-SAM recorded upon exposure to increasing HFPO-DA concentrations from 50 to 1500 nM (a to e) (full lines) compared to the blank (dotted line). (**D**) Current at 0.3 V vs HFPO-DA concentration relative to **C**). (**E**) Voltammograms of DDT-SAM recorded in increasing PFPA concentration from 50 to 1000 nM (a to d) (full lines) compared to the blank (dotted line). (**F**) Voltammograms of DDT-SAM recorded upon exposure to increasing HFBA concentration from 50 to 1500 nM (a to e) (full lines) compared to the blank (dotted line).*

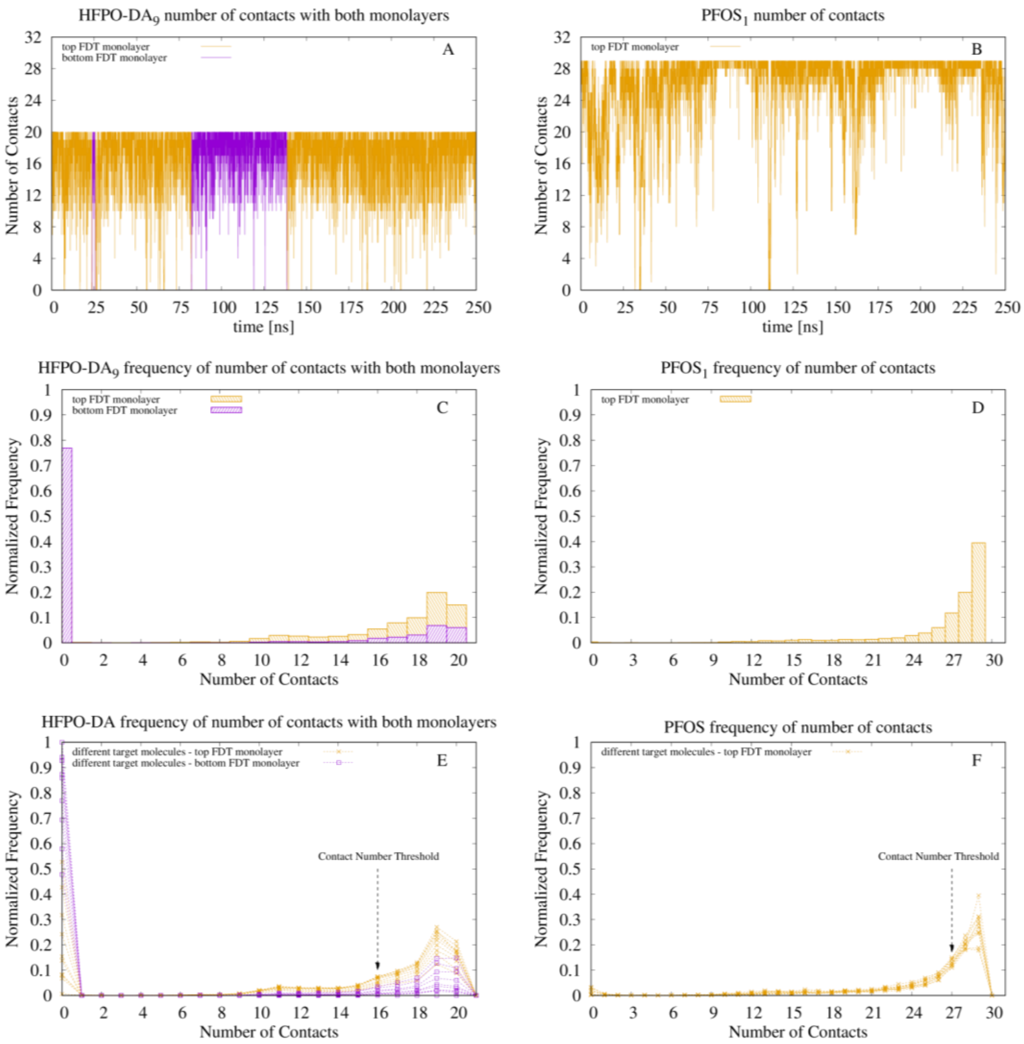

***Figure A8.6*. *Ordered FDT-SAM*:** *Number of contacts and their normalized frequency between the target molecule's atoms and the atoms of the FDT-SAM monolayer. We defined two atoms to be in contact if their distance is within 0.6 nm. (**A**) Number of contacts for a single HPFO-DA molecule versus simulation time; (**B**) number of contacts for a single PFOS molecule versus simulation time; (**C**) normalized frequency of number of contacts for a single HPFO-DA molecule; (**D**) normalized frequency of number of contacts for a single PFOS molecule; (**E**) normalized frequency of number of contacts for all HPFO-DA molecules simulated; the figure shows the threshold of the number of contacts used to compute the interaction energy; the value chosen is 16; (**F**) normalized frequency of number of contacts for all PFOS molecules simulated; the figure shows the threshold of the number of contacts used to compute the interaction energy; the value chosen is 27.*

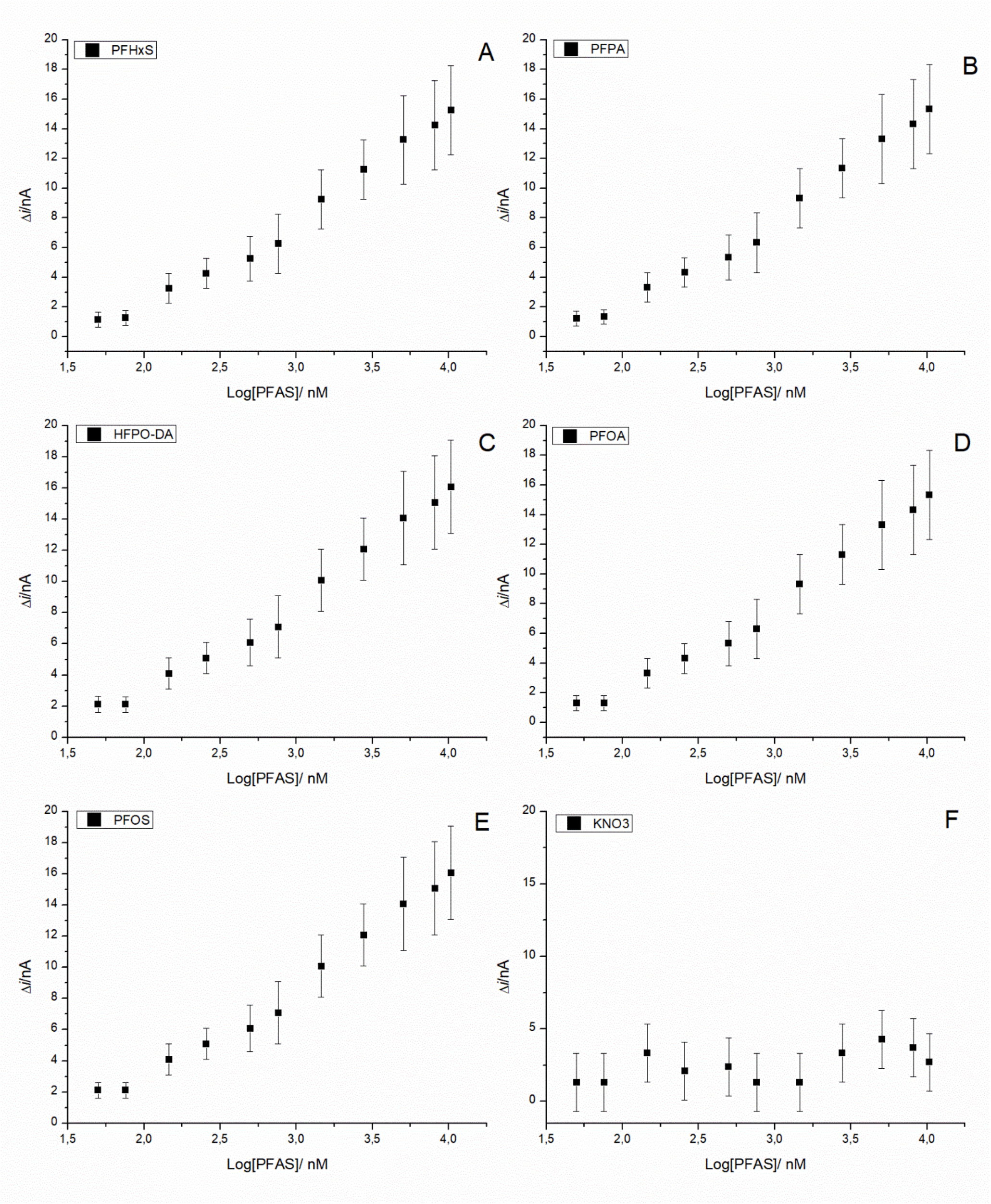

***Figure A8.7. Negative controls of unordered FDT-SAM**: Changes in the E_{pa} current intensities after DDT-SAM incubation with: (**A**) PFHxS, (**B**) PFPA, (**C**) HFPO-DA, (**D**) PFOA, (**E**) PFOS, (**F**)KNO_3.*

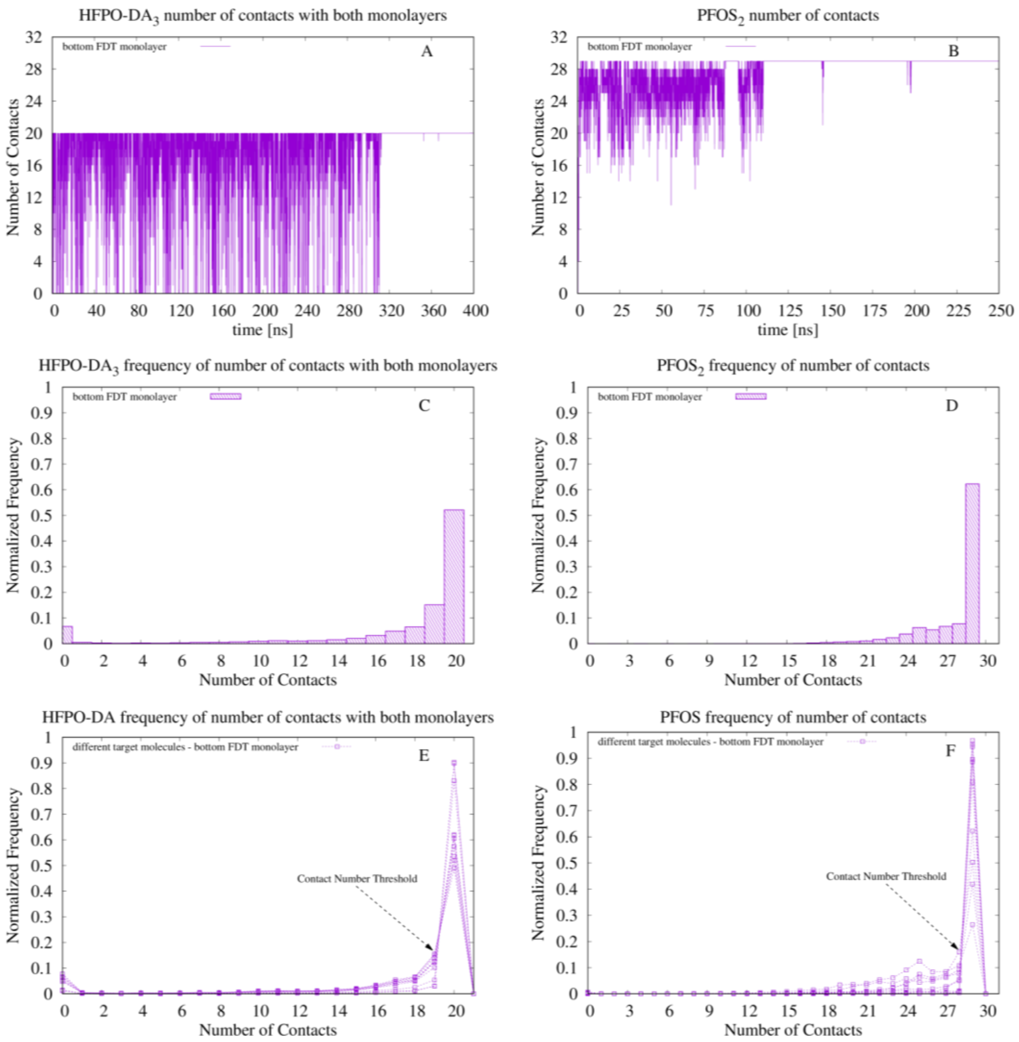

***Figure A8. 8. Unordered FDT-SAM**: Number of contacts and their frequency between the target molecule's atoms and the atoms of the FDT-SAM monolayer. We defined two atoms to be in contact if their distance is within 0.6 nm. (**A**) Number of contacts for a single HPFO-DA molecule versus simulation time; (**B**) number of contacts for a single PFOS molecule versus simulation time; (**C**) normalized frequency of number of contacts for a single HPFO-DA molecule; (**D**) normalized frequency of number of contacts for a single PFOS molecule; (**E**) normalized frequency of number of contacts for all HPFO-DA molecules simulated; the figure shows the threshold of the number of contacts used to compute the interaction energy; the value chosen is 19; (**F**) normalized frequency of number of contacts for all molecule PFOS simulated; the figure shows the threshold of the number of contacts used to compute the interaction energy; the value chosen is 28.*

|9

Final Remarks and Perspectives

This joint PhD project, ***PFASensing***, was entirely dedicated to the concept design of electrochemical and optical, bio- and biomimetic strategies for the quantitative or semi-quantitative determination of per- and polyfluorinated alkyl substances. The **endless evolution of PFAS** and urgent need of the development of analytical tools for monitoring were the starting point of this project. Indeed, in its proof-of-concept and case-studies, *PFASensing* does not aim to develop finalized sensors for PFAS detection but to scout for new sensing ways to face PFAS pollution, particularly in respect to water matrices. We investigated **three main ways**.

The **first way** focused on the development of novel electrochemical and optical protein-based biosensors starting from the idea of transposing toxicological findings in bioreceptor design. Globins, particularly neuroglobin, were first tested combining an electrochemical study with native mass spectroscopy-based screening. The results confirmed PFOS and PFOA capability to alter globins functionalities, even though these proteins resulted unsuitable for application as bioreceptors (**Chapter 2**). Delipidated human serum albumin (dhSA) was more promising in this respect. Prior of application in sensing, the binding kinetics, mechanism and sites as well as the complex stoichiometry and stability of albumin:PFOA complexes were elucidated within a complete multi-analytical study (**Chapter 3**). The results obtained confirmed that dhSA has all the characteristics required for being applied as bioreceptor for PFOA sensing. This study underlined the importance of an in-depth understanding of the analyte-bioreceptor interactions in different conditions. Daems *et al.*[1] stated that the characterisation of a ligand-aptamer complexes depends deeply on the working conditions (in solution or at a confined surface) suggesting the use of balanced multi-analytical approaches. Our study was applying this concept also to ligand-protein characterisation.

Afterwards dhSA was successfully applied in the design of an impedimetric label-free biosensor (**Chapter 4**). The protein bioreceptor was immobilized at screen-printed electrodes previously modified via electropolymerisation, developing a method compatible with EDC/NHS chemistry. We offered a straightforward method from bioreceptor covalent immobilization at screen-printed electrode. Despite the limited performances of the platform in terms of sensitivity, the concept design was found to be promising. Furthermore, the possibility of further combining albumin as a bioreceptor within a redox-mediated voltammetric detection strategy was tested and inspired again by nature. (**Chapter 5**). Here, the haem group, whose interaction with albumin depends on the protein conformation, was applied. However, the complexity of the equilibria at

---

[1] Elise Daems, Giulia Moro, Rui Campos, Karolien De Wael, TrAC Trends in Analytical Chemistry,Volume 142,2021

stake did not allow to develop a complete sensing strategy. In this preliminary phase of the study, we focused on the correlation between the changes in the hemin electrochemical signal and the presence/absence of dhSA:PFOA complex in solution. Again, we based our conceptualisation on previous biological findings showing how an interdisciplinary approach can help finding innovative solutions. Even though PFOA sensing with hemin probe seems difficult to combine with a real analytical context (oxygen-free conditions might be difficult to obtain *in-situ* with portable devices), the development of a sensor which combines nonelectroactive target and bioreceptor with an electroactive probe paved the way for the design of a new generation PFAS sensors.

PFASensing showed also the importance to test and compare different sensing platforms overcoming the common dichotomy between electrochemical and optical sensors. To this aim, dhSA was applied as biorecognition layer at D-shaped optical fibers developing a Lossy-Mode-Resonance-based label-free platform (**Chapter 6**). This proof-of-concept study is one of the first examples in which this kind of optical sensor is used for the determination of small-molecules, such as PFOA. The results confirmed the possibility to develop dhSA:PFOA optical as well as impedimetric sensors. These two platforms (optical and impedimetric one) should be further combined in a unique double-signal sensing platform following the innovative perspective of integrated sensors offered by Śmietana *et al.*[2]

The **second way** worked on the *redesign* of existing sensing platforms to move toward miniaturized and portable devices able to promote rapid advances in the TOT steps. *Redesign* is still an open challenge and its one of the main reasons why thousands of sensors never reached the market. As a case-study, we selected an existing molecularly imprinted polymers-based electrochemical sensor for PFOS detection (**Chapter 7**). Our redesign process gets soon stacked due to the scarce reproducibility of our results. This obstacle stimulated our interest in finding the reasons of the poor reproducibility and to develop a protocol for the surface characterization of the screen-printed electrode used. The presence of a fluorinated template molecule (PFOS) allowed us to visualise the MIP distribution. We deduced that the high roughness of screen-printed electrodes surface did not allow a homogenous deposition of the MIP modifiers. The results of this study emphasise the need of an in-depth comprehension of the possible redesign obstacles to avoid time-consuming trial-error approaches. Indirectly, we suggest the importance of investing time and energies even in this kind of *redesign processes* to stimulate the development and optimization of devices with real applicability.

---

[2] Mateusz Śmietana, Marcin Koba, Petr Sezemsky, Katarzyna Szot-Karpińska, Dariusz Burnat, Vitezslav Stranak, Joanna Niedziółka-Jönsson, Robert Bogdanowicz, Biosensors and Bioelectronics,Volume 154,(2020), 1129.

The **third way** was based on a preliminary study for the design of class selective screening tools. Fluorinated self-assembled monolayers with different architectures were tested aiming to take advantage from fluorophilic interactions for PFAS screening. The **promising results match the requirements of the market**: we should move toward the design of class-selective sensing platform for the preliminary screening of the total amount of PFAS in water, because single-substance detection devices are not able to follow the fast growth of this class of contaminants and do not match the needs of the market.

PFASensing is still ongoing: an open-challenge for future generation to assure environmental monitoring and biomonitoring, to face ecocrimes and PFAS water pollution in our territories and on a global scale.

Appendix I

Analytical Techniques

I.1 Electrochemical Techniques

I.1.1 Voltammetry

Electrochemical techniques are widely proposed for the quantitative or semi-quantitative screening of biomarkers [1, 2], neurotransmitters [3], drugs [4, 5], **environmental contaminants** [6, 7], or hazardous food compounds or additives [8, 9], with promising applications in point-of-care diagnostics and on-site monitoring [10]. The advantages of electrochemical sensors can be attributed to the sheer simplicity of converting a chemical reaction into an electrical signal, and the possibility to obtain highly sensitive and selective responses in a short timeframe with portable, miniaturized, and user-friendly devices. Numerous electrochemical detection strategies can be used online [11], offline [12], or in vivo [13, 14]: from indirect or mediated detection [15] to direct electrochemistry.

The electrochemical behaviour of small molecules can be investigated by **voltammetric techniques**, such as linear sweep voltammetry (**LSV**), cyclic voltammetry (**CV**), differential pulse voltammetry (**DPV**), and square wave voltammetry (**SWV**). Even the most basic potentiostat today is able to perform these voltammetric analyses with high sensitivity coupled with easy-to-use software and integrated data analysis.

CV and LSV are dynamic electrochemical measurements, in which a potential is scanned linearly in function of time [19] (**Figure I.1a,b**). In LSV, a fixed potential range is scanned from a lower to an upper potential (or vice versa) while CV is obtained by scanning/sweeping in between two potential values (i.e., scanning from one potential to another and back). CV is typically applied in a first screening to have an overview of the oxidation and reduction processes involved and their reversible/quasi-reversible or irreversible nature [20]. For these reasons, CV (and LSV to a lesser extent) studies are often carried out to characterize the electroactive behaviour of an analyte [21] or newly synthesized compounds [22, 23] (Fig. 3a, b) and to evaluate its applicability in preliminary electrochemical studies for sensor design [25], as well as in field deployable devices [26]. Very often, the complexity of the voltammetric pattern of one compound required an extensive CV study of the anodic and cathodic regions to correlate the different redox processes to the functionalities of the target. Recently, even in vivo detection of neurotransmitters was possible using fast-scan cyclic voltammetry (FSCV) [28].

LSV with the corresponding "reversal technique" CV are definitively the most frequently used voltammetric techniques. This is true when a qualitative approach to the study of the redox characteristics of one analyte in solution is pursued, as well as when a quantitative study of the electrode mechanism and even the evaluation of the relevant thermodynamic and kinetic parameters are faced, and also when electroanalytical quantitative information is sought. In all the voltammetric techniques the overall current flowing is given by the sum of three components: the faradic, the capacitive and the background one. Due to capacitive background interferences present in linear sweep voltammetry, pulsed techniques such as DPV and SWV, are usually preferred for more sensitive detections. In DPV, a series of potential pulses is applied and every potential pulse has a fixed small amplitude superimposed on a changing base potential [29], as shown in **Figure I.2c**. The potential is sampled at two points, just before the start and at the end of the pulse; this helps to discriminate between the faradaic current (resulting from redox reactions of electrochemical active compounds) and capacitive current (the background noise). This current difference is plotted in function of the base potential. DPV is largely applied in sensing devices, particularly for irreversible systems and to follow slow reaction kinetics (**Figure I.2c**). The comparison of the pattern of different DPV-based analytical methods can show that an in-depth data analysis can provide both analytical and physicochemical information on the system of interest [30]. In SWV, the applied potential waveform is a superimposition of a symmetric square wave perturbation on a staircase potential, as shown in **Figure I.1d**. The current is again sampled twice and its difference is plotted in function of the base potential [31]. In contrast to DPV, SWV is mostly applied to reversible redox reactions and in rapid reaction kinetics systems [32] (**Figure I.2d**). Numerous studies were carried out with SWV [33] combining oxidative and reductive square wave voltammetric scans that are presented as a cyclic voltammograms (**Figure I.1e** and **I.3e**); this protocol, known as cyclic square wave voltammetry (CSWV).

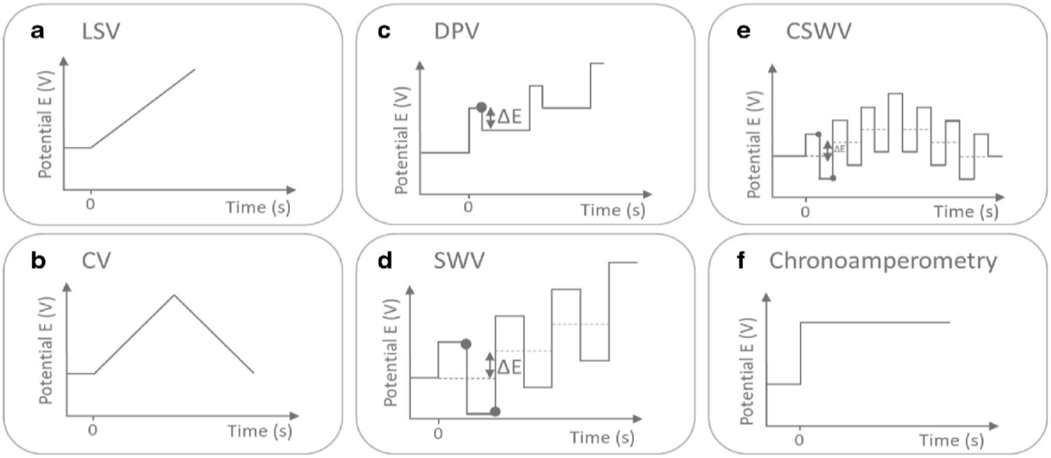

Figure I.1 Perturbation signal for a linear sweep voltammetry (LSV), b cyclic voltammetry (CV), c differential pulse voltammetry (DPV), d square wave voltammetry (SWV), e cyclic square wave voltammetry (CSWV), and f chronoamperometry (CA).

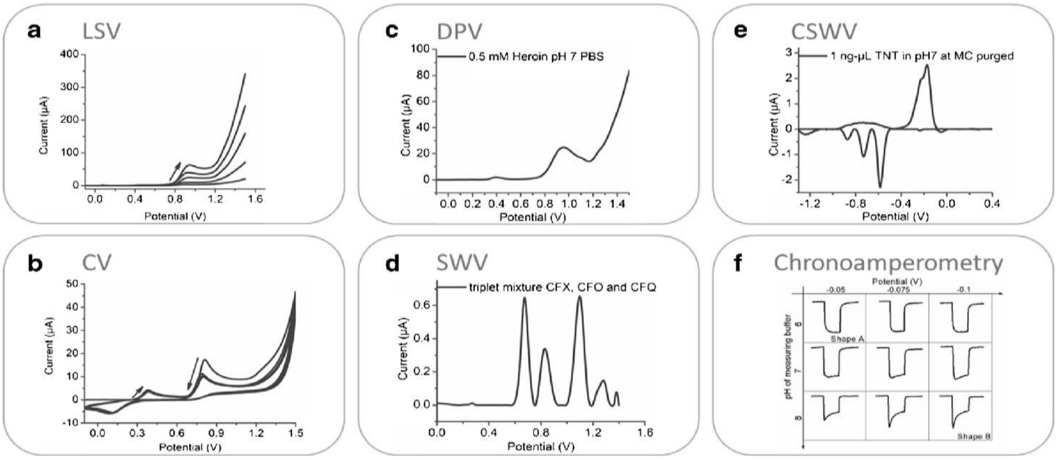

Figure I.2 *Examples of electrochemical fingerprints recorded by a CV, b DPV, c SWV, d CSW, e LSV, and f CA (photo-electrochemistry) [24]. The fingerprints are recorded in the AXES lab.*

I.1.2 Electrochemical Impedance Spectroscopy (EIS)

Since the middle of the 18th century, the Impedance Spectroscopy (IS) technique has been established as a popular theoretical approach to study the electrical properties of conducting materials and their interfaces. However, in the last quarter-century, IS becomes a practical tool that is successfully applied in electrochemistry as an analytical method widely used in many disciplines such as corrosion technology, electrochemistry, metallurgy, hydrodynamic, chemistry, biology, physics, mechanical, and medicine. **Electrochemical Impedance Spectroscopy (EIS)** is an electrochemical technique to measure the impedance of a system in dependence of the **AC potential frequency**. One reason for its popularity is that EIS allows the influences of different components in an electrochemical process to be separated, which means that the contribution of the electron transfer resistance, double layer capacity, etc. can be identified. Another reason is that EIS is very **surface sensitive**, which makes visible many changes that other techniques do not see, such as surface changes due to protein adsorption, changes in polymer layers due to swelling, or penetration of corrosion protection layers. These two main reasons made EIS very interesting for analytical electrochemistry, because molecules can be detected without a redox active marker.

While resistance is the ratio of voltage or potential and current for a DC (direct current) system, the **impedance** is the ratio of voltage or potential and **current for AC** (alternating current) systems. The wave nature makes it necessary to define the impedance with two parameters. If you consider the two periodic waves of current and voltage, the waves have the same frequency, because one wave causes the other. There is a constant time shift between the two waves, which is called the phase shift Φ. Its unit is degrees (°), because usually waves are considered to be vectors in a polar coordinate system or a sine function. The total impedance is the ratio of the potential amplitude and the current amplitude. The resulting impedance is a complex number. This number can be expressed in the complex plane in polar coordinates by using *Z* as the length of the vector and *Φ* as the angle. With the common knowledge about calculations for complex numbers the impedance can also be expressed as the real part of the impedance *Z′*, which is the resistance, and the imaginary part *Z′′*.

The two notations are the origin of the two most popular plots for impedance spectra: the **Bode plot** and **Nyquist plot**. A potentiostat measures the impedance by applying a potential wave to the working electrode and records the resulting current wave. From these two waves the potentiostat calculate *Z, Φ, Z′* and *Z′′*. The spectrum is made by measuring these parameters for potential waves with different frequencies (more details below).

Molecules can be measured with small *AC* amplitude of voltage as a function of the frequency without altering their properties. Systems such as solid–solution interface leading allow the ion charge transfer, conduction and electron flow that is governed by the free energy of the chemical reactions occurring at the interface region (named *double layer*), as is shown in the model of **Figure I.3**. The electrical properties of the double layer can be measured by an electrical equivalent circuit, considering that the double layer behaves as pure capacitor C_{dl} (ions charge) and the flow of ions through the metal surface is viewed as a resistance R_{ct} of current, in accordance with Ohm's law.

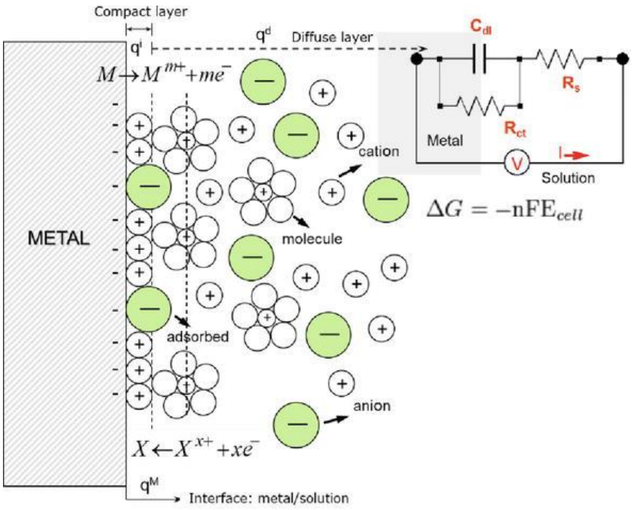

Figure I.3 *Schematic simulation of the electrochemical interface metal/electrolyte (electrical double layer) and its representative equivalent electrical circuit EEC model.* R_s *is the solution resistance,* R_{ct} *is the charge transfer resistance,* C_{dl} *is the capacity of the double layer.*

In general, EIS allows separating the contribution response of different components in terms of the resistance of electron charge transfer, double layer capacitance, solution resistance, inductance, and other parameters, where several electrochemical processes are proceeding at a different reaction rate.

I.1.3 AC Circuit and Representation of Complex Impedance Values

I.1.3.1 *Impedance Definition: Concept of Complex Impedance*

Almost everyone knows about the concept of electrical resistance. It is the ability of a circuit element to resist the flow of electrical current. Ohm's law (equation 1) defines resistance (*R*) in terms of the ratio between voltage, *E*, and current, *I*.

$$R = \frac{E}{I} \tag{1}$$

This is a well-known relationship, but is limited to only one circuit element, the ideal resistor, which has several simplifying properties: it follows Ohm's Law at all current and voltage levels, its resistance value is independent of frequency, AC current and voltage signals though a resistor are in phase with each other. However, the real world contains circuit elements that exhibit much more complex behaviour, forcing us to abandon the simple concept of resistance, and use **impedance**, a more general circuit parameter. Like resistance, impedance is a measure of the ability of a circuit to resist the flow of electrical current, but unlike resistance, it is not limited by the simplifying properties indicated above. As mentioned in the previous section, **electrochemical impedance** is usually measured by applying an AC potential to an electrochemical cell and then measuring the current through the cell. The application of a sinusoidal potential excitation results in a response that is an AC current signal. This current signal can be analysed as a sum of sinusoidal functions (a Fourier series). Electrochemical impedance is normally measured using a **small excitation** signal. This is done so that the cell's response is pseudo-linear. In a linear (or pseudo-linear) system the current response to a sinusoidal potential will be a sinusoid at the same frequency but shifted in phase.

The excitation signal, expressed as a function of time, has the form:

$$E_t = E_0 sin\,(wt) \tag{2}$$

where E_t is the potential at time t, E_0 is the amplitude of the signal, and ω is the radial frequency. The relationship between ω (expressed in rad /s) and f (expressed in Hz) is:

$$\omega = 2\pi f \tag{3}$$

In a linear system the response signal, I_t, is shifted in phase (Φ) and has a different amplitude than I_0.

$$I_t = I_0\, sin(\omega t + \emptyset) \tag{4}$$

An expression analogous to Ohm's Law allows us to calculate the **impedance** of the system as:

$$Z = \frac{E_t}{I_t} = \frac{E_0 sin\,(\omega t)}{I_0 sin(\omega t+\emptyset)} = Z_0 \frac{sin(\omega t)}{sin(\omega t+\emptyset)} \tag{5}$$

The impedance is therefore expressed in terms of a magnitude, Z_o, and a phase shift, Φ. Considering Euler's relationship,

$$exp(j\emptyset) = cos\emptyset + jsin\emptyset \tag{6}$$

it is possible to express the impedance as a complex function. The potential is described as,

$$E_t = E_0\, exp(j\omega t) \tag{7}$$

and the current response as

$$I_t = I_0 exp(j\omega t - \phi) \tag{8}$$

The impedance is then represented as a complex number,

$$Z(\omega) = \frac{E}{I} = Z_0 exp(j\phi) = \; Z_0(cos\phi + jsin\phi) \tag{9}$$

The expression for *Z(ω)* is composed of a **real** and an **imaginary part**. If the real part is plotted on the X-axis and the imaginary part is plotted on the Y-axis of a chart, we get a **Nyquist Plot** (see **Figure I.4A**). In this plot the Y-axis is negative and each point on the Nyquist Plot is the impedance at one frequency. In this figure the low frequency data are on the right side of the plot and the high frequencies are on the left.

On the Nyquist Plot the impedance can be represented as a vector (arrow) of length $|Z|$. The angle between this vector and the X-axis, commonly called the "**phase angle**", is *f (= arg Z)*.

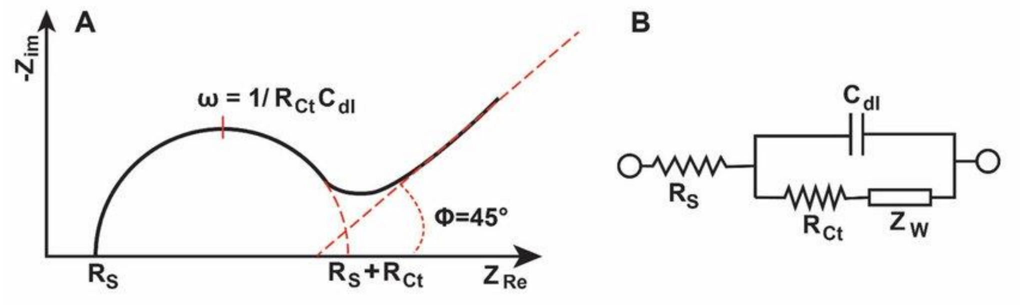

Figure I.4 ***(A)*** *Nyquist plot with impedance vector.* ***(B)*** *Example of the electrochemical equivalent circuit.*

Nyquist plots have one major shortcoming. When you look at any data point on the plot, you cannot tell what frequency was used to record that point. The Nyquist Plot in **Figure I.4A** results from the electrical circuit of **Figure I.4B**. The semicircle is characteristic of a single "**time constant**". Electrochemical impedance plots often contain several semicircles. Often only a portion of a semicircle is seen.

Another popular presentation method is the **Bode Plot**. The impedance is plotted with log frequency on the X-axis and both the absolute values of the impedance ($|Z|=Z_0$) and the phase-shift on the Y-axis. The Bode Plot for the electric circuit of **Figure I.4B** is shown in **Figure I.5**. Unlike the Nyquist Plot, the Bode Plot does show frequency information.

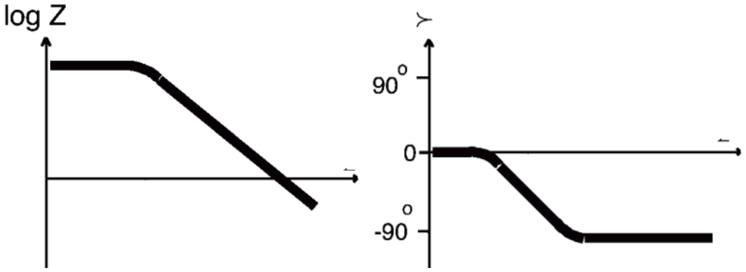

Figure I.5 *Bode plot with one time constant.*

I.1.3.2 Physical Electrochemistry and Equivalent Circuit Elements

I.1.3.2.1 *Electrolyte Resistance*

Solution resistance is often a significant factor in the impedance of an electrochemical cell. A modern three electrode potentiostat compensates for the solution resistance between the counter and reference electrodes. However, any solution resistance between the reference electrode and the working electrode must be considered in the model of the cell. The resistance of an ionic solution depends on the ionic concentration, type of ions, temperature and the geometry of the area in which current is carried. In a bounded area ***A*** and length ***l***, carrying a uniform current, the resistance is defined as,

$$R = \rho \frac{l}{A} \tag{10}$$

ρ is the solution **resistivity** and its reciprocal ***κ*** more commonly used is called the **conductivity** of the solution and its relationship with solution resistance is:

$$R = \frac{1}{k}\frac{l}{A} \quad and \; k = \frac{l}{RA} \tag{11}$$

Unfortunately, most electrochemical cells do not have uniform current distribution through a definite electrolyte area. The major problem in calculating solution resistance concerns determination of the current flow path and the geometry of the electrolyte that carries the current. Fortunately, you usually don't calculate solution resistance from ionic conductance. Instead, you calculate it when you fit experimental EIS data to a model.

I.1.3.2.2 *Double Layer Capacitance*

An **electrical double layer** exists on the interface between an electrode and its surrounding electrolyte. It is formed by ions from the solution adsorbed onto the electrode surface. The charged electrode is separated from the charged ions by an insulating space, often on the order of angstroms. Charges separated by an insulator form a **capacitor**, so a bare metal immersed in an electrolyte will behave like a capacitor. The capacitance for 1 cm^2 of electrode area is estimated to be 20 to 60 µF, even its value depends on many variables, such as electrode potential, temperature, ionic concentrations, types of ions, oxide layers, electrode roughness, impurity adsorption, etc.

I.1.3.2.3 *Polarization Resistance*

Whenever the potential of an electrode is forced away from its open-circuit value that is referred to as **polarization** of the electrode. A polarized electrode can cause electrochemical reactions that generate a current flow at the electrode surface. The intensity of the current is controlled by the kinetics of the reaction and the diffusion of reactants both towards and away from the electrode.

In a cell where there are two, simple, kinetically-controlled reactions occurring, the potential of the cell is related to the current by the following equation:

$$I = I_{corr}\left(e^{\frac{2.303(E-E_{OC})}{\beta_a}} - e^{-\frac{2.303(E-E_{OC})}{\beta_c}}\right) \tag{12}$$

where, I = measured cell current (A), I_{corr} = redox current (A), E_{oc} = open circuit potential (V), β_a = anodic beta coefficient (V/decade), β_c = cathodic beta coefficient (V/decade). Beta coefficients, are also known as **Tafel constants**. Applying a small signal approximation to equation (12), we get:

$$I_{corr} = \frac{\beta_a \beta_c}{2.303(\beta_a+\beta_c)}\left(\frac{1}{R_p}\right) \tag{13}$$

Which introduces a new parameter, R_p, the **polarization resistance**, indicating that is behaves like a resistor.

I.1.3.2.4 *Charge Transfer Resistance*

A resistance is formed by a single, kinetically-controlled electrochemical reaction. In this case we do not have a mixed potential, but rather a single reaction at equilibrium. Consider a redox species in solution in contact with a working electrode to which is applied a potential over the standard potential of the analyte. The charge transfer will begin with a certain speed.

$$Red \rightleftarrows Ox + ne^- \tag{14}$$

The speed depends on the kind of reaction, the temperature, the concentration of the reaction products and the potential. The general relation between the potential and the current (which is directly related with the number of electrons and so the charge transfer via Faradays law) is:

$$i = i_0 \left(\frac{C_0}{C_0^*} exp\left(\frac{\alpha nF\eta}{RT}\right) - \frac{C_R}{C_R^*} exp\left(\frac{-(1-\alpha)nF\eta}{RT}\right) \right) \qquad (15)$$

Where: i_0 = exchange current density; C_O and C_O* = concentration of the oxidized species at the electrode surface and in the bulk respectively; C_R and C_R* = concentration of the reduced species at the electrode surface and in the bulk respectively; η = overpotential (E_{app} - E_{oc}), and the other symbols have the usual meaning. When the concentration in the bulk is the same as at the electrode surface, C_O=C_O* and C_R=C_R*. This simplifies equation (15) into:

$$i = i_0 \left(exp\left(\alpha \frac{nF}{RT}\eta\right) - exp\left(-(1-\alpha)\frac{nF}{RT}\eta\right) \right) \qquad (16)$$

Equation (16) is called the **Butler-Volmer** equation. It is applicable when the polarization depends only on the charge-transfer kinetics. Stirring the solution to minimize the diffusion layer thickness can help minimize concentration polarization. When the overpotential, η, is very small and the electrochemical system is at equilibrium, the expression for the **charge-transfer resistance** changes to:

$$R_{ct} = \frac{RT}{nFi_0} \qquad (17)$$

From this equation the exchange current density can be calculated when R_{ct} is known.

I.1.3.2.5 *Diffusion*

Diffusion also can create an impedance called a **Warburg** impedance. The impedance depends on the frequency of the potential perturbation. At high frequencies, the Warburg impedance is small since diffusing reactants don't have to move very far. At low frequencies, the reactants have to diffuse farther, increasing the Warburg-impedance. The equation for the "infinite" Warburg impedance is:

$$Z_W = \sigma(\omega)^{-1/2}\,(1-j) \qquad (18)$$

On **a Nyquist Plot** the Warburg impedance appears as a diagonal line with a slope of 45°. On a **Bode Plot**, the Warburg impedance exhibits a phase shift of 45°. In equation (18), ***σ*** is the **Warburg coefficient** defined as:

$$\sigma = \frac{RT}{n^2F^2A\sqrt{2}}\left(\frac{1}{C_O^*\sqrt{D_O}} + \frac{1}{C_R^*\sqrt{D_R}}\right) \qquad (19)$$

In which, ω = radial frequency; *Do* and *DR* = diffusion coefficient of the oxidizing and reducing, respectively.

This form of the Warburg impedance is only valid if the diffusion layer has an infinite thickness. But quite often this is not the case. If the diffusion layer is bounded (as in thin-layer cell or coated samples), the impedance at lower frequencies no longer obeys the equation above. Instead, it has the form:

$$Z_O = \sigma\omega^{-1/2}(1-j)\, tanh\left(\delta\left(\frac{j\omega}{D}\right)^{1/2}\right) \tag{20}$$

With, δ = Nernst diffusion layer thickness; D = an average value of the diffusion coefficients of the diffusing species.

This more general equation is called the **"finite" Warburg**. For high frequencies where $\omega \rightarrow \infty$, or for an infinite thickness of the diffusion layer where $\delta \rightarrow \infty$, $tanh(\delta(j\omega/D)^{1/2}) \rightarrow 1$ and equation (18) simplifies to the infinite Warburg impedance.

I.1.3.2.6 *Coating Capacitance*

A capacitor is formed when two conducting plates are separated by a non-conducting media, called the dielectric. The value of the capacitance depends on the size of the plates, the distance between the plates and the properties of the dielectric. The relationship is,

$$C = \frac{\varepsilon_0 \varepsilon_r A}{d} \tag{21}$$

With, ε_0 = permittivity of free space (according to NIST is the electric constant); ε_r = dielectric constant); A = surface area of one plate; d = distance between the two plates. Whereas the permittivity of free space is a physical constant, the dielectric constant depends on the material. There is a large difference between the dielectric constant of water and that of an organic coating. The capacitance of a coated substrate changes as it absorbs water. EIS can be used to measure that change.

I.1.3.2.7 *Constant Phase Element*

Capacitors in EIS experiments often do not behave ideally. Instead, they act like a **constant phase element (CPE)** as defined below. The impedance of a capacitor can be expressed as:

$$Z_{CPE} = \frac{1}{(j\omega)^{\alpha} Y_0} \tag{22}$$

Where Y_0 = the capacitance; α = an exponent equal to 1 for a capacitor. For a constant phase element, the exponent α is less than one. The "double layer capacitor" on real cells often behaves like a CPE, not a capacitor. While several theories (surface roughness, “leaky” capacitor, non-uniform current distribution, etc.) have been proposed to account for the non-ideal behavior of the double layer, it is probably best to treat α as an empirical constant with no real physical basis.

I.2. X-Ray Techniques

I.2.1 X-Ray Crystallography

X-ray crystallography is a scientific field concerned with revealing the structure of matter at the atomic level. It is a method applied for various materials in the crystallized state to determine the arrangement of atoms within a crystal. The essential method involves exposing a crystallised sample of a molecule to x-rays, usually with an instrument called an X-ray camera. The underlying principle is that the crystalline atoms cause a beam of X-rays to diffract into many specific directions. Diffraction refers to the complicated constructive and destructive interference patterns that are generated when electromagnetic radiation, such as X-rays or light, interacts with matter. As crystals represent the form of solid matter in which a simple atomic arrangement repeats itself symmetrically to fill space, the pattern of diffracted X-rays that emerge after passing through such a material exhibits the discrete regular spacing and symmetry properties inherent to the crystal. By measuring the angles and intensities of the diffracted beams, it is possible to produce a photograph showing the pattern of diffracted X-rays as they passed through the crystal, from which scientists can then visually map its molecular structure using specific software.

This electron density image, the mean positions of the atoms in the crystal can be determined, as well as their chemical bonds, their disorder, and various other information. X-ray crystallography revealed the structure and function of many biological molecules, including vitamins, drugs, proteins, and nucleic acids, such as DNA. Advances in image reconstruction technology have made X-ray crystallography useful for the structural analysis of much larger complexes, such as viral particles. The major shortcoming of X-ray crystallography is that in some cases it is difficult to obtain a crystal of the molecules, which is a prerequisite for X-ray crystallography. Another shortcoming is that X-ray crystallography generally requires placing the samples in non-physiological environments, which can occasionally lead to functionally irrelevant conformational changes.

Crystallographic approaches have two key advantages over other techniques. First, the three-dimensional structure of the protein:ligand complex is, by definition, available from the outset, and second, that soaking of crystals can be performed using very high concentrations of compound (to the extent that some crystal-soaking experiments have been described as “slurries”). This allows the observation of very weakly binding compounds. Moreover, advances in technology over the past decades have reduced the experimental work significantly, such that screening a fragment library by crystallography is no longer a significant obstacle.

I.2.2 Small-Angle X-Ray Scattering (SAXS)

Small-angle X-ray scattering (**SAXS**) is an analytical technique that measures the intensities of X-rays scattered by a sample as a function of the scattering angle. Measurements are made at very small angles, typically in the range of **0.1 - 5 deg**. From Bragg's law it is understood that with decreasing scattering angle, increasingly larger structural features are being probed. A SAXS signal is observed whenever a material contains structural features on the length scale of nanometers, typically in the range of **1-100 nm**. On the other hand, wide-angle X-ray scattering (**WAXS**), also known as wide-angle X-ray diffraction (**WAXD**), probes for structures in the material on the much smaller length scale, that of **interatomic distances**. Small angle X-ray scattering and wide-angle X-ray scattering (SAXS and WAXS) are complementary techniques. In this work of thesis only SAXS was used. The experimental setup for SAXS measurements uses transmission geometry. X-ray optics that creates a very narrow, yet highly intense incident X-ray beam is essential. This is because the comparatively weak scattering signal from the sample has to be measured in the immediate vicinity of the direct beam. It is also essential to use a detector which has a high linearity, a high dynamic range and negligible intrinsic noise. A high spatial resolution of the detector is beneficial for high-end SAXS instrumentation, because it allows a good low-angle resolution to be achieved even with a compact experimental setup.

SAXS is a fundamental method for structure analysis of condensed matter. First X-ray applications date back to the late nineteen thirties, when the main principles of SAXS were developed in the seminal work of A. Guinier following his studies of metallic alloys. The applications cover various fields, from metal alloys to synthetic polymers in solution and in bulk, biological macromolecules in solution, emulsions, porous materials, nanoparticles, etc. The samples may be solid objects, powders, gels or liquid dispersions, and they may be amorphous, crystalline or semi-crystalline. Measurements require only minimal sample preparation and can often be done in situ. Being an ensemble technique, SAXS probes for structural features averaged over a large sample volume. Typical samples that can be studied by Small-angle X-ray scattering include: biomacromolecules, liquid nanoparticle dispersions /colloids, nanopowders, nanocomposites, polymers, surfactants, etc. From the evaluation of the measured scattering profiles a wide range of information about the structure and properties of the materials can be obtained, such as: nanoparticle size distribution, particle shape, particle structure (i.e., core-shell), specific surface area, agglomeration behaviour of nanoparticles, pore size distribution, liquid crystalline phases. SAXS is a tool that is useful both in R&D for the development of new materials.

I.3 Isothermal Titration Calorimetry (ITC)

Isothermal Titration Calorimetry (ITC) is a technique used in quantitative studies of a wide variety of biomolecular interactions. It works by directly **measuring the heat** that is either released or absorbed during a **biomolecular binding event**. ITC is the only technique that can simultaneously determine all binding parameters in a single experiment. Requiring no modification of binding partners, either with fluorescent tags or through immobilization, ITC measures the **affinity of binding partners** in their **native states**.

Measuring heat transfer during binding enables accurate determination of binding constants ($\boldsymbol{K_D}$), reaction stoichiometry (***n***), enthalpy ($\boldsymbol{\Delta H}$) and entropy ($\boldsymbol{\Delta S}$). This provides a complete thermodynamic profile of the molecular interaction. ITC goes beyond binding affinities and can elucidate the mechanisms underlying molecular interactions. This deeper understanding of structure-function relationships enables more confident decision making in hit selection and lead optimization.

When binding occurs, heat is either absorbed or released and this is measured by the sensitive microcalorimeter during gradual titration of the ligand into the sample cell containing the biomolecule of interest.

In the microcalorimeter there are two cells in the same temperature, one of which contains water and acts as a reference cell, the other contains the sample. The heat sensing devices detect temperature difference between the cells when binding occurs and give feedback to the heaters, which compensate for this difference and return the cells to equal temperature. The ligand is loaded into a syringe which sits in a very accurate injection device. If there is a binding of the ligand to the protein, heat changes of a few millionths of a degree Celsius are detected and measured. As the first injection is made, the microcalorimeter measures all heat released until the binding reaction has reached equilibrium. The quantity of heat measured is in direct proportion to the amount of binding. The molar ratio between the ligand and protein is gradually increased through a series of ligand injections. The protein gets more and more saturated, less binding of the ligand occurs and the heat change starts to decrease until ultimately the sample cell contains an excess of ligand versus protein, bringing the reaction towards saturation.

The area of each peak is then integrated and plotted versus the molar ratio of ligand to protein. The resulting isotherm can be fitted to a binding model from which the affinity (K_D) is derived. The molar ratio at the centre of the binding isotherm gives us the reaction stoichiometry. The enthalpy (ΔH) is also derived directly from the isotherm and is the amount of heat released per mole of ligand bound. This means that a single ITC experiment delivers a wealth of information about the binding reaction which helps understand the nature of the interaction and explore the thermodynamic drivers. ITC is widely used even in competition study, to compare the affinity of different ligands.

I.4 Mass Spectrometry

Mass spectrometry (MS) is an analytical technique that separates ionized particles such as atoms, molecules, and clusters by using differences in the ratios of their charges to their respective masses (mass/charge; m/z), and can be used to determine the molecular weight of the particles. MS is a powerful analytical technique used to quantify known materials, to identify unknown compounds within a sample, and to elucidate the structure and chemical properties of different molecules. The complete process involves the conversion of the sample into gaseous ions, with or without fragmentation, which are then characterized by their mass to charge ratios (m/z) and relative abundances.

This technique basically studies the effect of ionizing energy on molecules. It depends upon chemical reactions in the gas phase in which sample molecules are consumed during the formation of ionic and neutral species. In the basic experiment, a gaseous sample is bombarded with high energy electrons which cause one or more electrons to be ejected on impact. A magnetic field is used to separate the ions by their masses. A number of MS techniques have been developed to deal with a range of sample types. Molecular MS is used to characterise a broad range of compounds. The surfaces of materials may also be studied with MS techniques using secondary ion MS. A form of atomic MS, ICP–MS, has emerged in recent years for the identification of elements.

Analysis of Biomolecules using Mass Spectrometry

MS is fast becoming an indispensable field for analysing biomolecules. Till the1970s, the only analytical techniques which provided similar information were electrophoretic, chromatographic or ultracentrifugation methods. The results were not absolute as they were based on characteristics other than the molecular weight. Thus, the only possibility of knowing the exact molecular weight of a macromolecule remained its calculation based on its chemical structure.

The development of desorption ionization methods based on the emission of pre-existing ions such as plasma desorption (PD), fast atom bombardment (FAB) or laser desorption (LD), allowed the application of mass spectrometry for analyzing complex biomolecules.

I.5 Molecular Spectroscopic Techniques

Spectroscopy is the analysis of electromagnetic radiation absorbed, emitted or scattered by molecules or atoms as they undergo transitions between energy levels. Different types of spectroscopic techniques using radiation from different regions of the electromagnetic spectrum are used to investigate different magnitudes of energy level separation, which can give information about the composition and structure of the material under investigation.

Molecular spectroscopy involves rotational, vibrational and electronic transitions. The characteristic spectral frequencies associated with each molecule mean that spectroscopy can be used to identify and characterise many different materials. In this work of thesis two molecular spectroscopic techniques were applied: **infrared spectroscopy** which utilises infrared radiation to cause the excitation of vibrations of bonds in molecule and can be applied to a wide range of material; and **UV-visible spectroscopy** which utilises the radiation in the UV and visible regions, which involves transitions in the electronic energy levels of the bonds of a molecule.

Infrared spectroscopy (IR) is a technique based on the **vibrations of the atoms of a molecule** [Derrick *et al*., 1999; Stuart, 2004]. An infrared spectrum is commonly obtained by passing infrared radiation through a sample and determining what fraction of the incident radiation is absorbed at a particular energy. The energy at which any peak in an absorption spectrum appears corresponds to the frequency of a vibration of a part of a sample molecule. For a molecule to show infrared absorptions it must possess a specific feature: an electric dipole moment of the molecule must change during the vibration. This is the selection rule for infrared spectroscopy. Vibrations can involve either a change in bond length (stretching) or bond angle (bending). Some bonds can stretch in-phase (symmetrical stretching) or out-of-phase (asymmetric stretching). If a molecule has different terminal atoms, then the two stretching modes are no longer symmetric and asymmetric vibrations of similar bonds, but will have varying proportions of the stretching motion of each group known as coupling. There will be many different vibrations for even fairly simple molecules. The complexity of an infrared spectrum arises from the coupling of vibrations over a large part of or over the complete molecule and such vibrations are called skeletal vibrations. Bands associated with skeletal vibrations are likely to conform to a pattern or fingerprint of the molecule as a whole, rather than a specific group within the molecule.

Fourier-transform infrared spectroscopy (**FTIR**), both in transmission and in attenuated total reflectance (**ATR-FTIR**) mode, was employed in this thesis. FTIR (in particular in the mid-IR region) is an extremely widely employed technique mainly thanks to its highly specific instrumental response, directly dependent on the vibrational properties of the functional groups in the sample and therefore uniquely linked to its molecular composition.

Reflectance techniques may be used in the case when the surface properties are of interest. Attenuated total reflectance (**ATR**) spectroscopy utilises the phenomenon of total internal reflection. A beam of radiation entering a crystal will undergo total internal reflection when the angle of incidence at the interface between the sample and crystal is greater than the critical angle. The critical angle is a function of the refractive indices of the two surfaces. The beam penetrates a fraction of a wavelength beyond the reflecting surface and when a material that selectively absorbs radiation is in close contact with the reflecting surface, the beam loses energy at the wavelength where the material absorbs. The resultant attenuated radiation is measured and plotted as a function of wavelength by the spectrometer and gives rise to the absorption spectral characteristics of the sample. The depth of penetration in ATR is a function of wavelength, the refractive index of the crystal and the angle of incident radiation. As a consequence, the relative intensities of the infrared bands in an ATR spectrum will appear different to those observed in a transmission spectrum; the intensities will be greater at lower wave number values. The crystals used in ATR cells are made from materials that have low solubility in water and are of a very high refractive index. Such materials include zinc selenide (ZnSe), germanium (Ge) and thallium/iodide (KRS-5).

UV-visible spectrophotometers are used to examine electronic transitions associated with absorptions in the UV (200–400 nm) and visible (400–800 nm) regions of the electromagnetic spectrum [Anderson *et al., 2004; Denney and Sinclair, 1991; Field et al., 2002; Harwood and Claridge, 1997; Skoog and Leary, 1992].* The energies associated with these regions are capable of promoting outer electrons of a molecule from one electronic energy level to a higher level. Although many electronic transitions are allowed, if the orientation of the electron spin does not change and if the symmetry changes during the transition, it is not allowed. However, 'forbidden' transitions may still occur due to symmetry considerations and give rise to weak absorptions.

The types of transitions that result in UV-visible absorptions consist of the excitation of an electron from the highest occupied molecular orbital (usually of non-bonding p or bonding π orbital) to the next lowest unoccupied molecular orbital (an anti-bonding π^* or σ^* orbital). It is important to be aware that UV-visible spectra are very sensitive to differences in solvent, pH and conjugation. Solvent type is a significant factor as solvent electrons have the ability to stabilise the excited state of a molecule. This results in a change in the difference between the electronic energy levels of a molecule and, hence, a shift in the wavelength of the associated absorption band. The more conjugation appearing in a molecule, the greater the intensity of the absorption bands of the molecule and the transitions appear at higher wavelengths. Again, the energy difference of the transition is affected. Likewise, the pH of the solvent affects the spectra as the addition or removal of photons in a molecule changes the observed electronic transitions. When there is a shift in the λmax towards longer wavelengths it is known as a red or bathochromic shift. When the shift is towards a shorter wavelength, the change is known as a blue or hypsochromic shift.

I.6 Microscopy Techniques

I.6.1 Scanning Electron Microscopy

A scanning electron microscope (SEM) scans a focused electron beam over a surface to create an image. The electrons in the beam interact with the sample, producing various signals that can be used to obtain information about the surface topography and composition.

The **scanning electron microscope (SEM)** produces images by scanning the sample with a high-energy beam of electrons. As the electrons interact with the sample, they produce secondary electrons, backscattered electrons, and characteristic X-rays. These signals are collected by one or more detectors to form images which are then displayed on the computer screen. When the electron beam hits the surface of the sample, it penetrates the sample to a depth of a few microns, depending on the accelerating voltage and the density of the sample. Many signals, like secondary electrons and X-rays, are produced as a result of this interaction inside the sample.

The main SEM components include: source of electrons, column down which electrons travel with electromagnetic lenses, electron detector, sample chamber, computer and display to view the images. Electrons are produced at the top of the column, accelerated down and passed through a combination of lenses and apertures to produce a focused beam of electrons which hits the surface of the sample. The sample is mounted on a stage in the chamber area and, unless the microscope is designed to operate at low vacuums, both the column and the chamber are evacuated by a combination of pumps. The level of the vacuum will depend on the design of the microscope.

The maximum resolution obtained in a SEM depends on multiple factors, like the electron spot size and interaction volume of the electron beam with the sample. While it cannot provide atomic resolution, some SEMs can achieve resolution below 1 nm. Typically, modern full-sized SEMs provide resolution between 1-20 nm whereas desktop systems can provide a resolution of 20 nm or more.

I.6.2 Energy Dispersive Spectroscopy (EDS)

In scanning electron microscopy, an X-ray is emitted when the electron beam displaces an inner shell electron that is replaced by an outer shell electron. Because each element has a unique energy difference between outer and inner electron shells, the X-rays that are detected yield an elemental identification. EDS data can be obtained at a point, along with a line or mapped over an area.

Sample structures can be physically examined and their elemental composition determined. Viewing three-dimensional images of microscopic structures only solves half the problem when analyzing samples. It is often necessary to collect more than imaging data to be able to identify the different elements in a specimen. Using EDS with SEM addresses this need for elemental analysis.

1.6.3 Atomic Force Microscopy (AFM)

Since the introduction of the Nobel Prize-winning scanning tunneling microscope (STM) and then the invention of the **atomic force microscopy (AFM)** from the landmark publication by Binnig, Quate, and Gerber, the field of scanning probe microscopy has exploded well beyond using interatomic forces to image topography on the nanometer scale. The ability to measure intermolecular forces and see atoms is scientifically tantalizing. Topography imaging alone does not always provide the answers that researchers need and the surface topology often does not correlate to the material properties. For these reasons, advanced imaging modes have been developed to provide quantitative data on a variety of surfaces. Now, many material properties can be determined with AFM techniques, including friction, electrical forces, capacitance, magnetic forces, conductivity, viscoelasticity, surface potential, and resistance.

The atomic force microscope was developed to overcome a basic drawback with **Scanning Tunneling Microscopy** (**STM**): it can only image conducting or semiconducting surfaces. The AFM has the advantage of imaging almost any type of surface, including polymers, ceramics, composites, glass, and biological samples.

Analogous to how a Scanning Tunneling Microscope works, a sharp tip is raster-scanned over a surface using a feedback loop to adjust parameters needed to image a surface. Unlike STM, the AFM does not need a conducting sample. Instead of using the quantum mechanical effect of tunneling, atomic forces are used to map the tip-sample interaction.

Often referred to as scanning probe microscopy (SPM), there are Atomic Force Microscopy techniques for almost any measurable force interaction – van der Waals, electrical, magnetic, thermal. For some of the more specialized techniques, modified tips and software adjustments are needed. In addition to Angstrom-level positioning and feedback loop control, there are 2 components typically included in Atomic Force Microscopy: Deflection and Force Measurement.

Traditionally, most Atomic Force Microscopes use a laser beam deflection system where a laser is reflected from the back of the reflective AFM lever and onto a position-sensitive detector. AFM tips and cantilevers are typically micro-fabricated from Si or Si_3N_4. Typical tip radius is from a few to 10s of nm. Because the AFM relies on the forces between the tip and sample, these forces impact AFM imaging. The force is not measured directly, but calculated by measuring the deflection of the lever, knowing the stiffness of the cantilever. AFM has a feedback loop using the laser deflection to control the force and tip position. As shown, a laser is reflected from the back of a cantilever that includes the AFM tip. As the tip interacts with the surface, the laser position on the photodetector is used in the feedback loop to track the surface for imaging and measuring.

I.7 Optical Profilometry

Profilometry is a technique used to extract **topographical data** from a surface. This can be a single point, a line scan or even a full three-dimensional scan. The purpose of profilometry is to get surface morphology, step heights and surface roughness.
Such technique can be employed to characterise the crystalline structures that appear in materials such as polymers, fibres and biological materials. This can be done using a physical probe or by using light. All profilometers consist of at least two parts – a detector and a sample stage. The detector is what determines where the points on the sample are and the sample stage is what holds the sample. In some systems, the sample stage moves to allow for measurement, in others the detector moves and in some both move. There are two types of profilometers: stylus vs optical.

I.7.1 Stylus profilometry

It requires force feedback and physically touching the surface, so while it is extremely sensitive and provides high Z resolution, it is sensitive to soft surfaces and the probe can become contaminated by the surface. This technique can also be destructive to some surfaces. Stylus profilometers use a probe to detect the surface, physically moving a probe along the surface in order to acquire the surface height. This is done mechanically with a feedback loop that monitors the force from the sample pushing up against the probe as it scans along the surface. The feedback system is used to keep the arm with a specific amount of torque on it, known as the 'setpoint'. The changes in the Z position of the arm holder can then be used to reconstruct the surface.
Because a stylus profilometer involves physical movements in X, Y and Z while maintaining contact with the surface, it is slower than non-contact techniques. The stylus tip size and shape can influence the measurements and limit the lateral resolution.

I.7.2 Optical profilometry

It uses light instead of a physical probe. This can be done a number of ways. The key component to this technique is directing the light in a way that it can detect the surface in 3D. Examples include optical interference, using a confocal aperture, focus and phase detection, and projecting a pattern onto the optical image.

Appendix II

List of Publications

II.1 *Challenges in the electrochemical (bio)sensing of nonelectroactive food and environmental contaminants*

Giulia Moro, Karolien De Wael, Ligia Maria Moretto

Current Opinion in Electrochemistry, 16, (**2019**), 57-65

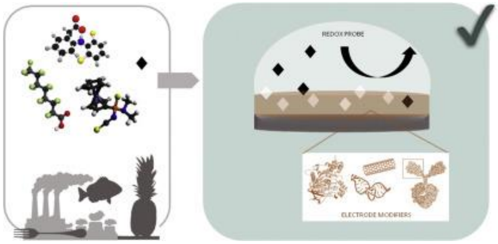

Electrochemical detection of nonelectroactive contaminants can be successfully faced via the use of indirect detection strategies. These strategies can provide sensitive and selective responses often coupled with portable and user-friendly analytical tools. Indirect detection strategies are usually based on the change in the signal of an electroactive probe, induced by the presence of the target molecule at a modified electrode. This critical review aims at addressing the developments in indirect electrosensing strategies for nonelectroactive contaminants in food and environmental analysis in the last few years. Emphasis is given to the strategy design, the electrode modifiers used and the feasibility of technological transfer.

https://doi.org/10.1016/j.coelec.2019.04.019

II.2 *Conductive imprinted polymers for the direct electrochemical detection of β-lactam antibiotics: The case of cefquinome*

Giulia Moro, Fabio Bottari, Nick Sleegers, AncaFlorea, Todd Cowen, Ligia Maria Moretto, Sergey Piletsky Karolien De Wael,

Sensors and Actuators B: Chemical, 297, (**2019**), 126786

A biomimetic sensor for cefquinome (CFQ) was designed at multi-walled carbon nanotubes modified graphite screen-printed electrodes (MWCNTs-G-SPEs) as a proof-of-concept for the creation of a sensors array for β-lactam antibiotics detection in milk. The sensitive and selective detection of antibiotic residues in food and environment is a fundamental step in the elaboration of prevention strategies to fight the insurgence of antimicrobial resistance (AMR) as recommended by authorities around the world (EU, WHO, FDA). The detection strategy is based on the characteristic electrochemical fingerprint of the target antibiotic cefquinome. A conductive electropolymerized molecularly imprinted polymer (MIP) coupled with MWCNTs was found to be the optimal electrode modifier, able to provide an increased selectivity and sensitivity for CFQ detection. The design of CFQ-MIP was facilitated by the rational selection of the monomer, 4-aminobenzoic acid (4-ABA). The electropolymerization process of 4-ABA have not been fully elucidated yet; for this reason a thorough study and optimization of electropolymerization conditions was performed to obtain a conductive and stable

poly(4-ABA) film. The modified electrodes were characterized by electrochemical impedance spectroscopy (EIS), scanning electron microscopy (SEM) and cyclic voltammetry (CV). CFQ-MIP were synthesized at MWCNT-G-SPEs by electropolymerization in pH≈1 (0.1 M sulphuric acid) with a monomer:template ratio of 5:1. Two different analytical protocols were tested (single and double step detection) to minimize unspecific adsorptions and improve the sensitivity. Under optimal conditions, the lowest CFQ concentration detectable by square wave voltammetry (SWV) at the modified sensor was 50 nM in 0.1 M phosphate buffer pH 2.
https://doi.org/10.1016/j.snb.2019.126786

II.3 *Disposable electrodes from waste materials and renewable sources for (bio)electroanalytical applications*

Giulia Moro, Fabio Bottari, Joren Van Loon, Els Du Bois, Karolien De Wael, Ligia Maria Moretto,
Biosensors and Bioelectronics, 146, (**2019**), 111758

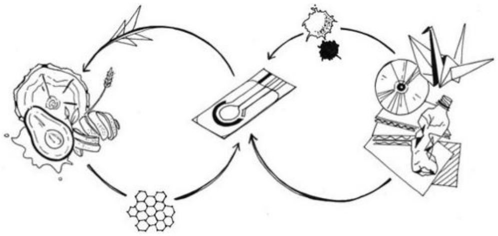

The numerous advantages of disposable and screen-printed electrodes (SPEs) particularly in terms of portability, sensibility, sensitivity and low-cost led to the massive application of these electroanalytical devices. To limit the electronic waste and recover precious materials, new recycling processes were developed together with alternative SPEs fabrication procedures based on renewable, biocompatible sources or waste materials, such as paper, agricultural by-products or spent batteries. The increased interest in the use of eco-friendly materials for electronics has given rise to a new generation of highly performing green modifiers. From paper based electrodes to disposable electrodes obtained from CD/DVD, in the last decades considerable efforts were devoted to reuse and recycle in the field of electrochemistry. Here an overview of recycled and recyclable disposable electrodes, sustainable electrode modifiers and alternative fabrication processes is proposed aiming to provide meaningful examples to redesign the world of disposable electrodes.
https://doi.org/10.1016/j.bios.2019.111758

II.4 *Improved Synthesis, Anticancer Activity and Electrochemical Characterization of Unusual Zwitterionic Palladium Compounds with a Ten-Term Coordinative Ring*
Thomas Scattolin, **Giulia Moro**, Flavio Rizzolio, Claudio Santo, Ligia Maria Moretto, Fabiano Visentin,
Chemistry Select, 4(36), (**2019**) 10911-10919

A new improved synthetic protocol for the preparation of uncommon zwitterionic palladium(II) complexes with a ten-term coordinative ring is reported. A suitable combination of reaction solvent and temperature allows to drastically reduce the reaction time and increase the yield. A detailed kinetic study, implemented by theoretical DFT calculations, clarifies and quantifies this solvent effect. The antiproliferative activity of the synthesized complexes was tested toward eight different cancer cell lines. The mesityl derivative showed potent and selective cytotoxicity toward several types of cancer cell lines, with IC50 values lower than cisplatin. Additionally, the anticancer activity against cisplatin-sensitive and cisplatin-resistant ovarian cancer cells suggested a different mechanism of action with respect to traditional platinum chemotherapeutics. Aiming to easily determine these promising metallo-drugs, a voltammetric study of their electrochemical fingerprint was carried out. For both compounds a suitable signal, ascribed to the reduction of the metallic center from palladium(II) to palladium(0), was identified and further investigated by Differential Pulse Voltammetry.
https://doi.org/10.1002/slct.201902316

II.5 *Redesigning an Electrochemical MIP Sensor for PFOS: Practicalities and Pitfalls*
Giulia Moro, Davide Cristofori, Fabio Bottari, Elti Cattaruzza, Karolien De Wael, Ligia Maria Moretto,
Sensors, 19(20), (**2019**), 4433

There is a growing interest in the technological transfer of highly performing electrochemical sensors within portable analytical devices for the in-situ monitoring of environmental contaminants, such as perfluorooctanesulfonic acid (PFOS). In the redesign of biomimetic sensors, many parameters should be taken into account from the working conditions to the electrode surface roughness. A complete characterization of the surface modifiers can help to avoid time-consuming optimizations and better interpret the sensor responses. In the present study, a molecularly imprinted polymer electrochemical sensor (MIP) for PFOS optimized on gold disk electrodes was redesigned on commercial gold screen-printed electrodes. However, its performance investigated by differential pulse voltammetry was found to be poor. Before proceeding with further optimization, a morphological study of the bare and modified electrode surfaces was carried out by scanning electron microscopy–energy-dispersive X-ray spectrometry

(SEM–EDS), atomic force microscopy (AFM) and profilometry revealing a heterogeneous distribution of the polymer strongly influenced by the electrode roughness. The high content of fluorine of the target-template molecule allowed to map the distribution of the molecularly imprinted polymer before the template removal and to define a characterization protocol. This case study shows the importance of a multi-analytical characterization approach and identifies significant parameters to be considered in similar redesigning studies.
https://doi.org/10.3390/s19204433

II.6 *Bio- and Biomimetic Receptors for Electrochemical Sensing of Heavy Metal Ions*

Angela Maria Stortini, Maria Antonietta Baldo, **Giulia Moro**, Federico Polo, Ligia Maria Moretto,
Sensors, 20(23), (**2020**), 6800.

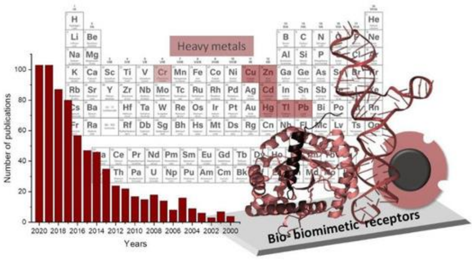

Heavy metals ions (HMI), if not properly handled, used and disposed, are a hazard for the ecosystem and pose serious risks for human health. They are counted among the most common environmental pollutants, mainly originating from anthropogenic sources, such as agricultural, industrial and/or domestic effluents, atmospheric emissions, etc. To face this issue, it is necessary not only to determine the origin, distribution and the concentration of HMI but also to rapidly (possibly in real-time) monitor their concentration levels in situ. Therefore, portable, low-cost and high performing analytical tools are urgently needed. Even though in the last decades many analytical tools and methodologies have been designed to this aim, there are still several open challenges. Compared with the traditional analytical techniques, such as atomic absorption/emission spectroscopy, inductively coupled plasma mass spectrometry and/or high-performance liquid chromatography coupled with electrochemical or UV–VIS detectors, bio- and biomimetic electrochemical sensors provide high sensitivity, selectivity and rapid responses within portable and user-friendly devices. In this review, the advances in HMI sensing in the last five years (2016–2020) are addressed. Key examples of bio and biomimetic electrochemical, impedimetric and electrochemiluminescence-based sensors for Hg^{2+}, Cu^{2+}, Pb^{2+}, Cd^{2+}, Cr^{6+}, Zn^{2+} and Tl^{+} are described and discussed.
https://doi.org/10.3390/s20236800

II.7 *Covalent immobilization of delipidated human serum albumin on poly(pyrrole-2-carboxylic) acid film for the impedimetric detection of perfluorooctanoic acid*

Giulia Moro, Fabio Bottari, Stefano Liberi, Sonia Covaceuszach, Alberto Cassetta, Alessandro Angelini, Karolien De Wael, Ligia Maria Moretto,
Bioelectrochemistry, 134, (**2020**), 107540

The immobilization of biomolecules at screen printed electrodes for biosensing applications is still an open challenge. To enrich the toolbox of bioelectrochemists, graphite screen printed electrodes (G-SPE) were modified with an electropolymerized film of pyrrole-2-carboxilic acid (Py-2-COOH), a pyrrole derivative rich in carboxylic acid functional groups. These functionalities are suitable for the covalent immobilization of biomolecular recognition layers. The electropolymerization was first optimized to obtain stable and conductive polymeric films, comparing two different electrolytes: sodium dodecyl sulphate (SDS) and sodium perchlorate. The G-SPE modified with Py-2-COOH in 0.1 M SDS solution showed the required properties and were further tested. A proof-of-concept study for the development of an impedimetric sensor for perfluorooctanoic acid (PFOA) was carried out using the delipidated human serum albumin (hSA) as bioreceptor. The data interpretation was supported by size exclusion chromatography and small-angle X-ray scattering (SEC-SAXS) analysis of the bioreceptor-target complex and the preliminary results suggest the possibility to further develop this biosensing strategy for toxicological and analytical studies.
https://doi.org/10.1016/j.bioelechem.2020.107540

II.8 *Electropolymerized o-Phenylenediamine on Graphite Promoting the Electrochemical Detection of Nafcillin*

Fabio Bottari, **Giulia Moro**, Nick Sleegers, Anca Florea, Todd Cowen, Sergey Piletsky, Alexander L. N. van Nuijs, Karolien De Wael,
Electroanalysis, 32, (**2020**), 135 –141

By combining molecular modelling and electrochemistry we envision the creation of modified electrodes tailored for a more sensitive and selective detection of a single analyte. In this study we report on a graphite screen printed electrode modified with electropolymerized o-phenylenediamine, selected by rational design, which promotes the detection of nafcillin (NAF), an antibiotic. Parameters such as monomer concentration, pH and number of electropolymerization cycles were optimized to obtain the highest current signal for the target upon amperometric detection. NAF identification was based on the redox process at +1.1 V (vs pseudo Ag), ascribed to the oxidation of the C-7 side chain. With the optimized modification protocol, a two-fold increase in nafcillin signal could be obtained: the calibration plot in 0.1 M Britton-Robinson buffer pH 4

showed a limit of detection of 80 nM with improved sensitivity and reproducibility (RSD<5 %) compared to the detection at non-modified electrodes.
https://doi.org/10.1002/elan.201900397

II.9 *Unlocking the full power of electrochemical fingerprinting for on-site sensing applications*

G. Moro, H. Barich, K. Driesen, N. Felipe Montiel, L. Neven, C. Domingues Mendonça, S. Thiruvottriyur Shanmugam, E. Daems, K. De Wael
Analytical and Bioanalytical Chemistry, 412, (**2020**) 5955–5968

Electrochemical sensing for the semi-quantitative detection of biomarkers, drugs, environmental contaminants, food additives, etc. shows promising results in point-of-care diagnostics and on-site monitoring. More specifically, electrochemical fingerprint (EF)–based sensing strategies are considered an inviting approach for the on-site detection of low molecular weight molecules. The fast growth of electrochemical sensors requires defining the concept of direct electrochemical fingerprinting in sensing. The EF can be defined as the unique electrochemical signal or pattern, mostly recorded by voltammetric techniques, specific for a certain molecule that can be used for its quantitative or semi-quantitative identification in a given analytical context with specified circumstances. The performance of EF-based sensors can be enhanced by considering multiple features of the signal (i.e., oxidation or reduction patterns), in combination with statistical data analysis or sample pretreatments or by including electrode surface modifiers to enrich the EF. In this manuscript, some examples of EF-based sensors, strategies to improve their performances, and open challenges are discussed to unlock the full power of electrochemical fingerprinting for on-site sensing applications.
10.3390/s20236800

II.10 *Mapping the gaps in chemical analysis for the characterisation of aptamer-target interactions*

Elise Daems, **Giulia Moro**, RuiCampos, Karolien De Wael
TrAC Trends in Analytical Chemistry, 142, (**2021**), 116311

Aptamers are promising biorecognition elements with a wide applicability from therapeutics to biosensing. However, to successfully use these biomolecules, a complete characterisation of their binding performance in the presence of the target is crucial. Several multi-analytical approaches have been reported including techniques to describe kinetic and thermodynamic aspects of the aptamer-target interaction, and techniques which allow an in-depth understanding of the aptamer-target structures. Recent literature shows the need of a critical data interpretation, a combination of characterisation techniques and suggests the key role of the characterisation protocol design. Indeed, the final application of the aptamer should be considered before choosing the characterisation method. All the limitations and capabilities of the analytical tools in use for aptamer characterisation should be taken into account. Here, we present a critical overview of the current methods and multi-analytical approaches to study aptamer-target binding, aiming to provide researchers with guidelines for the design of characterisation protocols.
https://doi.org/10.1016/j.trac.2021.116311

II.11 *Unveiling the binding mode of perfluorooctanoic acid to human serum albumin*

Lorenzo Maso, Matteo Trande, Stefano Liberi, **Giulia Moro**, Elise Daems, Sara Linciano, Frank Sobott, Sonia Covaceuszach, Alberto Cassetta, Silvano Fasolato, Ligia M. Moretto, Karolien De Wael, Laura Cendron, Alessandro Angelini
Protein Science, 30, (**2021**), 830–841

Perfluorooctanoic acid (PFOA) is a toxic compound that is absorbed and distributed throughout the body by noncovalent binding to serum proteins such as human serum albumin (hSA). Though the interaction between PFOA and hSA has been already assessed using various analytical techniques, a high resolution and detailed analysis of the binding mode is still lacking. We report here the crystal structure of hSA in complex with PFOA and a medium-chain saturated fatty acid (FA). A total of eight distinct binding sites, four occupied by PFOAs and four by FAs, have been identified. In solution binding studies confirmed the 4:1 PFOA-hSA stoichiometry and revealed the presence of one high and three low affinity binding sites. Competition experiments with known hSA-binding drugs allowed locating the high affinity binding site in sub-domain IIIA. The elucidation of the molecular basis of the interaction between PFOA and hSA might provide not only a better assessment of the absorption and elimination mechanisms of these compounds in vivo but also have implications for the development of novel molecular receptors for diagnostic and biotechnological applications.
https://doi.org/10.1002/pro.4036

II.12 *Chemical analysis and computed tomography of metallic inclusions in Roman glass to unveil ancient coloring methods*

Francesca Di Turo, **Giulia Moro**, Alessia Artesani, Fauzia Albertin, Matteo Bettuzzi,
Davide Cristofori, Ligia Maria Moretto, Arianna Traviglia
Scientific Reports, 11, (**2021**), 11187

This paper describes the analysis of two near-spherical metallic inclusions partially incorporated within two Roman raw glass slags in order to elucidate the process that induced their formation and to determine whether their presence was related to ancient glass colouring processes. The theory of metallic scraps or powder being used in Roman times for glass-making and colouring purposes is widely accepted by the archaeological scientific community, although the assumption has been mainly based on oral traditions and documented medieval practices of glass processing. The analysis of the two inclusions carried out by X-ray computed tomography, electrochemical analyses, and scanning electron microscopy, revealed their material composition, corrosion and internal structure. Results indicate that the two metallic bodies originated when, during the melting phase of glass, metal scraps were added to colour the material: the colloidal metal–glass system reached then a supersaturation condition and the latter ultimately induced metal expulsion and agglomeration. According to the authors' knowledge, these two inclusions represent the first documented and studied finds directly associated with the ancient practice of adding metallic agents to colour glass, and their analysis provides clear insights into the use of metallic waste in the glass colouring process.
https://doi.org/10.1038/s41598-021-90541-8

II.13 *Native mass spectrometry for the design and selection of protein bioreceptors for perfluorinated compounds*

Elise Daems, **Giulia Moro**, Herald Berghmans, Ligia M. Moretto, Silvia Dewilde,
Alessandro Angelini, Frank Sobott, Karolien De Wael,
Analyst, 146, (**2021**), 2065-2073

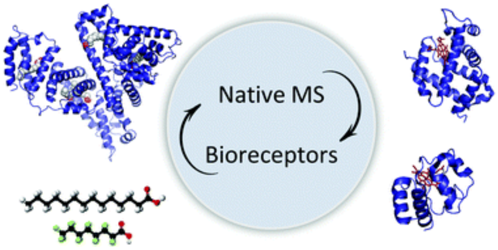

Biosensing platforms are answering the increasing demand for analytical tools for environmental monitoring of small molecules, such as per- and polyfluoroalkyl substances (PFAS). By transferring toxicological findings in bioreceptor design we can develop innovative pathways for biosensor design. Indeed, toxicological studies provide fundamental information about PFAS-biomolecule complexes that can help evaluate the applicability of the latter as bioreceptors. The toolbox of native mass

spectrometry (MS) can support this evaluation, as shown by the two case studies reported in this work. The analysis of model proteins' (i.e. albumin, haemoglobin, cytochrome c and neuroglobin) interactions with well-known PFAS, such as perfluorooctanoic acid (PFOA) and perfluorooctanesulfonic acid (PFOS), demonstrated the potential of this native MS screening approach. In the first case study, untreated albumin and delipidated albumin were compared in the presence and absence of PFOA confirming that the delipidation step increases albumin affinity for PFOA without affecting protein stability. In the second case study, the applicability of our methodology to identify potential bioreceptors for PFOS/PFOA was extended to other proteins. Structurally related haemoglobin and neuroglobin revealed a 1 : 1 complex, whereas no binding was observed for cytochrome c. These studies have value as a proof-of-concept for a general application of native MS to identify bioreceptors for toxic compounds.
https://doi.org/10.1039/D0AN02005B

II.14 *Nanocoated fiber label-free biosensing for perfluorooctanoic acid detection by lossy mode resonance*

Giulia Moro, Francesco Chiavaioli, Stefano Liberi, Pablo Zubiate, Ignacio Del Villar, Alessandro Angelini, Karolien De Wael, Francesco Baldini, Ligia Maria Moretto, Ambra Giannetti,
Results in Optics, 5, (**2021**), 100123

The determination of per- and polyfluoroalkyl substances (PFAS) in environmental samples, such as drinking waters, requires the design of high performing and versatile sensing strategies. Label-free biosensing platforms based on specialty fiber optics are a valid option to face this, lossy mode resonance (LMR) fiber optic biosensors are showing remarkable performance in terms of detection limit, selectivity, and reproducibility. The detection of small molecules, such as perfluorooctanoic acid (PFOA), can be achieved with the help of well-designed biological recognition layers. In this study, the biosensing potentialities of a label-free LMR-assisted optical platform based on nanocoated fibers are investigated. Delipidated human serum albumin (hSA) was used as biological recognition layer for PFOA in aqueous solution. Different fiber functionalization protocols based on the covalent immobilization of hSA were tested. The conformational changes related to the formation of hSA/PFOA complex were followed via optical monitoring of LMR spectral shift, showing a trend that can be modeled with Langmuir adsorption isotherm. These results confirmed the potentiality of LMR-based fiber biosensors for the detection of small molecules, such as PFOA, in synthetic samples.
https://doi.org/10.3390/bios11080246

II.15 *The Role of Peptides in the Design of Electrochemical Biosensors for Clinical Diagnostics*

Patrick Severin Sfragano, **Giulia Moro**, Federico Polo, Ilaria Palchetti
Biosensors, 11(8), (**2021**), 246

Peptides represent a promising class of biorecognition elements that can be coupled to electrochemical transducers. The benefits lie mainly in their stability and selectivity toward a target analyte. Furthermore, they can be synthesized rather easily and modified with specific functional groups, thus making them suitable for the development of novel architectures for biosensing platforms, as well as alternative labelling tools. Peptides have also been proposed as antibiofouling agents. Indeed, biofouling caused by the accumulation of biomolecules on electrode surfaces is one of the major issues and challenges to be addressed in the practical application of electrochemical biosensors. In this review, we summarise trends from the last three years in the design and development of electrochemical biosensors using synthetic peptides. The different roles of peptides in the design of electrochemical biosensors are described. The main procedures of selection and synthesis are discussed. Selected applications in clinical diagnostics are also described.

https://doi.org/10.3390/bios11080246

Thank you all for having carried on PFASensing with me in these years,

Giulia

PFASensing

Non è questione di cellule